NASA Contractor Report 3149

Acoustic and Aerodynamic Performance Investigation of Inverted Velocity Profile Coannular Plug Nozzles

P. R. Knott, J. T. Blozy,
and P. S. Staid

CONTRACT NAS3-19777
FEBRUARY 1981

NASA

NASA Contractor Report 3149

Acoustic and Aerodynamic Performance Investigation of Inverted Velocity Profile Coannular Plug Nozzles

P. R. Knott, J. T. Blozy,
and P. S. Staid
General Electric Company
Cincinnati, Ohio

Prepared for
Lewis Research Center
under Contract NAS3-19777

National Aeronautics
and Space Administration

**Scientific and Technical
Information Branch**

1981

TABLE OF CONTENTS

TABLE OF CONTENTS (Continued)

TABLE OF CONTENTS (Concluded)

1.0 SUMMARY

This report, along with the companion comprehensive data report NASA CR-159575 and the wind tunnel performance test report NASA CR-2990, summarizes the test and analysis results of a one-year static acoustic and wind tunnel aerodynamic performance model-scale test program performed by the General Electric Company on unsuppressed high radius ratio coannular plug nozzle configurations with inverted velocity profiles under NASA-Lewis sponsorship. The nozzles selected for test were a parametric set of configurations applicable to dual-stream exhaust systems typical of a Variable Cycle Engine for Advanced Supersonic Transport application.

In all, seven high radius ratio coannular plug nozzles were tested statically in the General Electric's Anechoic Jet Noise Facility, and eight similar nozzle configurations were tested for wind-tunnel aerodynamic performance trends in the NASA 8x6 foot supersonic wind-tunnel. The nozzle geometric variables included outer stream radius ratio (which ranged from a value of 0.853 to 0.926), inner stream to outer stream area ratio (which ranged from a value of 0.33 to 1.56 and inner stream plug shape. The tested nozzle flow conditions were of the inverted flow type - high velocity and high temperature flows on the outside annular stream, and lower velocity and temperature flows on the inner annular stream.

When compared to a conical nozzle at the same total thrust and mass flow, the high radius ratio coannular plug nozzle was observed to have noise suppression levels of up to 7 PNdB. Further, the static and simulated flight thrust coefficient measurements at typical takeoff conditions were found to be quite good - 0.98 at static conditions and up to 0.974 at a takeoff Mach number of 0.36. In addition the following major results were obtained:

- The characteristic flow stream properties which govern the overall noise levels (OAPWL, PNL_{max}, OASPL) of high-radius-ratio coannular-plug nozzles are the mixed stream velocity, V_j^{mix} (defined as the ratio of the ideal total thrust to the ideal weight flow or specific thrust) and the mixed stream density, ρ_j^{mix}. Using only the outer stream velocity instead of the mixed stream velocity was found to be insufficient and to result in a poor data collapse. However, when correlations for SPL spectra is approached, it is fully expected that the outer-stream velocity will play a role in the proper selection of characteristic velocity (particularly for high-frequency, coannular plug-nozzle noise).

- The parametric test measurements showed that the suppression levels of high-radius-ratio coannular nozzles are influenced by the geometric and flow parameters: outer stream radius ratio, inner stream plug geometry, and inner to outer stream velocity ratio.

- The acoustic data trends observed for geometry influences when comparisons are made at the same specific thrust are: 1) increasing the inner to outer area ratio, at a fixed outer stream radius ratio, correspondingly increases the noise; 2) increasing the outer stream radius ratio, at a fixed area ratio, decreases the noise; 3) for the same area ratio and outer stream radius ratio a bent inner stream plug shape is acoustically more beneficial compared to a typical conical plug geometry; 4) the high-radius-ratio coannular nozzle configurations have a considerable effect on the spectral and directivity shaping of the noise characteristics.

- The acoustic data trends observed for the flow management influences when comparisons are made at the same specific thrust are: 1) the ratio of inner stream to outer stream velocity ratio should be chosen judiciously. At inner stream to outer stream area ratios greater than or equal to one, as much as 4 PNdB higher noise levels can be obtained if the velocity ratio is not properly selected. For area ratios less than or equal to 0.53, the selection of velocity ratio is not as important. An optimum design velocity ratio range appears to lie between 0.6 to 0.7. 2) Inner stream to outer stream weight flow ratio does not appear to be a good acoustic design parameter.

- At supercritical flow conditions, the high radius ratio coannular nozzles were also observed to yield shock broadband noise level reductions relative to a conical nozzle. Reductions of 7 dB on model scale OASPL and scaled PNL were found. The measurements also revealed that for certain conditions the coannular nozzle shock noise benefits were lost. To maintain the coannular plug nozzle shock noise level reductions it is recommended that the pressure ratios of the two flow streams be less than 3.0 and the ratio of the inner stream total pressure to the outer stream total pressure be less than one.

- The characteristic shock broadband noise parameter was found to be a mixed stream shock strength parameter, $\beta_j^{mix} = \sqrt{(M_j^{mix})^2 - 1}$ where M_j^{mix} is defined as the mixed stream Mach number based on the mixed stream velocity and mixed stream static temperature.

- The coannular plug nozzle shock noise was found to vary approximately to a $(\beta_j^{mix})^4$. The shock spectra follows a classical Doppler shift in frequency. The shock broadband noise spectra appears to have two spectral peaks - one at a low frequency and one at a higher frequency. The low frequency peak can be associated with the equivalent diameter of the total area of the nozzle, whereas the high frequency peak appears to be associated with the outer stream annulus height.

- In formulating an engineering acoustic prediction method, it was found that the mixed stream velocity will play a strong role in establishing absolute levels as well as in the selection of the spectral similitude parameters. Phenominologically it is speculated that the low frequency noise which dominates the high radius ratio coannular plug nozzle spectra at the peak noise angles will have to be characterized by concepts derived from jet acoustic propagation theories. The outer stream velocity is expected to play the role of characteristic velocity for the high frequency noise. Additionally, a separate shock noise prediction method will have to be formulated.

- At low inner flow conditions significant thrust loss resulted.

- The inner stream conical plug geometry showed 1% to 2% higher performance levels than coannular plug nozzle geometries with a bent inner plug.

2.0 INTRODUCTION

In 1973, the General Electric Company under NASA Lewis Contract NAS3-18008 initiated an exploratory scale model static acoustic and aerodynamic performance test program to obtain parametric data of unsuppressed and suppressed coannular plug nozzles. One of the key findings of this initial program was that the unsuppressed coannular plug nozzle exhibited substantial acoustic benefits with very modest performance losses. A follow-on contract was awarded whose objectives were to determine the effects of key design variables of unsuppressed coannular plug nozzles through a systematic static acoustic and wind tunnel aerodynamic performance investigation. The key nozzle geometric variables considered are radius ratio, area ratio, inner stream plug geometry, and the nozzle flow variables considered are outer stream pressures and temperatures, inner stream pressures and temperatures, and ratios of weight flow and velocity. This contractor report summarizes the major findings of this follow-on research effort. A companion report, NASA CR-159575, contains all the detailed acoustic and aerodynamic performance test measurements. Additional details of the aerodynamic performance measurements are contained in NASA CR-2990.

In all, seven acoustic models and eight aerodynamic performance models were tested. The nozzle geometric variables included outer stream radius ratio (ranging from 0.853 to 0.926), inner stream to outer stream area ratio (ranging from 0.33 to 1.53), and inner stream plug shape (a simple conical nozzle shape and a bent plug shape simulating a flap/seal arrangement). Outer stream total temperatures ranged from 400 to 970 K. Outer stream velocities ranged from 300 to 780 m/sec. Inner stream velocities ranged from 0 (the inner stream was physically blocked off, but there existed an inner stream step) to 550 m/sec and inner stream total temperatures ranged from ambient to 925 K. All tests were of the inverted flow type - high velocity and temperature flows on the outer stream, and lower velocity and temperature on the inner stream. In total, one hundred ninety-six (196) acoustic test points were taken and three hundred nine (309) aerodynamic performance test points were obtained. All configurations were of a plug nozzle type and were designed for Variable Cycle Engine (VCE) application for Advanced Supersonic Technology (AST).

However, test results have a broader relevance toward the general description of acoustic characteristics of jet mixing and shock noise for high velocity dual stream nozzles. Other relevant university and industry investigations may be found in References 2-1 through 2-7.

3.0 TEST FACILITY DESCRIPTIONS AND DATA REDUCTION PROCEDURES

In this section the acoustic and aerodynamic test facilities are described. The acoustic testing was performed in the General Electric jet noise anechoic chamber while the aerodynamic testing was performed in the NASA Lewis 8 x 6-foot supersonic wind tunnel. The data acquisition and data reduction procedures utilized in each facility are also described.

3.1 TEST FACILITY DESCRIPTIONS

3.1.1 Jet Noise Test Facility

All acoustic testing was performed in the General Electric jet noise anechoic chamber located in Evendale, Ohio, which was built to support research in the jet engine aircraft noise. The facility can accommodate model exhaust nozzle configurations ranging in size from 2 mm to 17.3 cm diameter. In Figure 3-1 a cross section of the facility is shown. This cylindrical building is 21.95 meters high and 13.1 meters in diameter. The chamber inner surfaces are lined with anechoic wedges made of Owens Fiberglass "Intermediate Service Board". The installation is designed to meet a requirement of a low frequency cut-off below 220 Hz and a 0.99 absorption coefficient above 220 Hz.

To satisfy the aspiration effect of the test models, two air inlet ducts are located at the base of the test chamber. Air is drawn through the ducts into two separate acoustically lined plenums and then through a false floor where the middle wedges are omitted, and into the chamber. The air exhausts through an exhaust stack "T" silencer system at the top of the chamber.

The facility operating domain for single and dual flow operation is shown in Figure 3-2. The two heated flows are generated by separate burners in the fan and core streams. Both streams pass through a coannular plenum which includes acoustically treated walls and internal baffles for suppression of flow noise from valves, orifices, etc., as well as for suppression of burner noise.

This facility was certified for acoustic measurements under Task 1 of the DOT/FAA High Velocity Jet Noise Source Location and Reduction Program (Contract DOT-OS-30034). The complete results are presented in Reference 3-1.

For the subject testing program a separate low flow system was developed to obain low inner flows for a portion of the test matrix. This system is described in detail in the companion comprehensive data report, NASA CR-159575.

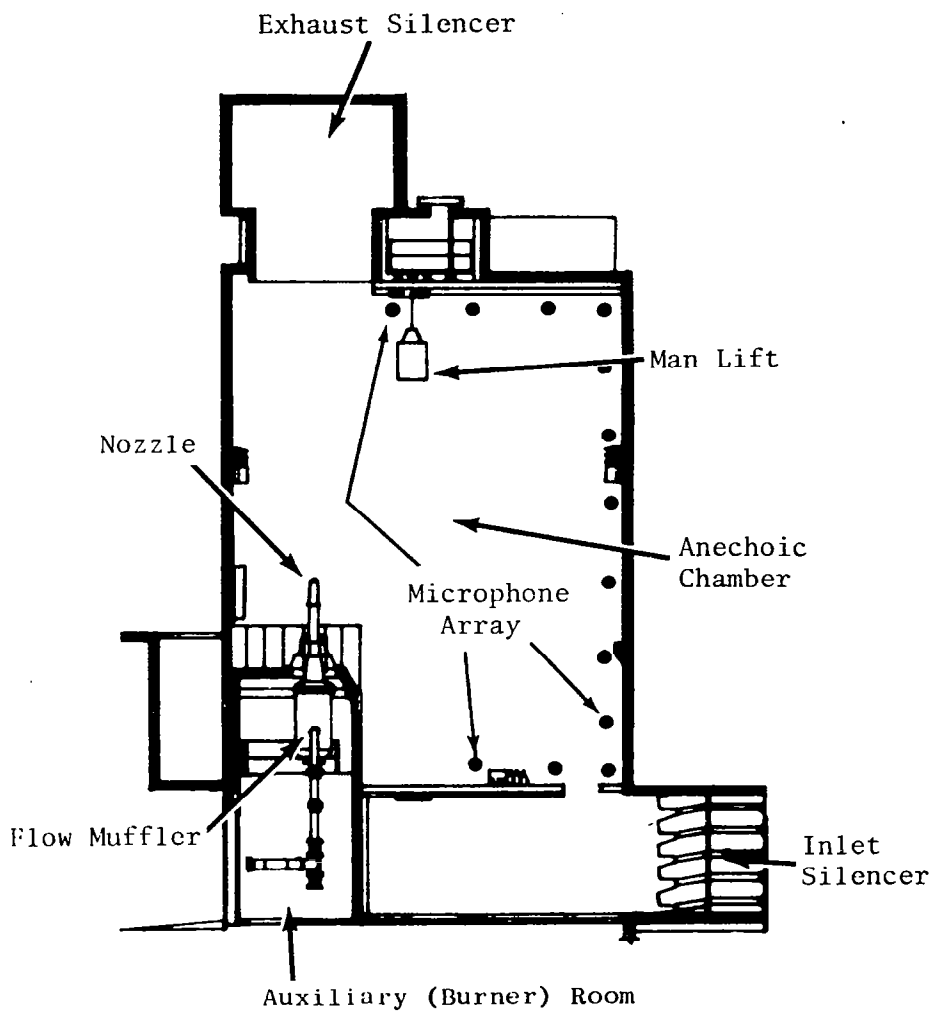

Figure 3-1. General Electric Anechoic Test Chamber Schematic.

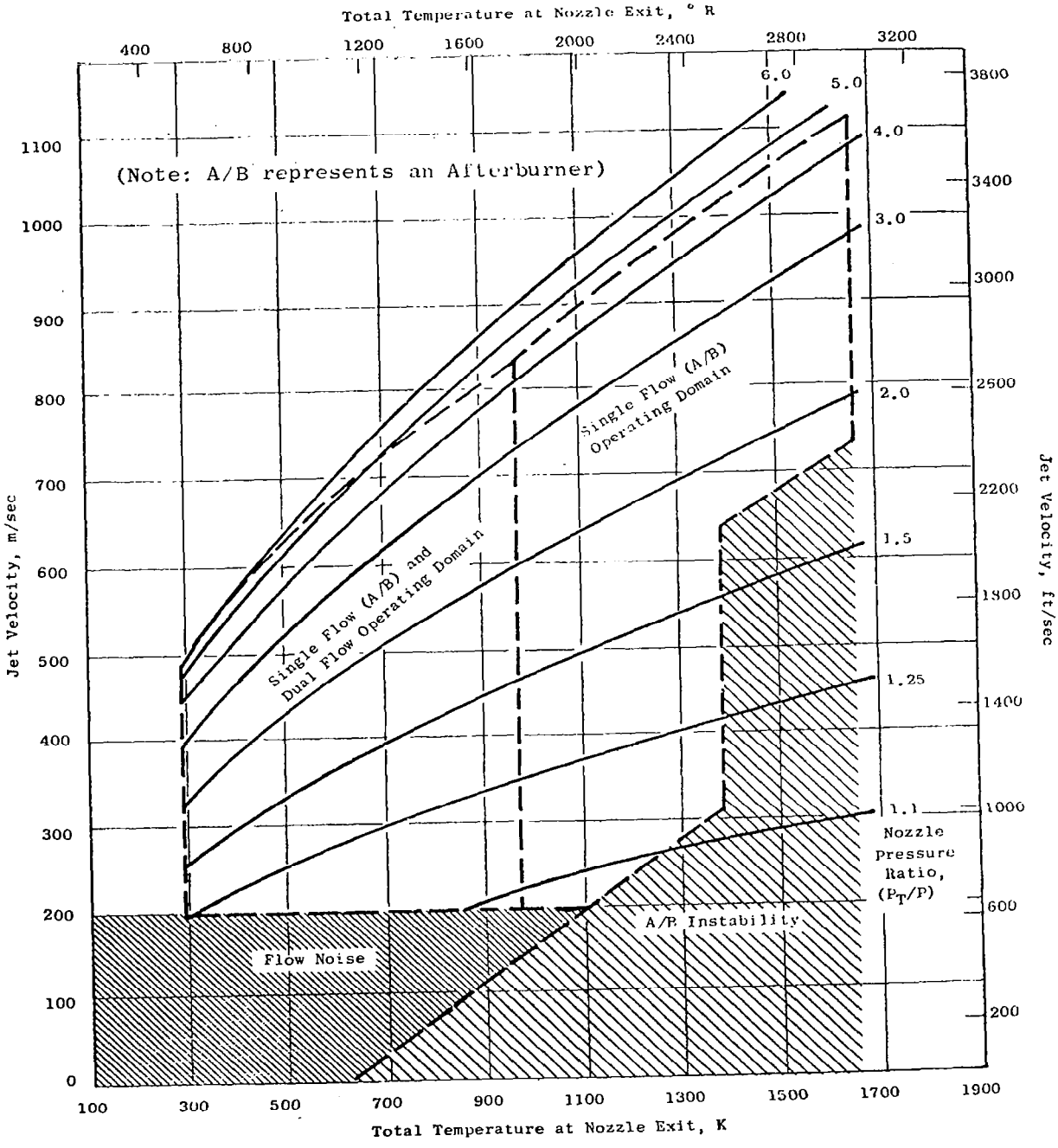

Figure 3-2. General Electric Anechoic Chamber Operating Domain.

3.1.2 Wind Tunnel Aerodynamic Performance Test Facility

The wind tunnel aerodynamic test program was conducted in the NASA Lewis 8 x 6-foot supersonic wind tunnel. The test nozzles were mounted to a 21.59 cm. diameter cylindrical sting which was supported in the test section by a perpendicular strut connected to the tunnel ceiling. A schematic illustrating this mounting system is shown in Figure 3-3. Air was supplied to the model through tubes running down the strut and emptying into coannular air passages which carried the air aft to the model. The air source was a continuous supply of 310.28 N/cm^2 compressor air which passed through a system of control valves, flow meters, and into the strut. The outer nozzle air was metered through a choked venturi 3.1699 cm. in diameter at the throat. The inner nozzle air supply was metered through either a 2.8951 cm. or a 1.0122 cm. diameter choked venturi, depending on the flow rate required. The air was directed down the strut through supply tubes fixed to the tunnel ceiling at the top and connected to the model flow passages at the bottom. Air flow from the supply tubes entered the model perpendicular to the sting axis and thus created no entering momentum force on the load cell.

The nozzle thrust was measured with a load cell mounted in the forward portion of the sting. The load cell was calibrated by assembling the Supersonic Tunnel Association (STA) model on the sting and applying a known axial force along the centerline of the model and load cell. The correlation of the known applied force and the millivolt output of the load cell comprised the desired calibration. This facility is described in detail in Reference 3-3.

3.2 DATA ACQUISITION AND REDUCTION PROCEDURES

3.2.1 Acoustic Procedures

3.2.1.1 Acoustic Data Acquisition System

A schematic of the microphone data acquisition system used to obtain the acoustic data during testing in the chamber is shown on Figure 3-4. This system has been optimized for obtaining the acoustic data up through the 80 kHz 1/3-octave center frequency. The microphone used to obtain 80 kHz data is the B&K 4135, 0.64 cm. condenser microphone for far-field measurements. All testing is conducted with microphone grid caps removed to obtain the best frequency response. The cathode followers used in the chamber are transistorized B&K 2619's for optimum frequency response and lower inherent system noise characteristics relative to the 2615 cathode follower. All systems utilize the B&K 2801 power supply operated in the direct mode.

The output of the power supply is connected to a line driver adding 10 dB of amplification to the signal as well as adding "pre-emphasis" to the high frequency portion of the spectrum. The net effect of this amplifier is a 10 dB gain at all frequencies, plus an additional 3 dB at 40 kHz and 6 dB at 80 kHz due to "pre-emphasis", increasing the ability to measure low amplitude high frequency data. In order to remove low frequency noise, high-pass filters with attenuations of approximately 26 dB at 12.5 Hz decreasing to 0 dB at 200 Hz, were installed in the system.

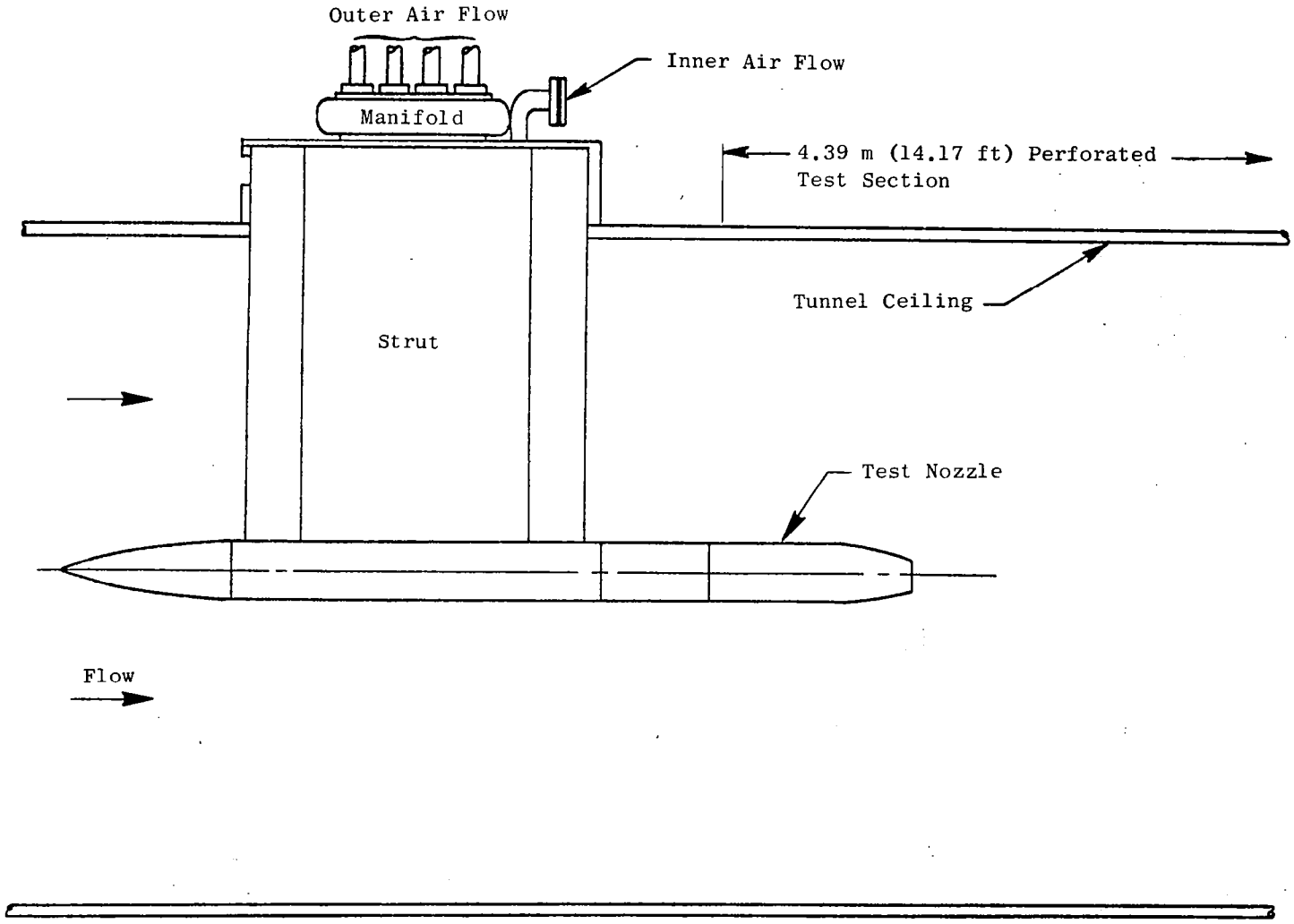

Figure 3-3. Schematic of Wind Tunnel Model Mount System.

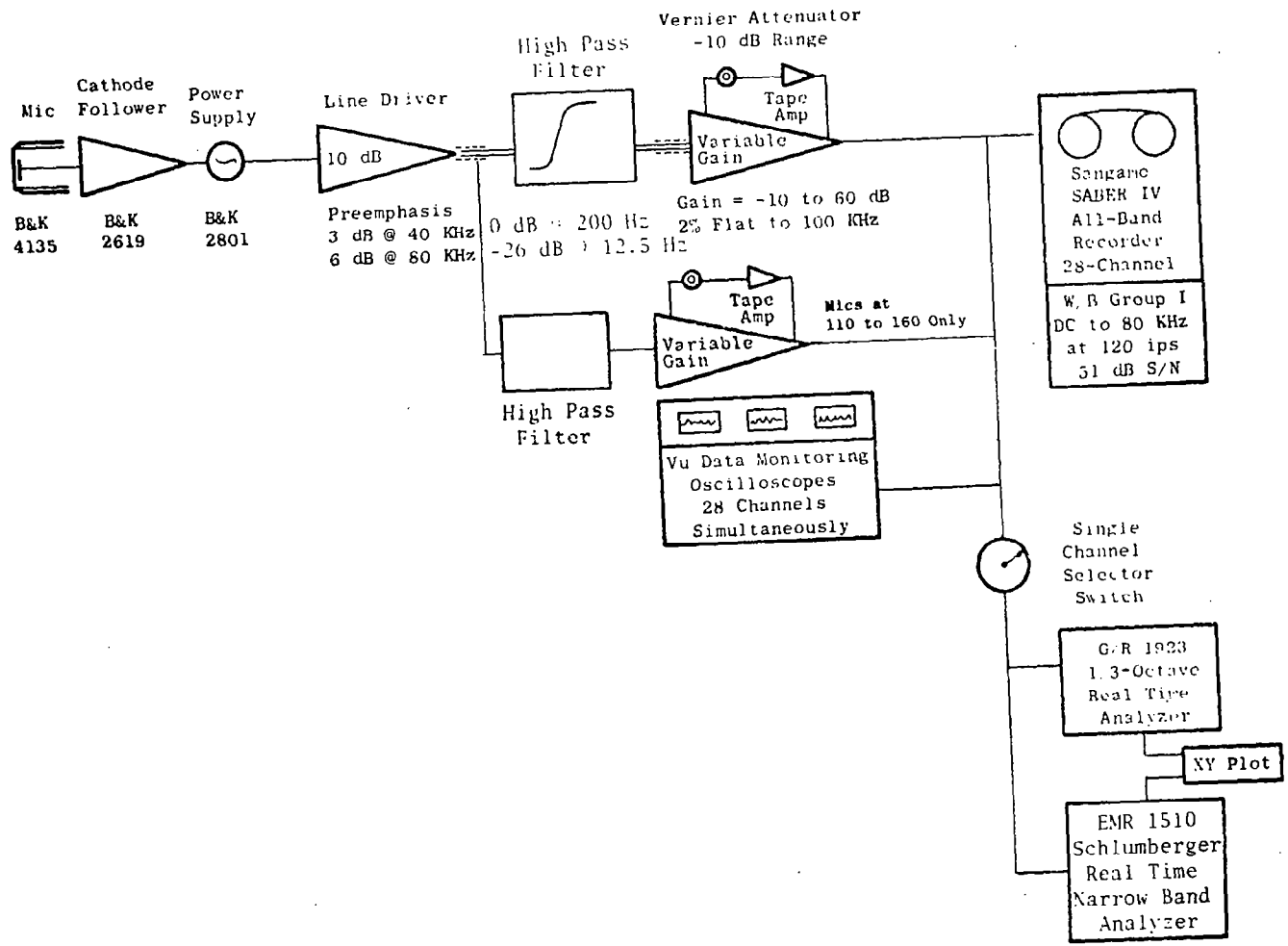

Figure 3-4. Acoustic Data Acquisition System.

The tape recorder amplifiers have a variable gain from -10 dB to +60 dB in 10 dB steps and a gain trim capability for normalizing incoming signals. The prime system used for recording acoustic data is a Sangamo/Sabre IV, 28-track FM recorder. The system is set up for Wideband Group I (intermediate band double extended) at 120 ips tape speed. Operating at 120 ips tape speed provides the improved dynamic range necessary for obtaining the high frequency/ low amplitude portion of the acoustic signal. The tape recorder is set up for ±40% carrier deviation with a recording level of 8 volts peak-to-peak. During recording, the signal is displayed on a calibrated master oscilloscope, and signal gain is adjusted to maximum without exceeding the 8 volt peak-to-peak level.

High-pass filters were incorporated in the acoustic data acquisition systems to enhance the high frequency data previously lost in the tape recorder electronic noise floor for microphones from 110° - 160°. The microphone signal below the 20 kHz 1/3-octave band was filtered out, and the gain was increased to boost the signal to noise ratio. For microphones from 110° - 160°, both the filtered and unfiltered signals were recorded on tape. For data below 20 kHz the unfiltered signal was used to calculate the sound pressure levels, while for high frequencies the filtered signal was used. The entire jet noise spectra at a given angle was then obtained by computationally merging these two spectra. Figure 3-5 illustrates how the high frequency spectrum was improved using this technique.

3.2.1.2 Acoustic Data Reduction

Standard data reduction is conducted in the General Electric AEG Instrumentation and Data Room (IDR). As shown in Figure 3-6, the data tapes are played back on a CBC3700B tape deck with electronics capable of reproducing signal characteristics within the specifications indicated for Wideband Group I. An automatic shuttling control is incorporated in the system. In normal operation, a tone is inserted on the recorder in the time slot designed for data analysis. Tape control automatically shuttles the tape initiating an integration start signal to the analyzer at the tone as the tape moves in its forward motion. This motion continues until an "intregation complete" signal is received from the analyzer at which time the tape direction is reversed and at the tone the tape restarts in the forward direction advancing the channel to be analyzed until all the channels have been processed. A time code generator is also utilized to signal tape position of the readings as directed by the computer program control. After each total reading is completed, the number of tape channels at each point is advanced to the next reading.

All 1/3-octave analysis are performed on a General Radio 1921 1/3-octave analyzer. Normal integration time is set for 32 seconds to ensure good interaction for the low frequency content. The analyzer has 1/3-octave filter sets from 12.5 Hz to 100 kHz, and has a rated accuracy of ±1/4 dB in each band. Each data channel is passed through an interface to the GEPAC 30 computer where the data is corrected for the frequency response of the microphone and the data acquisition system, corrected to Standard day (50° F, 70% RH) atomspheric attenuation conditions per SAE ARP866 Standards, and

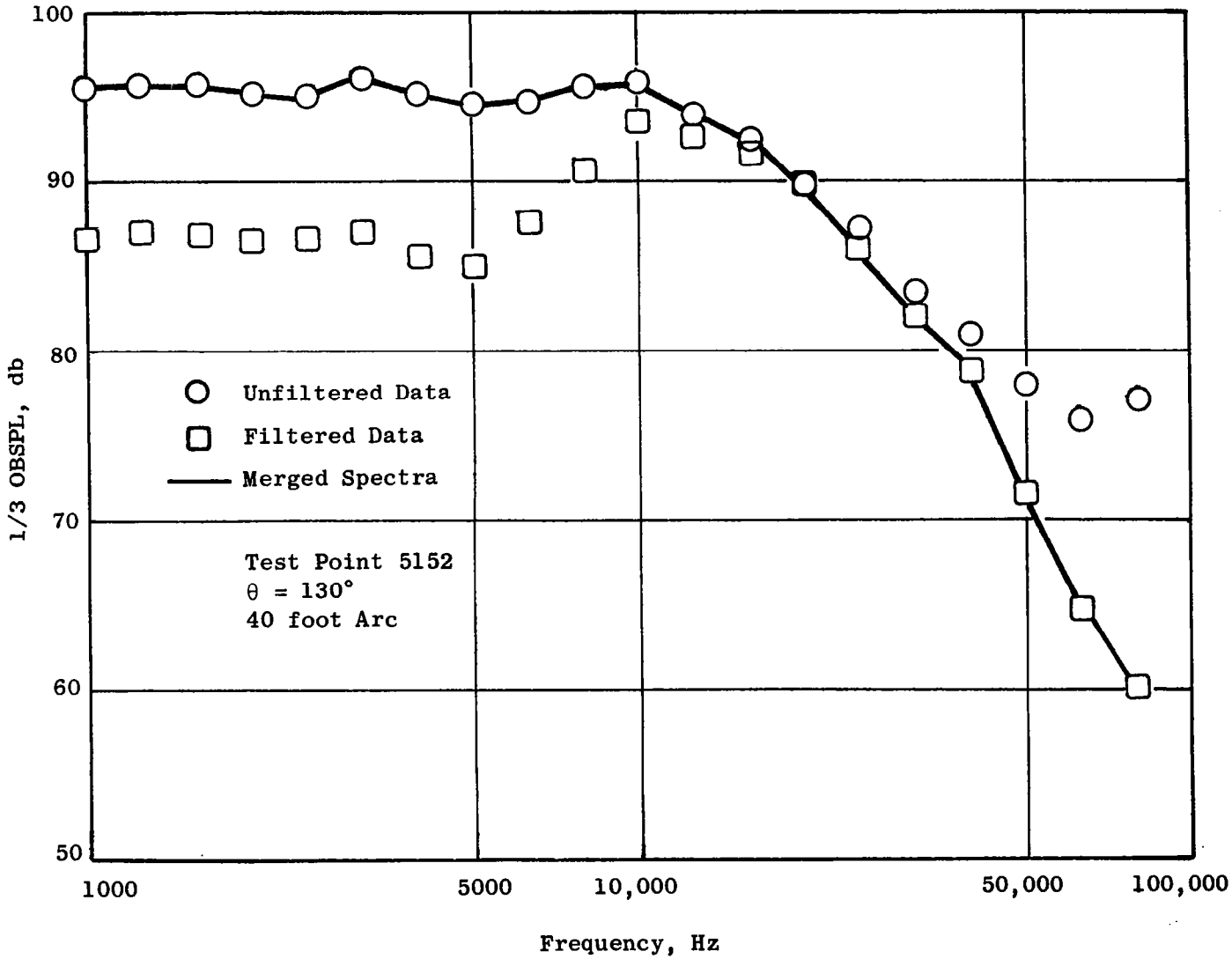

Figure 3-5. Effect of Dual Filter System in Measured High Frequency Data.

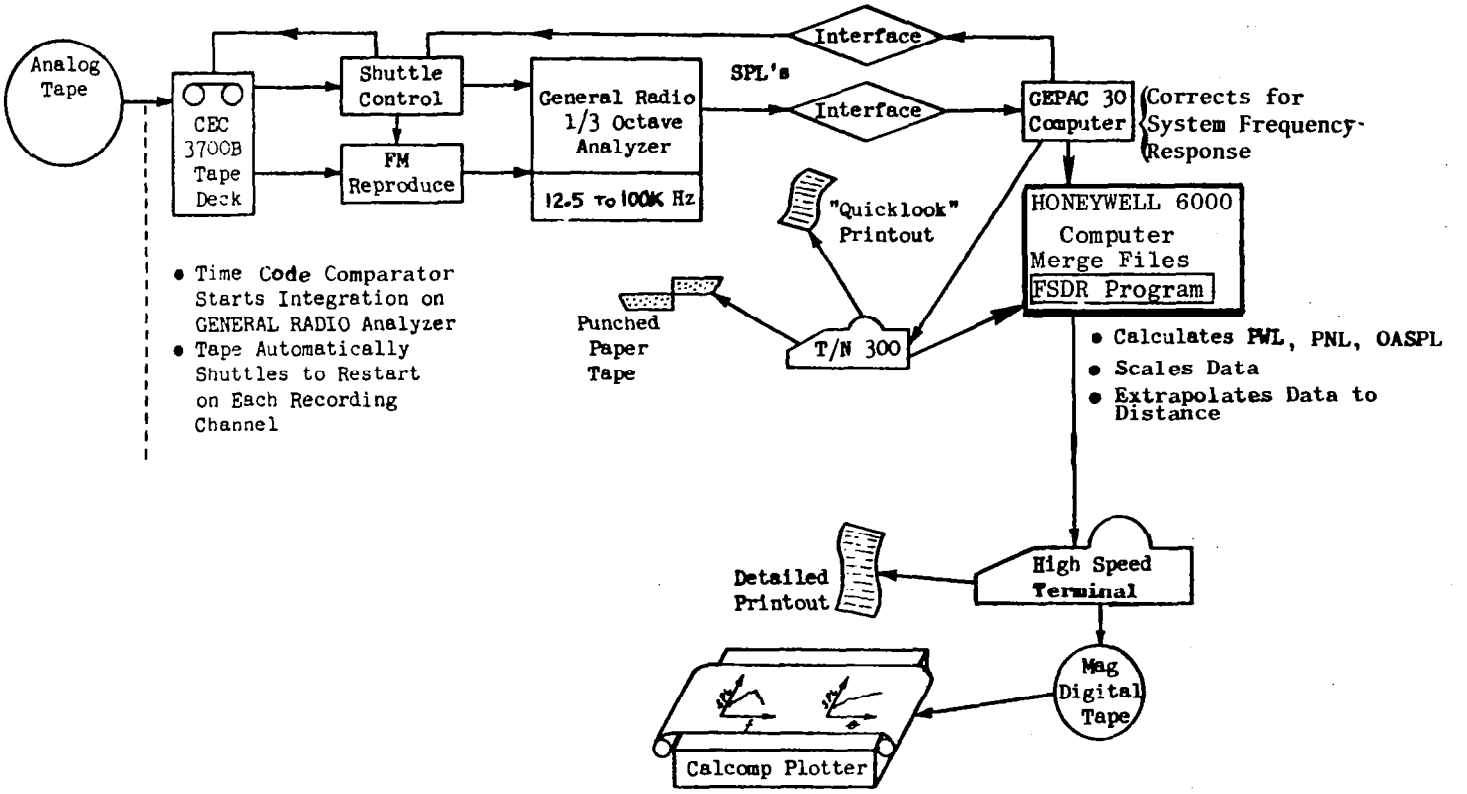

Figure 3-6. Acoustic Data Reduction System.

processed to calculate the perceived noise level and OASPL from the spectra. For calculation of the acoustic power, scaling to other nozzle sizes, or extrapolation to different farfield distances, the data are sent to the Honeywell 6000 computer for data processing. This step is accomplished by transmitting the SPL's via direct time share link to the 6000 computer through a 1200 Band Modem. In the 6000 computer, the data are processed through the Full Scale Data Reduction (FSDR) Program where the appropriate calculations are performed. The data print out is accomplished on a high speed "remote" terminal. In addition, the FSDR Program writes a magnetic tape for Calcomp plotting of the data. Detailed descriptions of the acoustic data reduction system are given in Reference 3-2.

3.2.2 Aerodynamic Data Reduction Procedures

Aerodynamic data reduction procedures adopted to reduce the data otained from wind tunnel tests, conducted in the NASA Lewis 8 x 6-foot supersonic wind tunnel, are described in detail in Reference 3-3. The data obtained was reduced to flow coefficients, C_D, and thrust coefficients, C_T, for comparison purposes. The flow coefficients of the nozzles is defined as the ratio of measured flow rate through the nozzle to the ideal isentropic flow rate at the temperature and pressure of the flow:

$$C_D = \frac{\dot{W}}{\dot{W}_j}$$

The thrust coefficient is the ratio of the nozzle thrust to the sum of the ideal thrust of the inner and the outer duct flows. The ideal thrust for each flow equals the actual mass flow rate that stress times the ideal velocity, i.e., the velocity of the stream expanded isentropically from the total pressure to ambient pressure. The equation for the thrust coefficient is thus:

$$C_T = \frac{F}{\dot{W}^o V_j^o + \dot{W}^i V_j^i}$$

During much of the lower flow rate testing, the total pressure of the inner nozzle flow was lower than ambient. In these cases, the ideal thrust of the inner nozzle was set equal to zero.

4.0 CONFIGURATION DESCRIPTION, TEST MATRIX DEFINITION, AND DATA

There were seven (7) acoustic nozzle configurations and eight (8) aero performance nozzle configurations on which acoustic and aero performance parametric tests were performed. Because of the constraints existing on facility compatibility for the acoustic and aero performance tests, separate acoustic and aerodynamic performance nozzle hardware was designed and fabricated. Static acoustic tests were performed in the General Electric Anechoic Jet Noise Facility, and the aerodynamic performance tests were performed in the NASA-Lewis Research Center 8 x 6-foot Wind Tunnel. While separate acoustic and aerodynamic performance nozzle hardware was built, the only difference in exhaust nozzle geometry between the seven common configuration was the size - the aerodynamic performance models were 80% scale-models of the acoustic models. In this section, the nozzle configurations are described, and test matrix is defined for both the acoustic and aerodynamic performance tests, and a summary of the data is presented.

4.1 DESCRIPTION OF NOZZLE TEST CONFIGURATIONS

Sketches of the eight (8) nozzle configurations tested are shown in Figure 4-1 along with the key design variables. For the selected configurations, the inner stream to outer stream area ratio (A^i/A^o) varies from 0.33 to 1.56 while the radius ratio of the outer stream ranges from 0.853 to 0.926. The radius ratio of the inner stream varies from 0.673 to 0.902. The inner-plug configurations were selected to simulate two basic concepts of varying the inner-nozzle flow area. The inner-nozzle area must be opened for noise suppression points and closed off at other mission points for the low inner-flow nozzle design; for the high inner-flow nozzle designs, the inner nozzle area must be varied from that required when the nozzle is operated in the high-flow mode to that required during normal operation. In both cases, the area variation may be accomplished by two methods: via flaps and seals on the plug crown or by translating the inner plug. The first method results in a somewhat flat plug crown in the open or suppressed mode, such as that simulated by Configurations 1, 4, and 8. The second method allows use of a smooth plug contour, illustrated in Configurations 2, 3, 5, 6 and 7 (see Figure 4-1).

In Table 4-1, a summary of the key aerodynamic model parameters is given. In addition to the eight coannular nozzle configurations, a Supersonic Tunnel Association (STA) model was also tested as a means of verifying the facility accuracy. The throat area of this nozzle was 81.07 cm^2. A photo of a coannular nozzle mounted in the NASA-Lewis 8 x 6-foot Wind Tunnel is shown in Figure 4-2.

Table 4-2 summarizes the key acoustic model parameters. Besides the seven coannular nozzle configurations, a conical nozzle was also tested to serve as a baseline with which to evaluate the acoustic effectiveness of the

Parameter \ Configuration		1	2	3	4	5	6	7	8
R_r^o		0.902	0.902	0.902	0.902	0.853	0.926	0.853	0.853
R_r^i		0.673	0.800	0.902	0.800	0.800	0.800	0.902	0.800
A^i/A^o	Acoustic	1.560	1.027	0.532	1.027	0.629	1.416	0.326	---
	Aerodynamic	1.558	1.036	0.537	1.036	0.629	1.416	0.326	0.629
Type Test	Acoustic	X	X	X	X	X	X	X	---
	Aerodynamic	X	X	X	X	X	X	X	X

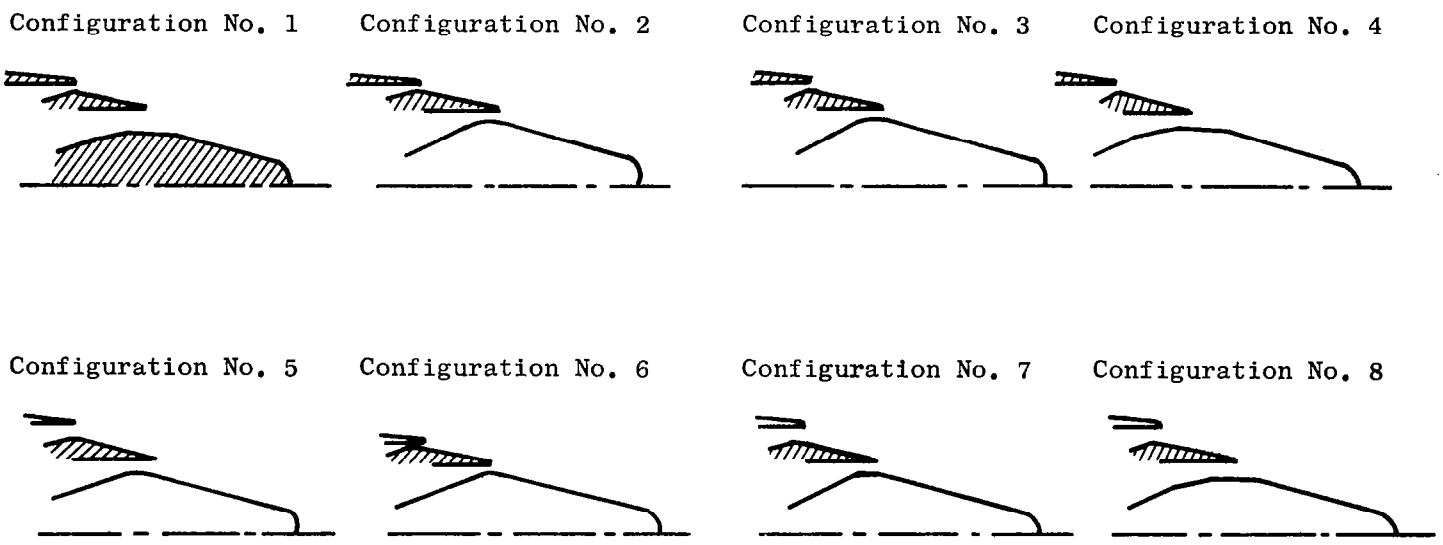

Figure 4-1. Summary of Test Nozzle Configurations and Key Geometric Parameters.

Table 4-1. Aerodynamic Model Geometric Parameters.

Configuration No.	$(R_r)^o$	$(R_r)^i$	A_o (cm^2)	A_i (cm^2)	Inner-Plug Geometry	Shroud Boattail Angle (°)
1	0.902	0.673	45.451	70.819	Bent	8.0
2	0.902	0.800	45.051	46.684	Conical	8.0
3	0.902	0.902	45.051	24.181	Conical	8.0
4	0.902	0.800	45.051	46.684	Bent	8.0
5	0.853	0.800	74.232	46.684	Conical	4.5
6	0.926	0.800	32.968	46.684	Conical	9.7
7	0.853	0.902	74.232	24.181	Conical	4.5
8	0.853	0.800	74.232	46.684	Bent	4.5

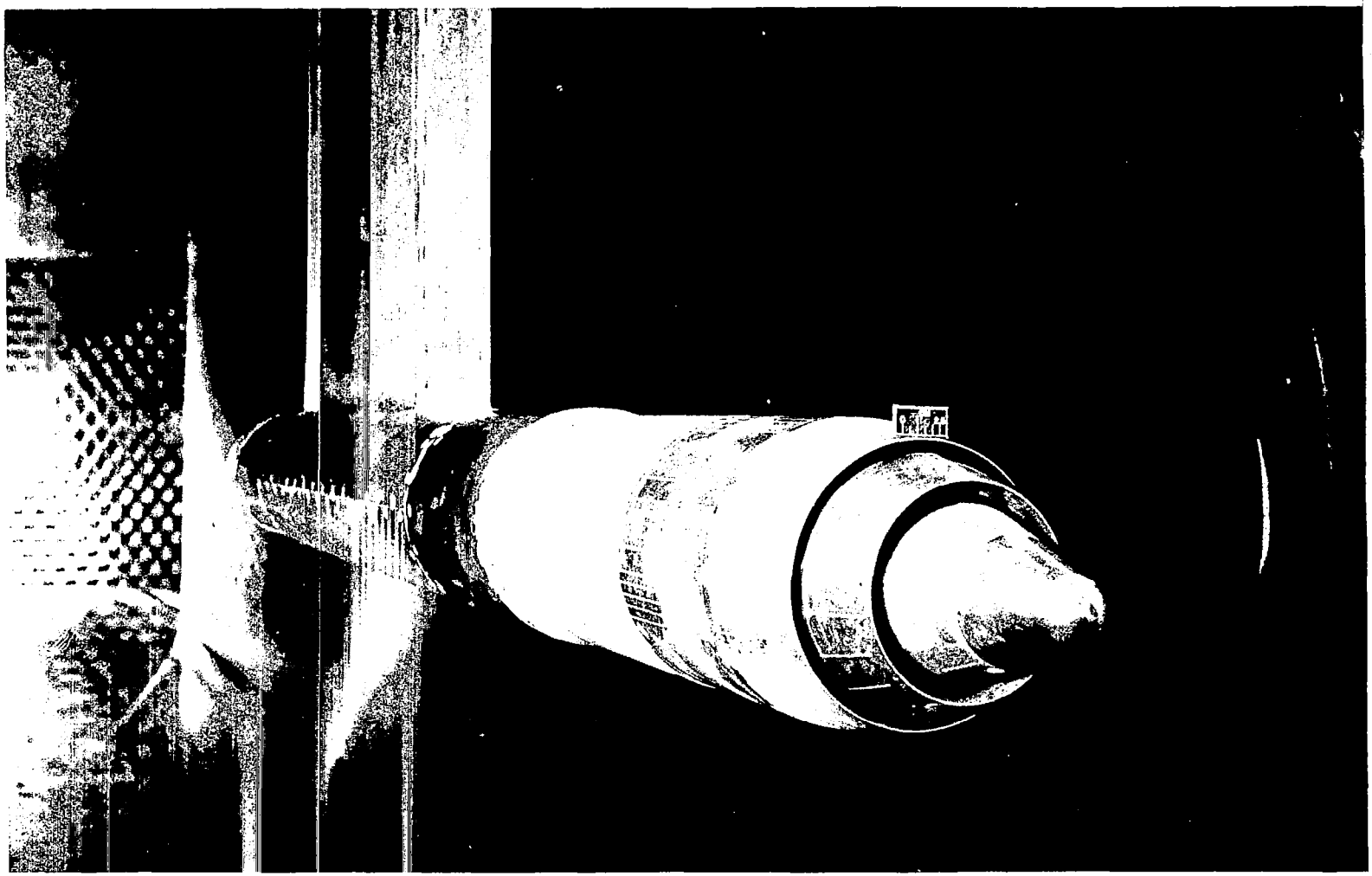

Figure 4-2. Configuration 2 Mounted in NASA Tunnel.

Table 4-2. Summary of Configuration Geometric Parameters for Acoustic Models.

Configuration	h^o, cm	h^i, cm	R^o_1	R^o_2	R^i_1	R^i_2	$R_r)^o$	$R_r)^i$	A^o, cm^2	A^i, cm^2	A^i/A^o	$h^i/D_{eq}{}^o$	X^o, cm	X^o/h^o	$\theta_s{}^1$, °	$\theta_s{}^2$, °	X_s, cm
1	1.082	2.631	9.952	11.034	5.420	8.047	0.902	0.673	71.335	111.277	1.560	0.28	7.846	7.25	2.9	15.0	5.126
2	1.082	1.610	9.952	11.034	6.436	8.047	0.902	0.800	71.335	73.226	1.027	0.17	7.846	7.25	15.0	15.0	---
3	1.082	0.790	9.952	11.034	7.259	8.047	0.902	0.902	71.335	37.923	0.532	0.08	7.846	7.25	15.0	15.0	---
4	1.082	1.610	9.952	11.034	6.436	8.047	0.902	0.800	71.335	73.226	1.027	0.17	7.846	7.25	2.9	15.0	5.126
5	1.714	1.610	9.952	11.666	6.436	8.047	0.853	0.800	116.445	73.226	0.629	0.13	7.780	4.54	15.0	15.0	---
6	0.795	1.610	9.952	10.747	6.436	8.047	0.926	0.800	51.697	73.226	1.416	0.20	7.874	9.90	15.0	15.0	---
7	1.714	0.790	9.952	11.666	7.259	8.047	0.853	0.902	116.445	37.923	0.326	0.06	7.780	4.54	15.0	15.0	---

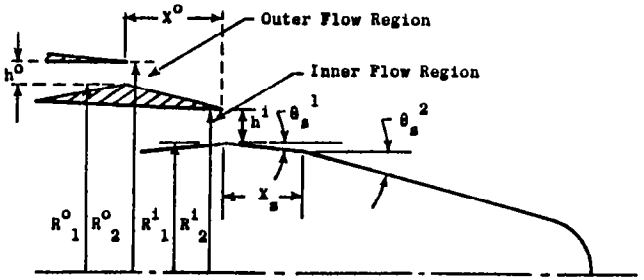

Schematic of Nozzle Configurations and Definition of Parameters

where R_r = Radius Ratio (R_1/R_2)
h = Step Height, cm
A = Area, cm^2
D_{eq} = Equivalent Circular Diameter Based on A, cm
θ_s = Ramp Angle of Inner Plug
R = Radius, cm
X = Distance, cm

Superscripts
o = Outer Flow Region
i = Inner Flow Region

coannular nozzles. This reference conical nozzle had its throat area equal to 109.14 cm^2. A photo of an acoustic coannular nozzle model mounted in the anechoic chamber is shown in Figure 4-3.

4.2 DEFINITION OF TEST MATRICES

4.2.1 Definition of Acoustic Test Matrix

All test points for the coannular nozzles had the basic inverted flow type profile where the outside flow is at a higher velocity and temperature than the inner flow to simulate VCE-type operation. The test points were defined to study basic coannular nozzle noise chracteristics along a typical VCE engine operating line and to determine the velocity and temperature dependence of coannular nozzle jet noise. The influence of velocity ratio (V_j^i/V_j^o) and inner pressure ratio was also examined. In order to study geometry influences, the same inner and outer stream velocity and total temperature were set for each of the configurations.

Test details of the actual static acoustic runs on the seven coannular nozzles are given in Tables 1-7 of Appendix I. The inner and the outer streamflow variables were selected to investigate the influence of a high inner flow on the noise reduction characteristics of a coannular plug nozzle. The velocity ratio and inner pressure ratio were changed from test point to test point along a tyupical VCE operating line to establish the test matrix. Test points 40-48 (60-81 for Configuration 7) constitute the test matrix for the high inner flow study. For these same configurations, the influence of velocity ratio was studied in test points 107-118 by holding the outer stream conditions constant and changing the inner stream velocity. For Configuration 7 a test series (90-104) was run to isolate the velocity and temperature dependence of the coannular nozzle. Configurations 1 and 3 were run with very low inner weight flows for test points 12 through 30. Tests were run on Configurations 1, 3, 5, and 6, to examine the noise levels of the coannular nozzle with no inner flow. The test points are numbered 150 through 154. For Configuration 1, ten test points (1-10) were run for comparison with previous acoustic measurements made in the General Electric outdoor test facility (JENOTS).

Test details of the acoustic runs using the reference conical nozzle are given in Table I-8 of Appendix I.

4.2.2 Aerodynamic Performance Test Matrix

The wind tunnel aerodynamic test matrix was designed to simulate takeoff and low-speed flight regimes - ambient Mach numbers form 0 to 0.45, outer stream pressure ratios of 1.5 to 3.5, and inner stream pressure ratios from 1.1 to 3.5. In addition low inner flow rates from zero to 6% of the outer stream weight flow were tested. Section 6.0 and Reference 3.3 contain a full description of the test results. The aerodynamic testing consisted of 309 test conditions for a total of 9 configurations. The entire test matrix is presented in Appendix II. Note that all testing was performed at ambient temperature.

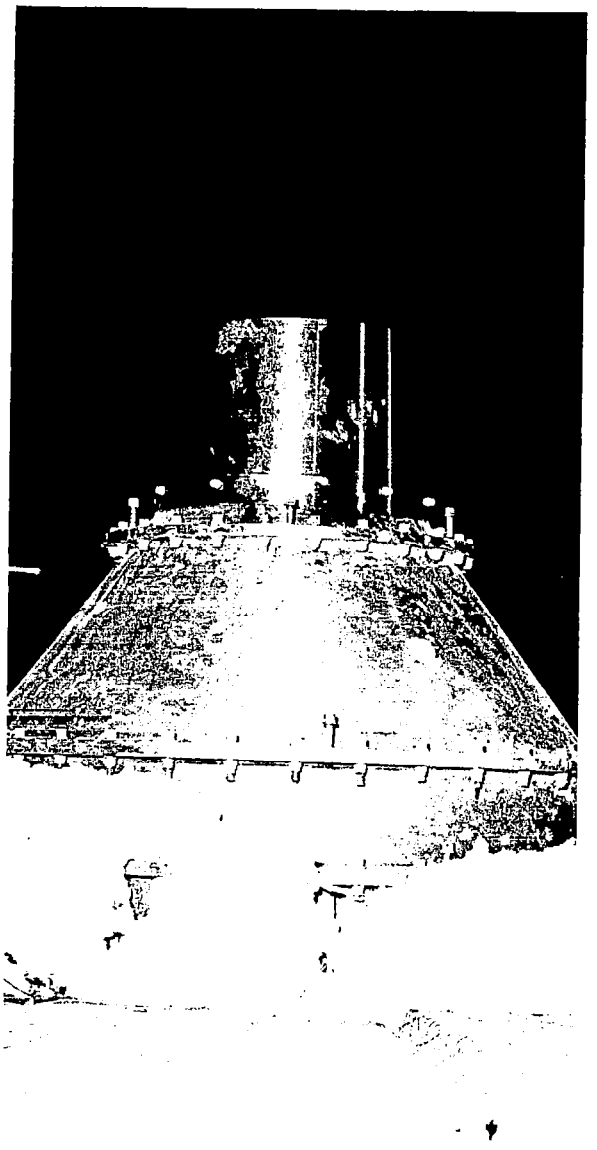

Figure 4-3. Acoustic Coannular Nozzle Model Installed in the General Electric Anechoic Chamber.

4.3 DATA

4.3.1 Acoustic Data

The data reduction techniques employed to obtain the acoustic data including operating procedures, corrections, analysis procedures, and data output formats are described in detail in Reference 3.2 and in Volume I of the Comprehensive Data Report, NASA CR-159575.

The measured OASPL directivities for each of the acoustic test runs along with the corresponding OAPWL at a 12.19 m arc are also presented in Tables 1-8 of Appendix I. Detailed acoustic test results including the spectral data for each of the test points are given in Volume I of the Comprehensive Data Report NASA CR-159575.

Section 5.0 describes the analysis of the test results. A total of 196 points on eight nozzle configurations were obtained during this program.

4.3.2 Wind Tunnel Test Data

Wind tunnel performance test results are presented in Volume III of the Comprehensive Data Report, NASA CR-159575, and discussed in NASA CR-2990.

5.0 ACOUSTIC TEST RESULTS

The jet acoustic measurements obtained with the model size coannular plug nozzle configurations of the program and the analyses of these data are presented in this section. The detailed description of the nozzle configurations and range of test conditions is covered earlier in Section 4.

This section consists of three major subsections. Subsection 5.1 is a discussion of the general acoustic characteristics of coannular nozzles with an inner stream plug. Analyses of the test measurements include the radiated acoustic power in terms of a Lighthill velocity parameter and coefficient; acoustic efficiency; velocity dependence of OAPWL, PNL_{max}, OASPL; temperature dependence; spectral characteristics and directivity characteristics. Subsection 5.2 presents an analysis of data to illustrate flow and geometry influence of small amounts of inner stream flow (including no inner flow); velocity ratio effects, outer stream radius ratio effects, and area ratio effects. Subsection 5.3 discusses the observed shock noise characteristics of coannular acoustic nozzles with an inner stream plug.

5.1 GENERAL ACOUSTIC CHARACTERISTICS OF HIGH RADIUS RATIO COANNULAR ACOUSTIC NOZZLES

5.1.1 Some Background Acoustic Equations

To analyze the acoustic test results from the point of view of helping to establish the governing parameters, there is benefit in evaluating the measured acoustic properties relative to some of the more fundamental aerodynamic and acoustic properties. One of the simplest and most convenient ways to do such an evaluation is to formulate the acoustic power in terms of a Lighthill expression. From a Lighthill point of view, the acoustic power for a dual flow stream sketched in Figure 5-1 may be defined as:

$$\pi = \frac{K^o\left(\rho_j^o\right)^2 A^o \left(V_j^o\right)^8 + K^i\left(\rho_j^i\right)^2 A^i \left(V_j^i\right)^8}{\rho_o a_o^5}, \text{ watts} \qquad (1)$$

or

$$\pi = K^o L^o + K^i L^i$$

where

π = Radiated Acoustic Power, watts
A = Jet Exhaust Nozzle Area, m^2
K = Lighthill Coefficient
L = Lighthill Parameter, watts
ρ = Jet Static Density, kgr/m^3
V_j = Ideal Jet Speed, m/sec
a = Speed of Sound, m/sec

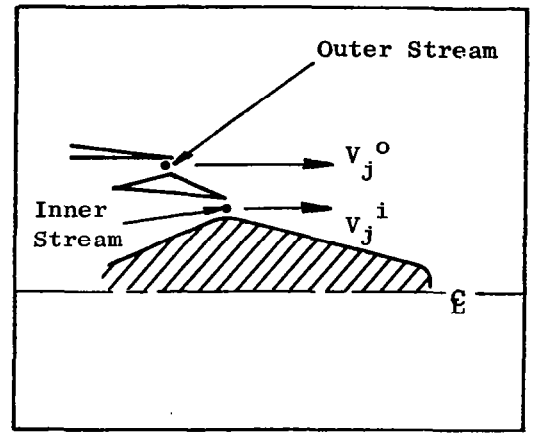

Figure 5-1 Sketch of a Dual Stream Exhaust Nozzle with Plug.

Subscripts

a = ambient conditions
j = ideal jet conditions

Superscripts

o = outer stream
i = inner stream

If we assume $K^o = K^i = K$, then equation 1 is written as:

$$\pi = K \frac{\left(\rho_j^o\right)^2 A^o \left(V_j^o\right)^8}{\rho_o a_o^5} \left\{1 + \rho_r^2 A_r V_r^8\right\} \tag{2}$$

or

$$\pi = K L^o \left\{1 + \rho_r^2 A_r V_r^8\right\}$$

where

r ≡ ratio of inner stream to outer stream

Introducting the ideal thrust F, total mass flow, $\dot{\omega}_T$, and a thrust averaged (or mixed) velocity, V_j^{mix}:

$$F = \left(\rho_j^o A^o V_j^o\right) V_j^o + \left(\rho_j^i A^i V_j^i\right) V_j^i$$

$$= \rho_j^o A^o V_j^{o\,2} \left(1 + \rho_r A_r V_r^2\right), \text{ newtons} \tag{3}$$

$$\dot{\omega}_T = \rho_j^o A^o V_j^o \left(1 + \rho_r A_r V_r\right), \text{ kgr/sec} \tag{4}$$

$$V_j^{mix} = F/\dot{\omega}_T$$

$$= V_j^o \left\{(1 + \rho_r A_r V_r^2)/(1 + \rho_r A_r V_r)\right\} \tag{5}$$

Equation 2 may be rewritten as:

$$\pi = K \frac{\left(\rho_j^o\right)^2 A^o}{\rho_o a_o^5} \left(V_j^{mix}\right)^8 \left\{\frac{1 + \rho_r A_r V_r}{1 + \rho_r A_r V_r^2}\right\}^8 \left(1 + \rho_r^2 A_r V_r^8\right) \tag{6}$$

Before we go further a few remarks regarding equations 1, 2 and 6 should be made. The first observation to be made is that the Lighthill coefficient, K, is considered here as an interaction parameter: Its functional form is not known a priori, but its value can be calculated from measurement and equations 2 or 6. The assumption that $K^i = K^o$ has been made for convenience only. It implies equal distribution of sources on inner and outer streams having the same values of velocity, temperature, and area. This assumption was made so as to arrive at a relatively simple method of examining the acoustics of a dual flow system as compared to a simple single circular jet. For a conical nozzle, K may be estimated from measurements and the single stream version of equation 1. In a similar way values of K can be determined for coannular systems; their value as compared to the conical nozzle is an estimate of the radiated power level difference. For example, if the value of K for a series of coannular nozzles is found to be somewhat less than the value of conical nozzle, a noise reduction in power level is implied.

Another observation is that the form of equations 1, 2 or 6 differ from the classical Lighthill expressions in that a density-squared power law was used. Originally, Lighthill used the approximation that $\rho_j^2 \sim \rho_o^2$ so that

$$L = \rho_o A \left(V_j^o\right)^8 / a_o^5$$

Experimental and theoretical investigations have shown that the jet density exponent varies from -1 to 2.0 depending on jet velocity. At high velocity conditions the density exponent is 2. Since most of the data taken for the program was at high velocity conditions, the density-squared power law was used in formulating the Lighthill parameter discussed above.

The last remark is that equations 2 and 6 are identical. The two expressions do however suggest two ways of selecting a characteristic velocity; Equation 2 suggests that the outer stream velocity may be a choice, while Equation 6 suggests that the mixed velocity should be chosen. In actuality, all the terms in the equations should be taken into account when either velocity is chosen. Nonetheless, the selection of the mixed velocity has a strong physical attractiveness. First, it would express the noise in terms of both velocity streams. Secondly, it would allow noise comparisons to be made for equal thrust and total mass flow and hence has an added meaningful propulsion significance. Pursuing the mixed concept further suggests that instead of equations 2 or 6 perhaps the following equation could be used:

$$\pi = K^{mix} \frac{\rho_j^{mix\,2} \; V_j^{mix\,8} \; A^{mix}}{\rho_o \; a_o^5} \qquad (7)$$

$$= K^{mix} \; L^{mix}$$

These ideas and others will be examined further in the data analyses sections.

Another physically useful acoustic expression to examine is the acoustic efficiency. The acoustic efficiency is defined as:

$$\eta = \frac{\text{radiated acoustic power}}{\text{mechanical power}} = \frac{\mathcal{I}}{M.P.} \tag{8}$$

where

$$M.P. \equiv \rho_j^o A^o V_j^{o\,3} (1 + \rho_r A_r V_r^3), \text{ watts.}$$

The acoustic efficiency allows one to consider the radiated acoustic power on a per unit mechanical power basis. Examination of this efficiency parameter allows consideration of any type of flow system to be compared on a one-to-one basis.

Thus, using equations 2, 6, 7 with 8 yields the following expressions:

$$\eta = K (\rho_j^o/\rho_o) M_o^5 \left\{\frac{1 + \rho_r^2 A_r V_r^8}{1 + \rho_r A_r V_r^2}\right\} \tag{9a}$$

or

$$\eta = K (\rho_j^o/\rho_o) M_o^{mix\,5} \left\{\frac{1 + \rho_r A_r V_r}{1 + \rho_r A_r V_r^2}\right\}^5 \left\{\frac{1 + \rho_r^2 A_r V_r^8}{1 + \rho_r A_r V_r^3}\right\} \tag{9b}$$

or

$$\eta = K^{mix} (\rho_j^{mix}/\rho_o) M_o^{mix\,5} \tag{9c}$$

where

$M_o = V_j^o/a_o$ (acoustic Mach Number for the outer stream)

$M_o^{mix} = V_j^{mix}/a_o$ (Mixed acoustic Mach Number)

5.1.2 Overall Power Level Test Results

5.1.2.1 Radiated Acoustic Power in Terms of the Lighthill Parameter

Typical results of the radiated acoustic power in terms of the Lighthill parameter for a conical nozzle and a high radius ratio coannular nozzle with plug for exhaust between 175 and 750 m/sec, are illustrated in Figure 5-2. Figure 5-3 illustrates the measured acoustic power for all the other test points taken during this program. Most of these figures contain two lines drawn through the data. The first line was obtained from a linear regression analysis of the measurements to obtain a regression equation as shown on each figure and summarized in Table 5-1. The data was analyzed in the form:

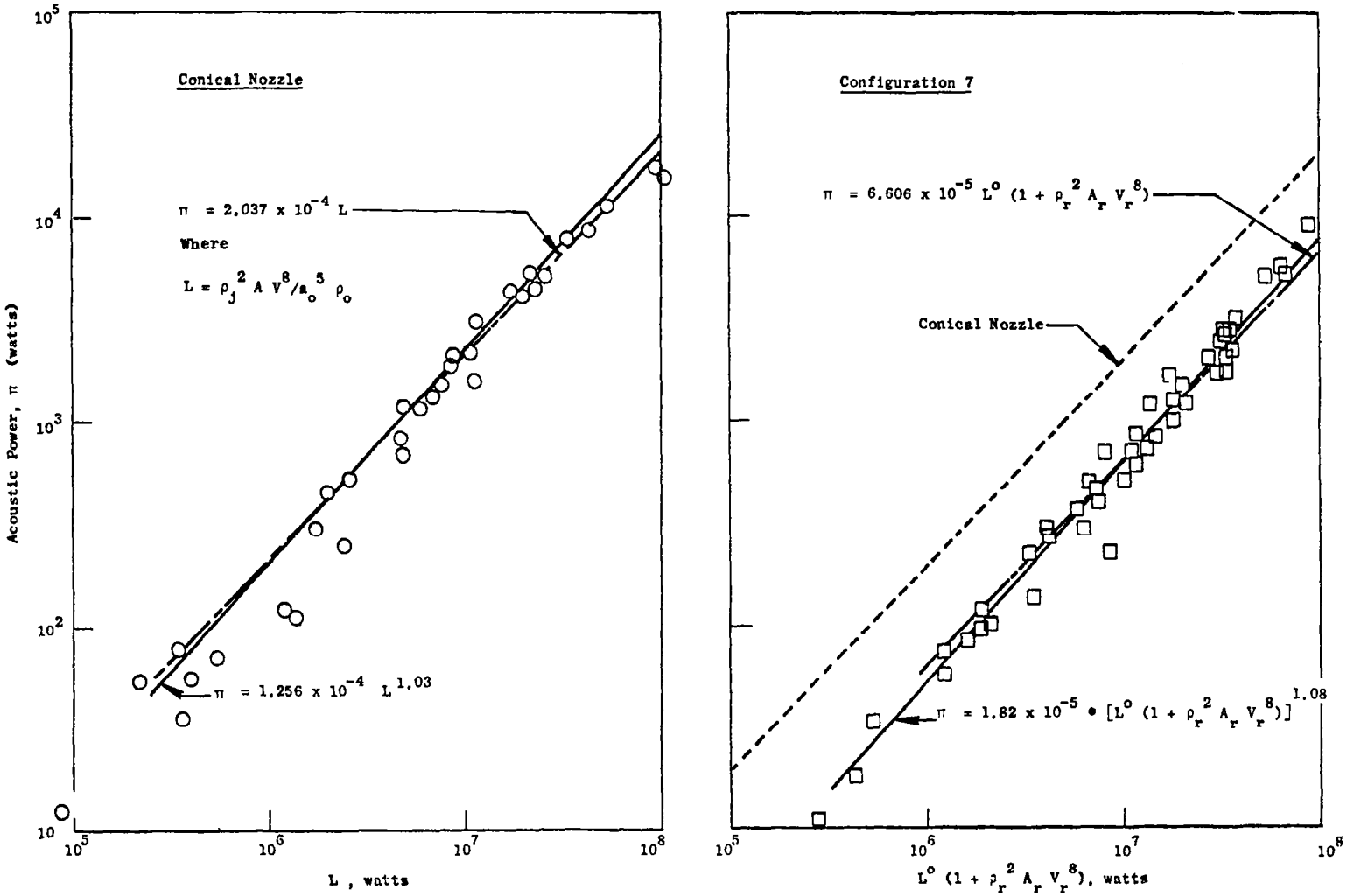

Figure 5-2. Acoustic Power Radiated for a Conical Nozzle and a High Radius Ratio Coannular Nozzle for Jet Exhaust Velocities Between 175 and 750 mps.

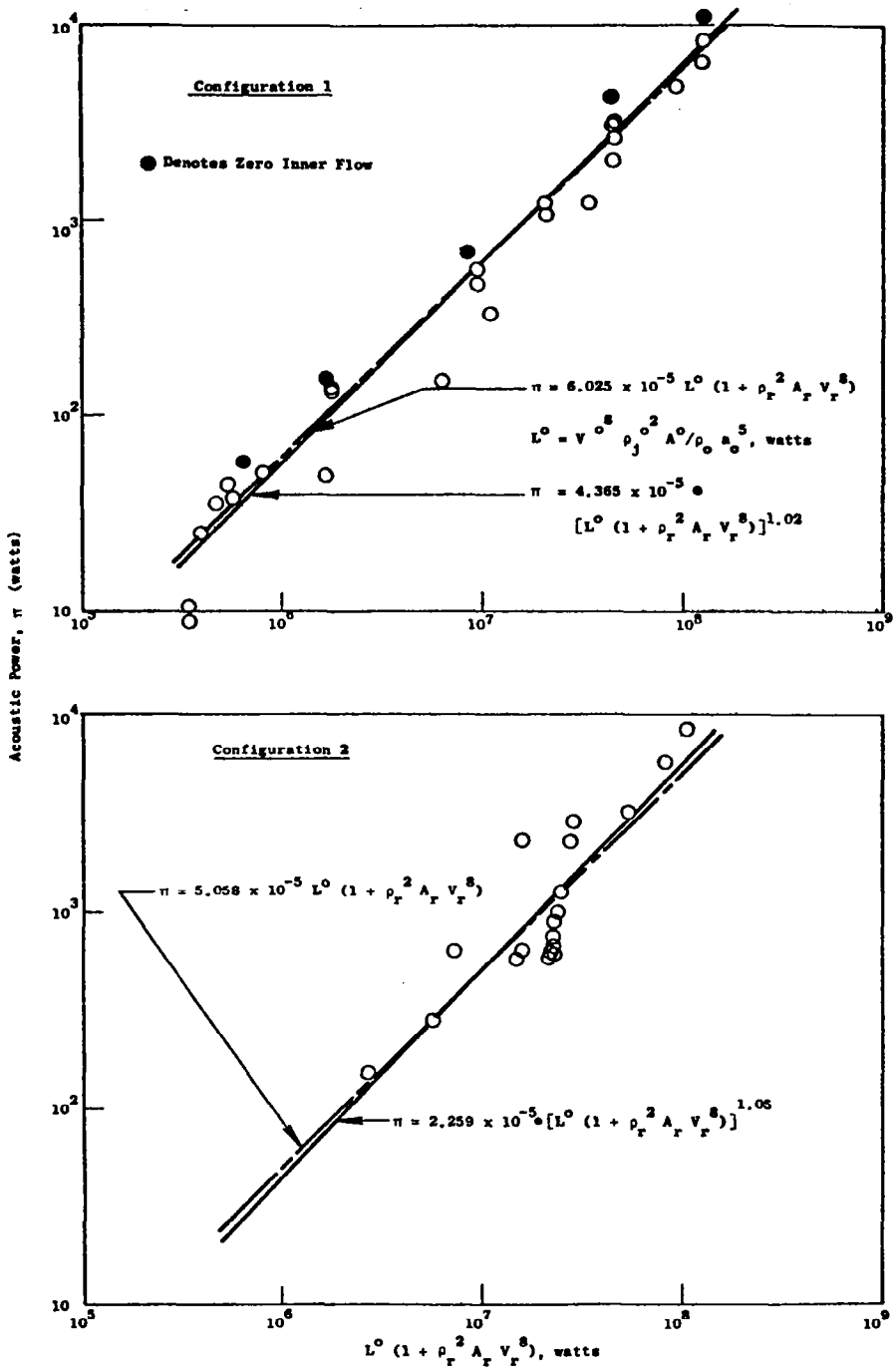

Figure 5-3. Acoustic Power Radiated for High Radius Ratio Coannular Nozzles with a Plug.

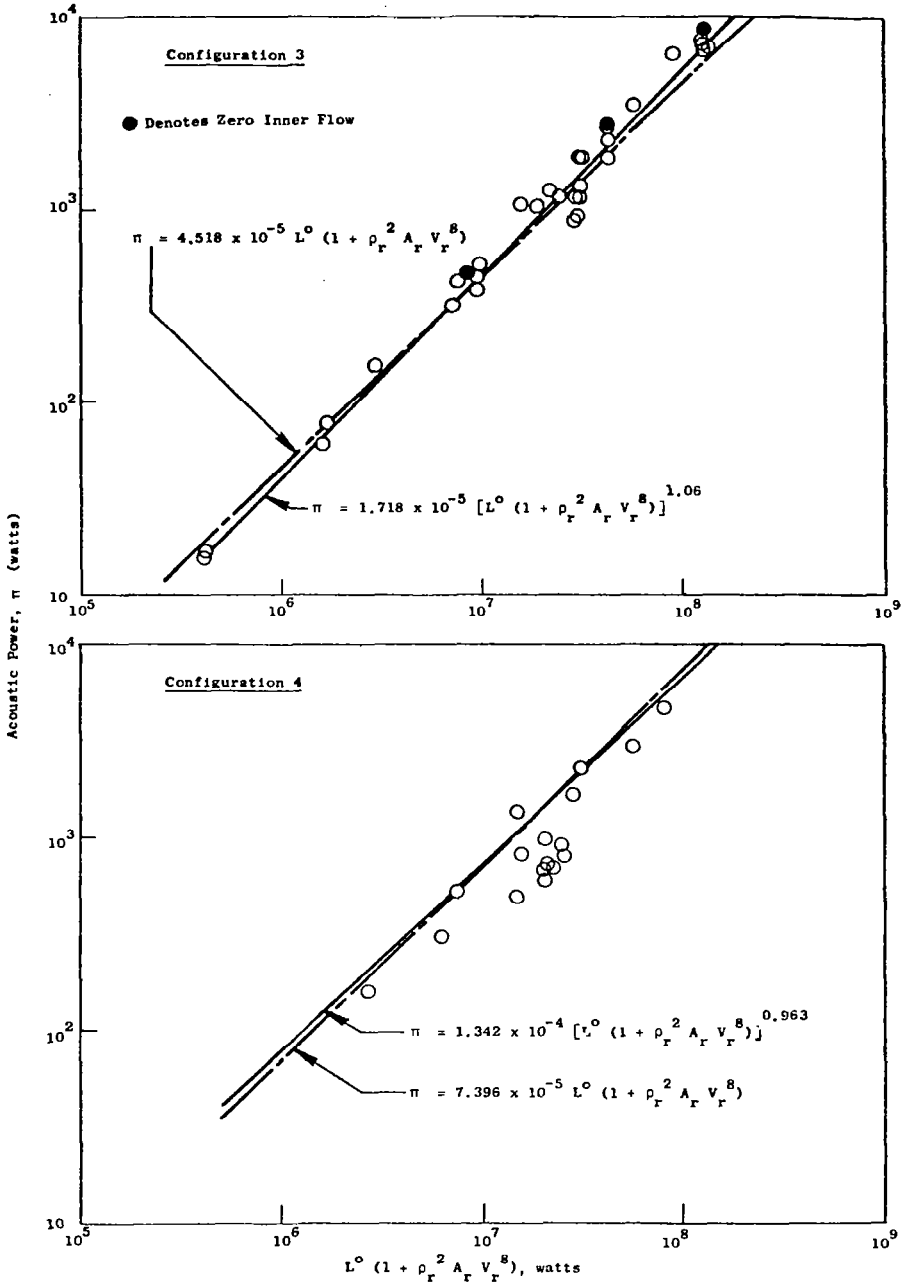

Figure 5-3. Acoustic Power Radiated for High Radius Ratio Coannular Nozzles with a Plug (Continued).

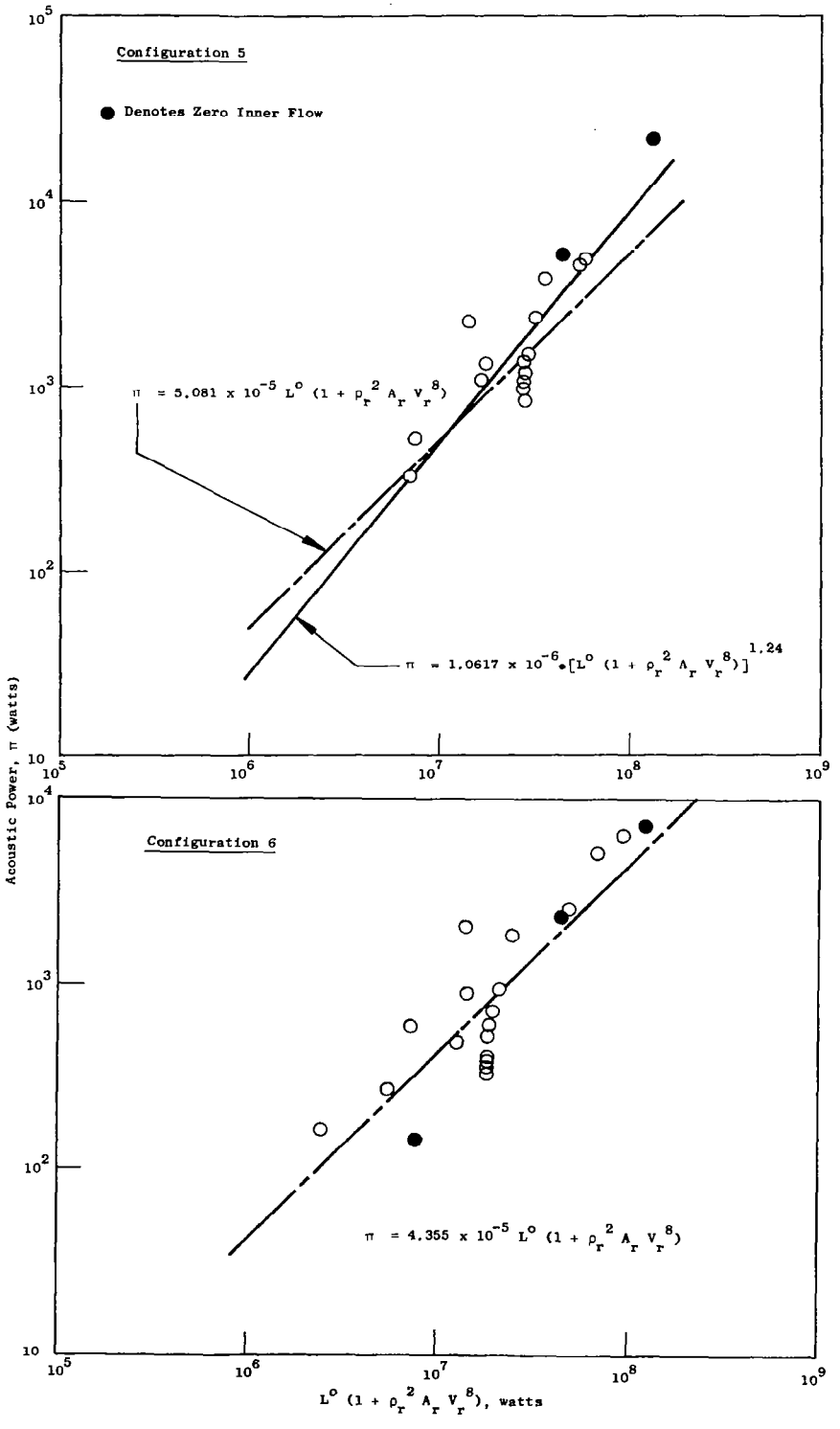

Figure 5-3. Acoustic Power Radiated for High Radius Ratio Coannular Nozzles with a Plug (Concluded).

Table 5-1. Prediction Equations for Acoustic Power for High Radius Ratio Coannular Nozzles with a Plug.

Prediction Form: a) $\pi = \hat{K}\left[L^o\left(1 + \rho_r^2 A_r V_r^8\right)\right]^a$, watts b) $\pi = K\left[L^o\left(1 + \rho_r^2 A_r V_r^8\right)\right]$, watts

Configuration	$\hat{K}$	a	$\sigma_{y/x}$,dB	Configuration	K
1	4.365×10^{-5}	1.02	1.6219	1	6.025×10^{-5}
2	2.259×10^{-5}	1.05	2.092	2	5.058×10^{-5}
3	1.7179×10^{-5}	1.06	.8558	3	4.518×10^{-5}
4	1.342×10^{-4}	.963	1.5004	4	7.396×10^{-5}
5	1.0617×10^{-6}	1.24	2.166	5	5.081×10^{-5}
6	1.4093×10^{-5}	1.07	2.4806	6	4.355×10^{-5}
7	1.8197×10^{-5}	1.08	1.0226	7	6.6069×10^{-5}
All Data	3.251×10^{-5}	1.03	1.695	All Data	5.272×10^{-5}
Conical Nozzle	1.254×10^{-4}	1.03	1.5745	Conical Nozzle	2.037×10^{-4}

where

π = Measured Acoustic Power, watts

L^o = Lighthill Parameter Based on Outer Stream Conditions $\left(\rho_j^o{}^2 A^o V_j^o{}^8 / \rho_o a_o^5\right)$, watts

a_o = Ambient Speed of Sound, m/s

ρ_o = Ambient Density, kgm/m^3

$K, \hat{K}$ = Lighthill Coefficient, dimensionless

ρ_r = Static Jet Density Ratio of inner to outer streams $\left(\rho_j^i/\rho_j^o\right)$

A_r = Area Ratio (A^i/A^o)

V_r = Velocity Ratio $\left(V_j^i/V_j^o\right)$

$\sigma_{y/x}$ = Standard Error of Estimate (68% of population lie within $\pm\sigma y/x$, 95% within $\pm 2\sigma y/x$) in dB.

a = Calculated coefficient from Linear Regression Analysis

$$10 \log (\pi/10^{-13}) = b + c\ [10 \log L^{o}\ (1 + \rho_r^2\ A_r\ V_r^8)/10^{-13}]$$

where the constants b and c are determined from the regression analysis (Reference 5-1), and from which equations of the form:

$$\pi = \hat{K}\ [L^{o}\ (1 + \rho_r^2\ A_r\ V_r^8)]^{a} \qquad (10)$$

were derived.

The second equation shown in each figure is the classical acoustic form:

$$\pi = K\ [L^{o}\ (1 + \rho_r^2\ A_r\ V_r^8)] \qquad (11)$$

where the value of K was selected so as to match the magnitude of π from equation 10 when

$$L^{o}\ (1 + \rho_r^2\ A_r\ V_r^8) = 10^7 \text{ watts}$$

The results given in Figures 5-2 and 5-3, and Table 5-1 elicit the following observations. The regression analysis results shown in Table 5-1a predicts the acoustic power for all the coannular nozzle data within the same accuracy as the conic nozzle data (the standard error of estimate, $\sigma_{y/x}$, for the conic nozzle data is nearly the same as for all the coannular nozzle data). Also the regression coefficient, a, is nearly 1.0 for the coannular nozzle data as well as the conic nozzle data. These results indicate that, at least on an overall power level basis, the classical notion of conic nozzle jet noise is similar to a coannular nozzle. The conical-nozzle-radiated acoustic power for high velocity and high temperature jets was found* (from Table 5-1) to be $\pi_{conical} = 2.037 \times 10^{-4}\ \rho_j^2\ A\ V_j^8/\rho_o\ a_o^5$. The typical coannular nozzle with plug results shown for comparison purposes in Figure 5-2 was Configuration 7 [$R_r^o = .853$, $R_r^i = .902$]. The comparison acoustic power equation for Configuration 7 is $\pi_{config\ 7} = 6.607 \times 10^{-5}\ L^{o}\ \{1 + \rho_r^2\ A_r\ V_r^8\}$. The difference in power level between the conical nozzle and Configuration 7 can be estimated by taking 10 log $K_{config\ 7}/K_{conical}$; it is -4.89 dB. Using the Lighthill coefficient for all the coannular nozzles show that typically the coannular nozzle with plug has a true source power-level reduction of ~5.9 dB relative to a conical nozzle.

*The approximation given by Lighthill (AIAAJ, July 1963) was $\pi \tilde{\equiv} 1/2 \times 10^{-4}\ \rho_o\ A\ V_j^8/a_o^5$. The difference between the two equations is that the parameter K considered in this text compared to the original Lighthill value is: $K(\rho_j/\rho_o)^2 = K_{original\ Lighthill}$. For the conical nozzle test points considered here $(\overline{\rho_j/\rho_o})^2 = .262$. Thus $K(\overline{\rho_j/\rho_o})^2 = .53 \times 10^{-4}$, the value approximate by Lighthill.

The data scatter about the regression lines shown in Figures 5-2 and 5-3 is seen to vary from configuration to configuration, in some cases by a significant amount. An estimate of the data scatter in dB is obtained from an examination for the "standard error of estimate," $\sigma_{y/x}$, tabulated in Table 5-2. As an estimate 68% of the data can be said to lie within $\pm\sigma_{y/x}$ (see Reference 5-1). Configurations 3 and 7 are observed to have the least data scatter ($\sigma_{y/x}$ = .8558 and 1.0226 respectively) while Configuration 6 is observed to have the greatest data scatter ($\sigma_{y/x}$ = 2.4806). One reason Configurations 3 and 7 had the least data scatter could be a geometry effect. Both these configurations have an inner stream radius ratio, R_r^i, equal to .902.

A comparison of the regression curves of the conical nozzle and the regression curve through all of the coannular nozzle data shows the results that the radiated acoustic power of the conical nozzle and coannular nozzle has identical forms and the $\sigma_{y/x}$ are approximately the same:

$$\pi_{conical} = 1.254 \times 10^{-4} L^{1.03}; \quad \sigma_{y/x} = 1.5745$$

$$\pi_{all\ coannular\ data} = 3.251 \times 10^{-5} L^{1.03}; \quad \sigma_{y/x} = 1.6954$$

Thus from the statistical analysis point of view, the acoustic power approximation equation for all the coannular nozzle data is nearly as accurate as the one found for the conical nozzle.

5.1.2.2 Model Scale Overall Power Level Test Results - Selection of a Characteristic Velocity and Density

Earlier expressions were written (Equations 1, 6, and 7) for the acoustic power in terms of the outer stream velocity, V_j^o, the mixed velocity, V_j^{mix}, the outer stream static density, ρ_j^o, and the mixed stream static density*, ρ_j^{mix}. To evaluate the best characteristic parameters, the model scale data was analyzed by again performing the simple linear regression analysis of the test results in the following form:

$$OAPWL - 10 \log (\rho_j^{characteristic}/\rho_o)^{\omega} = a + b\,(10 \log V_j^{characteristic}/a_o)$$

where the characteristics density, $\rho_j^{characteristic}$, could be the outer stream static density or the mixed stream static density. The density exponent ω was determined from Reference 5-2. The criterion that will be used in determining the "best" characteristic parameters will be based on the precision with

*The mixed stream static density is determined through the usual isentropic relationships once V_j^{mix} and the mixed total temperature T_T^{mix} are define

$$\left(T_T^{mix} \equiv \frac{T_T^o \dot{\omega}^o + T_T^i \dot{\omega}^i}{\dot{\omega}_T} \right).$$

Table 5-2. Linear Regression Results of OAPWL for High Radius Ratio Coannular Nozzles with a Plug for Various Forms of Outer Stream and Mixed Stream Parameters to Characterize the Noise.

- Model Size Data, $A_T = 189.68\ cm^2$

Predicted Form: a) $OAPWL - 10 \log (\rho_j^o/\rho_o)^w = a + b * [10 \log_{10} V_j^o/a_o]$ b) $OAPWL - 10 \log_{10} (\rho_j^o/\rho_o)^w = a + b * [10 \log_{10} V_j^{mix}/a_o]$ c) $OAPWL - 10 \log_{10} (\rho_j^{mix}/\rho_o)^w = a + b * [10 \log_{10} V_j^{mix}/a_o]$

Configuration	a	b	$\sigma_{y/x}$,dB	Configuration	a	b	$\sigma_{y/x}$,dB	Configuration	a	b	$\sigma_{y/x}$,dB
1	147.86	7.46	3.083	1	146.72	8.92	1.47	1	146.23 (146.22)*	9.03 (9.10)	0.847 (0.903)
2	150.90	5.84	2.84	2	148.57	9.61	1.61	2	144.33	10.36	1.0266
3	143.30	8.9	1.52	3	146.16	9.08	1.12	3	144.61 (144.39)	9.50 (9.67)	0.8469 (0.707)
4	151.61	5.4	2.072	4	150.61	8.42	1.26	4	146.13	9.34	1.136
5	149.73	6.93	3.00	5	151.00	8.16	1.96	5	144.74 (144.62)	10.07 (10.11)	1.155 (1.198)
6	149.54	6.00	3.38	6	154.24	6.45	1.26	6	148.52 (145.19)	7.95 (9.98)	1.85 (0.809)
7	145.73	8.53	1.78	7	146.18	9.83	1.29	7	144.11	10.09	0.786
All Data	147.14	7.46	2.746	All Data	147.59	9.16	1.97	All Data	145.6 (145.41)	9.39 (9.53)	1.215 (1.056)
Conical Nozzle	148.7	9.37	1.366	Conical Nozzle	148.7	9.37	1.366	Conical Nozzle	148.9	9.54	1.366

*Quantities in the parentheses correspond to the analysis of data without any of the zero inner flow test data.

which the regression curves approximate the data, i.e., the results which yield the smaller values of $\sigma_{y/x}$. This criterion mounts to saying which parameters best collapse or normalize the data.

Figures 5-4, 5-5, 5-6, and Table 5-2 summarize the results of this portion of the study. Figure 5-4 illustrates the model scale power levels in the following form:

$$\text{OAPWL} - 10 \log (\rho_j^o/\rho_o)^\omega \text{ vs } 10 \log V_j^o/a_o$$

Drawn through each data set is the linear regression curve for reference. The symbols shown as solid represent data where the coannular nozzle was operating with the inner stream completely (physically) blanked off - an annular nozzle configuration. The values of $\sigma_{y/x}$ are also given on each Figure as well as summarized in Table 5-2. The results shown illustrate a high order of data scatter for most of the configurations ($\sigma_{y/x} \sim 2 \rightarrow 3$). In general, the conclusion can be drawn that presenting, comparing, or characterizing a dual flow system based on the outer stream properties of the coannular streams would most likely lead to results of insufficient precision.

Figure 5-5 shows the measured test results in the form:

$$\text{OAPWL} - 10 \log (\rho_j^{mix}/\rho_o)^\omega \text{ vs } 10 \log V_j^{mix}/a_o$$

The linear regression curves and standard errors of estimate, $\sigma_{y/x}$ are also shown. These results clearly show a superior data collapse than those results of Figure 5-4. The standard error of estimate $\sigma_{y/x}$ also is observed to be smaller than the value found for the conical nozzle ($\sigma y/x \sim .786 \rightarrow 1.85$; see Table 5-2c). The results of characterizing the noise in the form:

$$\text{OAPWL} - 10 \log (\rho_j^o/\rho_o)^\omega \text{ vs } 10 \log V_j^{mix}/a_o$$

is summarized in Table 5-2b and illustrated in Figure 5-6. Although the results are seen to be better than those illustrated by using the outer stream density and velocity, they are found to be not as desirable (the $\sigma_{y/x}$ is somewhat greater than what was found above) as using the mixed stream density and velocity as the characteristic jet noise parameters.

Illustrative summaries of the prediction curves given in Table 5-2 are shown in Figures 5-7, 5-8 and 5-9. Each figure shows the predictive regression lines for all the tested configurations, and a comparison of the conical nozzle data with the regression line for all the data combined. The curves illustrate that on an overall power level basis, there is a geometry influence in the observed power level reductions relative to a conical nozzle. What is encouraging from a phenonmenological point of view are the results of

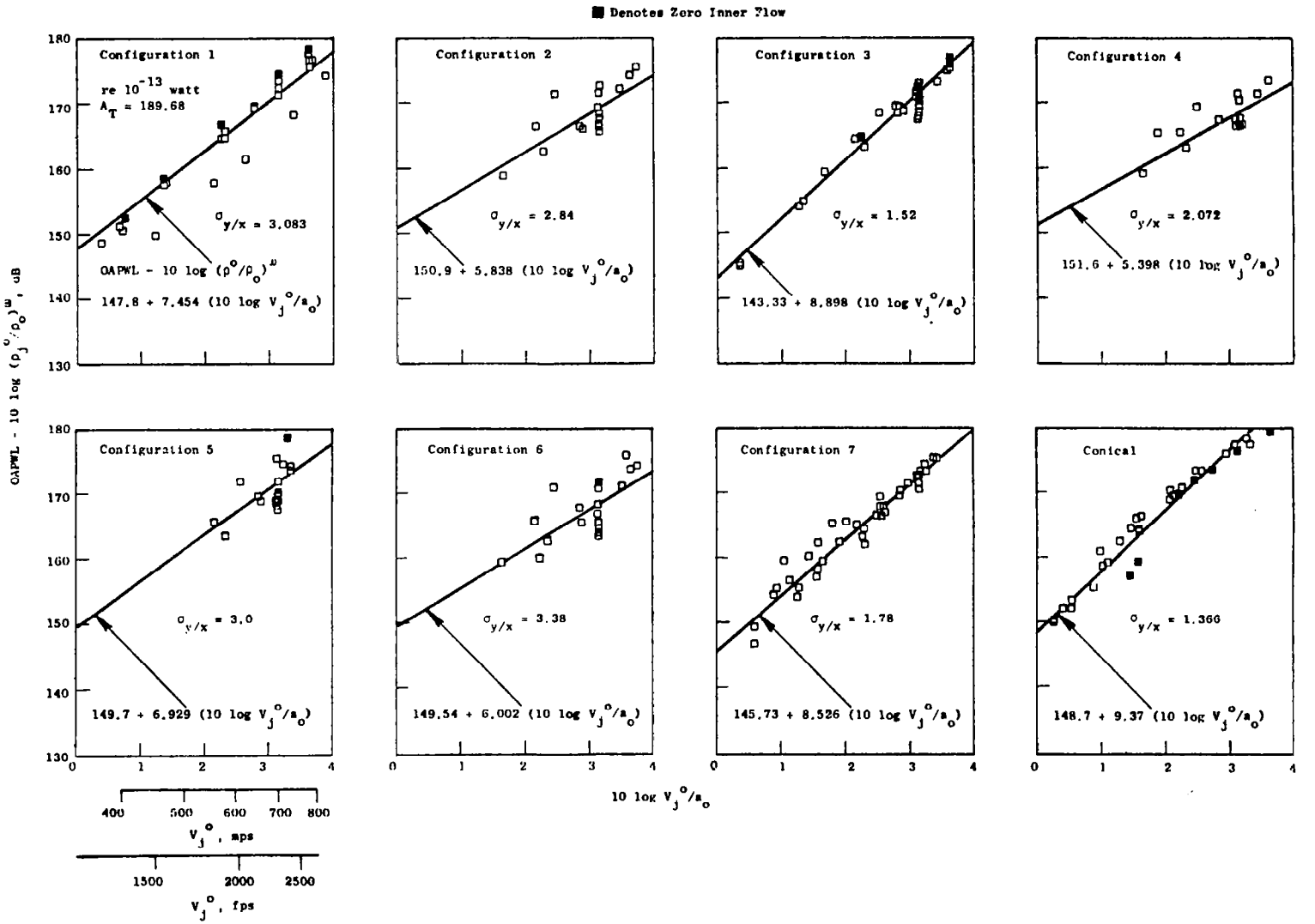

Figure 5-4. Summary of Overall Power Level Measurements for High Radius Ratio Coannular Nozzles Using the Outer Stream Density and Velocity as the Characteristic Noise Parameters.

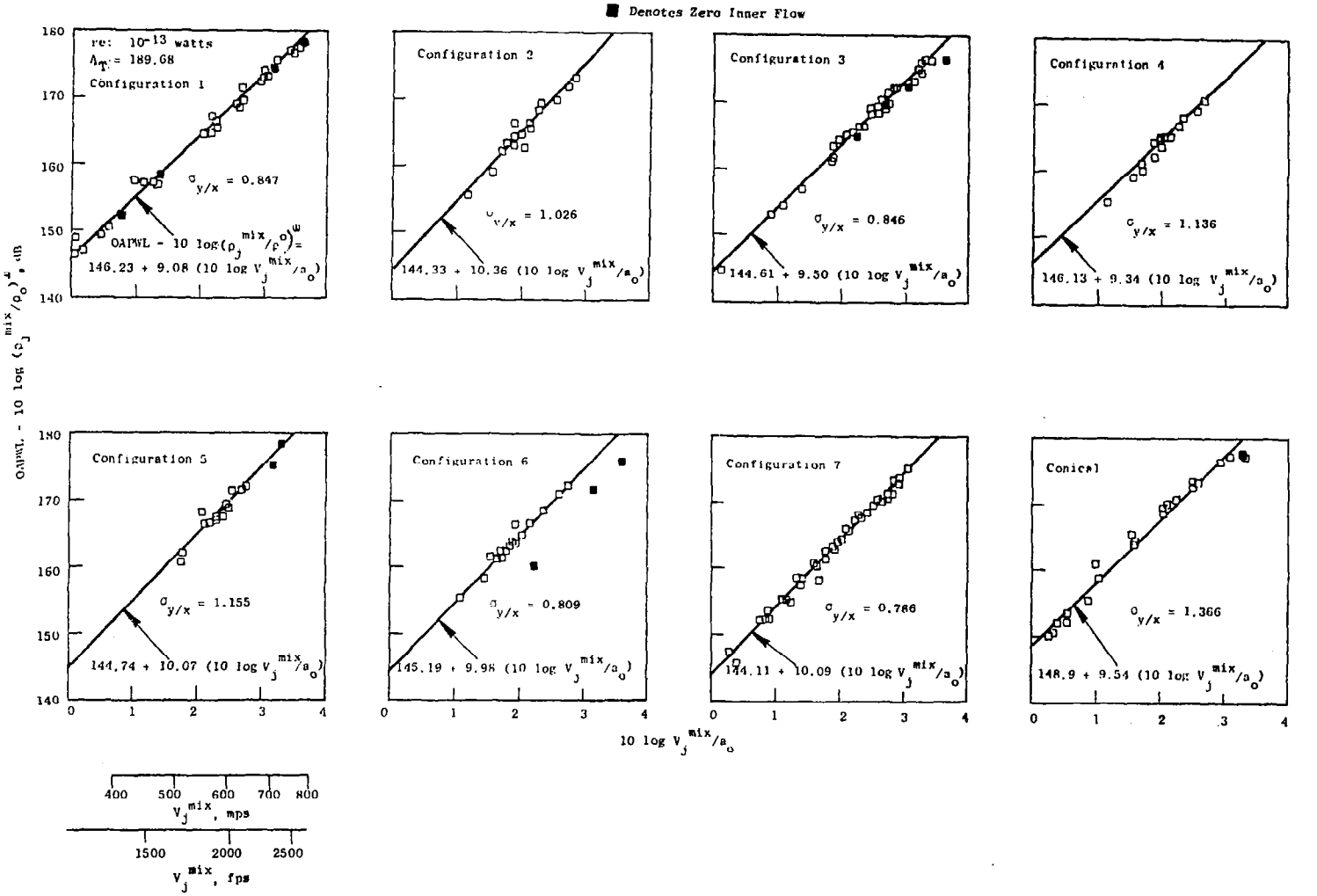

Figure 5-5. Summary of Overall Power Level Measurements for High Radius Ratio Coannular Nozzle Using the Mixed Stream Density and Velocity as the Characteristic Noise Parameters.

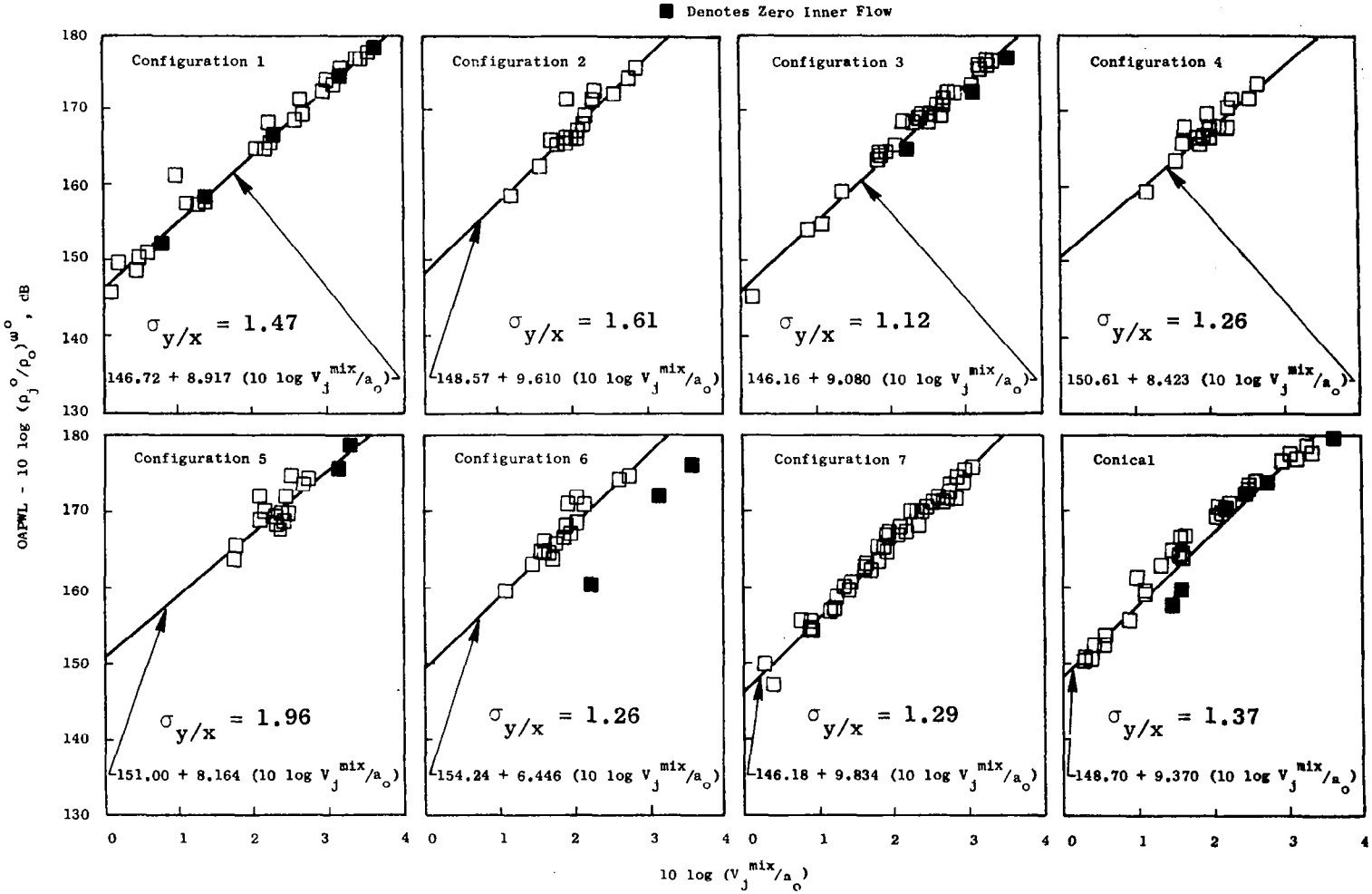

Figure 5-6. Summary of Overall Power Level Measurements for High Radius Ratio Coannular Nozzles Using the Outer Stream Density and the Mixed Stream Velocity as the Characteristic Noise Properties.

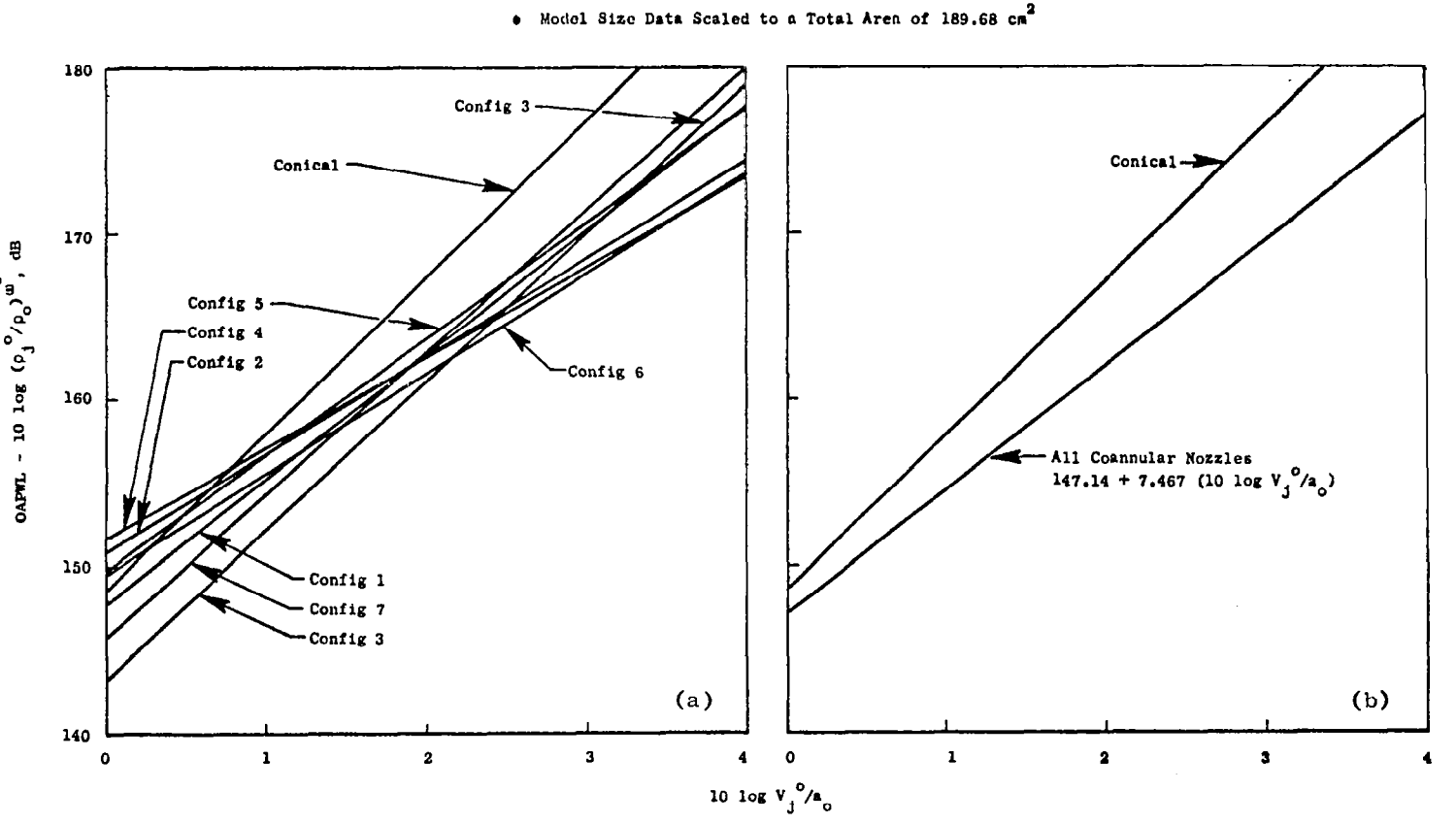

Figure 5-7. Summary of Regression Analysis of OAPWL Using the Outer Stream Density and Velocity as the Characteristic Noise Properties.

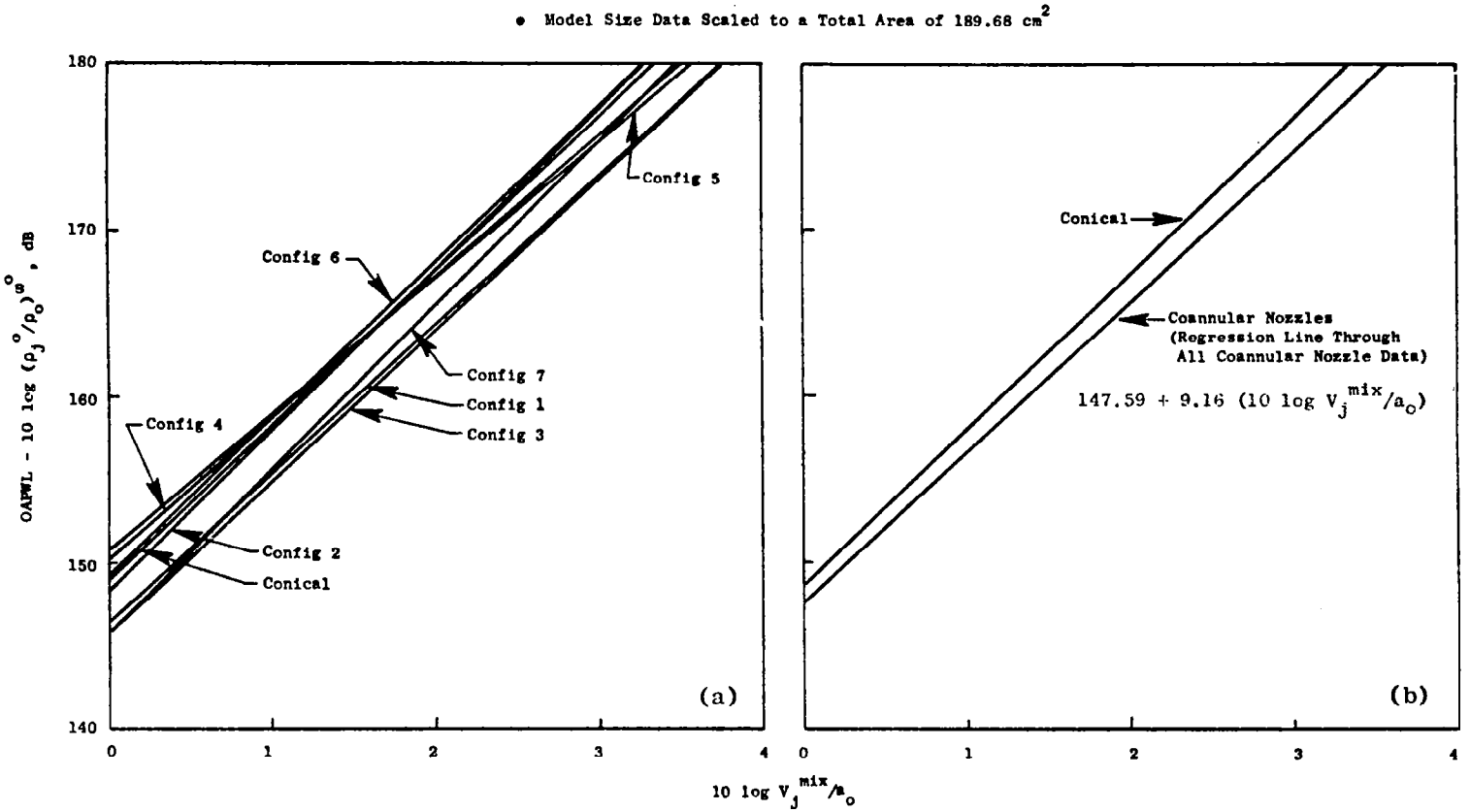

Figure 5-8. Summary of Regression Analysis of OAPWL Using the Outer Stream Density and the Mixed Stream Velocity as the Characteristic Noise Properties.

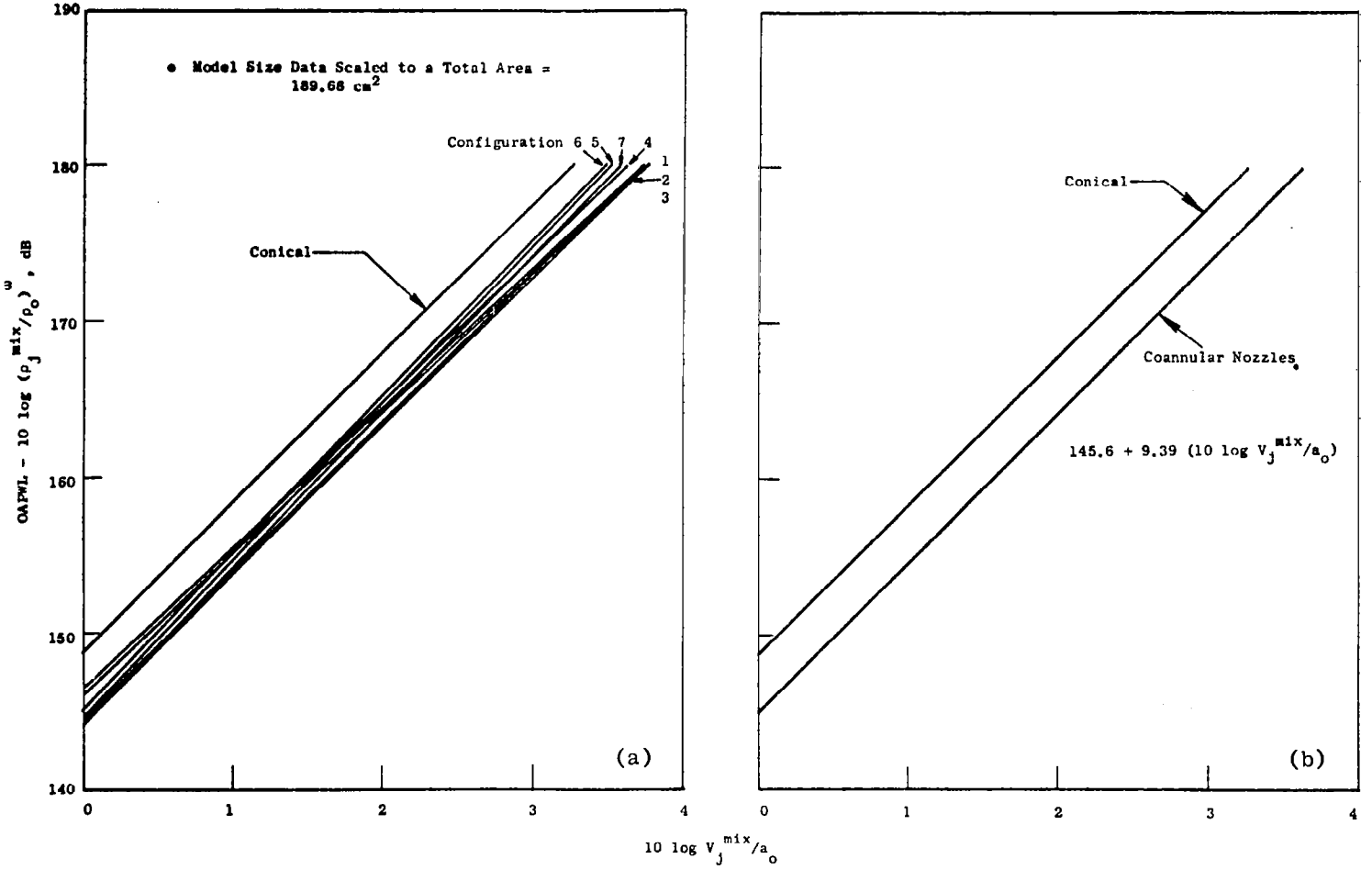

Figure 5-9. Summary of Regression Analysis of OAPWL Using the Mixed Stream Density and the Mixed Stream Velocity as the Characteristic Noise Properties.

Figure 5-9, employing the mixed velocity and static mixed density to correlate the data, which indicate that the velocity power laws obtained from the regression analysis are much the same as a conical nozzle. This observation suggests that the noise generation mechanisms similar to those that exist in the conical nozzle are also present in the coannular nozzle.

5.1.2.3 Acoustic Efficiency for High Radius Ratio Coannular Nozzles

In subsection 5.1.1 the acoustic efficiency for coannular nozzles was introduced (Equations 8, 9a, b, and c). This parameters is a useful parameter to study since it is the noise per unit mechanical power of a nozzle systems. This parameter then allows the noise to be compared more on a system one-to-one basis, regardless of whether the nozzle is a single stream or multiple stream nozzle.

Figure 5-10 shows typical acoustic efficiencies for a conical nozzle, high radius ratio annular nozzles (test results run where the inner stream of the coannular nozzles were completely blocked), and a coannular nozzle. Figure 5-11 shows the computed acoustic efficiencies for all the high radius ratio coannular nozzles tested. Table 5-3 summarizes the results of a regression analysis performed on the test results.

In Figure 5-10a the test results of the conical nozzle and the annular nozzles are shown. The regression analysis shows that $\eta = 9.549 \times 10^{-5} (M_o)^{5.11}$ [or when fitting the data M_o^5 classical noise result, $\eta = 1.004 \times 10^{-5} M_o^5$]. This result is typical of any high velocity and temperature conical nozzle. The measured results also show that high radius ratio annular nozzle radiate less noise than the conic nozzle.

Figure 5-10b illustrates the computed acoustic efficiencies for Configuration 7 versus the mixed stream acoustic Mach number. Shown on the Figure is the regression curve and the standard error of estimate of the resultant regression line, as well as a curve fit based on the prediction equation of the form $\eta = C (M_o^{mix})^5$ - the classical Lighthill form. The reduction of noise per unit mechanical power illustrated for Configuration 7 is 5.92 dB. This source noise level reduction is typical for the high radius ratio coannular nozzles tested. The exact level of noise reduction for each of the configurations tested is shown in Figure 5-11 and a summary of the regression expressions formulated from the data is given in Table 5-3.

5.1.2.4 Lighthills Coefficient

In Section 5.1.2.1., the acoustic power was formulated in terms of a Lighthill parameters L, and a Lighthill coefficient K (see Equations 2, 6, and 7). Table 5-1 gave calculated values of the Lighthill coefficient derived

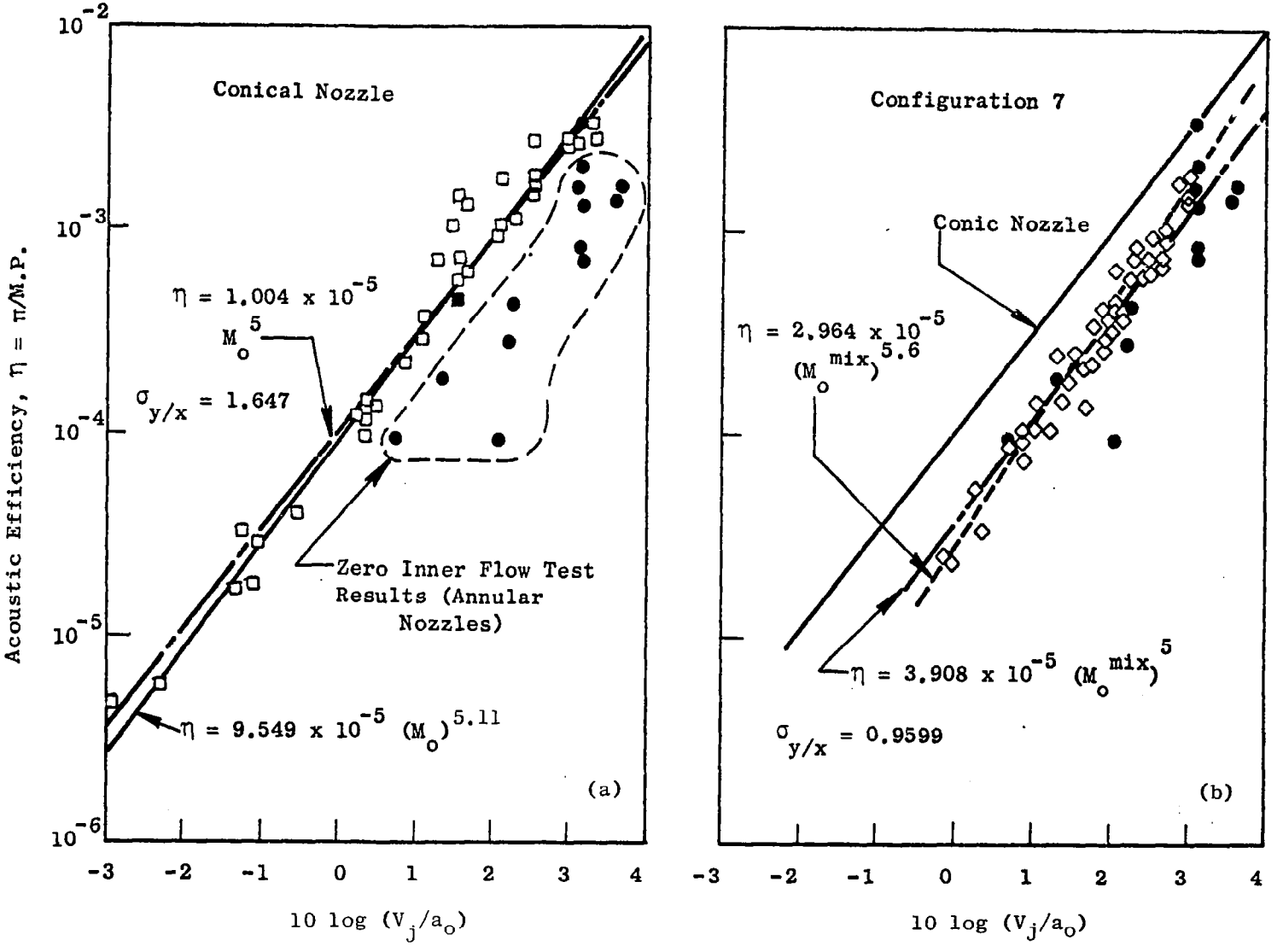

Figure 5-10. Typical Acoustic Efficiencies for a Conical Nozzle, Annular Nozzle, and Coannular Nozzle.

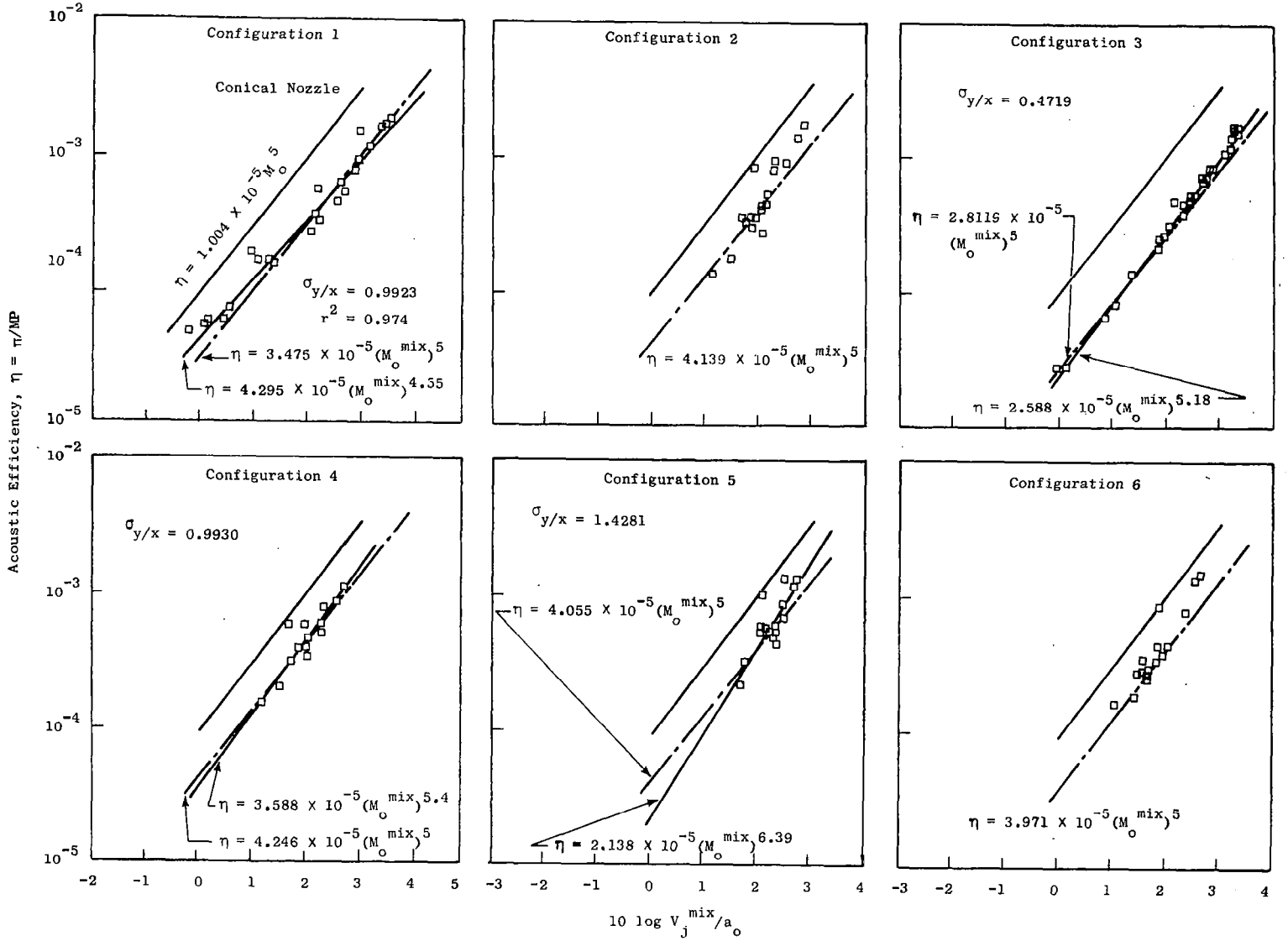

Figure 5-11. Acoustic Efficiencies for High Radius Ratio Coannular Nozzles.

Table 5-3. Linear Regression Analysis of Acoustic Efficiency for High Radius Ratio Coannular Nozzles with a Plug.

Prediction Form: a) $\eta = \hat{C} (M_o^{mix})^n$				b) $\eta = C (M_o^{mix})^{5.0}$	
Configuration	$\hat{C}$	n	$\sigma y/x$	Configuration	C
1	4.295×10^{-5}	4.55	.9923	1	3.475×10^{-5}
2	7.780×10^{-5}	3.63	2.293	2	4.139×10^{-5}
3	2.588×10^{-5}	5.18	.4719	3	2.8119×10^{-5}
4	3.588×10^{-5}	5.4	.9930	4	4.246×10^{-5}
5	2.138×10^{-5}	6.39	1.428	5	4.055×10^{-5}
6	6.412×10^{-5}	3.96	2.187	6	3.971×10^{-5}
7	2.964×10^{-5}	5.6	.9599	7	3.908×10^{-5}
All Data	3.908×10^{-5}	4.89	1.488	All Data	3.715×10^{-5}
Conical Nozzle	9.549×10^{-5}	5.11	1.6473	Concial Nozzle	1.004×10^{-5}

where

η = Acoustic Efficiency (π/M.P.)

π = Measured Acoustic Power, watts

M.P. = Mechanical Power, watts

$\hat{C}$, C = Constants of Proportionality

M_o^{mix} = Mixed Stream Mach Number, V_j^{mix}/a_o

V_j^{mix} = Mixed Stream Velocity

a_o = Ambient Speed of Sound

from curve fitting. The actual values of K, can be computed directly from Equations 2, 6, and 7. Figure 5-12 illustrates the results of the computed Lighthill coefficient using Equations 2 and 6 for high radius ratio annular plug nozzles, and a typical high radius ratio coannular nozzle.

Figure 5-12a shows the computed Lighthill coefficient, K, versus the outer radius ratio R_r^o for the annular nozzle test results (tests where the inner stream of the coannular nozzles was physically blocked off simulating a purely annular jet). The results show that increasing the radius ratio decreases the Lighthill Coefficient K - synonymous with a reduction in source noise. These results also suggest that the most benefit occurs for radius ratio of $R_r^o \geq 0.85$. The results of Figure 5-12a also suggest that the assumption that $K^o = K^i = K$ for the dual flow stream equations is not exact except when $R_r^i = R_r^o$, or when $R_r < 0.85$.

Figure 5-12b illustrate the influence of the flow variables of velocity ratio, V_r, inner stream pressure ratio, P_r^i, and outer stream pressure ratio, P_r^o for a typically high radius ratio coannular nozzle (Configuration 7) on the computed Lighthill coefficient using Equation 6. The results show that the value of K is a complicated function of the flow variables; i.e.,:

$$K = K\,(R_r^o\ R_r^i,\ V_r,\ A_r,\ P_r^o,\ P_r^i)$$

In retrospect, the nonuniqueness of the coefficient K should not be surprising. After all, Equations 2 or 6 are equations primarily reflective of the turbulent mixing noise alone. For instance, convective amplification, refraction, and fluid shielding effects are not included in these equations. This basic acoustic propagation influence would certainly affect the resultant power levels. Each of these acoustic propagation mechanisms are affected by the inner stream and outer stream flow and interaction conditions.

As a simple example to illustrate how the propagative mechanisms can influence the classical power level calculations, consider a simple subsonic jet such that the acoustic intensity I (R, θ) is given by

$$I\,(R,\theta) = \frac{\rho_j^2\ V_j^8\ D^2}{\rho_o\ a_o^5\ R^2}\ (1 - M_i \cos\theta)^{-5} \qquad (12)$$

were the last term on the right hand side of the equation is the subsonic classical Lighthill subsonic convection amplification term. The acoustic power, π, is computed from:

$$\pi = 2\pi\ R_o^2 \int^{\pi} I(R,\ \theta)\ \sin\theta\ d\theta \qquad (13)$$

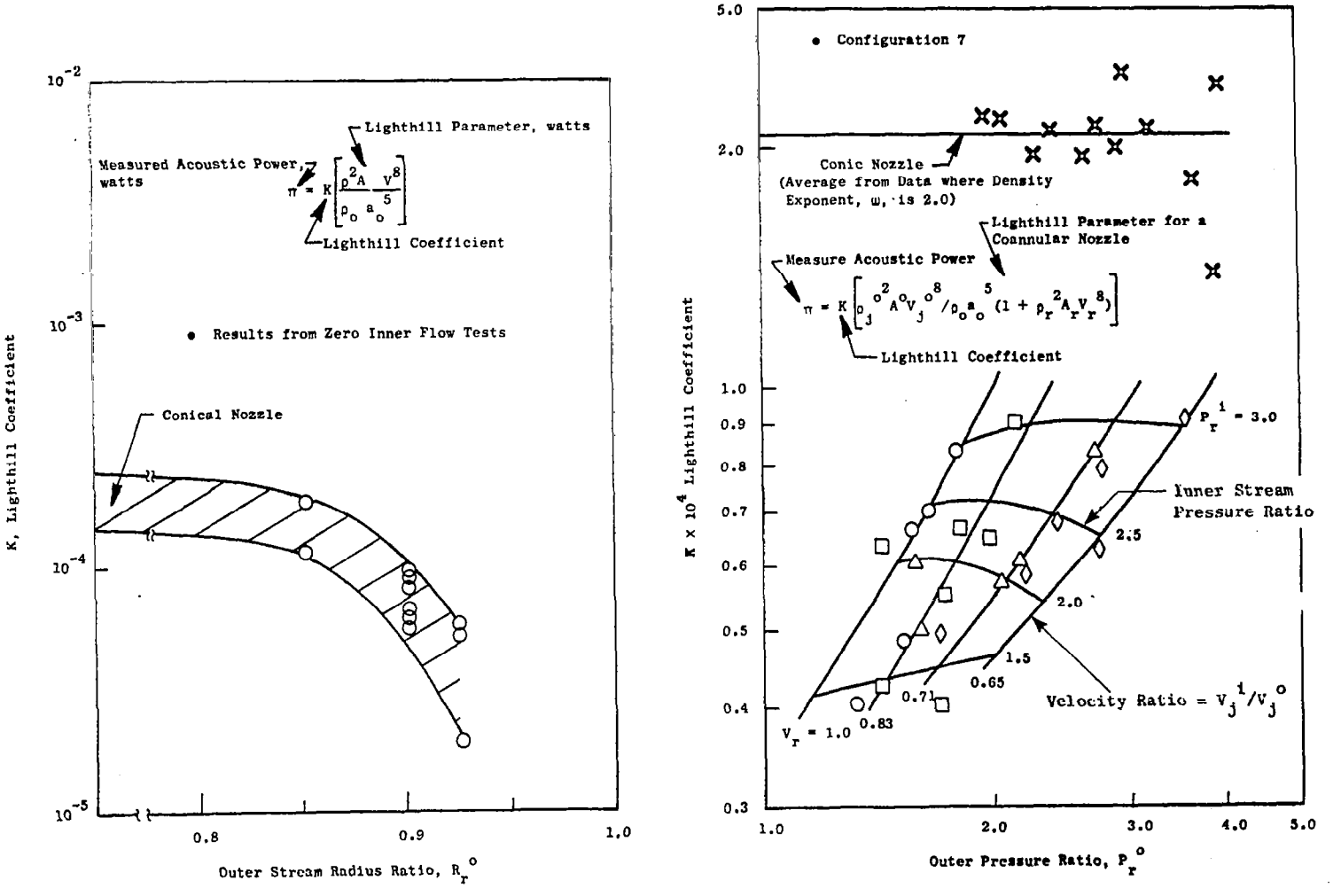

(a) Influence of Outer Stream Radius Ratio on K, for Annular Nozzles

(b) Influence of Flow Variables on K, for a Typical Coannular Nozzle

Figure 5-12. Influence of Geometry and Flow Variables on the Lighthill Coefficient for High Radius Ratio Annular and Coannular Nozzles.

Therefore

$$\pi \simeq 2\pi \frac{\rho_j^2 V_j^8 D^2}{\rho_o a_o^5} \cdot \frac{1+M_c^2}{(1-M_c^2)^4} \qquad (14)$$

where the last term on the right hand side of the equation is due to convection amplification for subsonic jets. A computation of this term will illustrate how a velocity power law greater than eight can occur. For a supersonic jet this term is quite complicated (see Reference 5-3):

$$\pi \sim 2\pi \frac{\rho_j^2 V_j^8 D^2}{\rho_o a_o^5} \cdot \frac{1}{3M_c q^2} \left\{ \frac{M_c-1}{[(1-M_c)^2 + q^2]^{1/2}} \left[\frac{1}{(1-M_c^2) + q^2} + \frac{2}{q^2} \right] \right.$$

$$\left. + \frac{M_c+1}{[(1+M_c)^2 + q^2]^{1/2}} \left[\frac{1}{(1+M_c)^2 + q^2} + \frac{2}{q^2} \right] \right\} \quad \text{where } q^2 \equiv (\alpha M_c)^2 \qquad (15)$$

Equations 14 and 15 illustrate how the simple K of equations 2, 6 and 7 have to account for the convection amplification effects. Refraction and fluid shrouding effects would generate additional factors as illustrated above for convection amplification. To expect a unique value for K without allowing for some functional dependence of the flow and geometry parameters of coannular nozzles of theoretical analysis is asking too much from such a simple analysis.

5.1.3 Maximum Perceived Noise Level and Test Results for High Radius Ratio Coannular Nozzles

5.1.3.1 Analysis of Results Based on all the Test Results

The results of subsection 5.1.2.2 have show that good data correlation is obtained when the mixed stream properties (velocity and density) are employed as the characteristic parameters. The results of subsection 5.1.2.3 illustrated the importance of acoustic efficiency as a basis for comparison of nozzles of different thrusts. In this section, the test results shall be considered on a PNL_{max} basis in order that some rational judgment can be made concerning which configuration is "best". This is illustrated by presenting the test results in the form

$$PNL_{max} - 10 \log F/F_{ref} - 10 \log (\rho_j^{mix}/\rho_o)^{\omega-1} \text{ vs } 10 \log V_j^{mix}/a_o$$

Presenting the results in this fashion uses the best of the correlating parameters found in 5.1.2.2, and also normalizes the results on a per unit thrust, F, basis similar to the results in subsection 5.1.2.3. Figures 5-13 and -14 present all the test results for Configurations 1 through 7 in this fashion, while Table 5-4 summarizes the results of the linear regression analysis performed on the data.

Figure 5-13 shows all the data results for Configurations 1 through 7 with the individual regression lines given as a reference line through the data. These test results show that the data is regular and systematic in nature for each configuration. On some of the configurations the data collapses quite well (particularly Configurations 3 and 5). On the other configurations (such as Configurations 2, 4 and 6) there appears to be some data clustering at 10 log $V_J^{mix}/a_o \sim 2.0$. As it happens, these clustered data points are those in which the outer stream velocity was held consistant while varying the inner velocity such that $V_r \simeq .1 \rightarrow .7$ (the inner stream was primarily subsonic for this test series). Nonetheless, the regression results are felt to be representative of the general PNL_{max} characteristics for each configuration. As was shown on the power level results these results also show definite geometry influences.

Figure 5-14 summarizes the resultant regression curves through all the data. Figure 5-14a shows a definite configuration dependence for the PNL_{max} per unit thrust levels. In the high velocity regions (10 log $V_J^{mix}/a_o \geq 2$) Configuration 6 is observed to have the lowest noise levels. Relative to the conic nozzle, a 7 PNdB noise reduction is observed at 700 mps for Configuration 6. Configuration 6 may be recalled as having the highest outer stream radius ratio (0.926). Comparing Configurations 2 and 4 (both have the same outer stream radius ratio (0.902) and area ratio (1.03), but Configuration 4 has a bent inner stream plug), Configuration 4 is found to be 2 PNdB lower than Configuration 2 at $V_J^{mix} \sim 700$ m/sec. At 10 log $V_J^{mix}/a_o \sim 2.0$ (.540 m/sec), the data variance for all the configurations was found to be a minimum (All configurations are within ± 1PNdB). At lower velocities (10 log $V_J^{mix}/a_o < 2$) the data trends were found to switch from what was observed at the higher velocities. Now Configuration 6 appears as the configuration least desirable, while the Configurations with the lower outer stream radius ratio ($R_r^o \sim 0.853$) appear the best configurations. Since the geometry influences shall be discussed in more detail later, no more specified geometry differences shall be discussed here.

Figure 5-14b is a comparison of the conic nozzle with a linear regression curve for all the configurtions. At $V_J^{mix} \sim 700$ m/sec, a comparison of the conic nozzle with the results for all the coannular nozzle data indicates a 5 PNdB noise level reduction.

5.1.3.2 Analysis of Results Based only on the High Flow Test Results

In the above subsection, a data clustering was observed when the inner stream of the coannular nozzles was at low flow (and subsonic) conditions. These results by themselves are at a higher level than the test results which

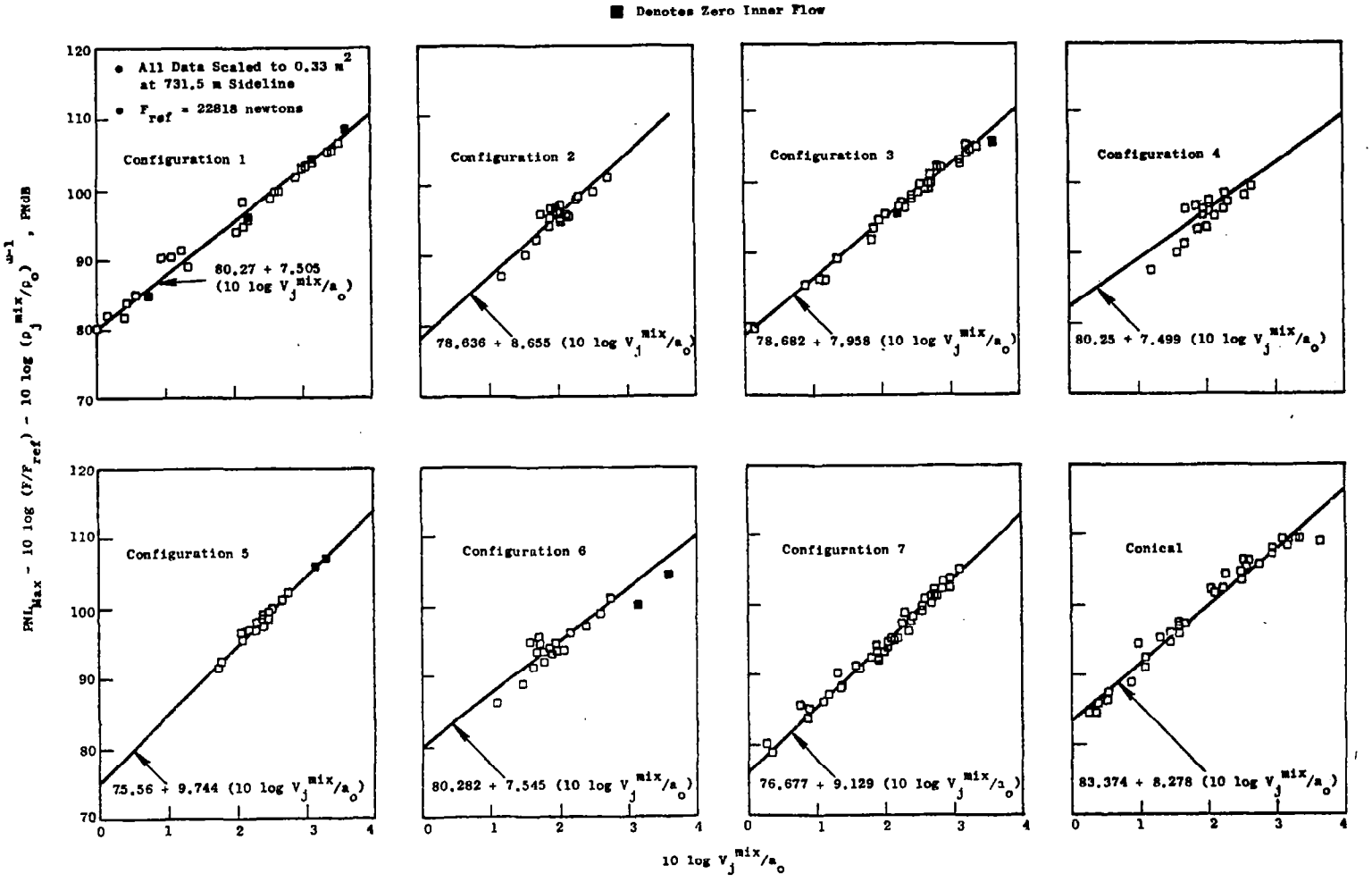

Figure 5-13. Summary of Maximum Perceived Noise Level Test Results for Configurations 1 through 7.

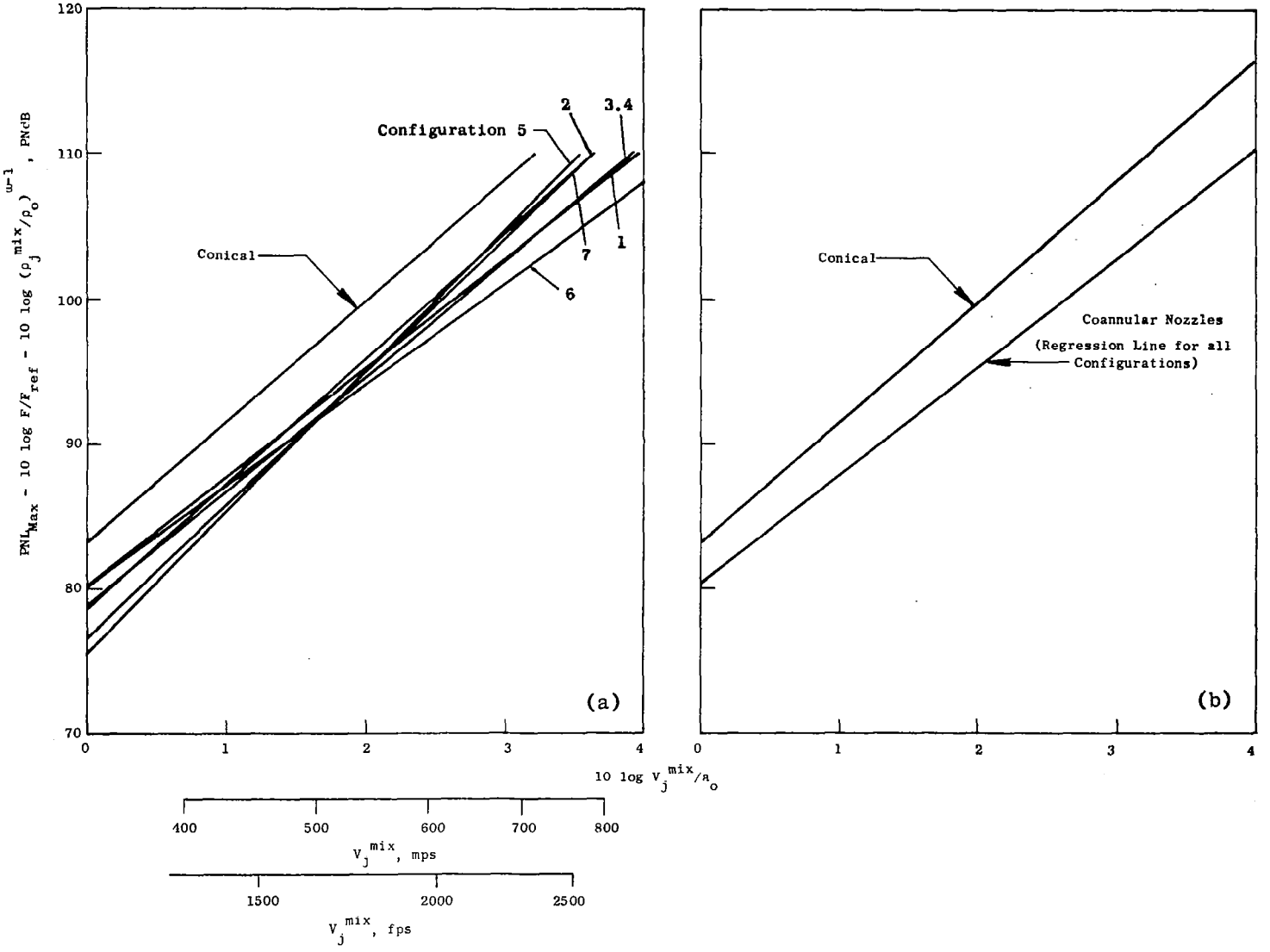

Figure 5-14. Summary of Regression Analysis of Maximum Perceived Noise Level - Illustration of Coannular Nozzle Geometry Influences Using All the Test Results.

were at high inner flows (and supersonic). Figure 5-15 summarizes results of an analysis of the test results when the low inner flow tests were omitted. Figure 5-15a shows the data, while Figure 5-15b compares the results of the regression analysis (see Table 5-4 for a summary of the regression prediction equations) for the different test nozzles. Differences between the results for all the test data (Figure 5-14) are observed. Configuration 6 is no longer the better configuration at the high mixed jet velocities. Configurations 3 and 4 are now found to be the best. The bent inner stream plug configuration (Configuration 4) is again observed to be better than its conic plug counterpart (Configuration 2).

5.1.3.3 Results From a Multiple Regression Analysis Using All the Data

When a variable depends on several factors such as velocity, density, area ratio, radius ratio etc., the regression analysis used above (two variables) can readily be generalized to a larger number of variables. To examine some of the thermodynamic and geometric trends depicted by the data, a multiple regression analysis calculation was performed using all of the test data results. The relationships thus obtained are given below:

$$OAPWL = 161.14 + 8.9\,[10 \log V_j^{mix}/a_o] + 2.51\,[10 \log (\rho_j^{mix}/\rho_o)];\ \sigma_{y/x} = 0.88 \tag{16}$$

$$PNL_{max} - 10 \log F/F_{ref} = 80.1 + 7.485\,[10 \log V_j^{mix}/a_o] + 0.879\,[10 \log \rho_j^{mix}/\rho_o];\ \sigma_{y/x} = 1.127 \tag{17}$$

$$PNL_{max} - 10 \log F/F_{ref} - 10 \log (\rho_j^{mix}/\rho_o)^{\omega-1} = 78.1 + 8.03\,\left[10 \log V_j^{mix}/a_o\right] + 0.159\,[10 \log A_r] - 2.29\,[10 \log R_r^o];\ \sigma_{y/x} = 1.77 \tag{18}$$

One of the motivations for Equation 16 was to evaluate the velocity and density exponents for overall power level for typically high radius ratio coannular nozzles with a plug. Equation 16 shows that when the mixed stream velocity, V_j^{mix}, and the mixed stream density, ρ_j^{mix}, are used to determine their functional dependence on the overall power level, OAPWL, an 8.9 velocity power law and a 2.51 density power law were obtained. Both of these power laws deviate from the classical Lighthill values of 8.0 and 2.0 respectively.

Equation 17 was considered in order to evaluate PNL_{max} per unit ideal thrust, F, at a 731.5 meter sideline for its velocity and density power laws when the mixed stream quantities are considered. The result found is that PNL_{max} has a velocity dependence of 9.485 (note that a factor of 2 was added

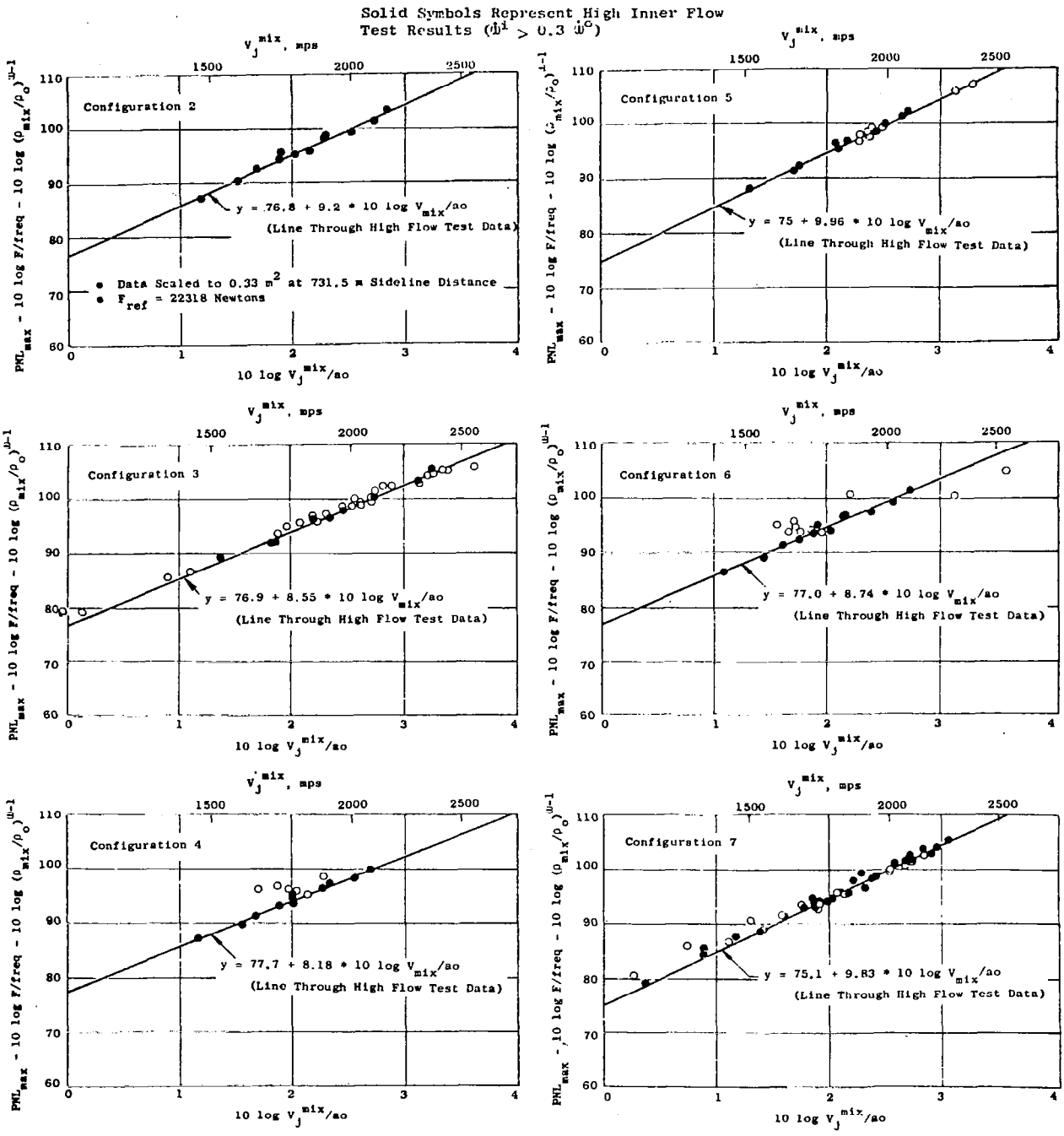

Figure 5-15a. Summary of Regression Analysis of Maximum Perceived Noise Levels for High Inner Flow Test Results Only.

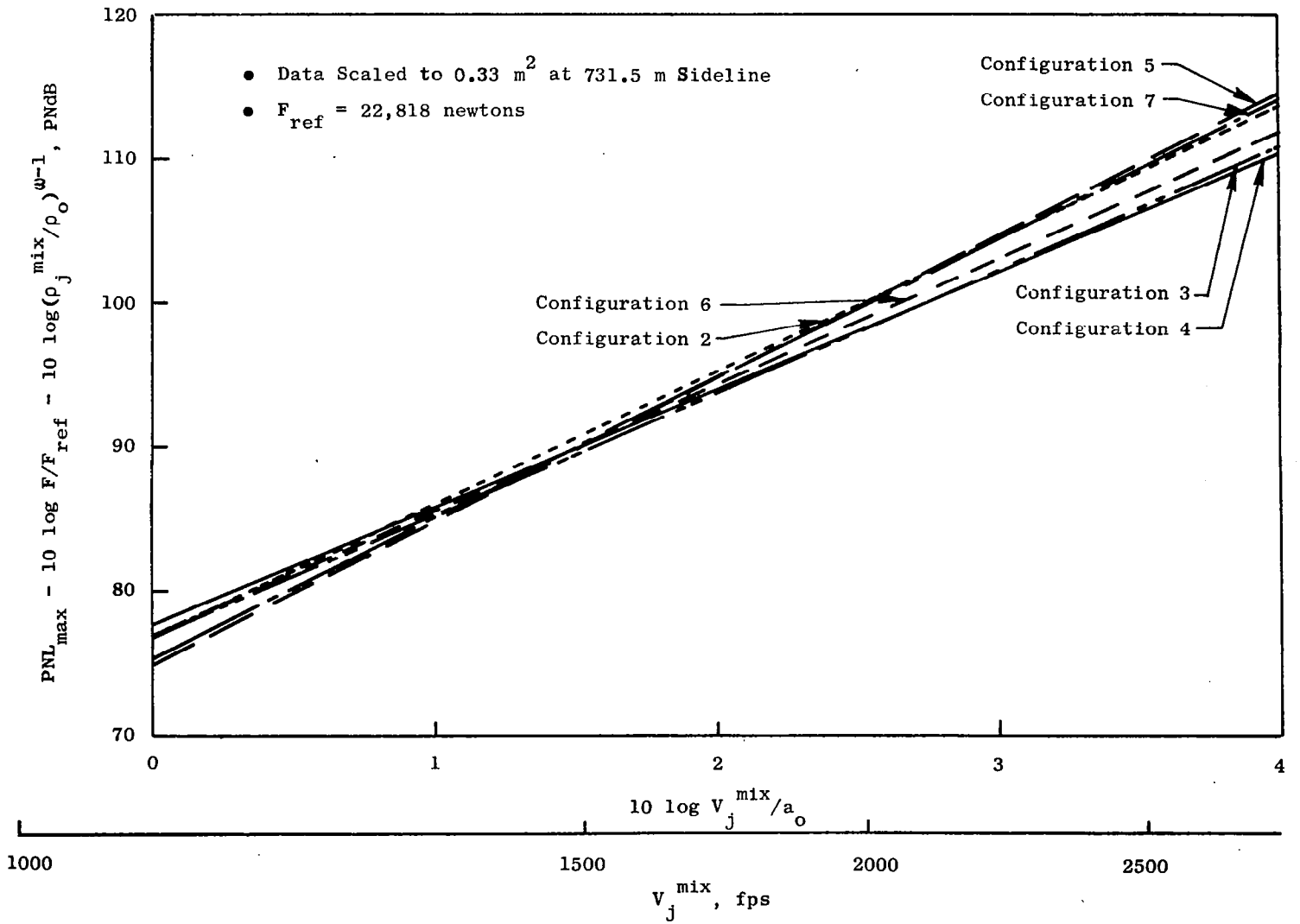

Figure 5-15b. Summary of Regression Analysis of Maximum Perceived Noise Level - Illustration of Geometry Influences Using High Inner Flow Test Results Only.

Table 5-4. Linear Regression Analysis of Maximum Perceived Noise Levels for High Radius Ratio Coannular Nozzles with a Plug.

Prediction Form: $PNL_{max} - 10 \log F/F_{ref} - 10 \log (\rho_j^{mix}/\rho_o)^{\omega-1} = a + b\ (10 \log V_j^{mix}/a_o)$

a) Results Using All Test Points

Configuration	a	b	$\sigma_{y/x}$
1	80.27	7.50	1.13
2	78.64	8.66	1.20
3	78.68	7.96	.65
4	80.25	7.50	1.66
5	75.56	9.74	.5
6	80.28	7.55	1.56
7	76.68	9.13	1.47
All Data	80.31	7.52	1.96
Conical Nozzle	83.37	8.28	1.34

b) Results Using High Inner Stream Flow Test Points Only

Configuration	a	b
1	-	-
2	76.8	9.2
3	76.9	8.55
4	77.7	8.18
5	75.0	9.96
6	77.0	8.74
7	75.1	9.83

to the calculated 7.485 to account for the $(V_j^{mix})^2$ contained in the thrust term F) and a density dependence of 1.879 (here a factor of 1 was added to the calculated 0.879 to account for the ρ_j^{mix} term also contained in the thrust term F). Hence on a PNL_{max} basis we find a substantial mixed velocity dependence with a nearly classical density power law.

The motivation for using Equation 18 was to get a first approximation of the influence of area ratio, A_r, and outer stream radius ratio on the PNL_{max} values (note that in determining the density exponent on the left-hand-side of the equation, ω-1, the SNECMA/NGTE values (Reference 5-2) for a conical nozzle were used). The result indicates that at a fixed thrust, mixed stream static temperature, and mixed stream velocity, an increase in area ratio tends to increase the noise (holding outer stream radius ratio constant), while an increase in outer stream radius ratio tends to decrease the noise (holding area ratio constant). As an illustrative example of the predicted geometry effect of outer stream radius ratio on noise reduction, an increase in outer stream radius ratio from 0.6 to 0.875 (holding thrust, mixed stream temperature, mixed stream velocity and area ratio constant), results in a 3.75 PNdB noise reduction. Some of these particular geometry effects will be considered in more detail in Section 5.2.

5.1.4 Velocity Dependence Study for a High Radius Ratio Coannular Nozzle with Plug - Configuration 7

One of the test series which was performed was a so-called velocity dependence study using the Configuration 7 [R_r^o = 0.850, R_r^i = 0.902]. The tests were run such that the outer stream static temperature was held constant at ~660 K, and the inner stream velocity and temperature were held constant at ~500 m/sec and 360 K respectively, while the outer stream pressure and total temperature were regulated such that the outer stream velocity varied over the range of 430 to 740 m/sec. The actual tested conditions resulted in an average static mixed stream temperature, T_s^{mix}, of 551 K. This average temperature had a maximum variation of ±5%. Using a classical density power law of 2 results in a maximum variation in noise level of ±0.42 dB due to this static temperature variation. Discussed below are the results of this test series.

Figure 5-16 illustrates the measured velocity dependence of overall power level, OAPWL, and the influence of increasing velocity on the one-third octave-band power spectra. Figures 5-16a and 16b show a comparison of the velocity dependence of OAPWL when the outer stream and the mixed stream velocity are used as the independent variables respectively. When the outer stream velocity was used as the independent variable, the outer stream density was used in the normalization process. When the mixed stream velocity was used as the independent variable the mixed stream density was used in the normalization process. These results corroborate the earlier results which show that when the mixed stream properties are used, a more uniform and smoother data trend is obtained. The primary result is that the OAPWL has an 8.18 velocity power law dependence when the characteristic velocity used is the mixed velocity.

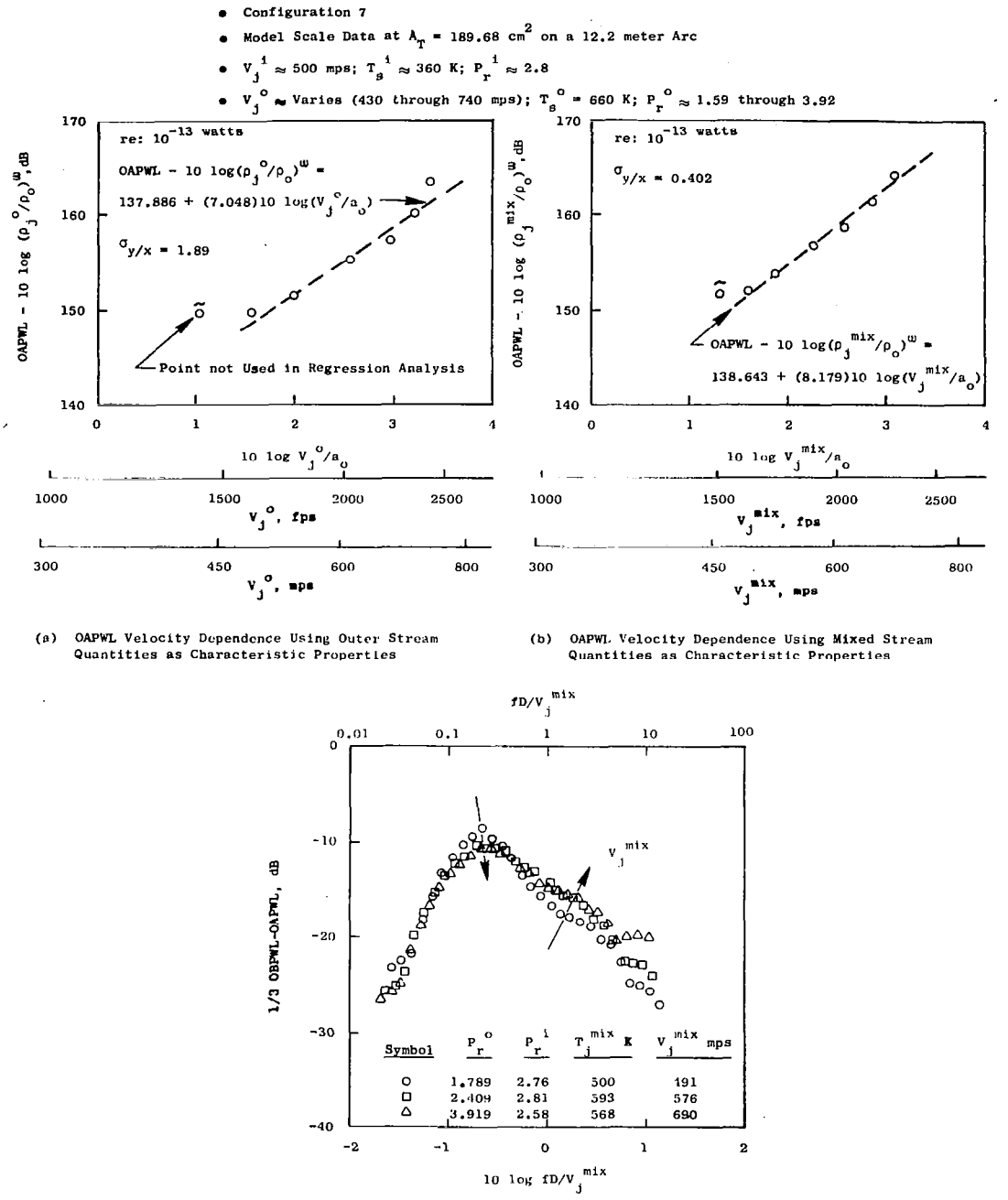

(a) OAPWL Velocity Dependence Using Outer Stream Quantities as Characteristic Properties

(b) OAPWL Velocity Dependence Using Mixed Stream Quantities as Characteristic Properties

(c) Influence of Mixed Stream Velocity on Power Spectrum Shape

Figure 5-16. Velocity Dependence of OAPWL and 1/3 OBPWL for a High Radius Ratio Coannular Nozzle with Plug,- Configuration 7 Test Results.

Figure 5-16c shows model scale one-third octave-band spectra for selected points from the velocity - dependence test series. The test results are presented as 1/3 OBPWL-OAPWL vs $f_{1/3}\ D/V_j^{mix}$ for mixed stream velocities, V_j^{mix}, of 451, 576 and 690 m/sec. The characteristic diameter, D, used was the equivalent diameter based on a total flow area of 189.68 cm^2. The test results show that increasing the velocity (at a fixed mixed stream temperature) increases the high frequency noise, somewhat flattens the peak frequency noise, and leaves the low frequency noise unaltered.

The velocity dependence results of OASPL at acoustic angles relative to the inlet, θ_I, of 150, 130, 110, 90, 70, and 50° for the velocity dependent test series are shown in Figures 5-17 and 5-18. Table 5-5 summarizes the results of the linear regression analysis performed on the data. The results shown in Figures 5-17 and 5-18 are presented in the same fashion as was illustrated earlier in Figure 5-16(a) and (b). Figure 5-17 shows that in the aft quadrant the velocity power law ranges as 8.75, 10.53 and 8.95 for acoustic angles θ_I = 110, 130 and 150 respectively (for noise correlated on the mixed stream properties). The standard error of estimate, $\sigma_{y/x}$, is seen to be relatively small. Figure 5-18 shows that in the forward quadrant the velocity power laws become progressively larger (10.05, 11.15, 11.62 for θ_I = 90, 70 and 50°). At these forward angles shock noise is influencing the data*; especially at the higher flow conditions. The regression analysis results when the normalization and independent parameters were the outer stream properties yielded prediction equations for OASPL similar in accuracy to those quoted above. But overall, using the mixed stream properties is still observed to yield the best fit for the data, and to be the key characteristic properties for the coannular nozzle.

5.1.5 Density Dependence for a Typical High Radius Ratio Coannular Nozzle with Plug - Configuration 7

In addition to the special series of controlled tests to examine the velocity dependence of coannular nozzles, a series of tests were performed to examine the density dependence of coannular nozzles. The tests were performed by holding the outer stream velocity, V_j^o, constant (~ 609 m/sec), the inner stream pressure ratio, P_r^i, constant (~ 2.8), the inner stream static temperature, T_s^i, constant (~ 230 K), while the outer stream static temperature, T_s^o, was varied over a range of values (430 K → 830 K).

5.1.5.1 Density Dependence of OAPWL, PNL and OASPL

Figures 5-19, 5-20 and 5-21 illustrate the test results for obtaining the density exponent for OAPWL, OASPL and PNL. Table 5-6 summarizes the linear regression analysis results obtained from the data presented in Figures 5-19 and 5-20.

*Shock noise will be considered in Section 5.3.

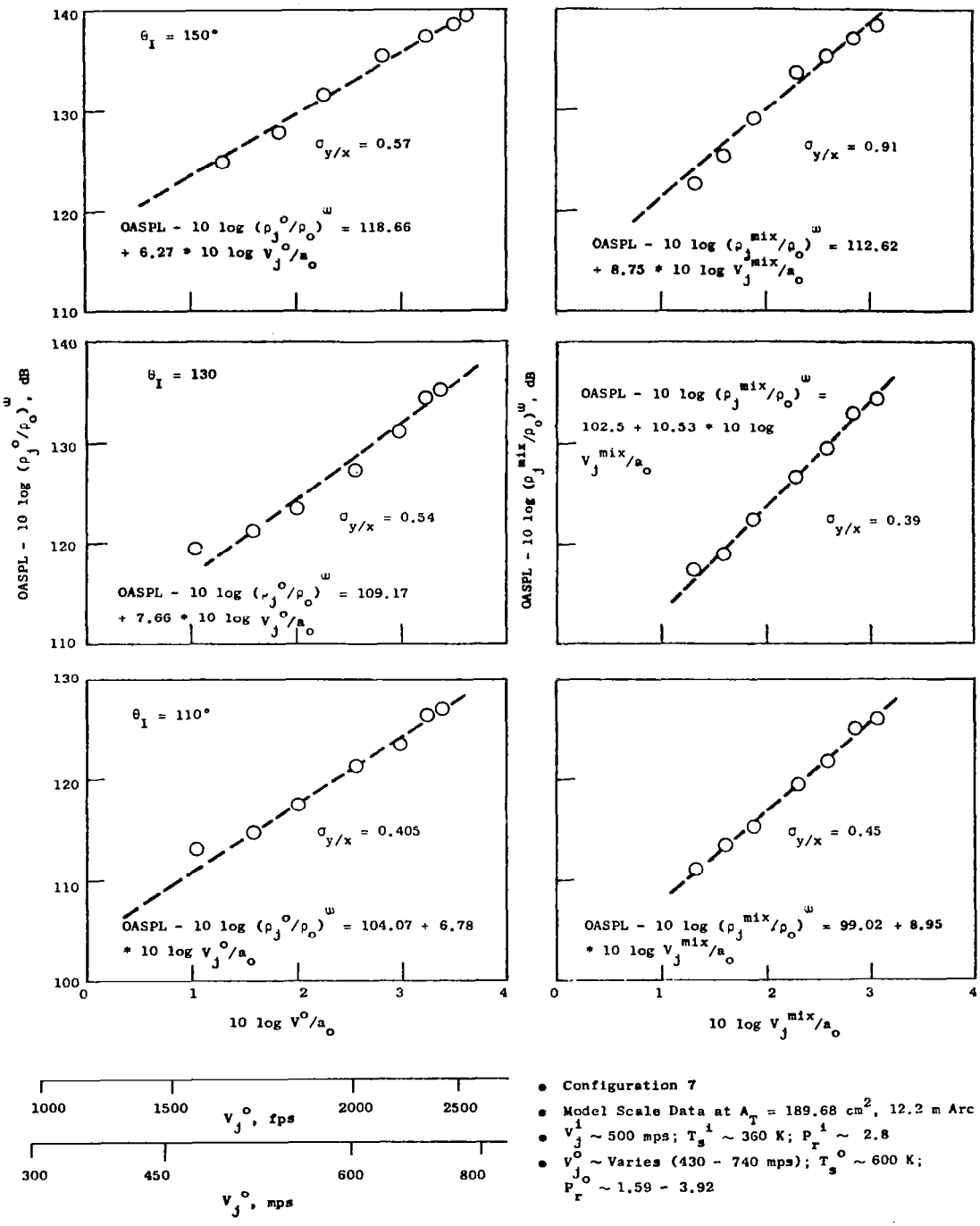

Figure 5-17. Velocity Dependence of OASPL at 150°, 130°, 110° for a Typical High Radius Ratio Coannular Nozzle with Plug, Configuration 7.

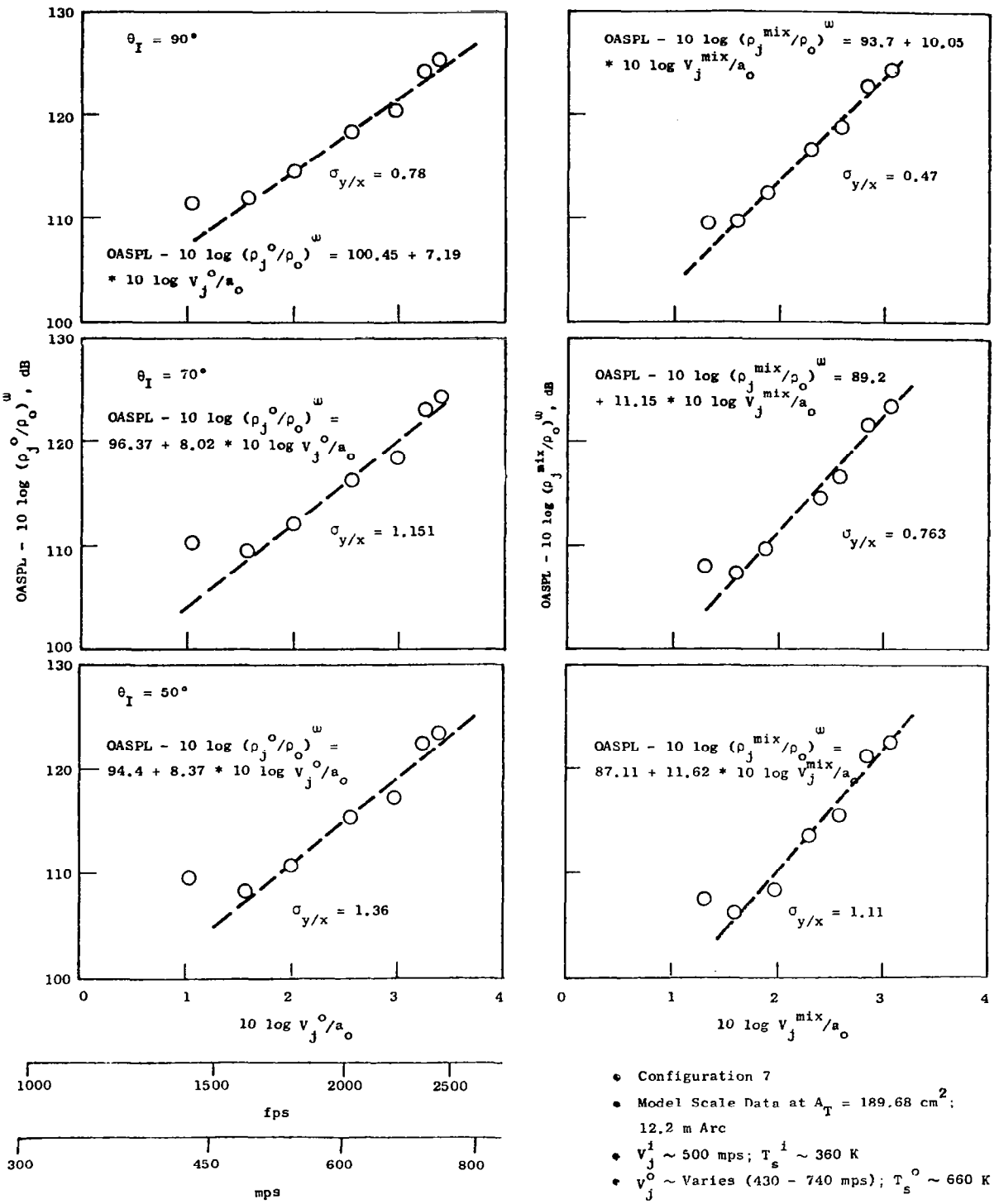

Figure 5-18. Velocity Dependence of OASPL at 90°, 70°, 50° for a Typical High Radius Ratio Coannular Nozzle with Plug, Configuration 7.

Table 5-5. Summary of Regression Analysis of OASPL Velocity Dependence Study for a Typical High Radius Ratio Coannular Nozzle with Plug - Configuration 7 [R_r^o = .853, R_r^i = .902].

Prediction Form: a) OASPL - 10 $\log_{10}$ $(\rho_j^o/\rho_o)^\omega$ = a + b [10 $\log_{10}$ V_j^o/a_o]

θ_I	a	b	$\sigma_{y/x}$
50	94.4	8.37	1.36
70	96.37	8.02	1.151
90	100.45	7.19	.78
110	104.07	6.78	.405
130	109.17	7.66	.54
150	118.66	6.27	.57
OAPWL-10 Log $(\rho_j^o/\rho_o)^\omega$	137.89	7.048	1.87

b) OASPL -10 log $(\rho_j^{mix}/\rho_o)^\omega$ = a + b [10 $\log_{10}$ V_j^{mix}/a_o]

θ_I	a	b	$\sigma_{y/x}$
50	87.11	11.62	1.11
70	89.20	11.15	.763
90	93.70	10.05	.47
110	99.02	8.95	.45
130	102.48	10.54	.39
150	112.62	8.75	.91
OAPWL-10 Log $(\rho_j^{mix}/\rho_o)^\omega$	138.64	8.18	.402

- Model Scale at A_T = 189.68 cm^2, 12.2 meter Arc
- V_j^i ~ 500 m/sec, T_s^i ~ 360° K, P_r^i ~ 2.8
- V_j^o ~ Varies (430 → 730 m/sec); T_s^o ~ 660° K, P_r^o: 1.59 → 3.92
- T_s^{mix} ~ 551° K ± 10%

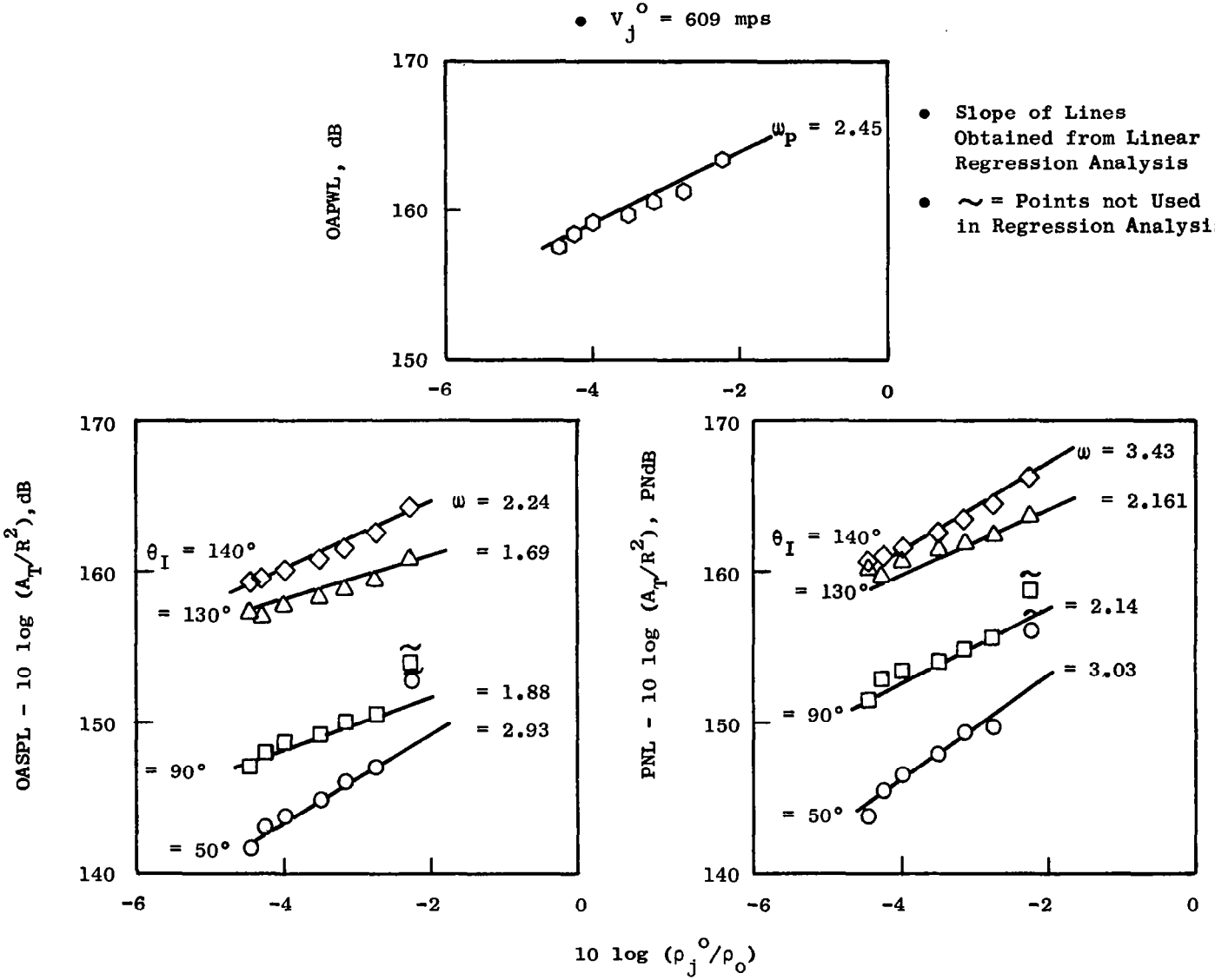

Figure 5-19. A Practical Determination of the Density Exponents for OAPWL, OASPL, and PNL for a Typical High Radius Ratio Coannular Nozzle with Plug, ρ_j^o Dependence.

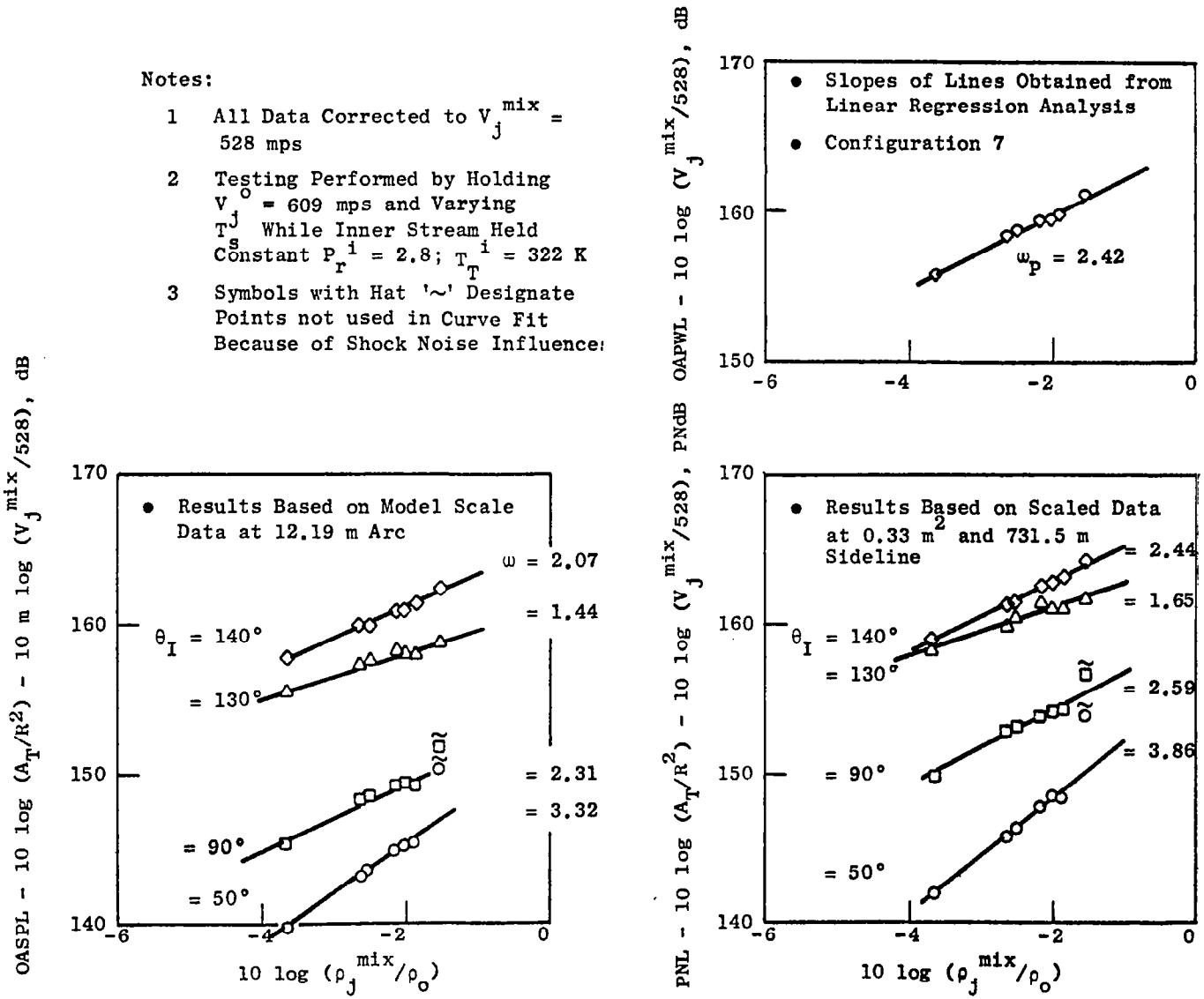

Figure 5-20. A Practical Determination of the Density Exponents for OAPWL, OASPL, and PNL for a Typical High Radius Ratio Coannular Nozzle with Plug, ρ_j^{mix} Dependence.

- Configuration 7 Test Results
- Test Performed by Holding $V_j^o \sim 609$ mps and Varying T_s^o While Inner Stream Held at Constant Conditions of $P_r^i \sim 2.8$; $T_T^i \sim 322$ K; $V_j^i \sim 410$ mps
- OASPL Results are Based on Model Scale Tests: $A_T = 189.68$ cm^2

  12.2 meter Arc
- PNL Results are Based on Scaled Data: $A_T = 0.33$ m^2; 731.5 meter Sideline
- Open Symbols Designate Results Based on Outer Stream Density
- Solid Symbols Designate Results Based on Mixed Stream Density

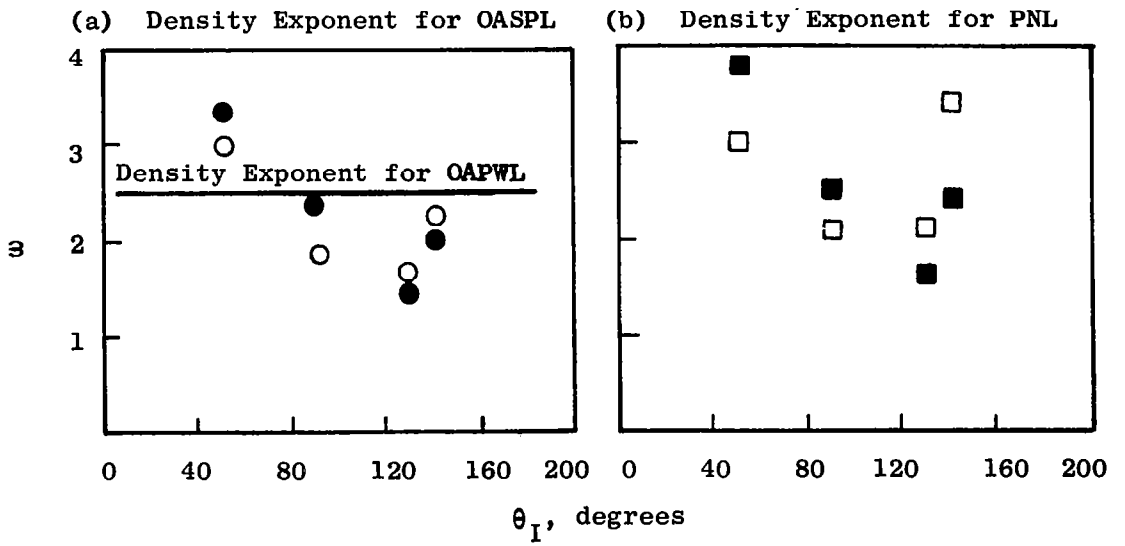

Figure 5-21. Summary of Density Exponents for OASPL and PNL with Acoustic Angle for a Typical High Radius Ratio Coannular Nozzle with Plug.

Table 5-6. Linear Regression Results for Density Exponents for High Radius Ratio Coannular Plug Nozzles.

	Results Based on Outer Stream Density			Results Based on Mixed Stream Density		
θ_I	Density Exponent for OASPL	Density Exponent for PNL	Density Exponent for OAWPL	Density Exponent for OASPL	Density Exponent for PNL	Density Exponent for OAPWL
50	-2.93	-3.03	-2.45	-3.32	-3.86	-2.42
90	-1.88	-2.14	----	-2.31	-2.59	----
130	-1.69	-2.16	----	-1.44	-1.65	----
140	-2.24	-3.43	----	-2.07	-2.44	----

Figure 5-19 illustrates the test results of OAPWL; OASPL at 50°, 90°, 130°, and 140° angles relative to the inlet, θ_I, and PNL at θ_I = 50°, 90°, 130°, 140° where the outer stream density was used as the independent variable. Figure 5-20 is a similar presentation of the test results, but the independent variable was the mixed stream density, ρ_J^{mix}. Since the mixed stream velocity varied to some extent, these test results were corrected for this variation as follows:

- For the OASPL, -10* b 10g (V_J^{mix}/528) was used. The values for b were obtained from Table 5-5.
- For OAPWL and PNL, -10* 10 log (V_J^{mix}/528) was used.

The test results show that for overall power level, using outer stream density or using the mixed stream density as the independent variable results in the density exponent for a high radius ratio coannular nozzle with plug to be approximately 2.45 (as compared to a conical nozzle where $\omega \sim$ 2.0). This result is found to be similar to the result obtained from the multiple regression analysis discussed in Subsection 5.1.3.3 where a density exponent of 2.51 was found.

The density exponents for OASPL and PNL are summarized in Figure 5-21. The open symbols designate the results based on the outer stream density, and the solid symbols designate the results based on the mixed stream density. The results show that in the forward quadrant, high values of ω are obtained for either OASPL or PNL up to 3.32 for OASPL and up to 3.86 for PNL. This result may be in part due to the broad band shock noise present at these angles (Note however that in the linear regression analysis for θ = 70° and 90° the symbols marked with a hat were not used since examination of the SPL spectra clearly showed a strong shock noise influence for those points. The other test points at θ = 70° and 90° are influenced by shock noise, but to a (visual) lesser extent. In the aft quadrant, the OASPL density exponents are approaching 2.0 or slightly greater, while for the PNL, at θ_I = 140°, $\omega \simeq$ 2.44 or 3.43 depending on the mixed stream or outer shown density parameter being considered. At the 140° angle, shock noise influences are not detectable in the spectra and the exponents found are assumed valid. At $\theta_I \sim$ 130° (close to the max PNL angle on a sideline), the density exponent was found to be close to 2.0. A similar result was obtained from the multiple regression analysis performed using all data and reported in Subsection 5.1.3.3.

5.1.5.2 Influence of Temperature on the Power Spectra for Some Typical High Radius Ratio Coannular Nozzles wth Plug

From the density dependence test series, the one-third octave-band power level, 1/3 OBPWL, was examined. The result is shown in Figure 5-22. The 1/3 OBPWL is normalized on OAPWL, and the frequency parameter chosen was f_D/V_J^{mix} (where D is the equivalent diameter based on A_T = 189.68 cm^2 and V_J^{mix} was the actual calculated value for the test condition). The results illustrated in Figure 5-22 show that increasing temperature (at approximately

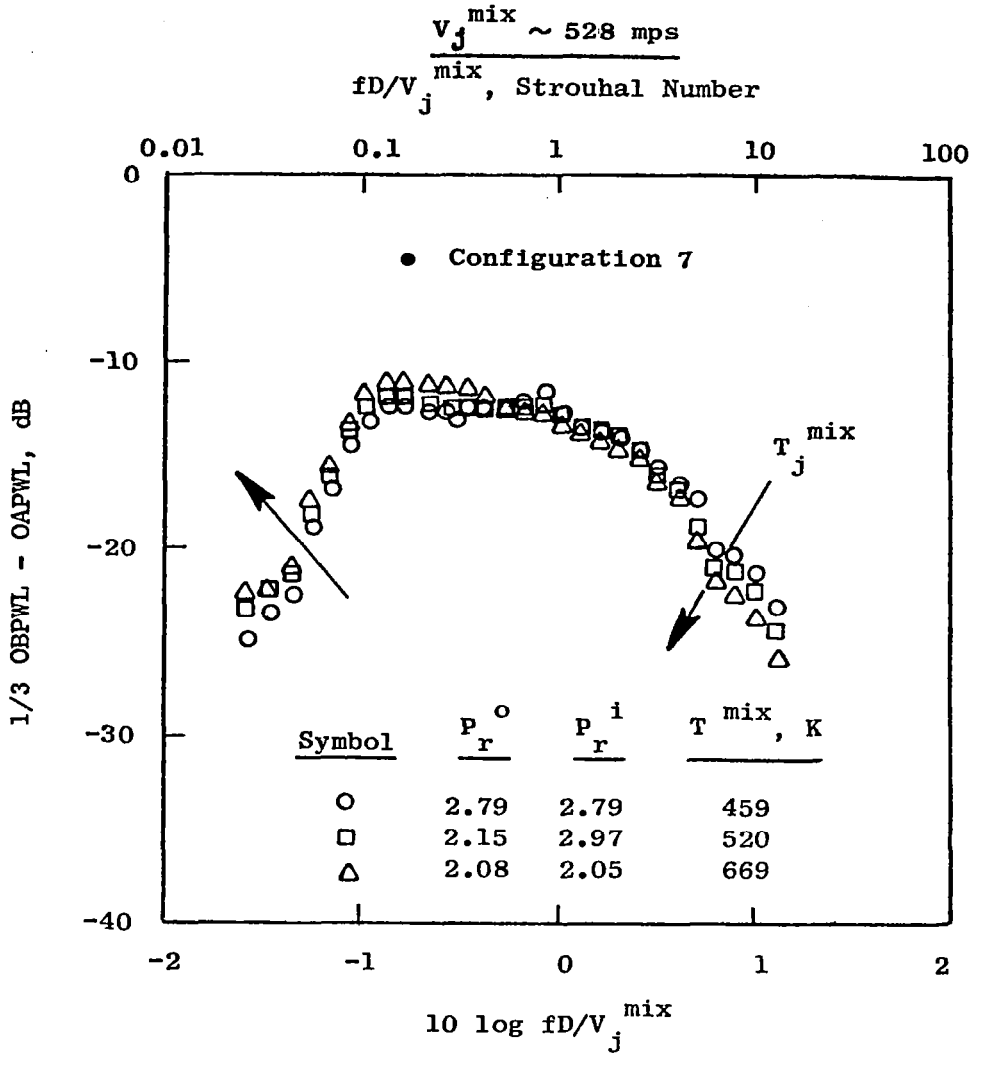

Figure 5-22. Influence of Mixed Stream Temperature on Normalized Power Spectra for a Typical High Radius Ratio Coannular Nozzle with Plug.

a constant V_j^{mix} ~ 528 m/sec) tends to increase the low frequency noise, and to decrease somewhat the high frequency noise. This result is similar to what is observed from a conical nozzle. Also the peak of the power level spectra for the coannular nozzle is observed to shift slightly to the lower frequencies with the increase in temperature.

5.1.6 Comparison of Typical Spectral Characteristics of High Radius Ratio Coannular Nozzles with Plug and a Conical Nozzle

To examine the typical spectral characteristics of high radius ratio coannular nozzles the with plug, the basic power spectral density, normalized one-third octave band spectra at three acoustic angles, and the directivity characteristics of one-third octave band spectra at three Strouhal numbers for Configuration 7 will be illustrated and compared with a conic nozzle. Appendix III contain equivalent data for Configurations 2 through 6.

5.1.6.1 Comparison of Power Spectral Density of a High Radius Ratio Coannular Nozzle with Plug and a Conical Nozzle

Three cycle flow conditions were chosen to illustrate the general power spectra of the coannular nozzle with plug; they are:

No.	Test Point	P_r^o	T_T^o,K	V_j^o, m/sec	P_r^i	T_T^i, K	V_j^i, m/sec	V_j^o/V_j^i	V_j^{mix} m/sec	V_j^o/V_{mix}
1	766R	1.73	836.7	496.52	2.01	469	413.3	1.20	468	1.06
2	771R	2.01	902.2	575.5	1.99	480	415	1.39	526	1.09
3	774	2.75	973.9	705.3	3.03	469	506	1.39	637	1.11

These points were chosen to represent high subsonic, sonic, and supersonic nozzle cycle conditions. The characteristic velocity chosen is the mixed stream velocity, V_j^{mix}. Correspondingly, three conical nozzle points* were chosen to match the conditions of the coannular nozzle with plug. The cycle points for the conic nozzle are:

N_o	P_r	T_T, K	V_j, m/sec
1	1.71	836.7	489.8
2	2.01	831	552
3	2.4	847	617

*These conic nozzle test points were obtained under FAA/DOT Contract DOT-OS-30034.

Figure 5-23 illustrates a comparison of power spectral density curves for Configuration 7 and the conic nozzle at the above cited conditions. Both sets of data are based in model scale test results at $A_T = 189.68$ cm^2. The characteristics velocity chosen is the mixed stream velocity V_j^{mix}.

For the high subsonic and sonic flow conditions (points 1, and 2), the peak of the spectra for the high radius ratio coannular nozzle is more narrow than the observed for the conic nozzles. For the supercritical test point (test point 3) the coannular nozzle with plug is more similar in spectral shape to the conic nozzle than for the previous two cases. The peak of each of the power spectra curves for the coannular nozzle data is between a Strouhal number, f_D/V_j^{mix}, of 0.09 to 0.13, and consistently 0.15 for the conic nozzle. The characteristic dimension, D, used in the Strouhal Number definition is an equivalent diameter of total area 189.68 cm^2. Additionally, secondary humps are observed for the coannular nozzle with plug at the high subsonic and sonic test points at $f_D/V_j^{mix} \sim 2 \rightarrow 3$.

As a reference line the classical f^{-2} frequency drop off rate for high frequency jet noise is shown on each figure. At the high Strouhal numbers, the coannular nozzle data for the first two cases is observed to approach the f^{-2} frequency law, but the noise in the region between the peak and the secondary humps is observed to deviate from any such frequency law. The shape of the power spectra in this latter region is suggestive of a complex transition region (perhaps similar to a multielement nozzle).

5.1.6.2 Comparison of Typical Sound Pressure Level Spectra of High Radius Ratio Coannular Nozzles with Plug (Configuration 7) and a Conic Nozzle

Comparisons of normalized one-third octave band sound-pressure level spectra at acoustic angles to the inlet of 50°, 90°, and 130° for a typical Coannular Nozzle with plug (Configuration 7) and a conical nozzle is shown in Figure 5-24. The same three test points described above are considered here as well.

The results of Figure 5-24 show that at the angle close to the peak noise ($\theta_I \sim 130$), the coannular nozzle spectra is much broader than the conic nozzle spectra. The broadness in spectra also appears to hold true at the 90°, and 50° spectra as well. There is also a difference in the relative level between the peak angle noise and the other two angles for the coannular nozzle as compared to the conic nozzle. The coannular nozzle realtive levels are smaller between the 130° spectra and 90° spectra than what are observed for the conic nozzle. This difference may be related to a lesser amount of convection amplification for the coannular nozzle and/or a combination of fluid shielding and refraction effects peculiar to the coannular nozzle results which were tested for inverted temperature and velocity profiles. The exact role that each of noise generation/reduction mechanisms play in the formation of the individual spectra is beyond the extent of this current discussion and requires further detailed theoretical work to outline and

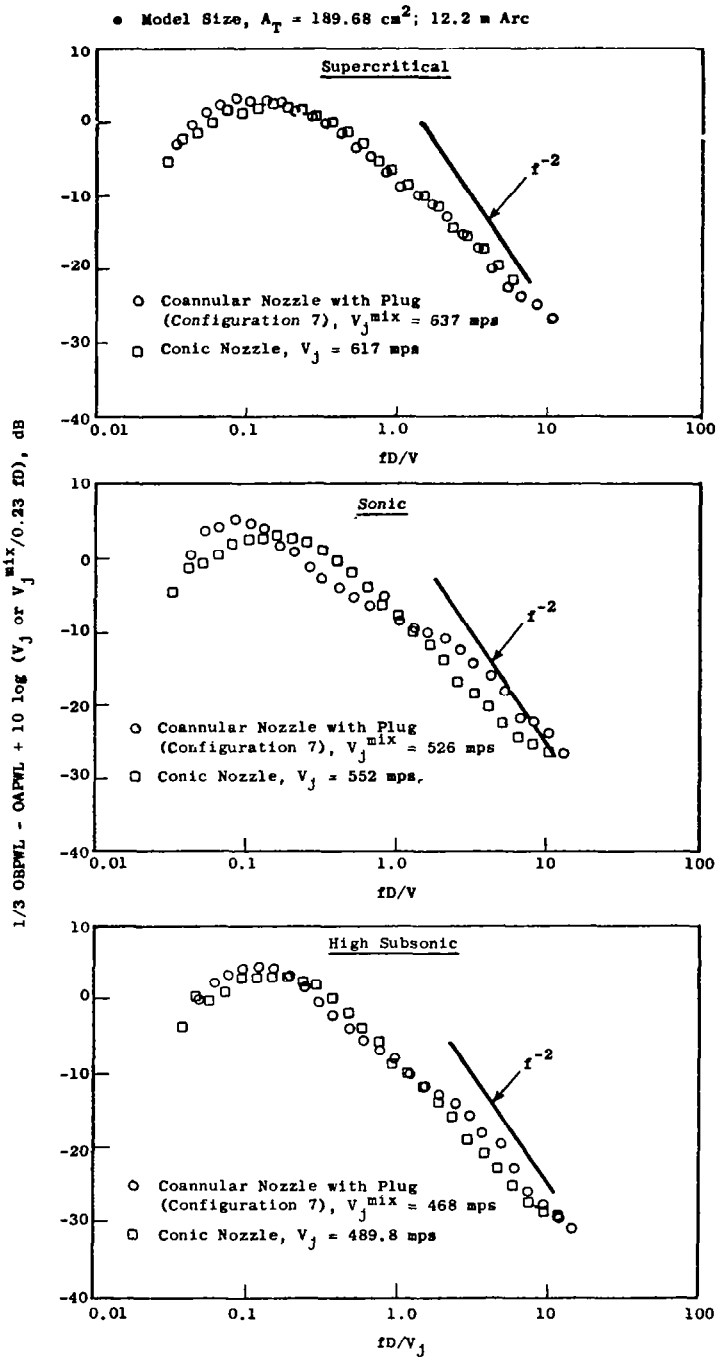

Figure 5-23. Power Spectral Density Comparison Between a High Radius Ratio Coannular Nozzle with Plug (Configuration 7) and a Conic Nozzle.

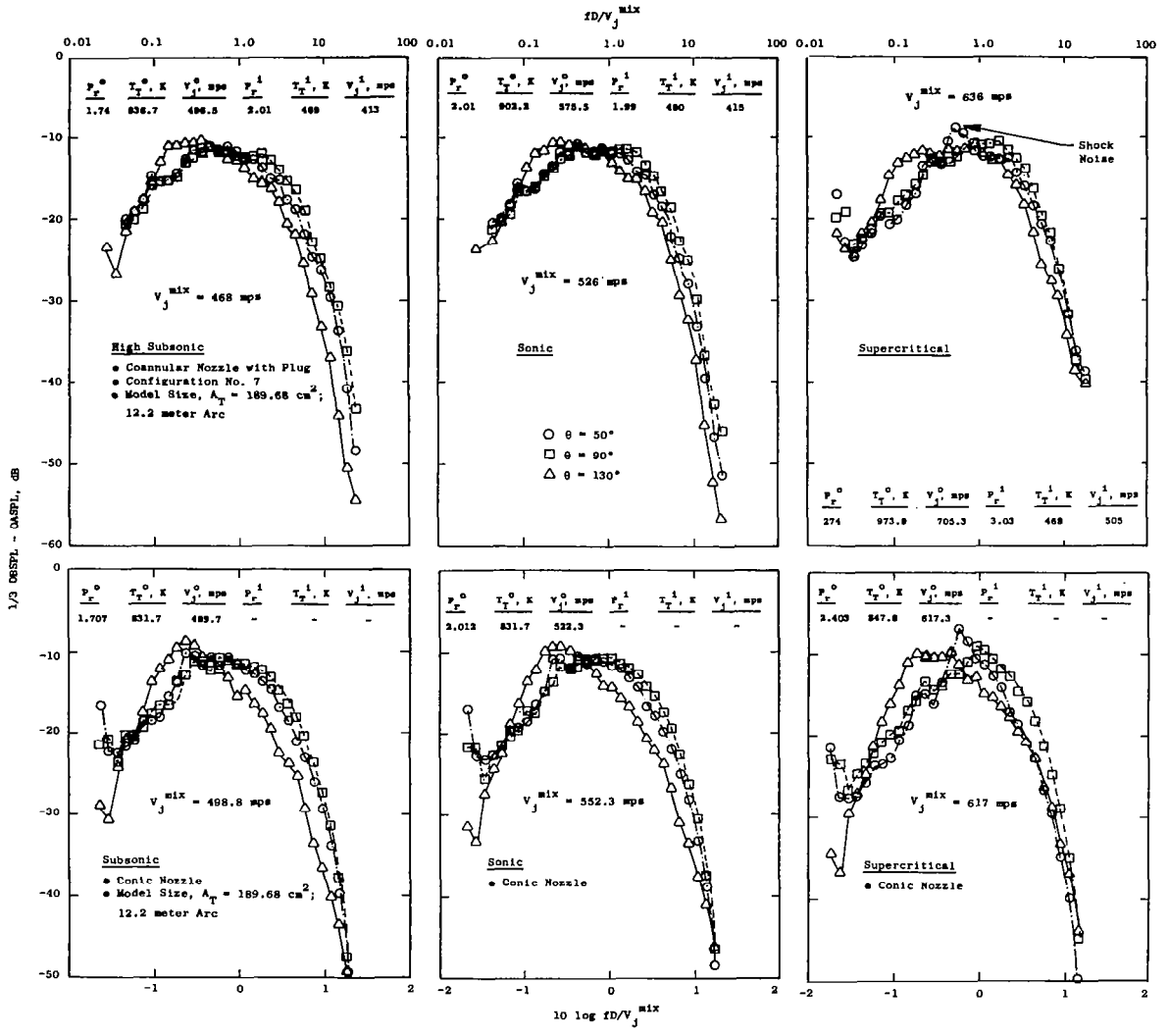

Figure 5-24. One-Third Octave-Band Sound Pressure Level Spectra Comparisons Between a High Radius Ratio Coannular Nozzle with Plug (Configuration 7) and a Conic Nozzle.

describe what is physically occurring within the aero-acoustic interaction framework. There does however exist a similarity between the coannular nozzle and the conic nozzles in the relative arrangement of spectra for each angle.

For the supercritical case, the coannular nozzle and the conic nozzle exhibit shock noise. For the coannular nozzle, the shock noise is only evident at the 50° spectra, while the conic nozzle data shows shock noise influences at 50° and 90°.

5.1.6.3 Comparison of Typical Sound Pressure-Level Directivity Characteristics between a High Radius Ratio Coannular Nozzle with Plug (Configuration 7) and a Conic Nozzle

As a last example of the typical spectral characteristics of a high radius ratio coannular nozzle with plug, Figure 5-25 illustrates the directivity characteristics between the high radius ratio coannular nozzle with plug and conic nozzle for one-third octave band sound-pressure-levels at Strouhal numbers, $f\ D/V_J^{mix}$, of 0.063, 0.25 and 1.0. The three conditions given in Subsection 5.1.6.1 are also considered here.

At the low Strouhal number, $f\ D/V_J^{mix} = 0.063$, the peak of the directivity is close to the jet axis for the coannular and conic nozzle data for all three test conditions - subsonic, sonic, and supersonic. The mid and higher Strouhal number directivities peak at angles further from the jet axis, with the higher Strouhal number data peaking at the largest angles from the jet axis. In general, the coannular nozzle data appears to peak about 10° closer to the jet axis than does the conic nozzle data.

For the supercritical cases, the conic nozzle data appears to be substantially more influenced by shock noise than does the coannular nozzle data. This observation is particularly true at $f\ D/V_J^{mix} = 1.0$, and at angles $\theta_I \leq 110°$. Later, discussions of coannular nozzle geometry effects on shock will be given. It is sufficient to say here that the coannular nozzle chosen for the "typical" comparisons has beneficial characteristics regarding shock noise as compared to a conical nozzle.

For completeness, the power spectra, one-third octave-band spectra, and one-third octave-band sound-pressure-level directivity characteristics for the higher radius ratio coannular nozzles with plug (Configuration 2 through 6) for a similar series of test conditions as described above is included in Appendix III. In general the comments made above in Subsection 5.1.6.1, 2, 3, are valid, except with regard to the shock noise. The shock noise for coannular nozzles must be considered separately and shall be in Subsection 5.3.

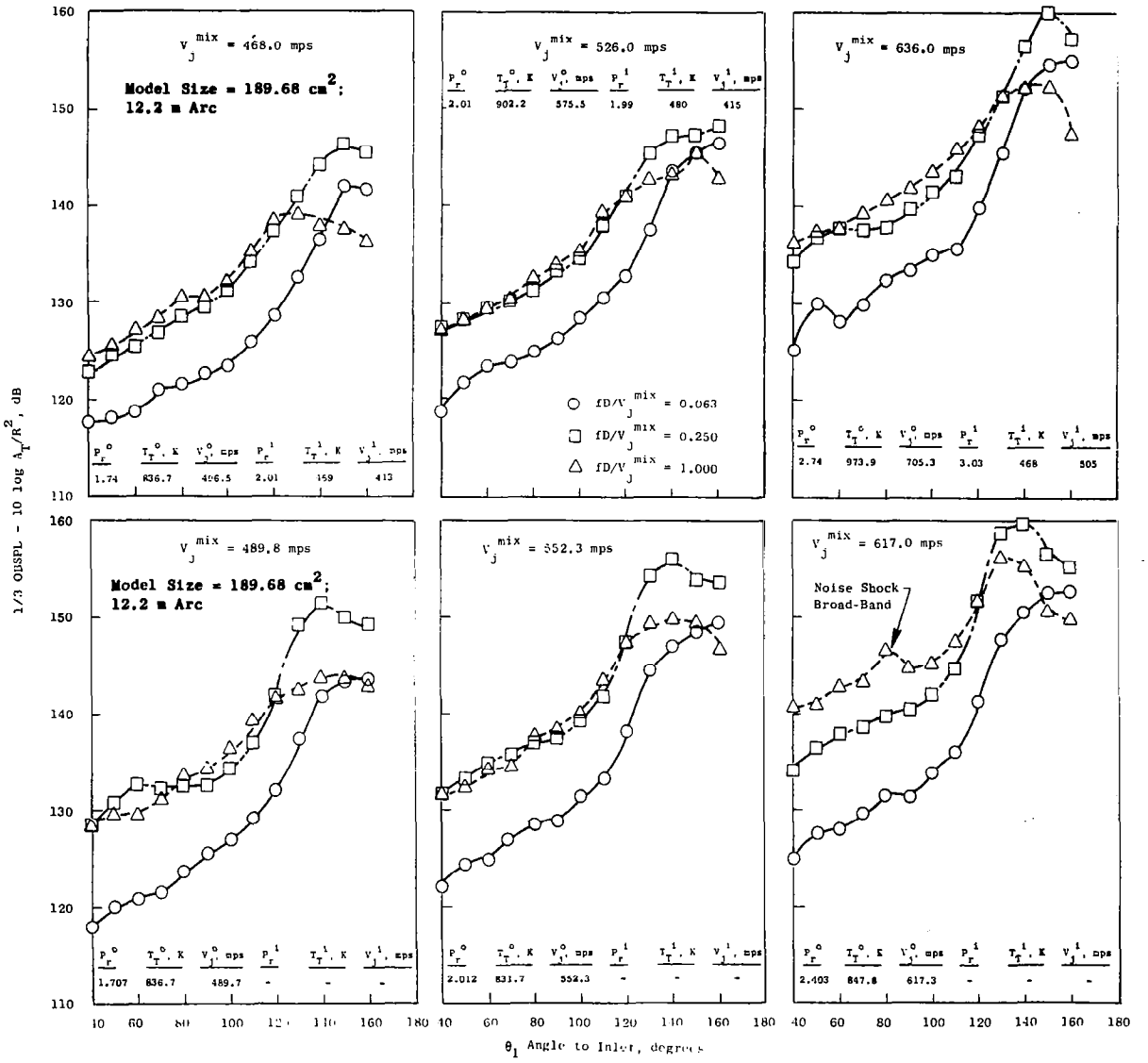

Figure 5-25. One-Third Octave-Band Sound Pressure Level Directivity Comparisons Between a High Radius Ratio Coannular Nozzle with Plug (Configuration 7) and a Conic Nozzle.

5.1.7 Typical Directivity and Spectral Characteristics of Several of the Tested High Radius Ratio Ratio Coannular Nozzles with Plug

To illustrate in some detail the basic directivity and spectral characteristics of the high radius ratio coannular nozzles tested, a series of test points shall be illustrated where the outer stream was held constant and inner stream flow conditions were regulated over a range of subsonic and supersonic flow conditions. The basic flow conditions chosen are:

Outer Stream

$P_r^o \simeq 2.75$

$V_j^o \simeq 700$ m/sec

$T_T^o \simeq 972$ K

Inner Stream

$T_T^i \sim 472$ K

P_r^i = Varies (2.0 → 3.0)

V_j^i = Varies (396 → 503 m/sec)

The data presented is model scale data at a total area of $A_T = 189.68$ cm^2 on a 12.2 meter arc.

5.1.7.1 Overall Sound Pressure Level Directivity

The overall sound-pressure-level, OASPL, directivity results for Configurations 2 through 7 are presented in Figure 5-26. As an example, consider Configuration 2 [$R_r^o = 0.902$; $R_r^i = 0.80$]. Figure 5-26a show these test results. What is observed is that when the inner stream flow conditions are close to sonic but the outer stream and mixed stream conditions are supersonic, there exists a regular and systematic directivity pattern. As the inner stream is increased in pressure ratio from 2.06 to 3.04, a rather dramatic change in the directivity occurs in the forward quadrant. In the forward quadrant, a "lift" in the noise levels are observed. This "lift" in the forward quadrant noise is also observed for Configurations 4, 5, and 6 [R_r^o = 0.902, 0.853, 0.926 and A_r = 1.03, 0.63, 1.42 respectively], in Figures 5-26c, d and e. Configuration 6 showed the greatest forward quadrant "lift." For Configuration 6 there exists a 17.5 dB increase of noise in the forward quadrant, while the peak angle noise increased by only 6 dB. As will be shown in the next subsection this forward quadrant lift is associated with shock noise.

Of all the configurations shown in Figure 5-26 Configuration 7 (A_r = 0.330) resulted in the least amount of forward quadrant lift (or shock noise). This configuration has the highest inner stream radius ratio $R_r^i = 0.902$, or the smallest inner stream annular height ($h^i/D = 0.06$). Figure 5-26f illustrates the test results for Configuration 7.

● Model Scale at 189.68 cm^2; 12.2 meter Arc

Test Point	P_T^o/P_o	P_T^i/P_o	P_r^o	P_r^i	T_T^o	T_T^i	T_T^{mix}	V_j^o	V_j^i	V_j^{mix}	M_j^o	M_j^i	M_j^{mix}	β_j^{mix}
45	2.697	3.041	2.70	3.04	971	467	654	699	506	577	1.297	1.368	1.304	0.838
112	2.734	2.063	2.74	2.06	962	475	705	700	422	553	1.307	1.073	1.178	0.622
113	2.736	2.784	2.74	2.79	959	474	668	699	492	575	1.307	1.304	1.279	0.797
117	2.742	2.307	2.75	2.31	956	472	687	698	449	560	1.306	1.162	1.214	0.689

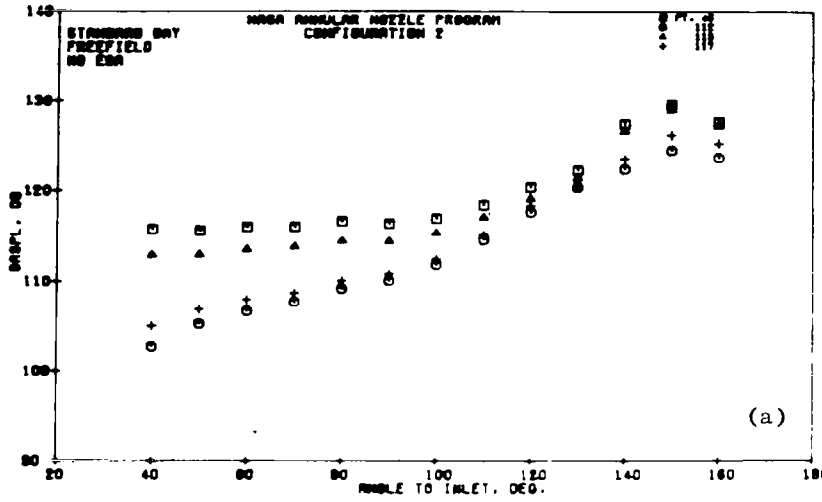

Test Point	P_T^o/P_o	P_T^i/P_o	P_r^o	P_r^i	T_T^o	T_T^i	T_T^{mix}	V_j^o	V_J^i	V_j^{mix}	M_j^o	M_j^i	M_j^{mix}	β_j^{mix}
45	2.728	2.179	2.73	2.18	968	637	853	701	506	634	1.305	1.122	1.242	0.736
113	2.728	1.967	2.73	1.97	968	694	882	701	497	637	1.305	1.041	1.224	0.706
115	2.714	1.927	2.72	1.93	971	322	751	701	365	574	1.301	1.015	1.186	0.639

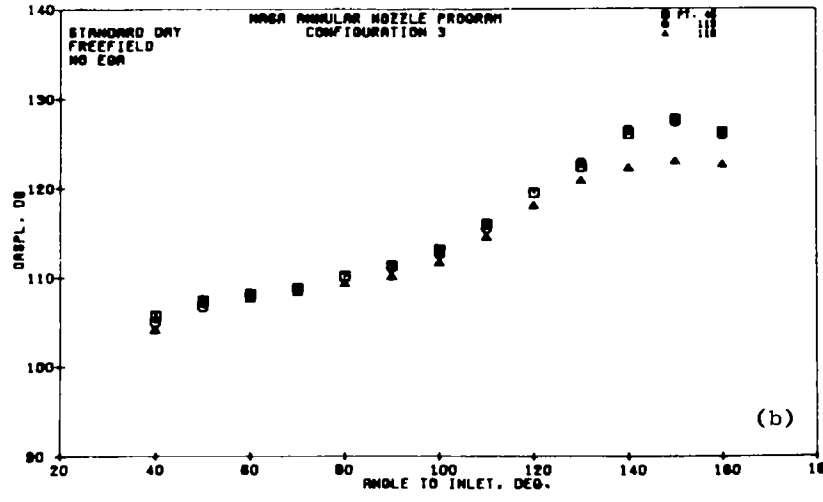

Figure 5-26. Overall Sound Pressure Level Directivity for Configurations 2 Through 7, Outer Stream Constant: V_j^o = 701 mps, P_r^o = 2.7, T_T^o = 972 K; Inner Stream Varies: V_j^i (365-510 mps), P_r^i (1.92-3.05), T_T^i (320-694 K).

Test Point	P_T^o/P_o	P_T^i/P_o	P_r^o	P_r^i	T_T^o	T_T^i	T_T^{mix}	V_j^o	V_j^i	V_j^{mix}	M_j^o	M_j^i	M_j^{mix}	β_j^{mix}
45	2.798	3.050	2.80	3.05	946	472	654	701	509	582	1.323	1.371	1.320	0.862
112	2.760	2.048	2.74	205	983	471	713	710	419	557	1.314	1.067	1.178	0.622
113	2.746	2.787	2.75	2.79	972	467	667	705	488	574	1.310	1.304	1.278	0.796

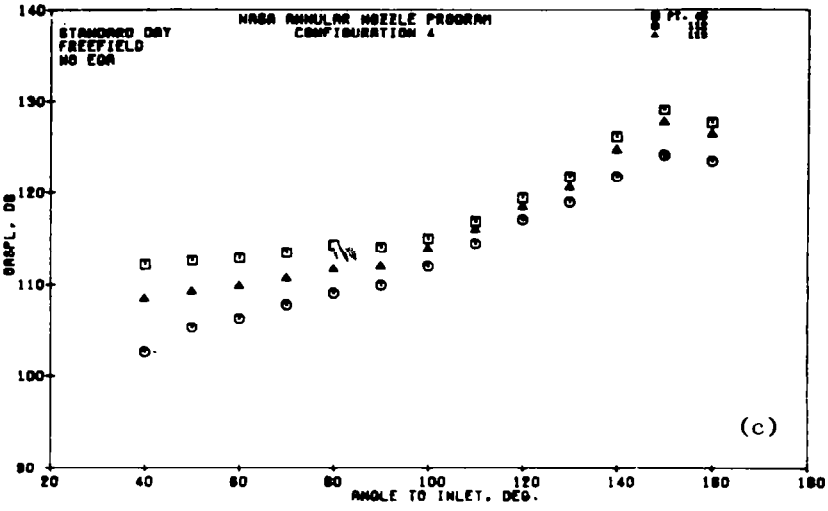

Test Point	P_T^o/P_o	P_T^i/P_o	P_r^o	P_r^i	T_T^o	T_T^i	T_T^{mix}	V_j^o	V_j^i	V_j^{mix}	M_j^o	M_j^i	M_j^{mix}	β_j^{mix}
45	2.739	3.006	2.74	3.01	998	462	726	714	501	606	1.309	1.360	1.300	0.827
112	2.734	2.157	2.74	2.16	967	464	756	702	429	587	1.306	1.109	1.215	0.690
113	2.732	2.774	2.74	2.78	960	456	720	703	482	595	1.306	1.302	1.275	0.791

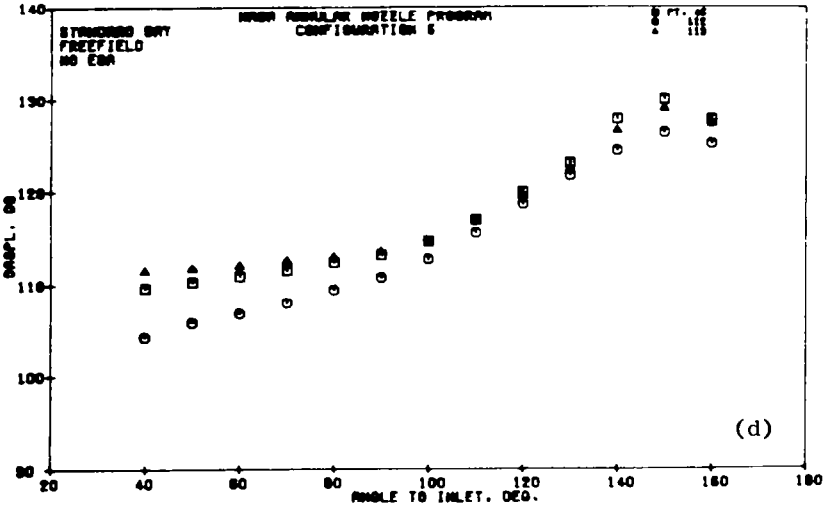

Figure 5-26. Overall Sound Pressure Level Directivity for Configurations 2 Through 7, Outer Stream Constant; V_j^o = 701 mps, P_r^o = 2.7, T_T^o = 972 K; Inner Stream Varies: V_j^i (365-510 mps), P_r^i (1.92-3.05), T_T^i (320-694 K) (Continued).

Test Point	P_T^o/P_o	P_T^i/P_o	P_r^o	P_r^i	T_T^o	T_T^i	T_T^{mix}	V_j^o	V_j^i	V_j^{mix}	M_j^o	M_j^i	M_j^{mix}	β_j^{mix}
45	2.759	2.989	2.76	2.99	958	456	610	701	496	559	1.313	1.356	1.309	0.844
112	2.719	2.069	2.72	2.07	962	482	671	698	426	533	1.302	1.074	1.159	0.586
113	2.729	2.971	2.73	2.77	965	471	630	700	489	557	1.304	1.301	1.275	0.791
117	2.726	2.321	2.73	2.32	962	478	655	699	453	543	1.304	1.167	1.204	0.671

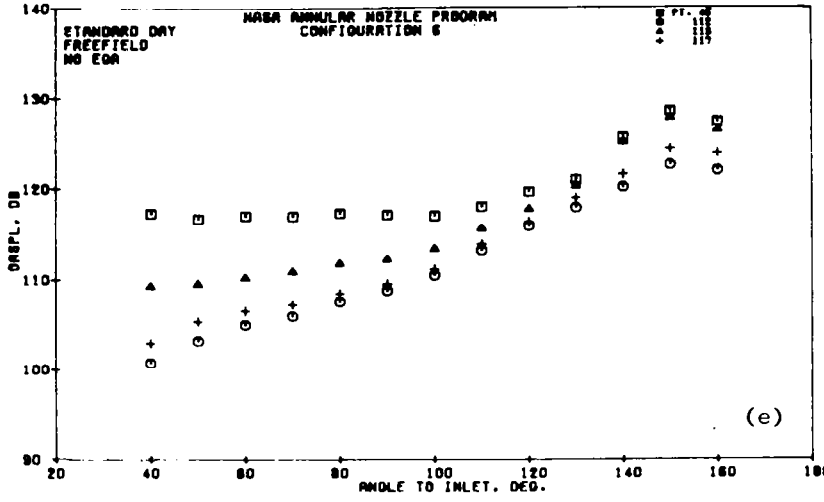

Test Point	P_T^o/P_o	P_T^i/P_o	P_r^o	P_r^i	T_T^o	T_T^i	T_T^{mix}	V_j^o	V_j^i	V_j^{mix}	M_j^o	M_j^i	M_j^{mix}	β_j^{mix}
74	2.742	3.026	2.75	3.03	974	469	800	705	506	637	1.309	1.364	1.301	0.832
78	2.727	2.257	2.73	2.26	955	559	851	696	483	640	1.304	1.146	1.260	0.767
94	2.803	2.841	2.81	2.84	877	463	746	674	490	616	1.321	1.319	1.304	0.837
99	2.797	2.780	2.80	2.79	722	322	590	610	406	543	1.314	1.306	1.284	0.807
113	2.723	2.773	2.73	2.78	954	500	810	696	504	635	1.303	1.301	1.286	0.808
78	2.753	2.502	2.76	2.5	957	476	814	700	470	631	1.311	1.224	1.273	0.788

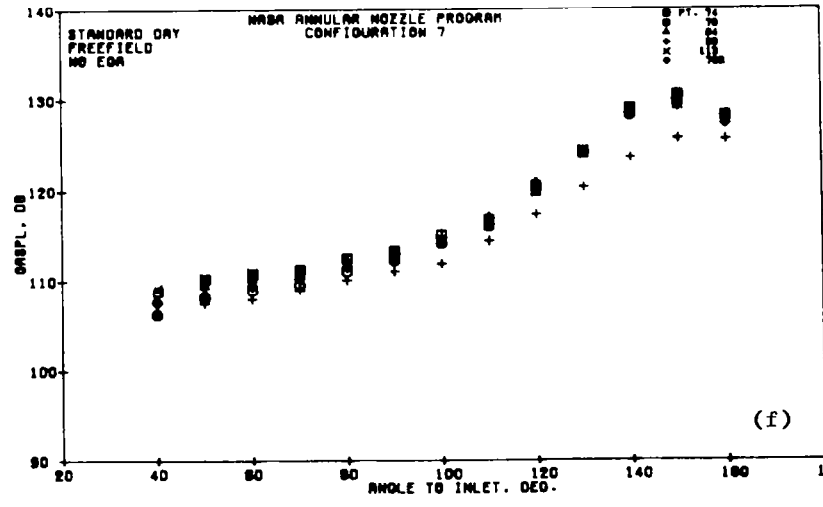

Figure 5-26. Overall Sound Pressure Level Directivity for Configurations 2 Through 7, Outer Stream Constant; V_j^o = 701 mps, P_r^o = 2.7, T_T^o = 972 K; Inner Stream Varies: V_j^i (365-510 mps), P_r^i (1.92-3.05), T_T^i (320-694 K) (Concluded).

In trying to sort out the noise characteristics for shock noise, it should be noted, however, that if the outer pressure ratio and inner pressure ratio are high enough for Configuration 7 ($P_r^i \sim P_r^o \geq 3.0$), the forward quadrant lift can also occur. When the inner stream is held constant and supercritical, but the outer stream is allowed to vary from subsonic to supersonic conditions, the forward quadrant "lift" is not as dramatic as observed above. These last two features are illustrated in Figure 5-27a and b. Figure 5-27a shows the OASPL directivity for Configuration 7 when the outer pressure ratio, P_r^o, was held to ~ 3.1 and the inner pressure ratio varied from 2.8 → 3.1. Figure 5-27b shows the OASPL directivity for Configuration 6 when the inner stream pressure ratio was held constant at 2.5 and the outer pressure ratio varied from 2.39 to 3.61.

5.1.7.2 One-Third Octave-Band Sound Pressure Level Spectra

Figures 5-28, 5-29, 5-30 illustrate the one-third octave-band sound pressure level spectra at acoustic angles to the inlet, θ_I, of 140°, 90° and 50° for Configurations 2 through 7 for the test conditions described at the beginning of this subsection.

The 140° spectra shown in Figure 5-28 illustrate the double hump spectra many times referred to for the coannular nozzle. The double humped spectra is particularly prominent when the inner stream flow conditions are subsonic or low supersonic. As the inner stream becomes more and more supercritical the low frequency hump increases in amplitude and the location of the peak also increases to a higher frequency. The sound-pressure levels in the intermediate frequency bands (500 Hz → 5000 Hz) fill in the "valley" between the two "humps." It appears also that during this process of increasing the inner stream flow the high frequency "hump" location remains fixed although its amplitude seems to rise with increasing inner pressure ratio. The increase in amplitude of the high frequency hump may be due, however, to the increase in noise from intermediate frequencies. It should be noted that although the low frequency hump shifts to higher frequencies with increasing inner flow, the spectral shift is somewhat greater than what would be predicted by a simple Strouhal scaling based on either the inner stream velocity or the mixed stream velocity. As an example consider Configuration 2:

Calculation of Low Frequency Strouhal Number

a) Based on Inner Stream Velocity

- $f_{1/3}^P$ (at lowest inner stream condition = 400 Hz

(a) Outer Pressure Ratio Held Constant but Inner Stream Conditions Vary - Configuration 7

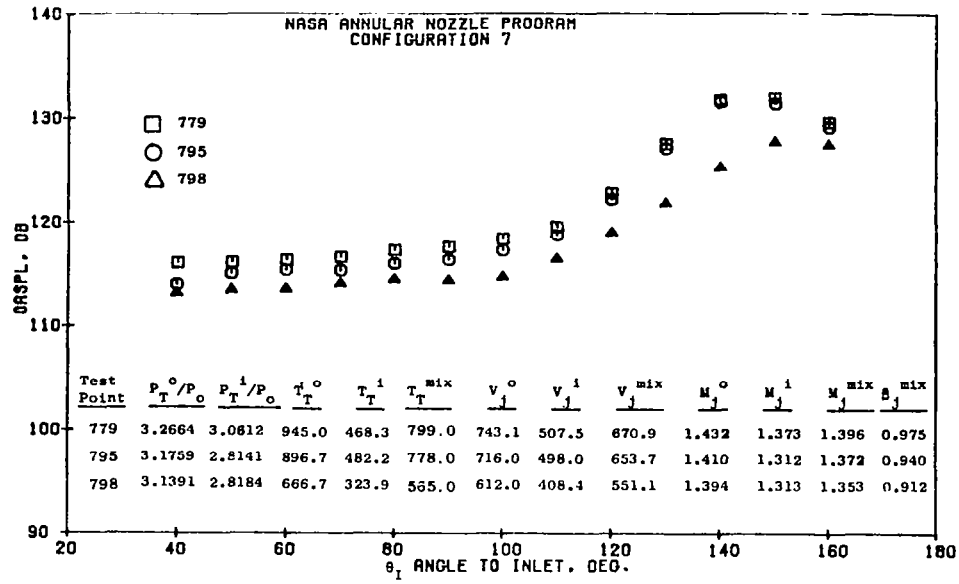

Test Point	P_T^o/P_o	P_T^i/P_o	T_T^o	T_T^i	T_T^{mix}	V_j^o	V_j^i	V_j^{mix}	M_j^o	M_j^i	M_j^{mix}	β_j^{mix}
779	3.2664	3.0812	945.0	468.3	799.0	743.1	507.5	670.9	1.432	1.373	1.396	0.975
795	3.1759	2.8141	896.7	482.2	778.0	716.0	498.0	653.7	1.410	1.312	1.372	0.940
798	3.1391	2.8184	666.7	323.9	565.0	612.0	408.4	551.1	1.394	1.313	1.353	0.912

• Model Scale at 189.68 cm^2; 12.2 meter Arc

(b) Inner Stream Conditions Held Constant but Outer Stream Conditions Vary - Configuration 6

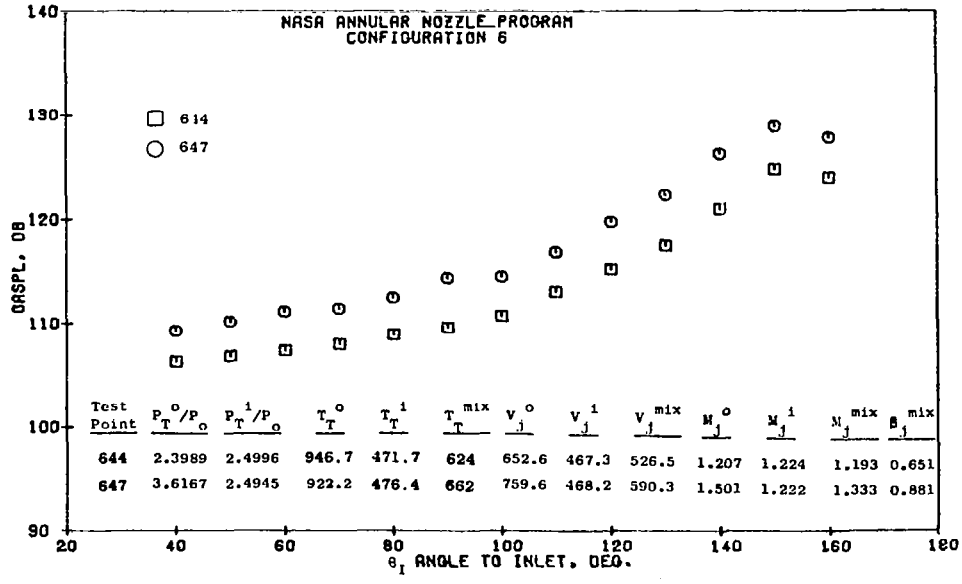

Test Point	P_T^o/P_o	P_T^i/P_o	T_T^o	T_T^i	T_T^{mix}	V_j^o	V_j^i	V_j^{mix}	M_j^o	M_j^i	M_j^{mix}	β_j^{mix}
644	2.3989	2.4996	946.7	471.7	624	652.6	467.3	526.5	1.207	1.224	1.193	0.651
647	3.6167	2.4945	922.2	476.4	662	759.6	468.2	590.3	1.501	1.222	1.333	0.881

Figure 5-27. Overall Sound Pressure Level Directivity Patterns for Configurations 7 and 6.

- Model Scale at a Total Area of 189.68 cm^2; 12.2 meter Arc
- $\theta_I = 140°$

Test Point	P_T^o/P_o	P_T^i/P_o	P_r^o	P_r^i	T_T^o	T_T^i	T_T^{mix}	V_j^o	V_j^i	V_j^{mix}	M_j^o	M_j^i	M_j^{mix}	β_j^{mix}
□ 45	2.697	3.041	2.70	3.04	971	467	654	699	506	577	1.297	1.368	1.304	0.838
○ 112	2.734	2.063	2.74	2.06	962	475	705	700	422	553	1.307	1.073	1.178	0.622
△ 113	2.736	2.784	2.74	2.79	959	474	668	699	492	575	1.307	1.304	1.279	0.797
+ 117	2.742	2.307	2.75	2.31	956	472	687	698	449	560	1.308	1.162	1.214	0.689

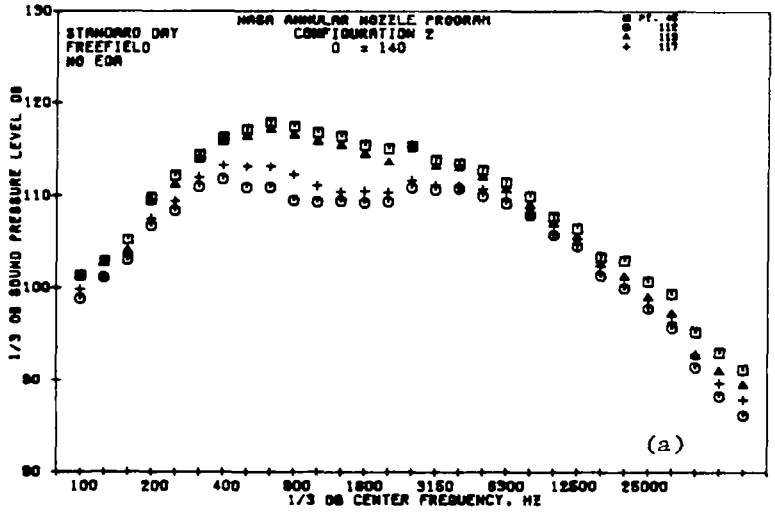

Test Point	P_T^o/P_o	P_T^i/P_o	P_r^o	P_r^i	T_T^o	T_T^i	T_T^{mix}	V_j^o	V_j^i	V_j^{mix}	M_j^o	M_j^i	M_j^{mix}	β_j^{mix}
□ 45	2.728	2.179	2.73	2.18	968	637	853	701	506	634	1.305	1.122	1.242	0.736
○ 113	2.728	1.967	2.73	1.97	968	694	882	701	497	637	1.305	1.041	1.224	0.706
△ 115	2.714	1.927	2.72	1.93	971	322	751	701	365	574	1.301	1.015	1.186	0.639

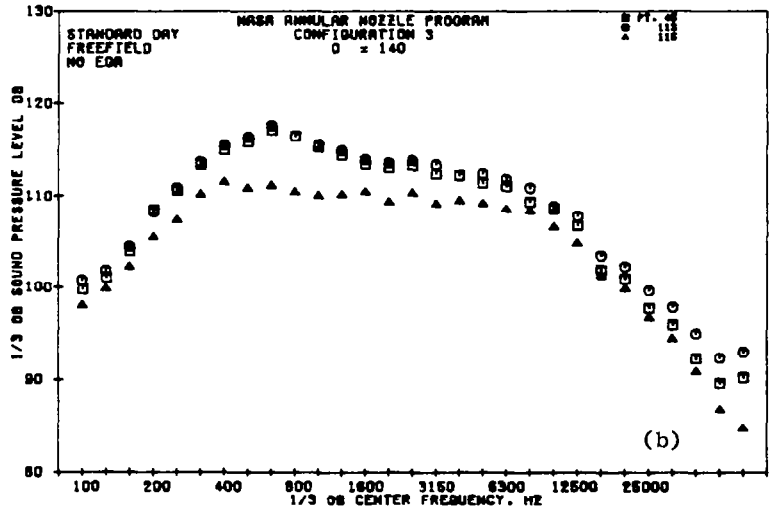

Figure 5-28. One-Third Octave Band Sound Pressure Level Spectra for High Radius Ratio Coannular Nozzle Configurations 2 through 7 at $\theta_I = 140°$, Outer Stream Constant: $V_j^o = 700$ mps, $T_T^o = 972$ K, $P_r^o = 2.75$; Inner Stream Varies: $T_T^i = 472$ K, V_j^i (396 - 503 mps), P_r^i (2.0 - 3.0).

Test Point	P_T^o/P_o	P_T^i/P_o	P_r^o	P_r^i	T_T^o	T_T^i	T_T^{mix}	V_j^o	V_j^i	V_j^{mix}	M_j^o	M_j^i	M_j^{mix}	β_j^{mix}
□ 45	2.798	3.050	2.80	3.05	946	472	654	701	509	582	1.323	1.371	1.320	0.862
○ 112	2.760	2.048	2.74	2.05	983	471	713	710	419	557	1.314	1.067	1.178	0.622
△ 113	2.746	2.787	2.75	2.79	972	467	667	705	488	574	1.310	1.304	1.278	0.796

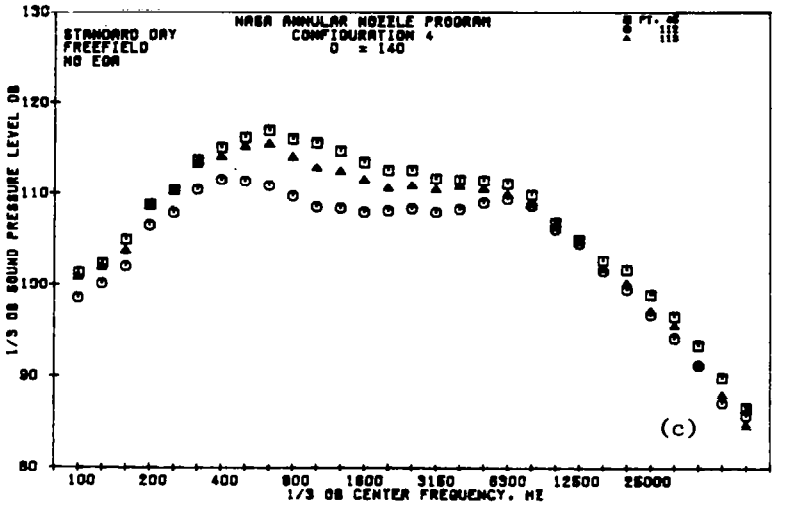

Test Point	P_T^o/P_o	P_T^i/P_o	P_r^o	P_r^i	T_T^o	T_T^i	T_T^{mix}	V_j^o	V_j^i	V_j^{mix}	M_j^o	M_j^i	M_j^{mix}	β_j^{mix}
□ 45	2.739	3.006	2.74	3.01	998	462	726	714	501	606	1.309	1.360	1.300	0.827
○ 112	2.734	2.157	2.74	2.16	967	464	756	702	429	587	1.306	1.109	1.215	0.690
△ 113	2.732	2.774	2.74	2.78	970	456	720	703	482	595	1.306	1.302	1.275	0.791

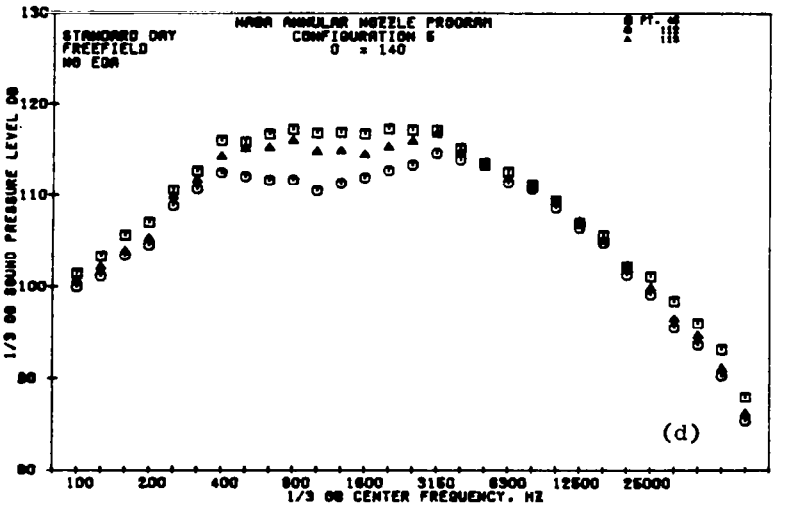

Figure 5-28. One-Third Octave Band Sound Pressure Level Spectra for High Radius Ratio Coannular Nozzle Configurations 2 through 7 at θ_I = 140°, Outer Stream Constant: V_j^o = 700 mps, T_T^o = 972 K, P_r^o = 2.75; Inner Stream Varies: T_T^i = 472 K, V_j^i (396 - 503 mps), P_r^i (2.0 - 3.0) (Continued).

Test Point	P_T^o/P_o	P_T^i/P_o	P_r^o	P_r^i	T_T^o	T_T^i	T_T^{mix}	V_j^o	V_j^i	V_j^{mix}	M_j^o	M_j^i	M_j^{mix}	β_j^{mix}
□ 45	2.759	2.989	2.76	2.99	958	456	610	701	496	559	1.313	1.356	1.309	0.844
○ 112	2.719	2.069	2.72	2.07	962	482	671	698	426	533	1.302	1.074	1.159	0.586
△ 113	2.729	2.971	2.73	2.77	965	471	630	700	489	557	1.304	1.301	1.275	0.791
+ 117	2.726	2.321	2.73	2.32	962	478	655	699	453	543	1.304	1.167	1.204	0.671

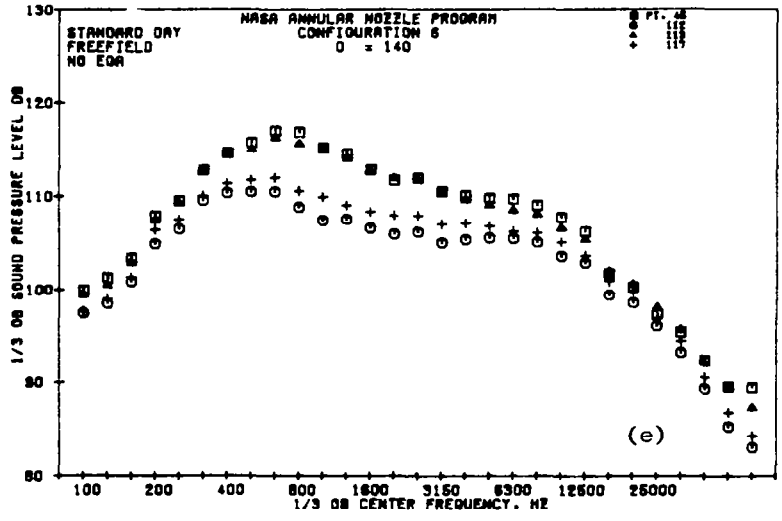

Test Point	P_T^o/P_o	P_T^i/P_o	P_r^o	P_r^i	T_T^o	T_T^i	T_T^{mix}	V_j^o	V_j^i	V_j^{mix}	M_j^o	M_j^i	M_j^{mix}	β_j^{mix}
□ 74	2.742	3.026	2.75	3.03	974	469	800	705	506	637	1.309	1.364	1.301	0.832
○ 78	2.727	2.257	2.73	2.26	955	559	851	696	483	640	1.304	1.146	1.260	0.767
△ 94	2.803	2.841	2.81	2.84	877	463	746	674	490	616	1.321	1.319	1.304	0.837
+ 99	2.797	2.780	2.80	2.79	722	322	590	610	406	543	1.314	1.306	1.284	0.807
× 113	2.723	2.773	2.73	2.78	954	500	810	696	504	635	1.303	1.301	1.286	0.808
◇ 78	2.753	2.502	2.76	2.5	957	476	814	700	470	631	1.311	1.224	1.273	0.788

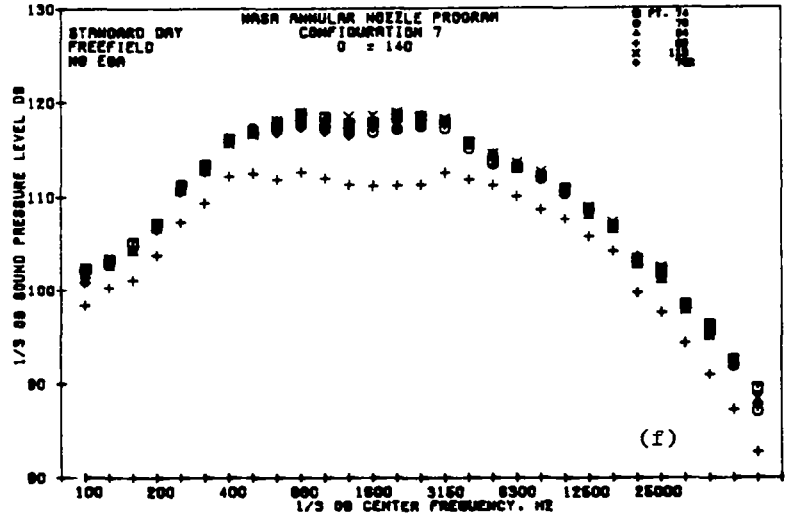

Figure 5-28. One-Third Octave Band Sound Pressure Level Spectra for High Radius Ratio Coannular Nozzle Configurations 2 through 7 at θ_I = 140°, Outer Stream Constant: V_j^o = 700 mps, T_T^o = 972 K, P_r^o = 2.75; Inner Stream Varies: T_T^i = 472 K, V_j^i (396 - 503 mps), P_r^i (2.0 - 3.0) (Concluded).

- Model Scale at a Total Area of 189.68 cm^2; 12.2 meter Arc
- $\theta_I = 90°$

Test Point	P_T^o/P_o	P_T^i/P_o	P_r^o	P_r^i	T_T^o	T_T^i	T_T^{mix}	V_j^o	V_j^i	V_j^{mix}	M_j^o	M_j^i	M_j^{mix}	β_j^{mix}
□ 45	2.697	3.041	2.70	3.04	971	467	654	699	506	577	1.297	1.368	1.304	0.838
○ 112	2.734	2.063	2.74	2.06	962	475	705	700	422	553	1.307	1.073	1.178	0.622
△ 113	2.736	2.784	2.74	2.79	959	474	668	699	492	575	1.307	1.304	1.279	0.797
+ 117	2.742	2.307	2.75	2.31	956	472	687	698	449	560	1.308	1.162	1.214	0.689

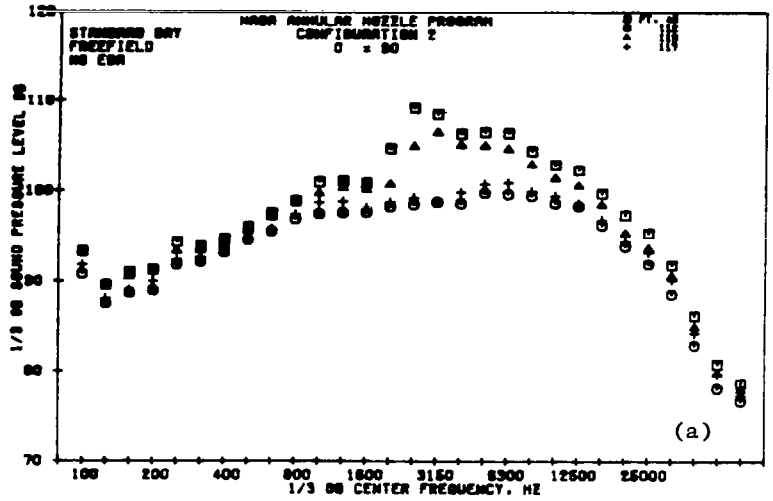

Test Point	P_T^o/P_o	P_T^i/P_o	P_r^o	P_r^i	T_T^o	T_T^i	T_T^{mix}	V_j^o	V_j^i	V_j^{mix}	M_j^o	M_j^i	M_j^{mix}	β_j^{mix}
□ 45	2.728	2.179	2.73	2.18	968	637	853	701	506	634	1.305	1.122	1.242	0.736
○ 113	2.728	1.967	2.73	1.97	968	694	882	701	497	637	1.305	1.041	1.224	0.706
△ 115	2.714	1.927	2.72	1.93	971	332	751	701	365	574	1.301	1.015	1.186	0.639

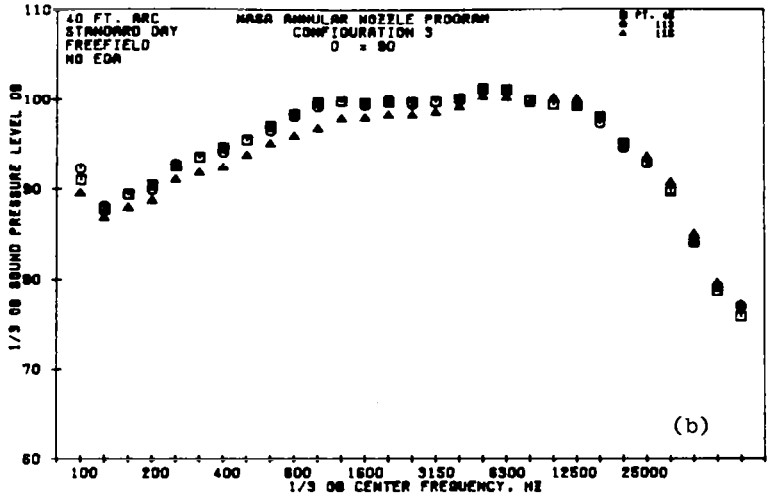

Figure 5-29. One-Third Octave Band Sound Pressure Level Spectra for High Radius Ratio Coannular Nozzle Configurations 2 through 7 at $\theta_I = 90°$, Outer Stream Constant: $V_j^o = 700$ mps, $T_T^o = 972$ K, $P_r^o = 2.75$; Inner Stream Varies: $T_T^i = 472$ K, V_j^i (396 - 503 mps), P_r^i (2.0 - 3.0).

Test Point	P_T^o/P_o	P_T^i/P_o	P_r^o	P_r^i	T_T^o	T_T^i	T_T^{mix}	V_j^o	V_j^i	V_j^{mix}	M_j^o	M_j^i	M_j^{mix}	β_j^{mix}
□ 45	2.798	3.050	2.80	3.05	946	472	654	701	509	582	1.323	1.371	1.320	0.862
○ 112	2.760	2.048	2.74	2.05	983	471	713	710	419	557	1.314	1.067	1.178	0.622
△ 113	2.746	2.787	2.75	2.79	972	467	667	705	488	574	1.310	1.304	1.278	0.796

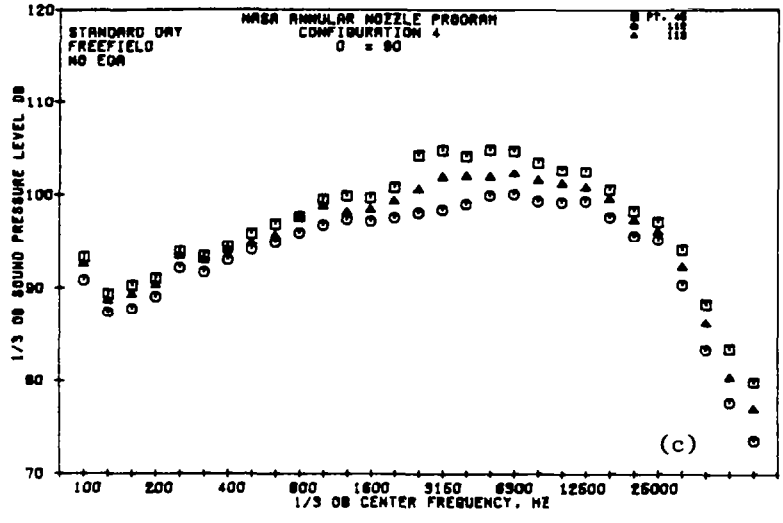

Test Point	P_T^o/P_o	P_T^i/P_o	P_r^o	P_r^i	T_T^o	T_T^i	T_T^{mix}	V_j^o	V_j^i	V_j^{mix}	M_j^o	M_j^i	M_j^{mix}	β_j^{mix}
□ 45	2.739	3.006	2.74	3.01	998	462	726	714	501	606	1.309	1.360	1.300	0.827
○ 112	2.734	2.157	2.74	2.16	967	464	756	702	429	587	1.306	1.109	1.215	0.690
△ 113	2.732	2.774	2.74	2.78	970	456	720	703	482	595	1.306	1.302	1.275	0.791

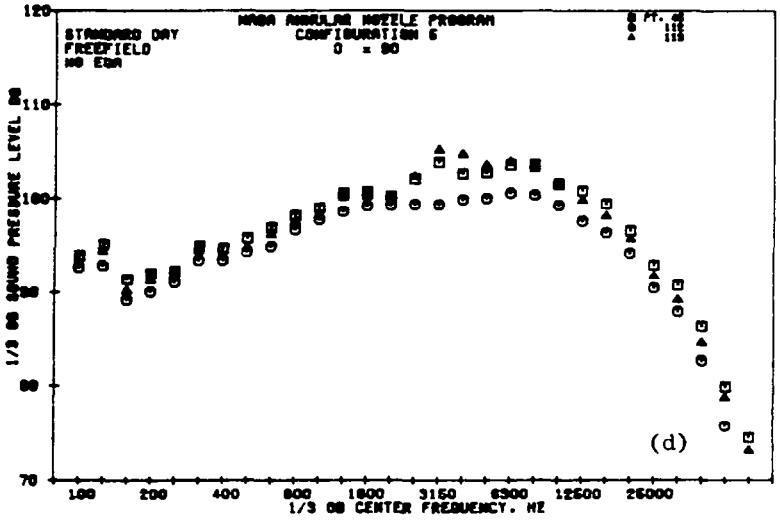

Figure 5-29. One-Third Octave Band Sound Pressure Level Spectra for High Radius Ratio Coannular Nozzle Configurations 2 through 7 at $\theta_I = 90°$, Outer Stream Constant: $V_j^o = 700$ mps, $T_T^o = 972$ K, $P_r^o = 2.75$; Inner Stream Varies: $T_T^i = 472$ K, V_j^i (396 - 503 mps), P_r^i (2.0 - 3.0) (Continued).

Test Point	P_T^o/P_o	P_T^i/P_o	P_r^o	P_r^i	T_T^o	T_T^i	T_T^{mix}	V_j^o	V_j^i	V_j^{mix}	M_j^o	M_j^i	M_j^{mix}	β_j^{mix}
□ 45	2.759	2.989	2.76	2.99	958	456	610	701	496	559	1.313	1.356	1.309	0.844
○ 112	2.719	2.069	2.72	2.07	962	482	671	698	426	533	1.302	1.074	1.159	0.586
△ 113	2.729	2.971	2.73	2.77	965	471	630	700	489	557	1.304	1.301	1.275	0.791
+ 117	2.726	2.321	2.73	2.32	962	478	655	699	453	543	1.304	1.167	1.204	0.671

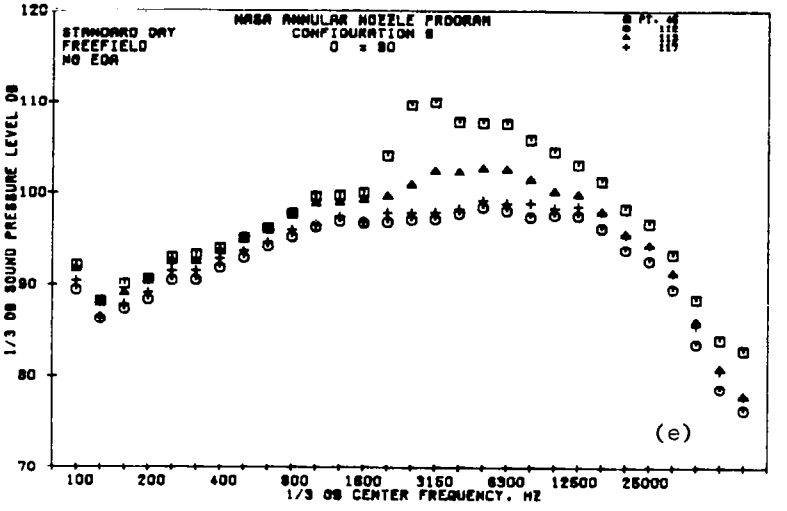

Test Point	P_T^o/P_o	P_T^i/P_o	P_r^o	P_r^i	T_T^o	T_T^i	T_T^{mix}	V_j^o	V_j^i	V_j^{mix}	M_j^o	M_j^i	M_j^{mix}	β_j^{mix}
□ 74	2.742	3.026	2.75	3.03	974	469	800	705	506	637	1.309	1.364	1.301	0.832
○ 78	2.727	2.257	2.73	2.26	955	559	851	696	483	640	1.304	1.146	1.260	0.767
△ 94	2.803	2.841	2.81	2.84	877	463	746	674	490	616	1.321	1.319	1.304	0.837
+ 99	2.797	2.780	2.80	2.79	722	322	590	610	406	543	1.314	1.306	1.284	0.807
× 113	2.723	2.773	2.73	2.78	954	500	810	696	504	635	1.303	1.301	1.286	0.808
◇ 78	2.753	2.502	2.76	2.5	957	476	814	700	470	631	1.311	1.224	1.273	0.788

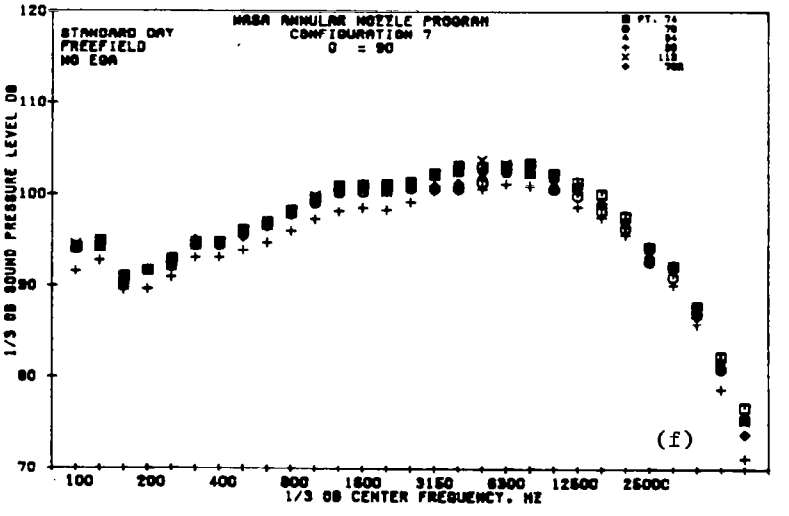

Figure 5-29. One-Third Octave Band Sound Pressure Level Spectra for High Radius Ratio Coannular Nozzle Configurations 2 through 7 at $\theta_I = 90°$, Outer Stream Constant: $V_j^o = 700$ mps, $T_T^o = 972$ K, $P_r^o = 2.75$; Inner Stream Varies: $T_T^i = 472$ K, V_j^i (396 - 503 mps), P_r^i (2.0 - 3.0) (Concluded).

- Model Scale at a Total Area of 189.68 cm^2; 12.2 meter Arc
- $\theta_I = 50°$

	Test Point	P_T^o/P_o	P_T^i/P_o	P_r^o	P_r^i	T_T^o	T_T^i	T_T^{mix}	V_j^o	V_j^i	V_j^{mix}	M_j^o	M_j^i	M_j^{mix}	β_j^{mix}
□	45	2.697	3.041	2.70	3.04	971	467	654	699	506	577	1.297	1.368	1.304	0.838
○	112	2.734	2.063	2.74	2.06	962	475	705	700	422	553	1.307	1.073	1.178	0.622
△	113	2.736	2.784	2.74	2.79	959	474	668	699	492	575	1.307	1.304	1.279	0.797
+	117	2.742	2.307	2.75	2.31	956	472	687	698	449	560	1.308	1.162	1.214	0.689

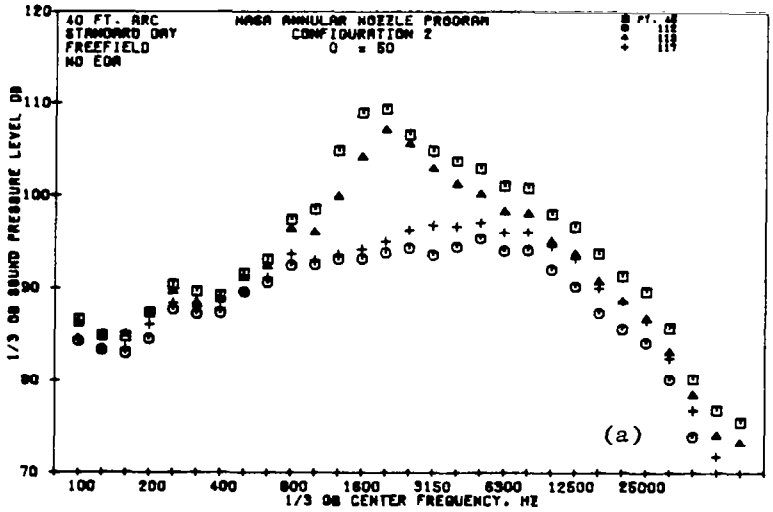

	Test Point	P_T^o/P_o	P_T^i/P_o	P_r^o	P_r^i	T_T^o	T_T^i	T_T^{mix}	V_j^o	V_j^i	V_j^{mix}	M_j^o	M_j^i	M_j^{mix}	β_j^{mix}
□	45	2.728	2.179	2.73	2.18	968	637	853	701	506	634	1.305	1.122	1.242	0.736
○	113	2.728	1.967	2.73	1.97	968	694	882	701	497	637	1.305	1.041	1.224	0.706
△	115	2.714	1.927	2.72	1.93	971	322	751	701	365	574	1.301	1.015	1.185	0.639

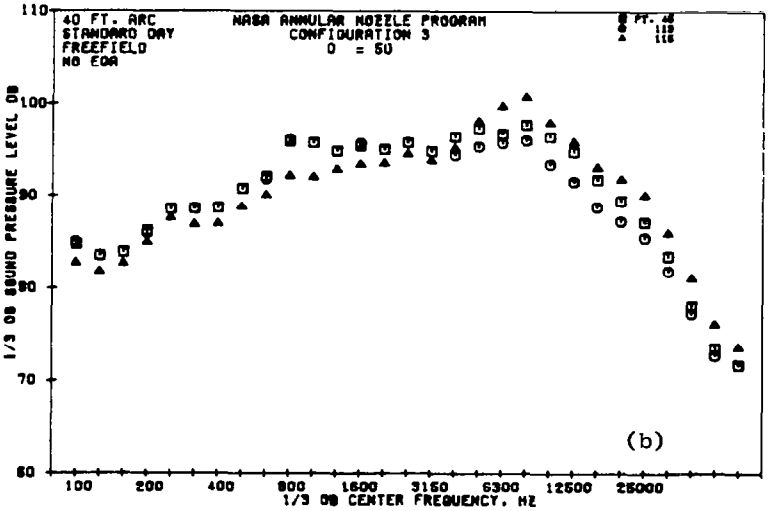

Figure 5-30. One-Third Octave Band Sound Pressure Level Spectra for High Radius Ratio Coannular Nozzle Configurations 2 through 7 at $\theta_I = 50°$, Outer Stream Constant: $V_j^o = 700$ mps, $T_T^o = 972$ K, $P_r^o = 2.75$; Inner Stream Varies: $T_T^i = 472$ K, V_j^i (396 - 503 mps), P_r^i (2.0 - 3.0).

Test Point	P_T^o/P_o	P_T^i/P_o	P_r^o	P_r^i	T_T^o	T_T^i	T_T^{mix}	V_j^o	V_j^i	V_j^{mix}	M_j^o	M_j^i	M_j^{mix}	β_j^{mix}
□ 45	2.798	3.050	2.80	3.05	946	472	654	701	509	582	1.323	1.371	1.320	0.862
○ 112	2.760	2.048	2.74	2.05	983	471	713	710	419	557	1.314	1.067	1.178	0.622
△ 113	2.746	2.787	2.75	2.79	972	467	667	705	488	574	1.310	1.304	1.278	0.796

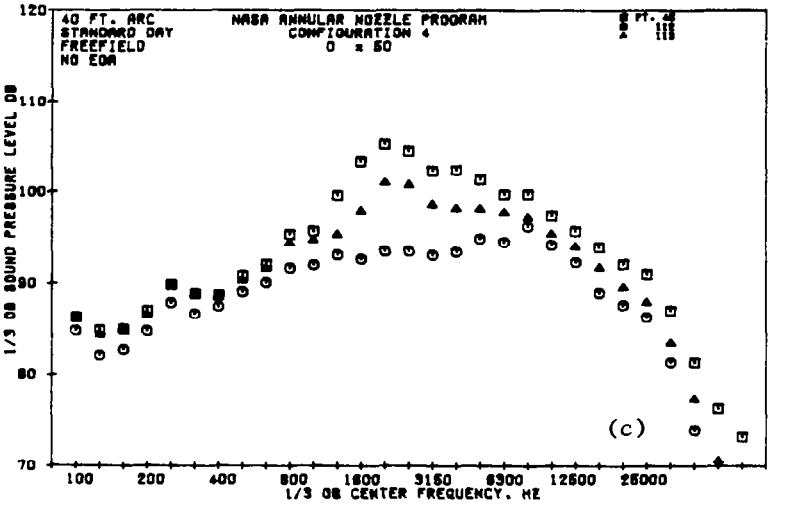

Test Point	P_T^o/P_o	P_T^i/P_o	P_r^o	P_r^i	T_T^o	T_T^i	T_T^{mix}	V_j^o	V_j^i	V_j^{mix}	M_j^o	M_j^i	M_j^{mix}	β_j^{mix}
□ 45	2.739	3.006	2.74	3.01	998	462	726	714	501	606	1.309	1.360	1.300	0.827
○ 112	2.734	2.157	2.74	2.16	967	464	756	702	429	587	1.306	1.109	1.215	0.690
△ 113	2.732	2.774	2.74	2.78	970	456	720	703	482	595	1.306	1.302	1.275	0.791

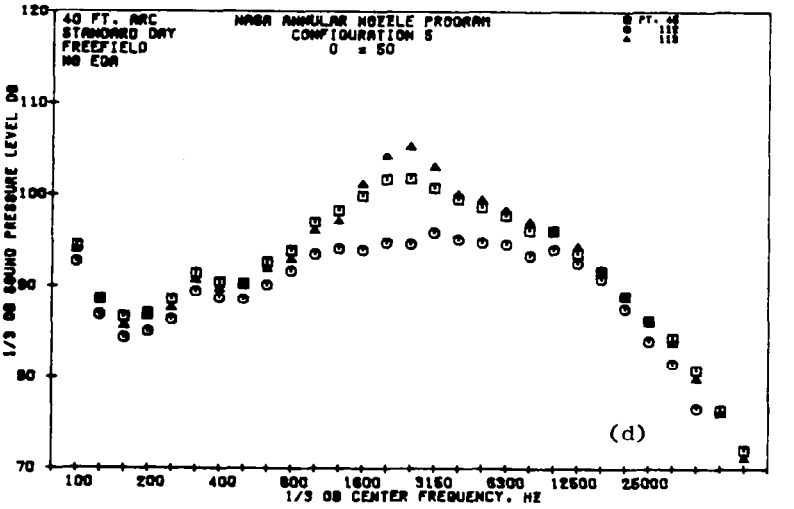

Figure 5-30. One-Third Octave Band Sound Pressure Level Spectra for High Radius Ratio Coannular Nozzle Configurations 2 through 7 at $\theta_I = 50°$, Outer Stream Constant: $V_j^o = 700$ mps, $T_T^o = 972$ K, $P_r^o = 2.75$; Inner Stream Varies: $T_T^i = 472$ K, V_j^i (396 - 503 mps), P_r^i (2.0 - 3.0) (Continued).

Test Point	P_T^o/P_o	P_T^i/P_o	P_r^o	P_r^i	T_T^o	T_T^i	T_T^{mix}	V_j^o	V_j^i	V_j^{mix}	M_j^o	M_j^i	M_j^{mix}	β_j^{mix}
□ 45	2.759	2.989	2.76	2.99	958	456	610	701	496	559	1.313	1.356	1.309	0.844
○ 112	2.719	2.069	2.72	2.07	962	482	671	698	426	533	1.302	1.074	1.159	0.586
△ 113	2.729	2.971	2.73	2.77	965	471	630	700	489	557	1.304	1.301	1.275	0.791
+ 117	2.726	2.321	2.73	2.32	962	478	655	699	453	543	1.304	1.167	1.204	0.671

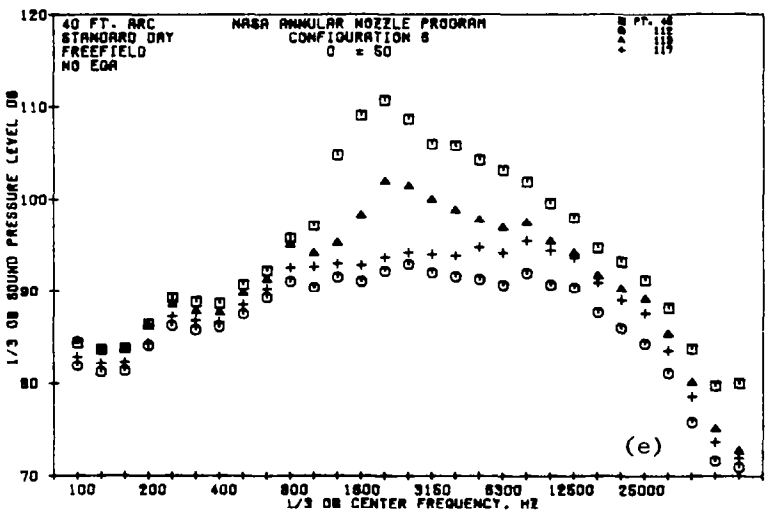

Test Point	P_T^o/P_o	P_T^i/P_o	P_r^o	P_r^i	T_T^o	T_T^i	T_T^{mix}	V_j^o	V_j^i	V_j^{mix}	M_j^o	M_j^i	M_j^{mix}	β_j^{mix}
□ 74	2.742	3.026	2.75	3.03	974	469	800	705	506	637	1.309	1.364	1.301	0.832
○ 78	2.727	2.257	2.73	2.26	955	559	851	696	483	640	1.304	1.146	1.260	0.767
△ 94	2.803	2.841	2.81	2.84	877	463	746	674	490	616	1.321	1.319	1.304	0.837
+ 99	2.797	2.780	2.80	2.79	722	322	590	610	406	543	1.314	1.306	1.284	0.807
× 113	2.723	2.773	2.73	2.78	954	500	810	696	504	635	1.303	1.301	1.286	0.808
◇ 78	2.753	2.502	2.76	2.5	957	476	814	700	470	631	1.311	1.224	1.273	0.788

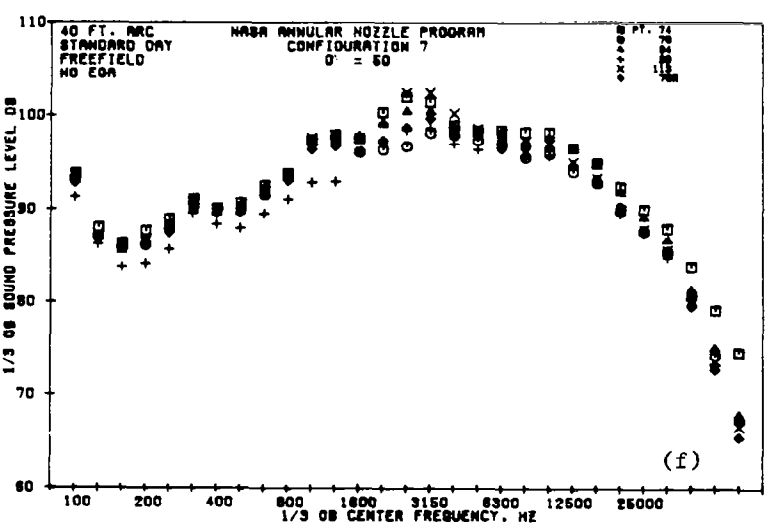

Figure 5-30. One-Third Octave Band Sound Pressure Level Spectra for High Radius Ratio Coannular Nozzle Configurations 2 through 7 at $\theta_{I_o} = 50°$, Outer Stream Constant: $V_j^o = 700$ mps, $T_T^o = 972$ K, $P_r^o = 2.75$; Inner Stream Varies: $T_T^i = 472$ K, V_j^i (396 - 503 mps), P_r^i (2.0 - 3.0) (Concluded).

Calculation for Strouhal Number*

- $f^{p}_{1/3}\ D/V^{i}_{j} = \frac{(400)\ (.1554)}{(442.5} = .1471$

- At the highest inner stream conditions V^{i}_{j} = 505.6 m/sec thus:

$$f^{p}_{1/3} = \frac{(.1471)\ 505.6}{.1554} = 478 \text{ Hz}$$

- But the observed peak frequency at the high flow conditions is ~ 630 Hz.

b) Based on Mixed Stream Velocity

- $f^{p}_{1/3}$ (at lowest mixed stream condition) = 400 Hz

- $f^{p}_{1/3}\ D/V^{mix}_{j} = \frac{(400)\ (.1554)}{553} = .11$

- At the highest mixed flow condition V^{mix}_{m} = 577 m/sec thus:

$$f^{p}_{1/3} = \frac{(.11)\ (577)}{.1554} = 403 \text{ Hz}$$

- But the observed peak frequency at the high flow condition is 630 Hz.

Based on the above crude observations a simple physical model suggests itself. The stationarity of the high frequency hump suggests that the outer stream velocity characterizes this region (the outer stream conditions are constant for the tests in Figure 5-28). Phenominologically this is satisfying since the high velocity stream is the outer stream and one immediately suspects that close to the nozzle exit region, before there is a decay into a transition and fully developed flow region, this high velocity stream is associated with the high frequency noise. The mid-frequency noise, and to some degree the low frequency noise seems to be governed by the mixed stream velocity - this is concluded since the increase in overall amplitude of noise can be accounted for in the classical way (velocity, thrust and temperature differences for each test point). The low frequency noise is somewhat muddled because of the greater than expected spectral shift of the low frequency noise hump. The inner stream velocity is ruled out based on it; and, because the amplitude of noise is more representative of the mixed stream

*For this example case the characteristic dimension used was D, the equivalent diameter based on the total area of the inner stream and the outer stream ($A^{i} + A^{o} = A_{T} = 189.08\ cm^{2}$). It may be argued that some other dimension is more proper, but for the purpose of this discussion and example it does not matter.

velocity variation. There are good reasons to believe that perhaps this region is more closely associated with acoustic propagation effects (convection, fluid shielding, refraction, or some coupled interaction of these effects).

Figure 5-29 shows the 90° spectrum for Configurations 2 through 7. From a theoretical point of view the 90° spectrum is a cornerstone for the acoustic spectra. The 90° spectra is the spectra which yields the most information regarding the source of noise without regard for the acoustic propagative influences such as convection, fluid shielding, and refraction. Unfortunately, shock noise does influence this spectra. For the moment, neglecting the shock noise spectra evident in some of the data, the source spectra of the noise appears to be quite regular in shape and, to a large degree without a strong double hump spectra*. Based on these observations, it can be concluded that the low frequency hump (of the double hump) observed in the 140° spectra is not associated with any basic turbulent mixing source noise phenomenon. The construction of the low frequency hump will need more insight from the fundamental theoretical acoustic formulations. The notion that the low frequency jet noise humb for coannular nozzles may be associated with the fully developed turbulent noise source region, and superimposed with a high frequency jet noise hump associated with the initial high velocity jet seems inappropriate without other influences taken into account. However, the 90° spectral shape is so broad as to suggest that two broad band peaks of near equal magnitude may be present.

Figure 5-30 illustrates the 50° spectra for Configurations 2 through 7. The results show that when the inner stream pressure ratio is around 2.0 only a small amount of shock noise is observed. At higher inner flow pressure ratios the usual shock noise spectra appears.

5.1.7.3 Variation of Sound Pressure Level Spectra with the Acoustic Angle

As two final examples of the spectral noise composition of high radius ratio coannular nozzles with plug, Figures 5-31 and 5-32 are presented. Figures 5-31 and 5-32 illustrate a manifold of spectra for Configuration 7 at subsonic conditions and fully supersonic conditions for acoustic angles to the inlet, θ_I, of 150°, 140°, 130°, 120°, 110°, 90°, 70°, and 50°. Appendix IV shows similar illustrations for Configurations 2, 3, 4, 5, and 6.

In Figure 5-31, a and b, the spectral variation with increasing acoustic angle for a basically high subsonic, or sonic (M_j^i = 0.936, M_j^o = 1.052,

*The results of Figure 5-29 do give the appearance of a high frequency hump around 6300 Hz. For these test conditions there does exist shock noise, and this high frequency hump is likely to be the broadband shock noise rather than noise from the high velocity outer jet. If this hump is taken out of the spectrum the assumption is that the 90° spectra would appear smooth and without two humps.

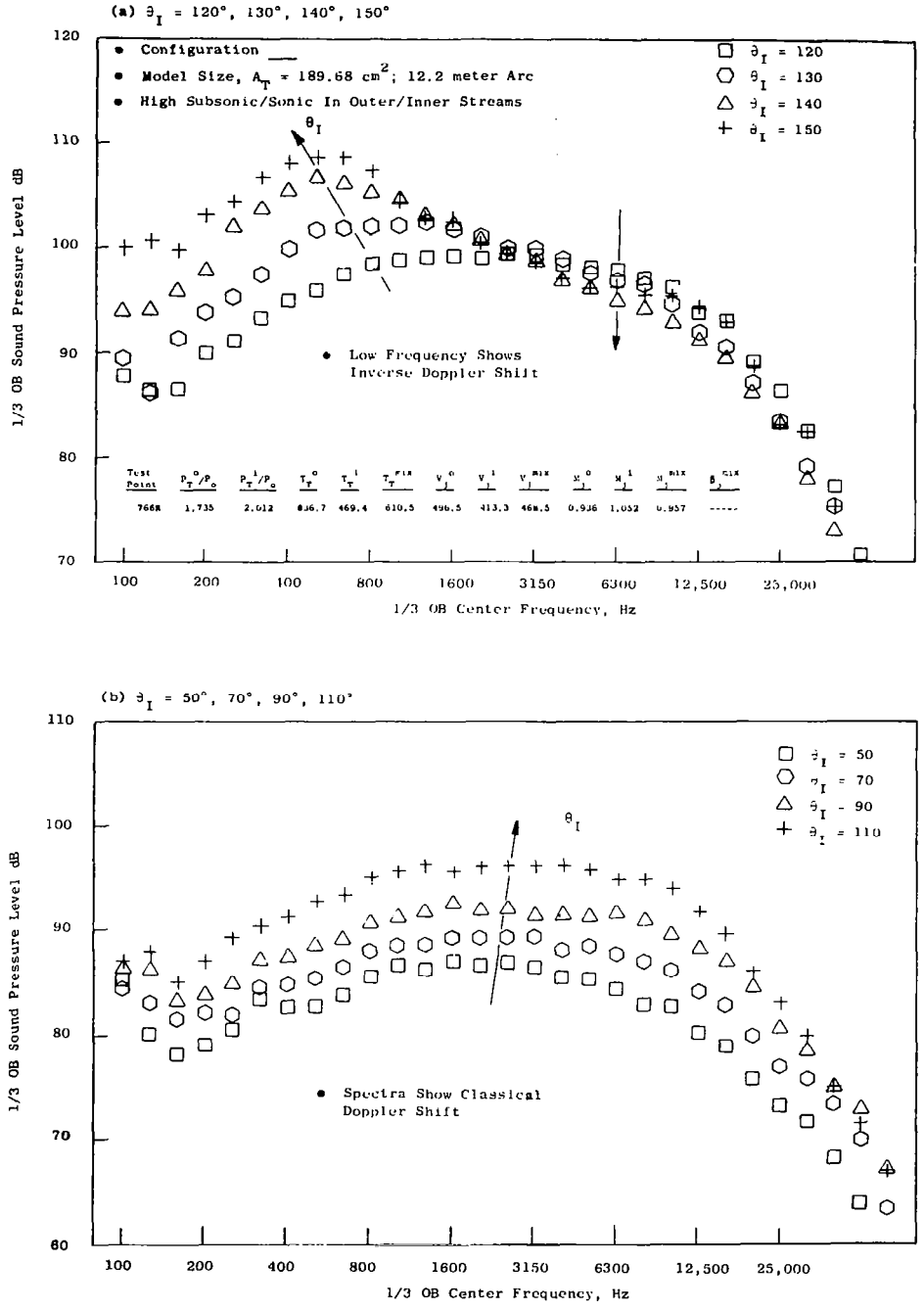

Figure 5-31. One-Third Octave Band Spectra at Various Angles and with High Subsonic/Sonic Test Conditions for a High Radius Ratio Coannular Nozzle with Plug, Configuration 7.

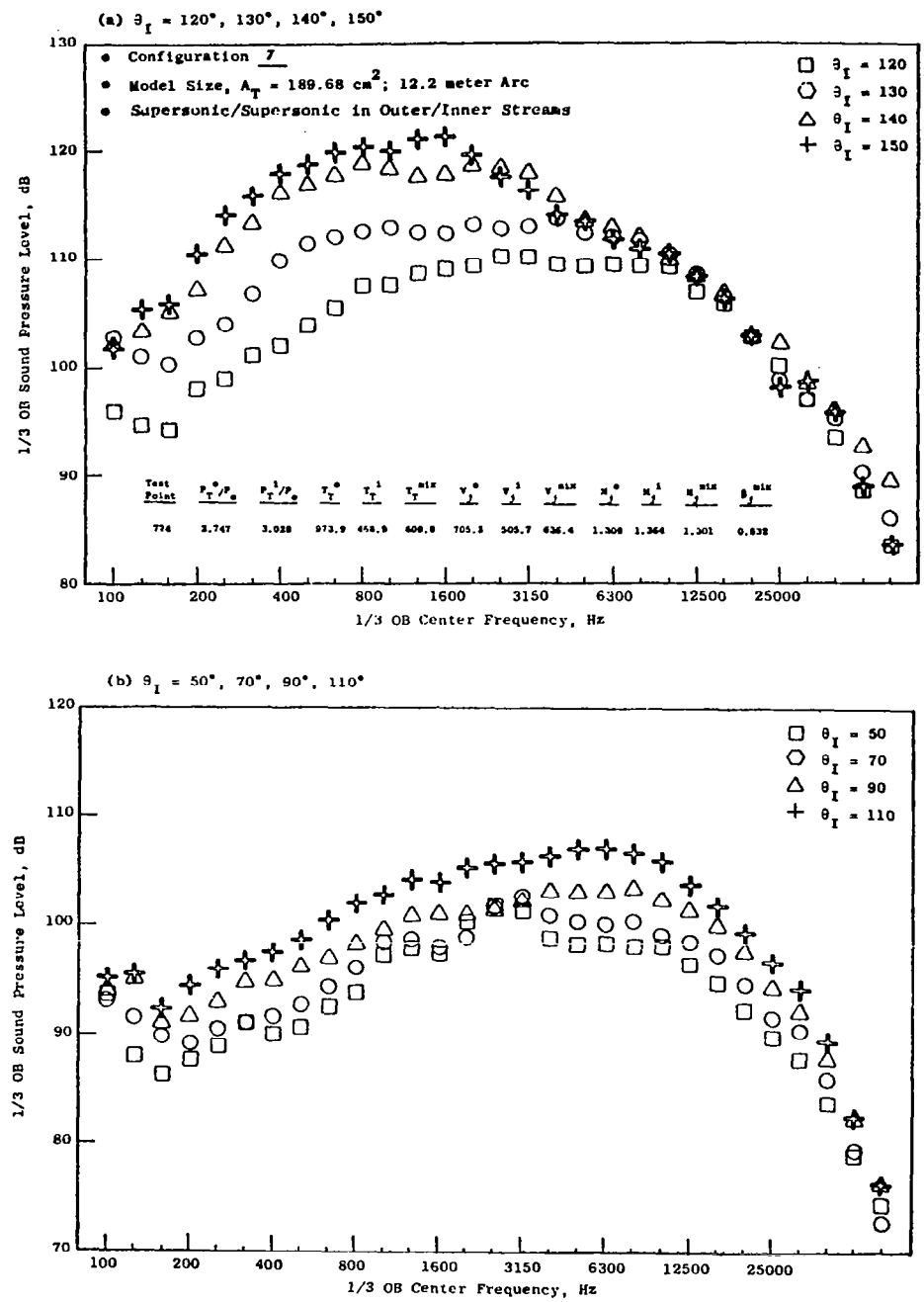

Figure 5-32. One-Third Octave Band Spectra at Various Angles and with Supersonic Conditions in Both Streams for a High Radius Ratio Coannular Nozzle with Plug, Configuration 7.

M_j^{mix} = 0.957) coannular nozzle with plug is shown. The test results show that as θ_I increases from 50° to 110°, the nozzle spectra is regular in shape, but somewhat broad in the mid-frequencies (800 → 5000 Hz) and the spectra shifts to higher frequencies (the Doppler shift for turbulent mixing noise). As the acoustic angle increases from 110° to 150° with respect to the inlet, the formation of the large amplitude/low frequency hump of noise is evident and a simultaneous reduction (about 2 dB) in the higher frequency noise is observed. The low frequency hump is observed to follow an inverse Doppler shift in frequency (indicative of acoustic propagative phenomenon).

Figure 5-32 illustrates the spectral composition and variation with acoustic angle for Configuration 7 operating at fully supersonic conditions (M_j^I = 1.36, M_j^O = 1.309, M_j^{mix} = 1.301). The forward quadrant noise behaves in a similar fashion as was observed in the sonic test case, however, the existence of shock noise is more evident. In the aft quadrant, the development of the low frequency hump observed in the subsonic test case is also evident.

The possible existence of two humps of the source noise at 90° is best examined by considering Figure 5-31 and the subsonic or sonic test results presented in Appendix IV for Configurations 2 through 6. From the coannular nozzles with plug that were tested, no strong double hump feature at 90° exists. However, each of the configurations seem to show two slight peaks at approximately 1600 Hz and 6300 Hz for all the subsonic/sonic 90° spectra.

5.2 INFLUENCE OF FLOW AND GEOMETRY ON THE ACOUSTIC CHARACTERISTICS OF HIGH RADIUS RATIO COANNULAR NOZZLES WITH PLUG

Within this subsection several aspects regarding the influence of inner flow velocity ratio and coannular nozzle geometry (radius ratio and area ratio) will be discussed.

5.2.1 The Influence of No Flow and Small Amounts of Inner Stream Flow on the Acoustic Characteristics of Coannular Nozzles with Plug

5.2.1.1 Annular Nozzle Test Results - Coannular Nozzle Test Results When the Inner Stream was Physically Blocked to Prevent any Inner Flow

In order to evaluate the influence of high radius ratio effects on annular plug nozzle acoustic characteristics, several tests were performed on Configurations 5, 1 and 3, and 6. These configurations represent annular nozzles with outer radius ratios, R°_r, of 0.853, 0.902 and 0.926 respectively. For these tests the inner stream was physically blocked to prevent any inner stream flow, and the outer stream flow conditions were varied. In Subsection 5.1 (particularly Figures 5-6, 5-10, 5-11, 5-12a, and 5-13), the zero inner flow (or annular nozzle) test results were already illustrated as part of all the test data in the analysis of OAPWL, acoustic efficiency, the Lighthill coefficient and velocity trends for the coannular nozzles. At this point the annular nozzle test results will be examined in more detail.

5.2.1.1.1 Outer Radius Ratio Effect on PNL_{max}

Figure 5-33a illustrates a normalized PNL_{max} (normalized on ideal thrust and annulus stream density) for all the annular nozzle test conditions. Also shown on this figure is a series of conical nozzle test results for comparison purposes. The test results clearly show an advantage in noise reduction with increasing outer radius ratio. A tabulation of the ΔPNL_{max} reduction obtained from Figure 5-33a is:

R°_r V_j,m/sec	570	700	780
0.853	No data	3	1
0.902	6	5-1/2	2-1/2
0.926	11	8-1/2	4-1/2

The magnitude of the PNL_{max} reductions relative to a conic nozzle are somewhat surprising. The reason for these noise reductions is the fact that relative to the conic nozzle spectra the annular nozzle spectra is considerably lower at high frequencies as well as in the peak frequency regions. The companion comprehensive data report (NASA CR-159575) contains a number of

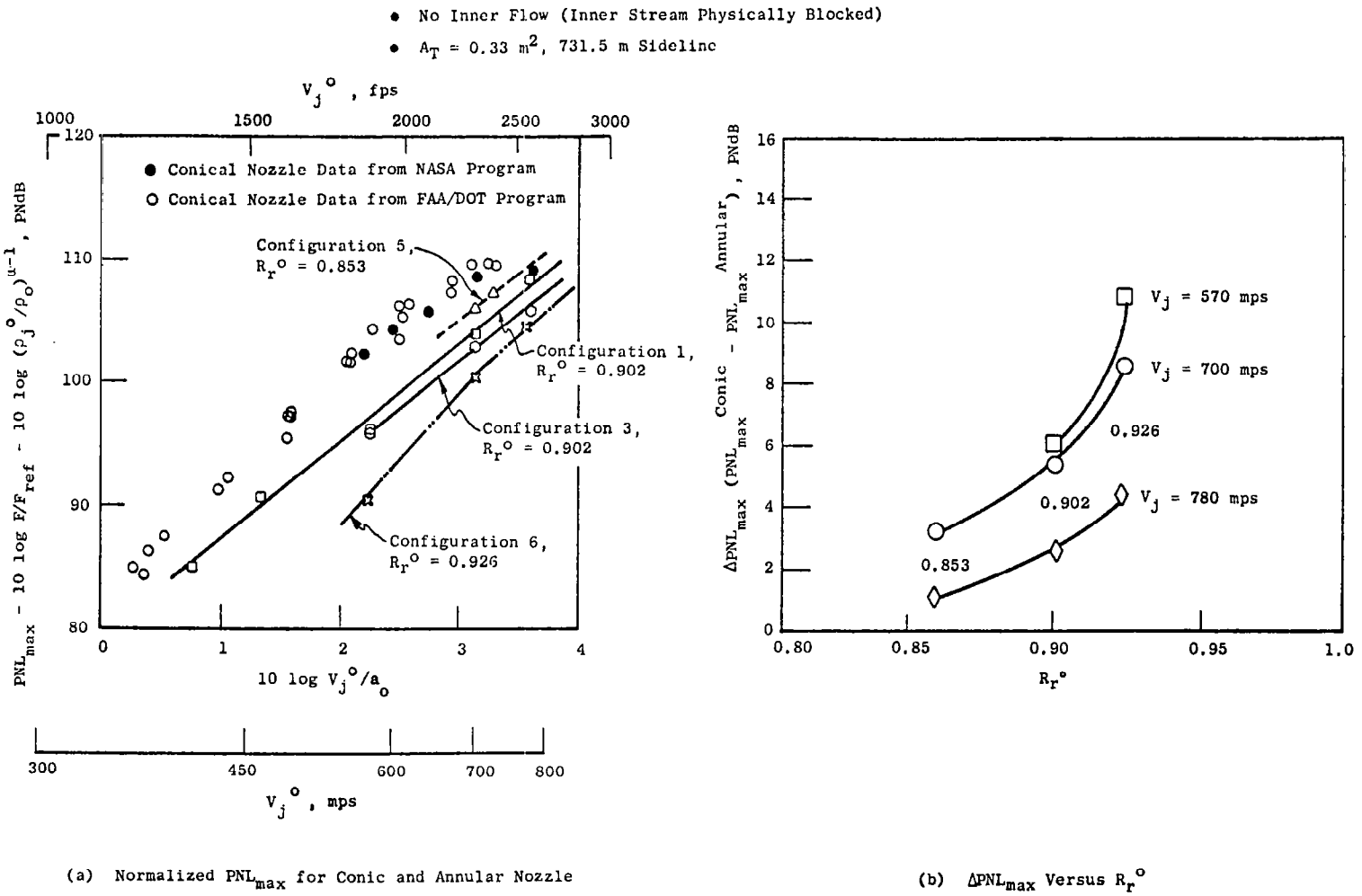

(a) Normalized PNL_{max} for Conic and Annular Nozzle

(b) ΔPNL_{max} Versus R_r^o

Figure 5-33. Influence of Outer Radius Ratio on PNL_{max} for Annular Nozzle Test Conditions.

spectral plots of various acoustic angle locations for the different test conditions (the interested reader is referred to that document). In the next subsection, some of these spectra results will be illustrated. Suffice it to say at this point, however, that for practical applications, aerodynamic performance and installation limitations would prevent the selection of an annular nozzle with as high a radius as 0.926. The limit of the practical range of the outer radius ratio is somewhere between 0.85 and 0.9.

5.2.1.1.2 Outer Radius Ratio Effect on Directivity and Spectral Shape

Figure 5-34 is presented to illustrate the effect of increasing outer radius ratio on the directivity and spectral characteristics of annular nozzles. Figure 5-34 shows the model scale OASPL directivity, the PNL directivity scaled to $0.33m^2$ at a 731.5 meter sideline distance, and model scale spectra at acoustic angles to the inlet of 130°, 90° and 50°. The test condition chosen was V_j^o = 700 m/sec, P_r^o = 2.73, T_T^o = 970 K for Configurations 5, 1 and 3, and 6 (outer ratios of 0.853, 0.902 and 0.926 respectively).

Figures 5-34a and b show the model scale OASPL, and the scaled PNL directivity respectively. Also shown on the figures is conic nozzle data for comparison purposes. For the OASPL directivity on an arc (12.2 meter), the annular high radius ratio nozzles are seen to have their peak noise further aft (140 - 150°) than does the conic nozzle (θ_p ~130°). At all angles, the OASPL's are observed to decrease with increasing outer radius ratio. At the 90° location, however, all the annular nozzle data fall within 2-1/2 dB. At the forward angles (40 → 80°) and the aft angles (100° → 150°), a wider spread in noise level is found. These results indicate that the source noise (90° location) for all the annular nozzle data (R_r^o 0.853 → 0.926) is similar; but the acoustic propagation influences (convection, fluid shielding, refraction etc.) and the shock noise characteristics are playing a strong role in the directivity shaping for the annular nozzles. The PNL directivity for the scaled results elicit remarks similar to those made on the OASPL directivity properties.

Figures 5-34 c, d, e illustrate the measured model scale sound-pressure-level spectra at 130°, 90°, and 50° respectively. Considering the 130° spectra first, the results for the annular nozzle show that as the radius ratio is increased from 0.853 to 0.926 a dramatic shaping of the spectra occurs. At a 0.853 radius ratio the spectral distribution of the annular nozzle is similar to the conic nozzle. The peak noise region is observed, however, to occur at slightly lower frequencies than the conic nozzle data. As the radius ratio increases to 0.902 and 0.926, the spectra for the annular nozzles show a dramatic decrease in peak frequency noise and high frequency noise relative to the conic nozzle spectra.

The 90° spectra (which is related to the noise source strength) for the annular nozzles is shown in Figure 5-34e. The results show that the spectra for the annular nozzles are quite broad in the mid-frequencies (800 - 8000 Hz). There probably exists shock broad-band noise in the annular nozzle spectra,

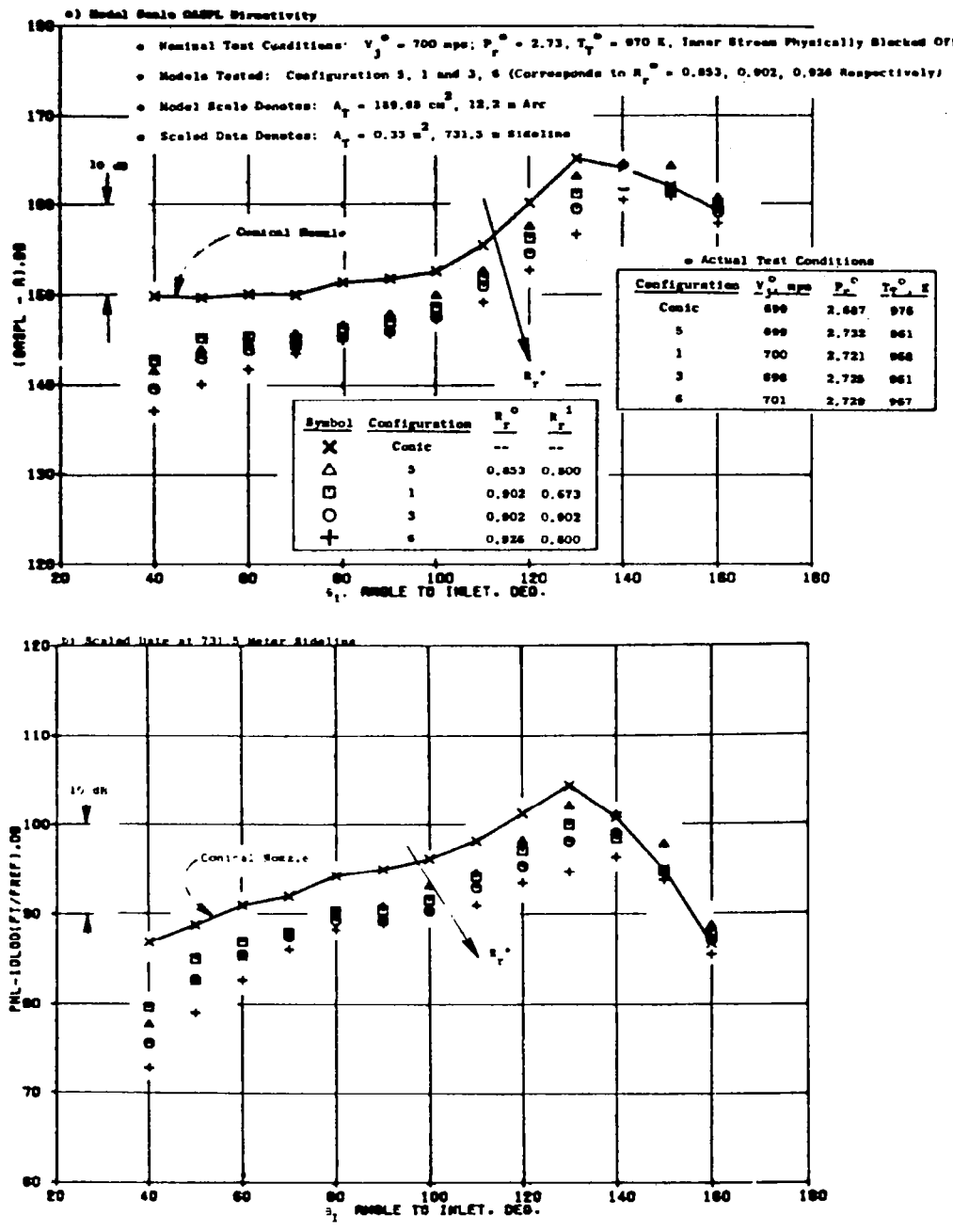

Figure 5-34. Influence of Outer Radius Ratio on Directivity and Spectral Shaping for High Radius Ratio Annular Nozzles - Inner Stream Physically Blocked.

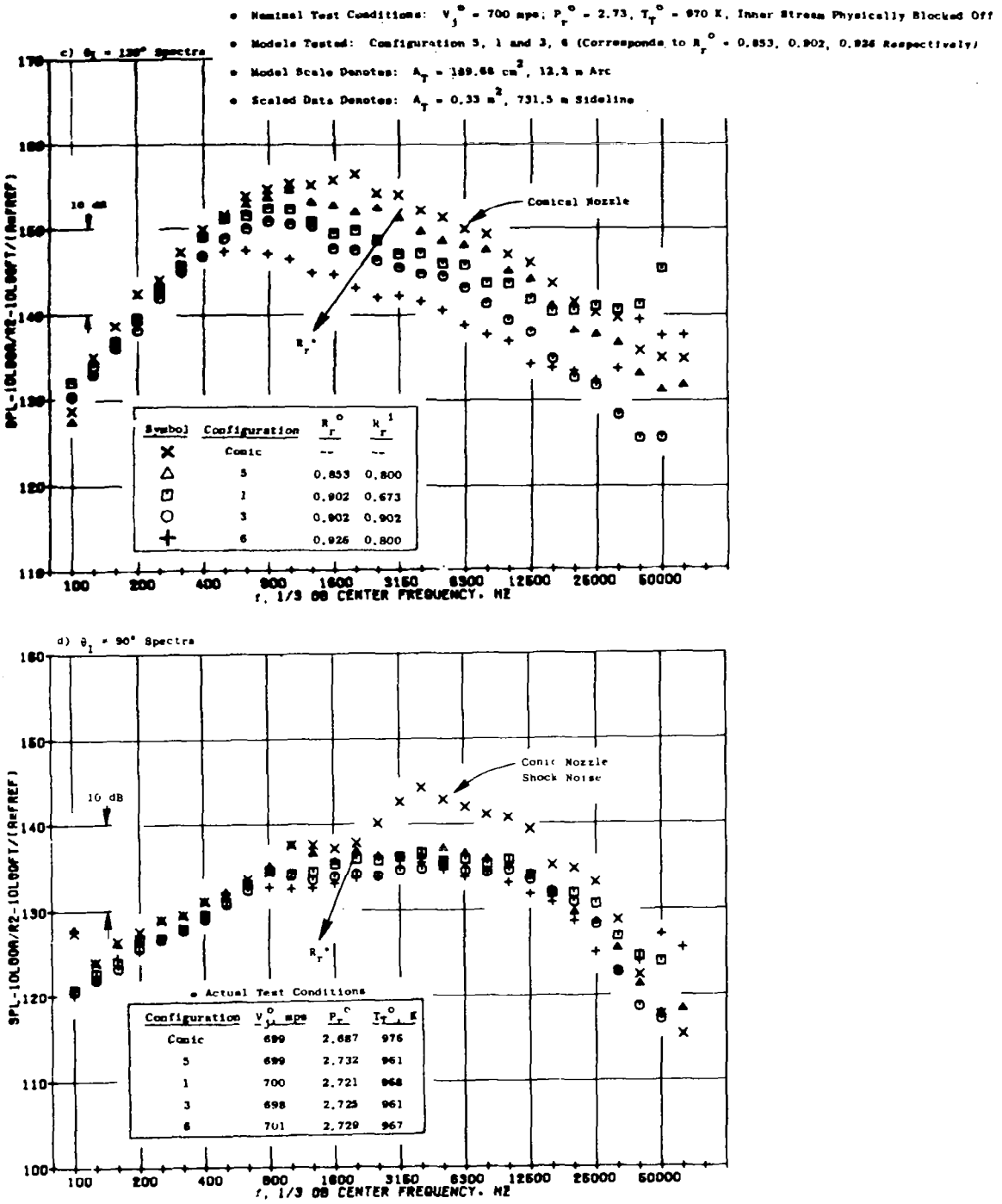

Figure 5-34. Influence of Outer Radius Ratio on Directivity and Spectral Shaping for High Radius Ratio Annular Nozzles - Inner Stream Physically Blocked (Continued).

- Nominal Test Conditions: V_j^o = 700 mps; P_r^o = 2.73, T_T^o = 970 K, Inner Stream Physically Blocked Off
- Models Tested: Configuration 5, 1 and 3, 6 (Corresponds to R_r^o = 0.853, 0.902, 0.926 Respectively)
- Model Scale Denotes: A_T = 189.68 cm^2, 12.2 m Arc
- Scaled Data Denotes: A_T = 0.33 m^2, 731.5 m Sideline

Symbol	Configuration	R_r^o	R_r^i
×	Conic	--	--
△	5	0.853	0.800
□	1	0.902	0.673
○	3	0.902	0.902
+	6	0.926	0.800

• Actual Test Conditions

Configuration	$V_{j_t}^o$ mps	P_r^o	T_T^o, K
Conic	699	2.687	976
5	699	2.732	961
1	700	2.721	968
3	698	2.725	961
6	701	2.729	967

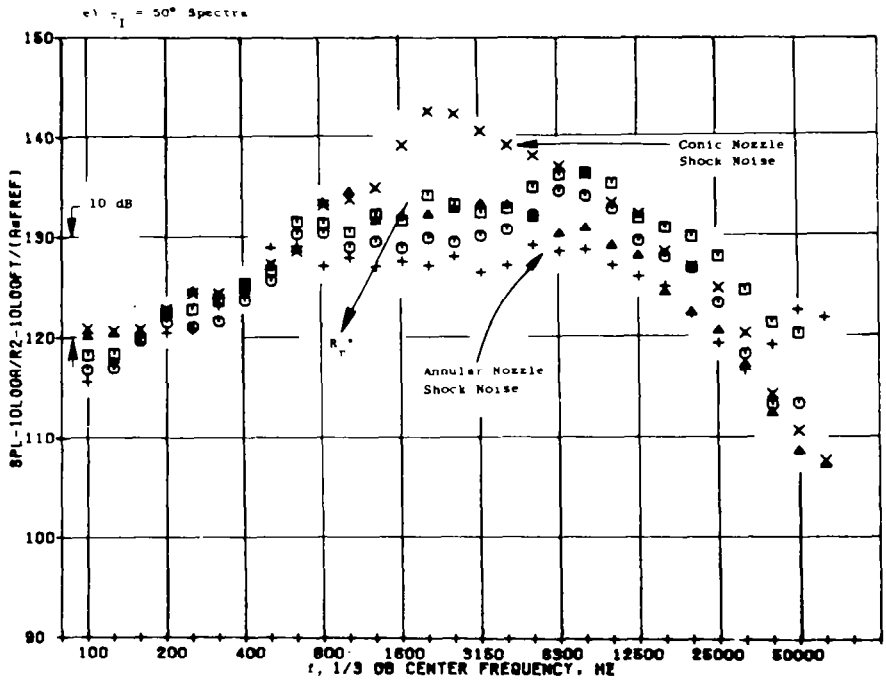

Figure 5-34. Influence of Outer Radius Ratio on Directivity and Spectral Shaping for High Radius Ratio Annular Nozzles - Inner Stream Physically Blocked (Concluded).

but not nearly the amount observed for the conic nozzle. The spectra variation for the three radius ratio annular nozzles is observed to be within 2-1/2 dB, but there does exist a systematic decrease with increasing radius ratio - an indication of source noise reduction.

The 50° spectra for the annular nozzles tested is shown in Figure 5-34f. Here again there exists a systematic decrease in noise with increasing radius ratio. Now the presence of shock noise is more easily recognized (around 8000 Hz), but again, not of the amplitude measured for the conic nozzle.

5.2.1.2 Influence of the Variation of Small Amounts of Inner Stream Flow on the Acoustic Characteristics of Annular Nozzles

To study the directivity and spectral shaping influences due to the addition of small amounts of inner stream flow, a series of tests were performed where the outer stream conditions were fixed and the inner stream was gradually varied so that the inner to outer weight flow ratio, $\dot{\omega}^i/\dot{\omega}^o$, ranged from $0 \rightarrow 0.17$. Configurations 1 and 3 were chosen for this study. All the inner stream flows were quite subsonic for these test conditions ($M_j^i \approx 0.019 \rightarrow 0.13$ for Configuration 1; $M_j^i = 0.149 \rightarrow 0.394$ for Configuration 3). Both of these configurations have an outer radius ratio, R_r^o, of 0.902, but Configurations 1 and 3 have an inner stream radius ratio variation of 0.673 to 0.902 (representing the largest and smallest inner stream annulus heights respectively).

5.2.1.2.1 Overall Sound Pressure Level and Perceived Noise Level Directivity Characteristics

To illustrate the influence of the addition of small amounts of inner flow on the directivity of coannular/annular nozzles, test results will be shown where the outer stream was fixed at:

$V_j^o = 700$ m/sec

$P_r^o = 2.72$

$T_T^o = 955$ K

The inner stream temperature was held constant* ($T_T^i \sim 694 \rightarrow 833$), while the inner stream pressure was varied to obtain a weight flow ratio, $\dot{\omega}^i/\dot{\omega}^o$, of $0 \rightarrow 0.17$. Figure 5-35 compares the model scale overall sound-pressure-level,

*Originally an inner stream temperature of 472 K was planned for this test series. However, when the low flows were set for the inner stream, while the outer stream was operating at 955 K, the temperature of the inner stream would rise due to heat conduction of the outer stream to the inner stream. Thus it was not possible to maintain the desired inner stream temperature.

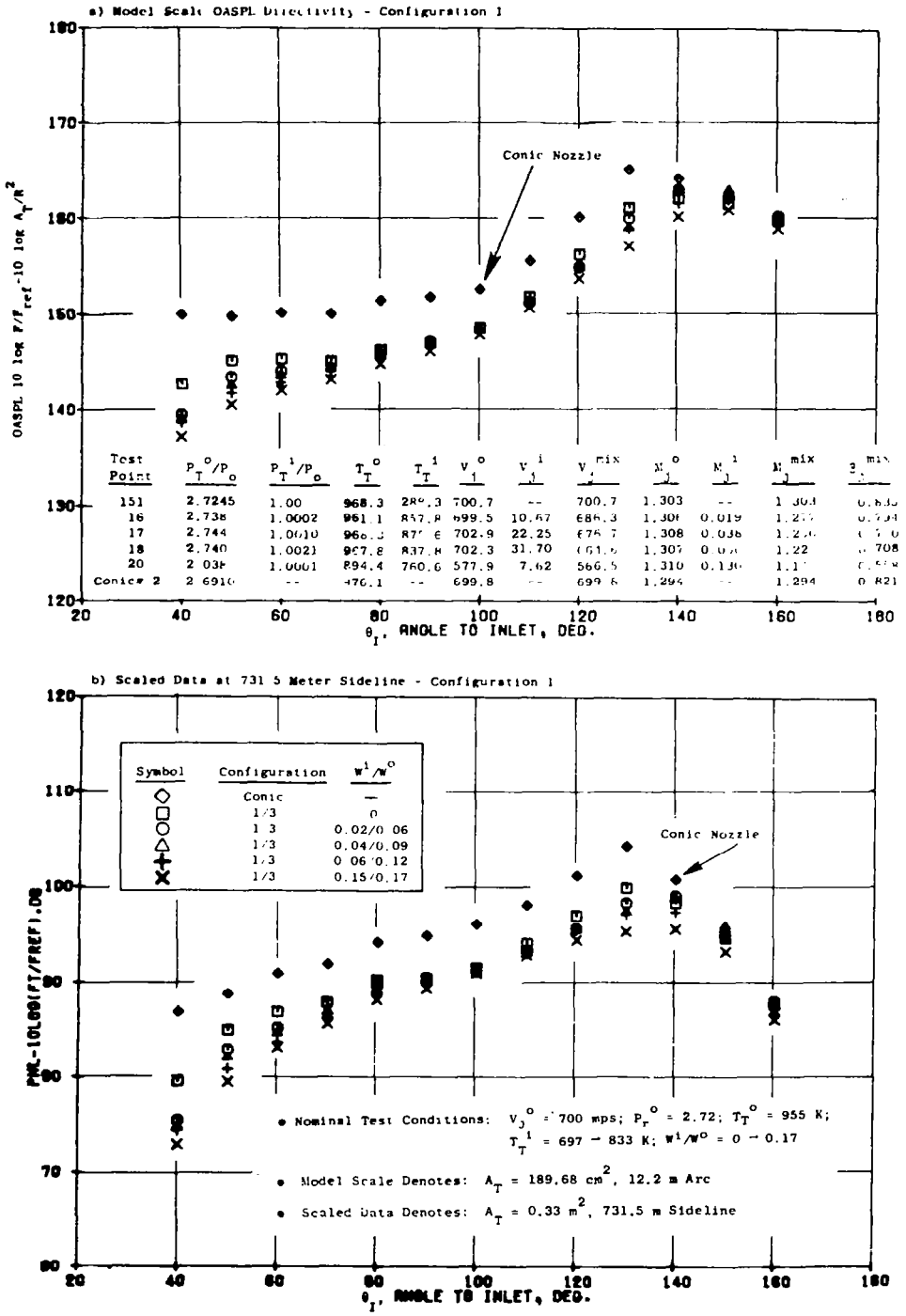

Test Point	P_T^o/P_o	P_T^i/P_o	T_T^o	T_T^i	V_j^o	V_j^i	$V_{j_{mix}}$	M_j^o	M_j^i	$M_{j_{mix}}$	θ_{mix}
151	2.7245	1.00	968.3	289.3	700.7	--	700.7	1.303	--	1.303	0.000
16	2.738	1.0002	961.1	837.8	699.5	10.67	686.3	1.301	0.019	1.277	0.734
17	2.744	1.0010	960.3	837.6	702.9	22.25	678.7	1.308	0.038	1.256	0.730
18	2.740	1.0021	957.8	837.8	702.3	31.70	661.5	1.307	0.058	1.22	0.708
20	2.038	1.0001	894.4	760.6	577.9	7.62	566.5	1.310	0.130	1.11	0.518
Conic# 2	2.6916	--	476.1	--	699.8	--	699.8	1.294	--	1.294	0.821

Figure 5-35. The Influence of Subsonic Inner Flow Variations of W^i/W^o = 0 - 0.17 on Thrust Normalized Overall Sound Pressure Level and Perceived Noise Level Directivities for High Radius Ratio Coannular Nozzles - Configurations 1 and 3.

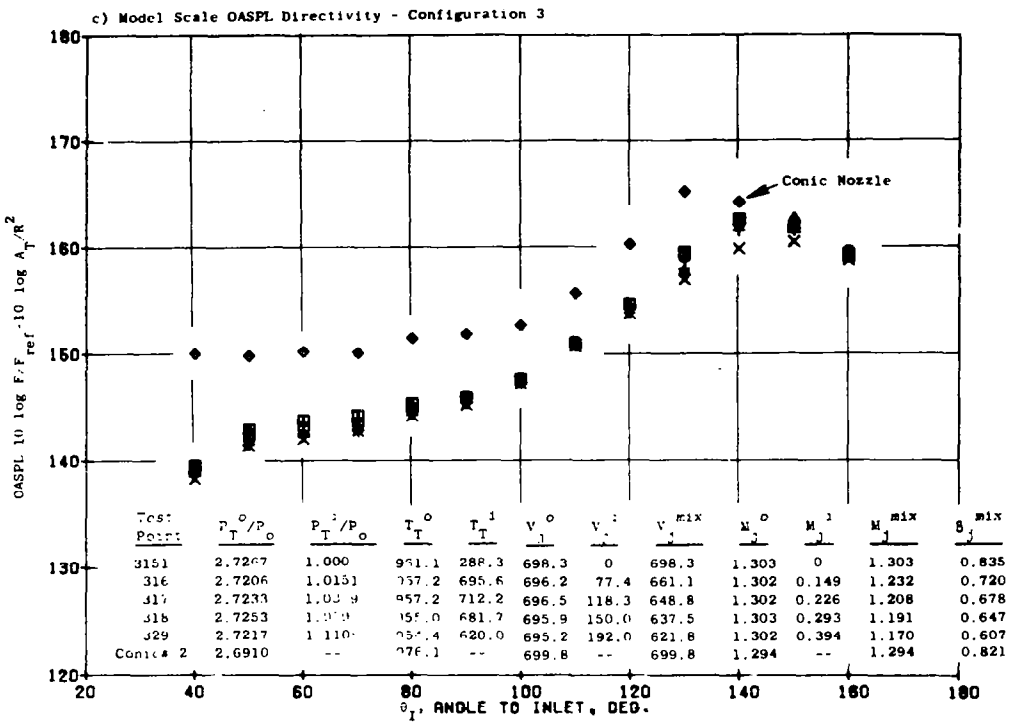

Test Point	P_T^o/P_o	P_T^i/P_o	T_T^o	T_T^i	V_j^o	V_j^i	V_j^{mix}	M_j^o	M_j^i	M_j^{mix}	θ_j^{mix}
3151	2.7267	1.000	961.1	288.3	698.3	0	698.3	1.303	0	1.303	0.835
316	2.7206	1.0151	957.2	695.6	696.2	77.4	661.1	1.302	0.149	1.232	0.720
317	2.7233	1.0[illegible]	957.2	712.2	696.5	118.3	648.8	1.302	0.226	1.208	0.678
318	2.7253	1.0[illegible]	958.0	681.7	695.9	150.0	637.5	1.303	0.293	1.191	0.647
329	2.7217	1.1104	956.4	620.0	695.2	192.0	621.8	1.302	0.394	1.170	0.607
Conic# 2	2.6910	--	976.1	--	699.8	--	699.8	1.294	--	1.294	0.821

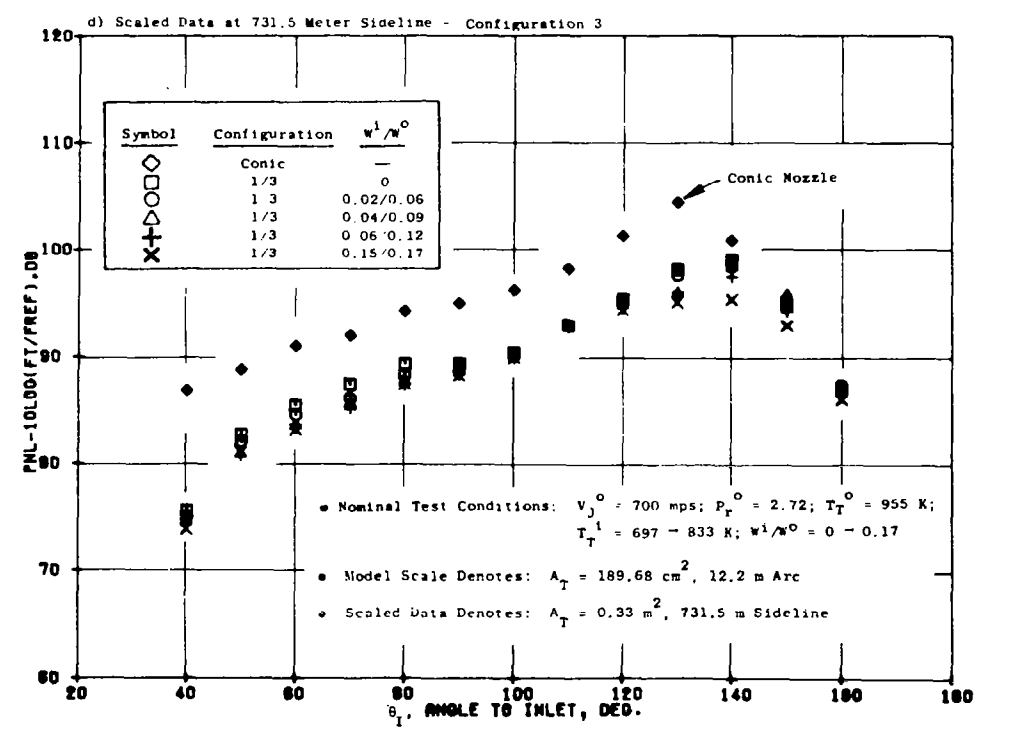

Figure 5-35. The Influence of Subsonic Inner Flow Variations of W^i/W^o = 0 - 0.17 on Thrust Normalized Overall Sound Pressure Level and Perceived Noise Level Directivities for High Radius Ratio Coannular Nozzles - Configurations 1 and 3 (Concluded).

(OASPL) directivity and the scaled perceived noise level (PNL) directivity patterns at a 731.5 meter sideline distance for Configurations 1 and 3. Figures 5-35a and b show the thrust normalized** OASPL and PNL directivities for Configuration 1, and Figures 5-35c and d show the thrust normalized OASPL and PNL directivities for Configuration 3.

Comparing Figure 5-35a to 5-35c shows that the peak OASPL levels for small amounts of inner flow occur at angles further aft than the conic nozzle test results. This observation was also made for the purely annular nozzle test results discussed above. In the aft quadrant the thrust normalized directivity shapes between Configurations 1 and 3 appear identical in character (the inner stream size does not appear to be a factor in the aft quadrant). By inspection, using the adjustment factors for constant V_J^{mix} cited in the footnote above, the data around the peak angle would collapse to a single curve. In the forward quadrant (40° + 80°), Configuration 3 shows less of a data spread than Configuration 1. As will be seen in the spectral presentations below, this is attributable to the variation in the shock noise characteristics. The observations made for the thrust normalized OASPL directivity can also be cited for the thrust normalized PNL directivity patterns shown in Figures 5-35b and d.

5.2.1.2.2 Sound-Pressure-Level Variations

The comparisons of the sound-pressure-level spectral variations due to the addition of inner stream weight flow for Configurations 1 and 3 are shown in Figure 5-36. Thrust normalized, one-third octave-band sound-pressure-level (SPL) spectra at θ_I = 130°, 90°, and 50° are shown. Similar spectral shaping characteristics are observed between Configurations 1 and 3 at θ_I = 130° (see Figures 5-36a and d). As the inner stream flow increased, the spectra peak shifts to a lower frequency, and the mid-frequency bands flatten. At θ_I = 90°, the spectra are quite flat for all test conditions compared to the conic nozzle. Using the mixed stream velocity corrections cited in the foot note above would indicate that the roles between the highest inner stream

---

**For these illustrations the noise parameters of OASPL and PNL were normalized with respect to the total nozzle ideal thrust. However, for absolute comparisons the test results should also have been adjusted for the proper characteristic velocity. Thus, although the tests were performed at V° ~700 m/sec, the mixed stream velocity decreased from 700 m/sec to 620 m/sec. Based on the results of Section 5.1, this would amount to a reduction in PNL_{max} of ~3.92 PNdB. Nonetheless, the characteristics of the results, if not the absolute levels, can be examined here. Using 75 log $700/V_J^{mix}$ correction for Configuration 1, additions of 0, 0.67, 1.11, 1.7, and 3.96 PNdB can be applied to the test points as $\dot{\omega}^1$ increased from 0 to 0.15 $\dot{\omega}^o$ respectively and 0, 1.89, 2.53, 3.1, and 3.98 PNdB for the configuration 3 test points for $\dot{\omega}^1$ = 0 to 0.17 $\dot{\omega}^o$.

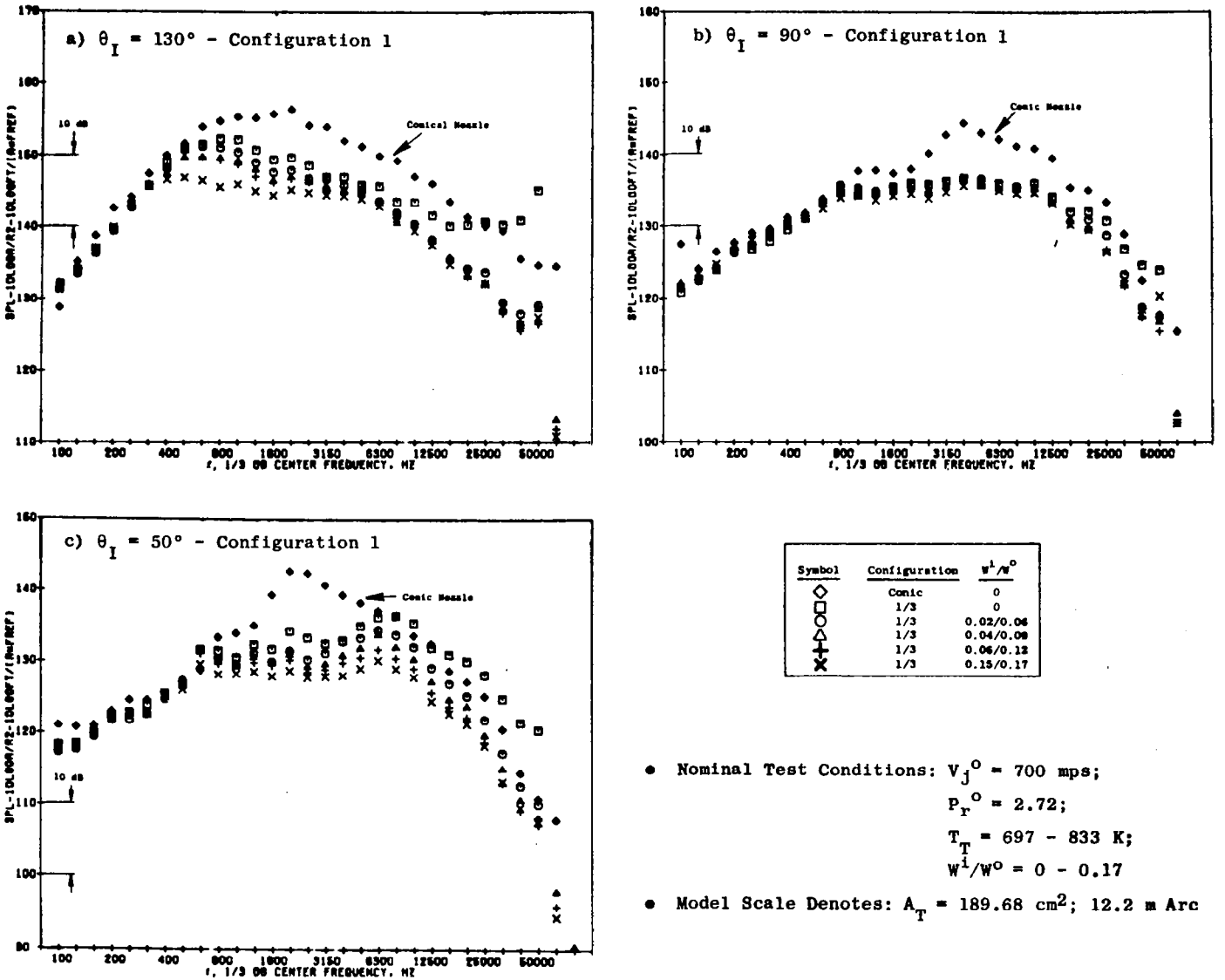

Figure 5-36. The Influence of Subsonic Inner Flow Variations of W^i/W^o = 0 → 0.17 on Thrust Normalized One-Third Octave-Band Sound Pressure Level Spectra for High Radius Ratio Coannular Nozzles - Configurations 1 and 3.

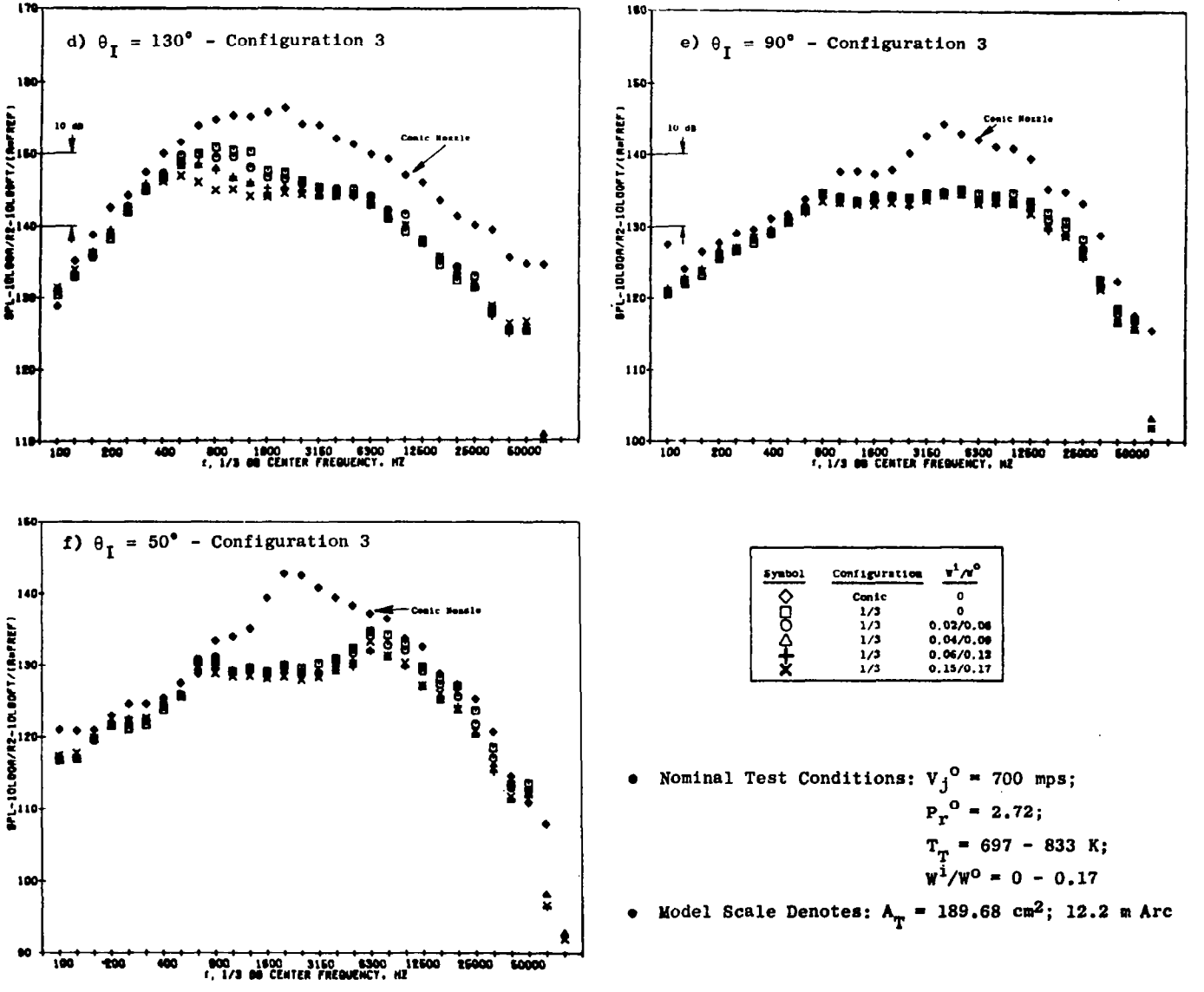

Figure 5-36. The Influence of Subsonic Inner Flow Variations of W^i/W^o = 0 → 0.17 on Thrust Normalized One-Third Octave-Band Sound Pressure Level Spectra for High Radius Ratio Coannular Nozzles - Configurations 1 and 3 (Concluded).

flows condition and the zero inner stream test condition would interchange (there would be a slight increase in source noise with increasing inner stream flow above the purely annular jet results) for both Configurations. At θ_I = 50°, the existence of shock noise is observed around 8000 Hz for the coannular nozzle test results. The shock noise is, however, substantially reduced as compared to the conical nozzle (ΔSPL_{peak} 7.5 dB). The larger inner stream annulus for Configuration 1 show somewhat less favorable shock noise characteristics than does Configuration 3.

5.2.2 Velocity Ratio Effects on High Radius Ratio Coannular Nozzles with Plug

Another study which was undertaken to examine the possible flow management of noise control for high radius ratio coannular nozzles was a study where the velocity ratio of the inner stream to the outer stream, V_j^i/V_j^o, was varied. This study was performed by holding the outer stream constant (V_j^o ~ 700 m/sec, T_T^o ~ 961 K, P_T^o ~ 2.75) and regulating the inner stream flow over a velocity ratio range V_j^i/V_j^o of 0.2 → 0.7 while keeping the inner stream total temperature constant (T_T^i ~ 475 K). The configurations tested in this mode were Configurations 2 through 7. The inner stream conditions for these tests were different than those discussed above in Subsection 5.2.1 in that the weight flow ratios, $\dot{\omega}^i/\dot{\omega}^o$, were higher (0.09) → 0.46 for Configuration 7, to 0.54 → 2.0 for Configuration 6, while the other configurations fell within those two ranges) and the inner stream Mach numbers went from modest Mach numbers to fully supercritical conditions for the highest velocity ratios tested (See test points 107 to 117 for the actual flow conditions for this test series).

The main results are presented on a normalized maximum perceived-noise-level, PNL_{max}, bases scaled to a total area of 0.33m^2 for a 731.5 meter sideline distance. Figure 5-37a illustrates the test results in the form of PNL_{max} normalized with respect to the total thrust and the mixed density (-10 log F/F_{ref} - 10 log ρ_j^{mix}/ρ_o) versus velocity ratio, V_j^i/V_j^o. Accompanying this figure is Figure 5-37b which illustrates the variation in mixed stream velocity, V_j^{mix}, as a function of velocity ratio for all the test conditions. From Figure 5-37a alone, the misleading conclusion might be drawn that there exists a continued decrease in noise with increasing area from A_r = 0.33 (Configuration 7) to A_r = 1.42 (Configuration 6), that the peak region of suppression is at V_j^i/V_j^o ~ 0.5 and that the maximum change in level in configurations is 6 PNdB. Examination of Figure 5-37b which presents the variation of the mixed velocity with velocity ratio illustrates that the shapes of the curves shown in Figure 5-37a are similar in shape and variation of level as are the shape and variation of the V_j^{mix} distributions. Thus to draw a better insight into what is occurring, the noise comparisons should also be normalized with respect to V_j^{mix}. This normalization is illustrated in Figure 5-38.

- Nominal Test Conditions: V_j^o = 700 mps; P_r^o = 2.75; T_T^o = 961 K
  $T_T^i \approx$ 475 K; V_j^i/V_j^o Varies
- Test Results for Configurations 2 through 7
- F_{ref} = 22,818 newtons

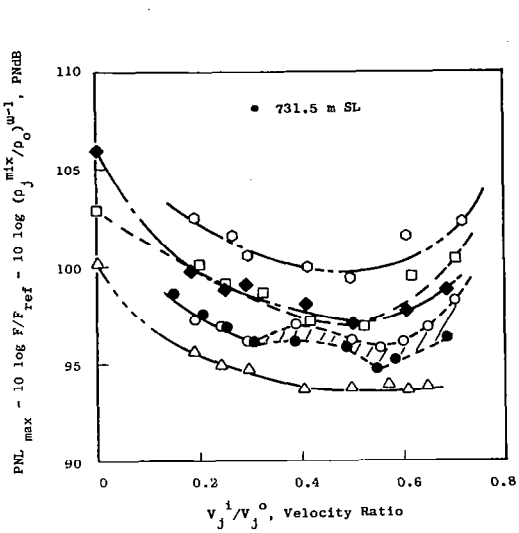

Thrust and Density

a) Normalized PNL_{max} - Scaled to A_T = 0.33 m^2, 731.5 meter Sideline

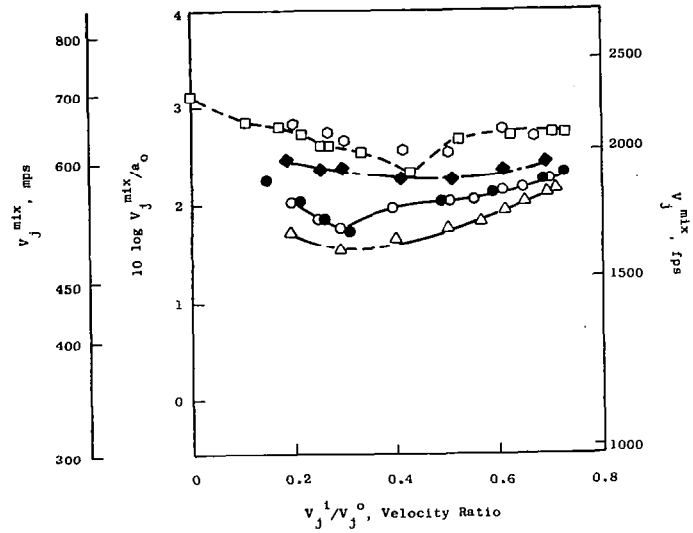

b) Mixed Stream Velocity Distribution with Velocity Ratio

Symbol	Configuration	R_r^o	R_r^i	A_r
○	2	0.902	0.800	1.03
□	3	0.902	0.902	0.53
● *	4	0.902	0.800	1.03
◆	5	0.853	0.800	0.63
△	6	0.926	0.800	1.42
◇	7	0.853	0.902	0.33

* The Difference Between Configurations 2 and 4 is that 4 has a Bent Inner Stream Plug

R_r^o = Outer Stream Radius Ratio (ID Radius to OD Radius)

R_r^i = Inner Stream Radius Ratio (ID Radius to OD Radius)

A_r = Area Ratio (Inner Stream to Outer Stream)

Figure 5-37. Influence of Velocity Ratio (Inner Stream Velocity, V_j^i, to Outer Stream Velocity, V_j^o) on Thrust and Density Normalized Maximum Perceived Noise Levels - Results Not Normalized to a Constant Mixed Stream Velocity.

Figure 5-38 shows the tested results corrected to a constant V_J^{mix*}. From the curves of Figure 5-38 the following observations can be made. For some of the configurations a sinusoidal shape is exhibited, while for some of the other configurations a relatively uniform distribution is found. For those configurations which exhibit the sinusoidal normalized PNL_{max} distribution with velocity ratio (Configuration 2, 4 and 6 primarily, and Configurations 3 and 5 to a much lesser extent), a minimum noise level occurs at a velocity ratio, $V_J^i/V_J^o \sim 0.6 \rightarrow 0.7$. For Configurations 2, 4 and 6, an improper selection of velocity ratio can mean as much as 3.29, 4.44 and 4.96 PNdB noise levels off minimum. Configurations 3 and 5 show a minimum noise level also around $V_J^i/V_J^o \sim 0.6 \rightarrow 0.7$, and a 1.84 and 1.3 PNdB level difference between off-minimum and the minimum velocity ratio region. Configuration 7 test results are observed to be relatively uniform over the velocity ratio range tested. Categorizing these results according to area ratio - Configurations 2, 4, and 6 represent area ratios greater than one (1.03, 1.03 and 1.42 respectively); Configurations 3 and 5 are somewhat smaller area ratio configurations (0.53 and 0.63 respectively) and Configuration 7 represents the smallest area ratio configuration tested ($A^i/A^o = 0.33$). From these test results it can be concluded that where a large area ratio configuration is being selected ($A^i/A^o \leq 1$) substantial care is needed in selecting its proper operational velocity ratio - $V_J^i/V_J^o \sim 0.6 \rightarrow 0.7$. For area ratios less than one, the selection of velocity ratio is not as critical, nonetheless a velocity ratio of $V_J^i/V_J^o \sim 0.6$ seems a good selection.

One question which may be asked is whether there is an optimum weight flow ratio, ω^i/ω^o, which could be recommended. Figure 5-39 illustrates the normalized PNL_{mix} for Configurations 2 through 7 against weight flow ratio for the same test series.

The results show that the weight flow ratio is not a parameter that has as much universality as does the velocity ratio. This is understable since the weight flow ratio is equal to the product of the density ratio, area ratio and velocity ratio, $\omega^i/\omega^o = \rho_r A_r V_r$. Thus for the test conditions presented, the density and velocity ratios are common from configuration to configuration, but the area ratio variation is 4.3 to 1 (Configuration 6 to Configuration 7). This variation acts to sharply contract or expand the weight flow ratio curve from configuration to configuration. At this time therefore,

---

*The normalization used for V_J^{mix} was $[8.14 * 10 \log V_J^{mix}/a_o + 78.83]$. This factor was based on an average of all test data for Configuration 1 through 7 described in Section 5.1. To perform the normalization exactly, each configuration should be normalized to its own velocity dependence. One normalization factor was used because, for this test series it is most important from a design point-of-view to decide at which velocity ratio a minimum occurred. Thus the correct shape of the velocity ratio curve was examined. Also noteworthy is the fact that the velocity ratio study points were the points on the curves shown in Figure 5-13, which showed the maximum variation about the regression curves.

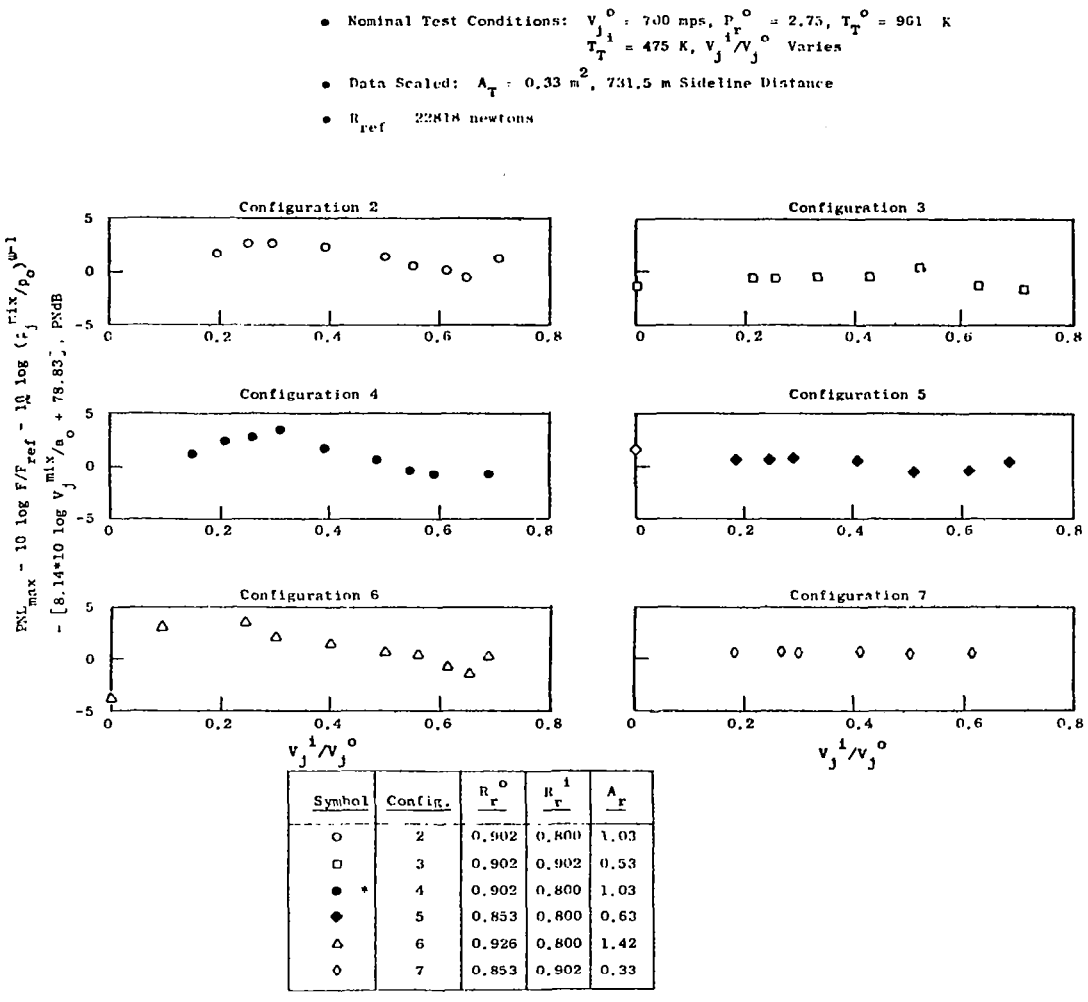

Symbol	Config.	R_r^o	R_r^i	A_r
○	2	0.902	0.800	1.03
□	3	0.902	0.902	0.53
● *	4	0.902	0.800	1.03
◆	5	0.853	0.800	0.63
△	6	0.926	0.800	1.42
◇	7	0.853	0.902	0.33

* The difference between Configurations 2 and 4 is that 4 has a bent inner stream plug

R_r^o = Outer Steam Radius Ratio (ID Radius to OD Radius)

R_r^i = Inner Steam Radius Ratio (ID Radius to OD Radius)

A_r = Area Ratio (Inner Stream to Outer Stream)

Figure 5-38. Influence of Velocity Ratio (Inner Stream Velocity, V_j^i, to Outer Stream Velocity, V_j^o) on Thrust, Density and Velocity Normalized Maximum Perceived Noise Levels - Results Normalized to a Constant Mixed Stream Velocity.

- Nominal Test Conditions: V_j^o = 700 mps; P_r^o = 2.75, T_T^o = 961 K, T_T^o = 475 K, $\dot{W}^i/\dot{W}^o$ = Varies
- Data Scaled: A_T = 0.33 m^2; 731.5 meter Sideline Distance
- F_{ref} = 22,818 newtons

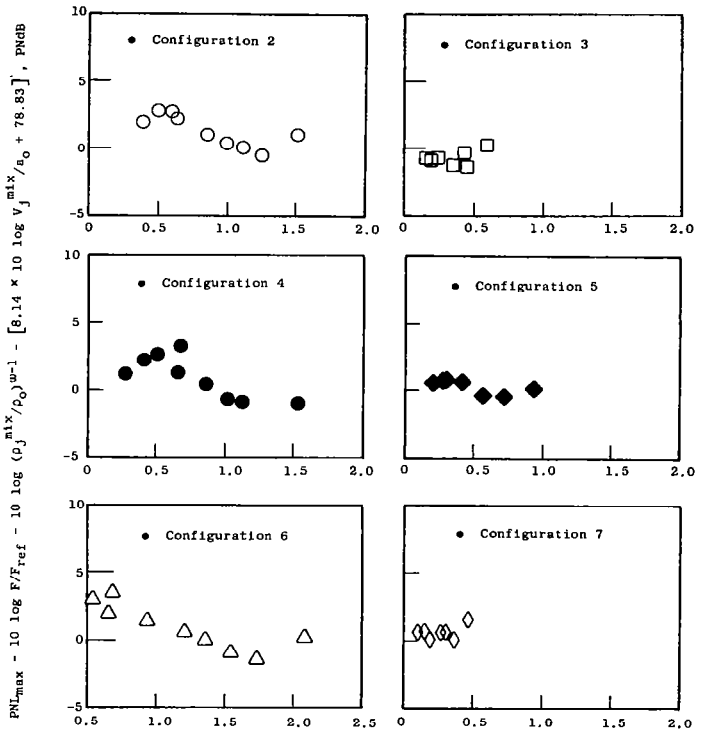

Symbol	Configuration	R_r^o	R_r^i	A_r
	2	0.902	0.8	1.03
	3	0.902	0.902	0 53
*	4	0.902	0.8	1.03
	5	0.853	0.8	0.63
	6	0.926	0.8	1.42
	7	0.853	0.902	0.33

* The Difference Between Configurations 2 and 4 is that 4 has a Bent Inner Plug

R_r^o = Outer Stream Radius Ratio (ID Radius to OD Radius)

R_r^i = Inner Stream Radius Ratio (ID Radius to OD Radius)

A_r = Area Ratio (Inner Stream to Outer Stream)

Figure 5-39. Influence of Weight Flow Ratio (Inner Stream, ω^i, to Outer Stream, ω^o) on Thrust, Density, and Velocity Normalized Maximum Perceived Noise Level - Results Normalized to a Constant Mixed Stream Velocity.

the velocity ratio is considered to be a more appropriate design parameter for coannular nozzles than weight flow ratio.

5.2.3 The Influence of Outer Stream Radius Ratio, Area Ratio, and Inner Stream Plug Geometry Effects on the Acoustic Characteristics of High Radius Ratio Coannular Nozzles with Plug

There were three key geometric parameters which were considered in the study of the influence of geometry on the acoustic characteristics of high radius ratio coannular nozzles with plug; they are: inner to outer area ratio - holding radius ratio constant; radius ratio - holding area ratio constant; and inner stream plug shape - holding area ratio and radius ratio constant. The configurations used for each of these studies are as follows:

- Area Ratio Study

1. Configurations 5 and 7:

   $R_D^j = 0.853$, $A_r = 0.63$ and 0.33 respectively

2. Configurations 2 and 3:

   $R_r^o = 0.902$, A_r, = 1.03 and 0.53 respectively

- Radius Ratio Study

1. Configurations 5 and 3:

   $A_r = 0.53 \rightarrow 0.63$, $R_r^o = 0.853$ and 0.902 respectively

2. Configurations 1 and 6:

   $A_r = 1.42 \rightarrow 1.53$, $R_r^o = 0.902$ and 0.926 respectively

- Inner Stream Plug Shape

1. Configurations 2 and 4

   $R_r^o = 0.902$, $R_r^i = 0.80$, $A_r = 1.03$
   but inner stream plug shapes are different.

Based on the analysis of test results presented in Subsection 5.1.3, Figure 5-13 or Table 5-4, an immediate evaluation of these geometric parameters is possible on a thrust and density normalized PNL_{max}. This evaluation is presented in Figures 5-40 and 5-41 using the regression prediction equations presented earlier.

Figures 5-40a and b show that for a fixed outer stream radius ratio, R_r^o, increasing area ratio increases the PNL_{max} for a given mixed stream velocity, V_J^{mix}. This effect is greater at higher V_J^{mix} (> 600 m/sec) and greater with higher outer stream radius ratios ($R_r^o = 0.902$ test results in Figures 5-40b).

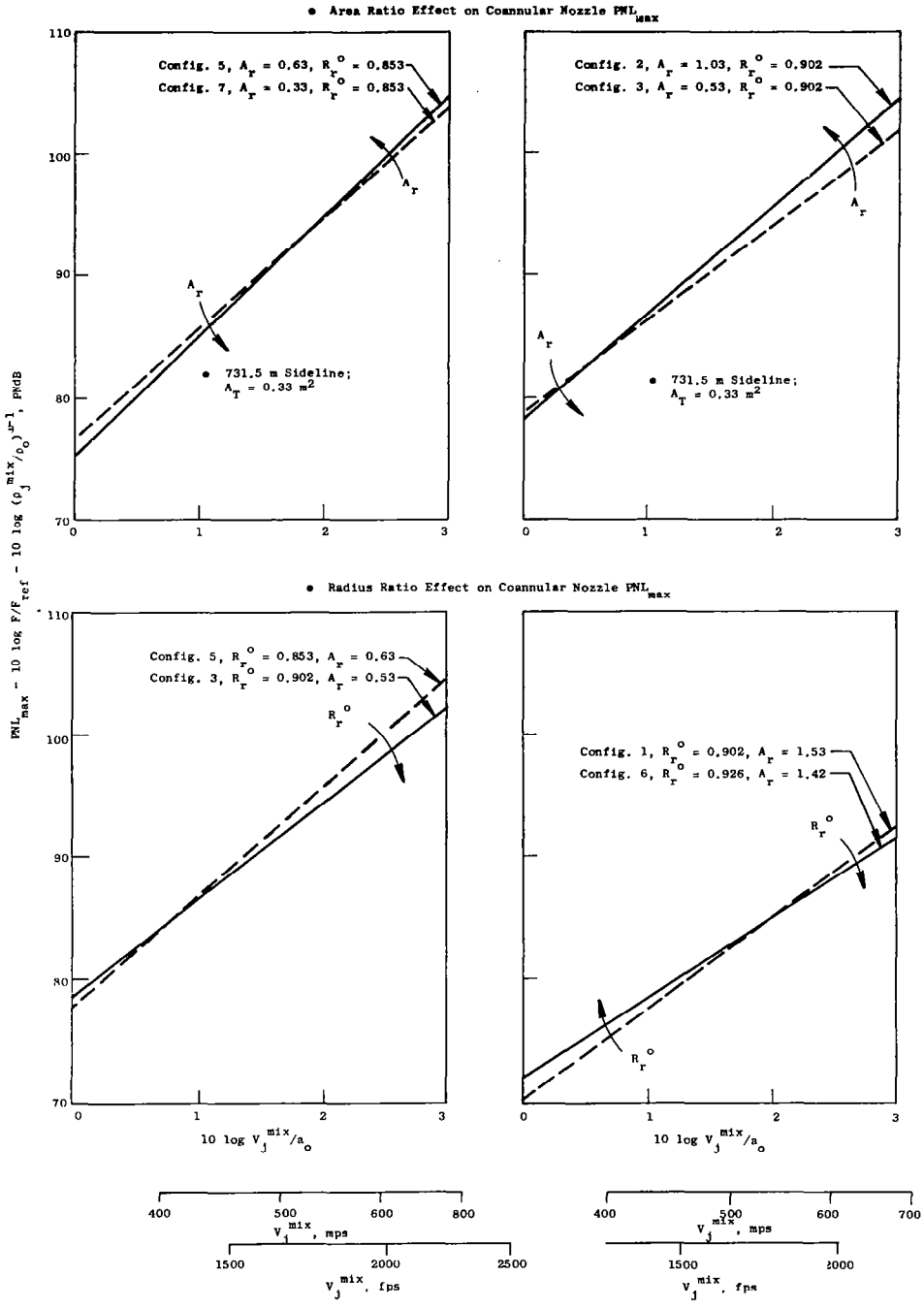

Figure 5-40. Influence of Area Ratio and Outer Stream Radius Ratio on Normalized PNL_{max}.

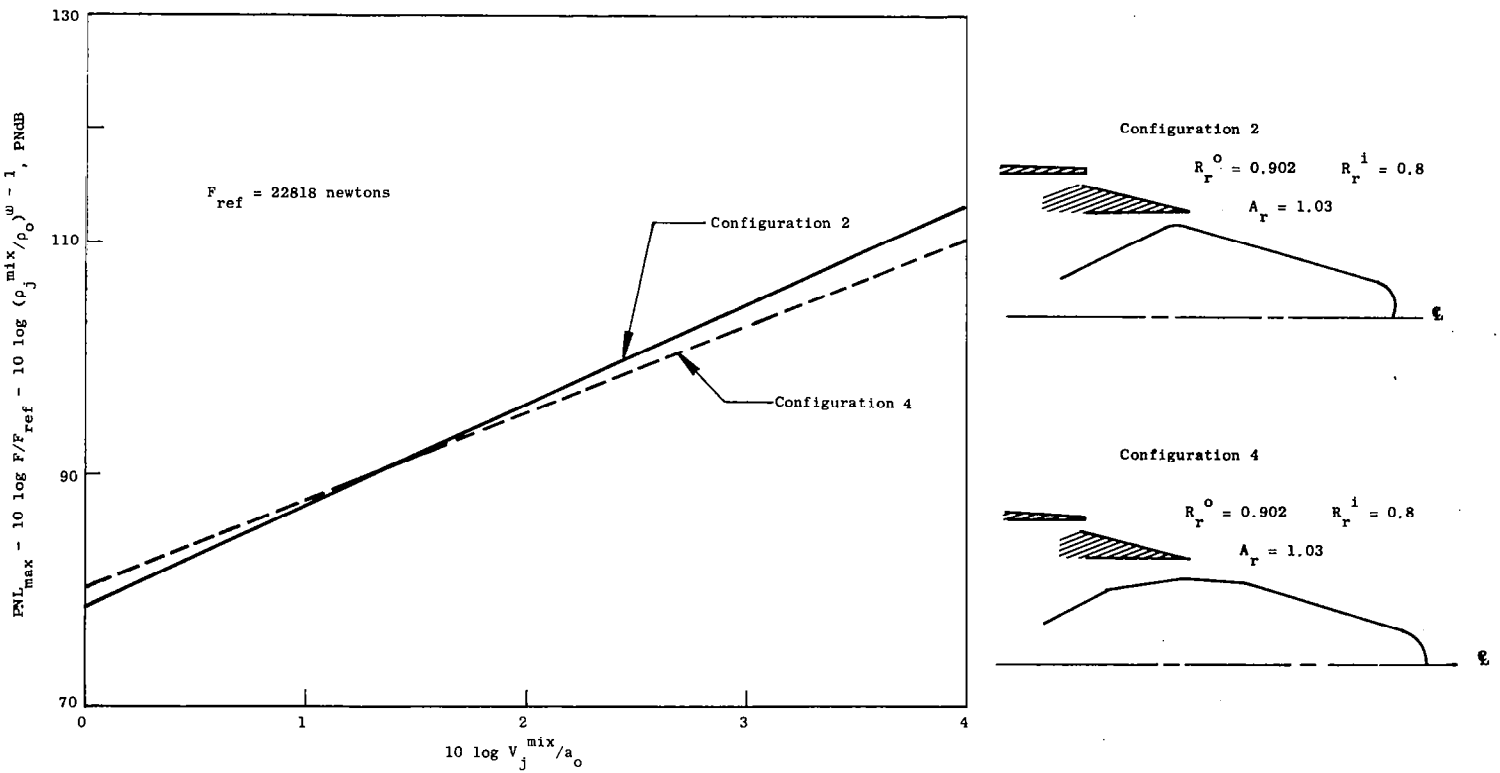

Figure 5-41. Influence of Inner Stream Plug Geometry on Normalized PNL_{max}.

Figures 5-40c and d show that for a fixed area ratio, increasing outer stream radius ratio is beneficial in the high velocity regions (V_j^{mix} > 550 m/sec) and this benefit becomes better at lower area ratios (A_r ~ 0.63 as opposed to A_r ~ 1.53 test results).

Figure 5-41 shows that for a fixed area ratio and radius ratio, the bent inner stream plug is more beneficial than the simple conic plug geometry. As an example, at V_j^{mix} ~ 700 m/sec, the bent plug nozzle configuration is 2 PNdB lower than the same configuration without a bent plug.

Described below are some of the specific test results for directivity and spectral characteristics that correspond to the geometry influences of area ratio and outer stream radius ratio. The specific test point comparisons for the inner stream plug will not be given here*.

5.2.3.1 Influence of Area Ratio on the Acoustic Characteristics of High Radius Ratio Coannular Nozzles with Plug

The results presented in Figure 5-40 and 5-41 are results based on linear regression analysis of all test data for the individual configurations. Discussed in this subsection as well as the others to follow are point-to-point data comparisons to more fully illustrate the test results.

Figure 5-42a and b illustrate normalized PNL_{max} test results for scaled data to 0.33 m^2 at a 731.5 meter sideline distance. Figure 5-42a shows actual data comparison between Configurations 5 and 7 where the outer radius ratio was held to 0.853 and the area ratio was varied from 0.63 to 0.33 respectively. Only data where the mixed velocities were the same were chosen for illustration. Figure 5-42b shows actual data comparisons between Configurations 2 and 3 where the outer radius ratio was held to 0.902 and the area ratio was varied from 1.03 to 0.53 respectively. These results confirm the linear regression equation results presented in Figure 5-40a and b; i.e., an increase in area ratio at a fixed outer stream radius ratio and fixed mixed velocity tends to increase the PNL_{max} noise levels, and this result is greater with the higher outer stream radius ratio configurations.

Figure 5-43 shows test results for scaled PNL directivity and model scale OASPL directivity at a V_j^{mix} ~ 634 m/sec. The test results show that at all angles the higher area ratio data has higher noise levels than the lower area ratio comparison test case. In the forward quadrant, the increase in noise

*Several directivity and spectral cases are given in the companion comprehensive data report, NASA CR-159575. The main conclusion that can be drawn from the test data is that the general noise characteristics for Configurations 2 and 4 are similar except that Configuration 4 is always slighty lower. Since the PNL_{max} curves given in Figure 5-13 show the range of conditions and levels of noise radiated for these configurations, it was decided not to go any further with these presentations.

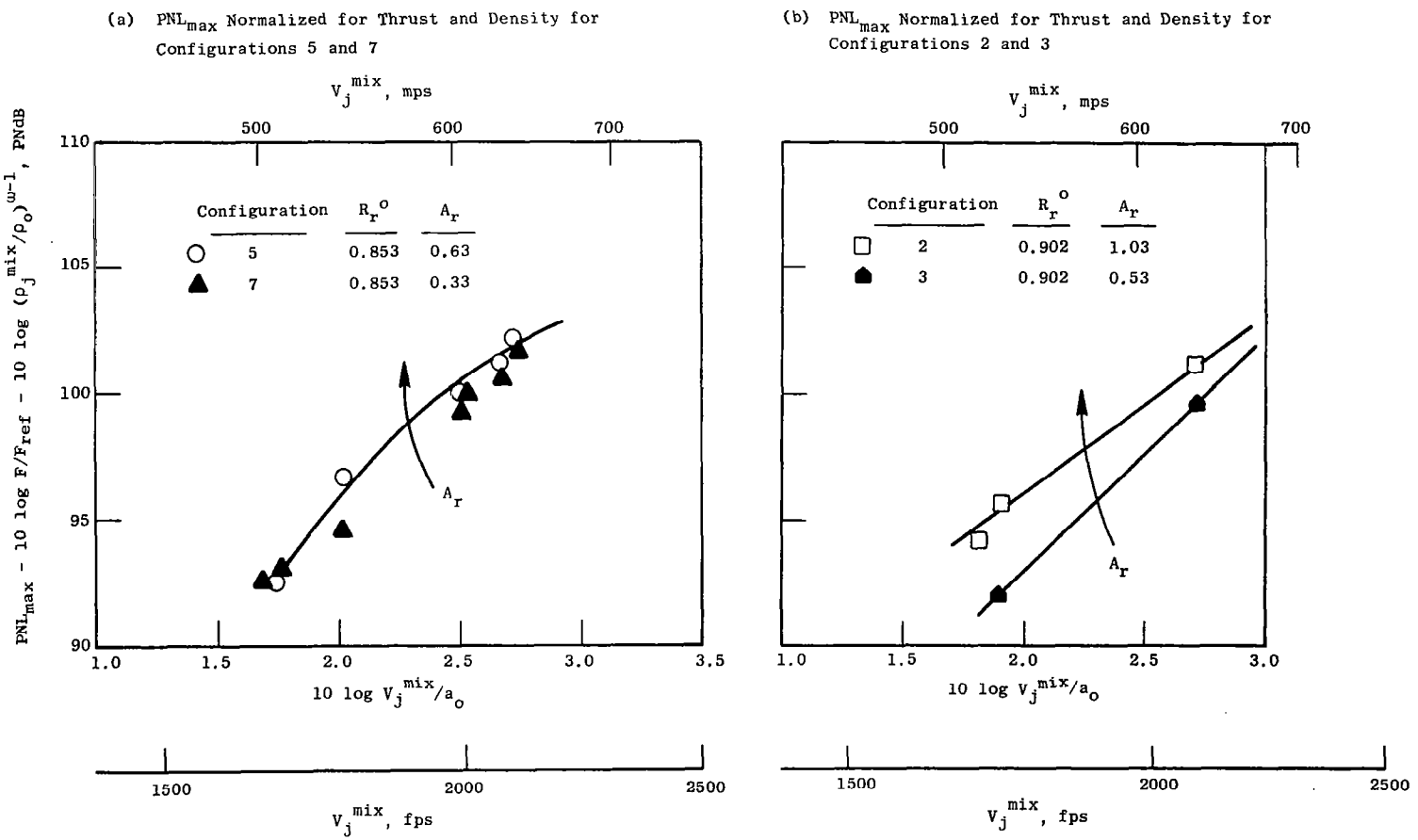

Figure 5-42. Influence of Area Ratio, at a Fixed Outer Stream Radius Ratio, on PNL_{max} at $A_T = 0.33\ m^2$, 731.5 m Sideline Distance for a Range of Mixed Stream Velocities.

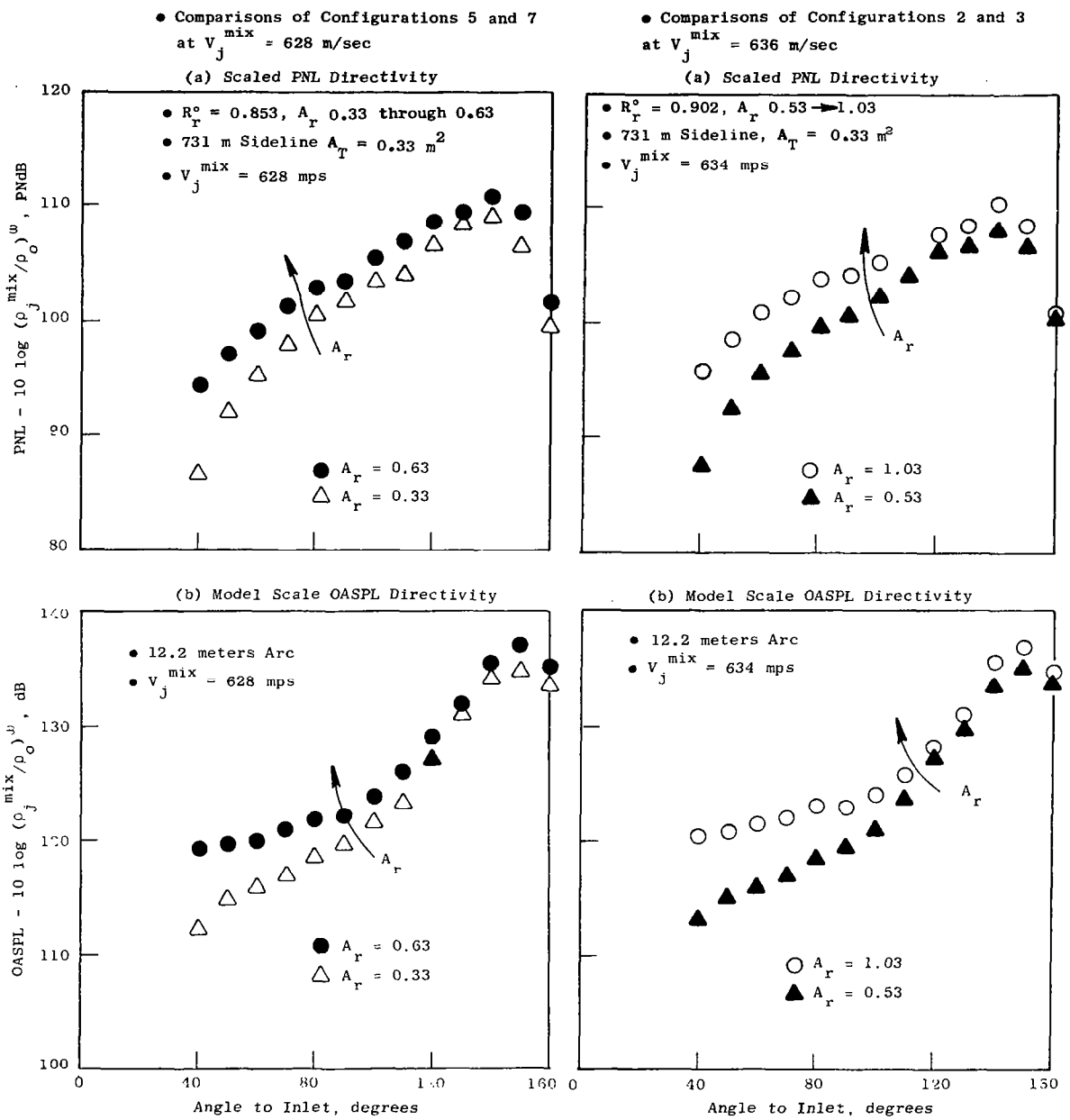

Figure 5-43. Influence of Area Ratio, at a Fixed Outer Stream Radius Ratio, on PNL Scaled at a Sideline Distance and OASPL Model Scale on an Arc Directivity Pattern.

with increasing area ratio result is even more evident. The reason for the larger noise levels in forward quadrant for the higher area ratio configuration is due in part to shock noise effects.

Figure 5-44 shows spectral comparisons for the model scale area ratio SPL spectra tests at θ_I = 50°, 90°, and 130°. At θ_I = 130° the basic difference in spectra occurs in the higher frequencies (f > 3000 Hz). At the higher frequencies, the higher area ratio data is greater than its counter part test configuration at the lower area ratio. At θ_I = 90° and 50°, the shock noise can be considered the primary reason for the difference in data level between the two configurations.

5.2.3.2 Influence of Radius Ratio on the Acoustic Characteristics of Coannular Nozzles with Plug

In a fashion similar to the presentation given above, the data illustrating the influence of outer stream radius ratio at a fixed area ratio and at the same mixed stream velocity will be discussed in this subsection. Figure 5-45 presents data taken for Configurations 3, 5, 6, and 1. These comparisons are used to show the acoustic differences between configurations of approximately the same area ratio, but varying outer stream radius ratio at the same mixed stream velocity. These actual data presentations for PNL_{max} at AT = 0.33 m^2, and a 731.5 meter sideline distance show that a fixed area ratio, increasing radius ratio decreases the noise. This is observed at low area ratios (A_r ~ 0.53 → 0.63) as well as for the high area ratio configurations tested (A_r = 1.42 → 1.53).

Figure 5-46 presents a PNL and OASPL directivity for the test results of Configurations 3 and 5 at a V_j^{mix} = 634 m/sec. Figure 5-47 illustrates this model scale one-third octave-band sound-pressure-level spectra at θ_I = 50°, 90°, 130° for the same test point presented in Figure 5-46. In general, the results found are that at all angles the higher radius ratio configuration has more beneficial acoustic characteristics than the lower radius ratio configuration; at the peak sideline noise angle (θ_I = 130°), the higher radius ratio nozzle reduces the SPL spectra from 1000 Hz on out to 80,000 Hz; the 50° and 90° spectra are contaminated with shock noise for the R_r^o = 0.853 Configuration.

Certainly a very important conclusion to keep in mind from this study is that outer stream radius ratio is a key coannular (or annular) plug nozzle noise reduction parameter; the higher the radius ratio the greater the noise reduction.

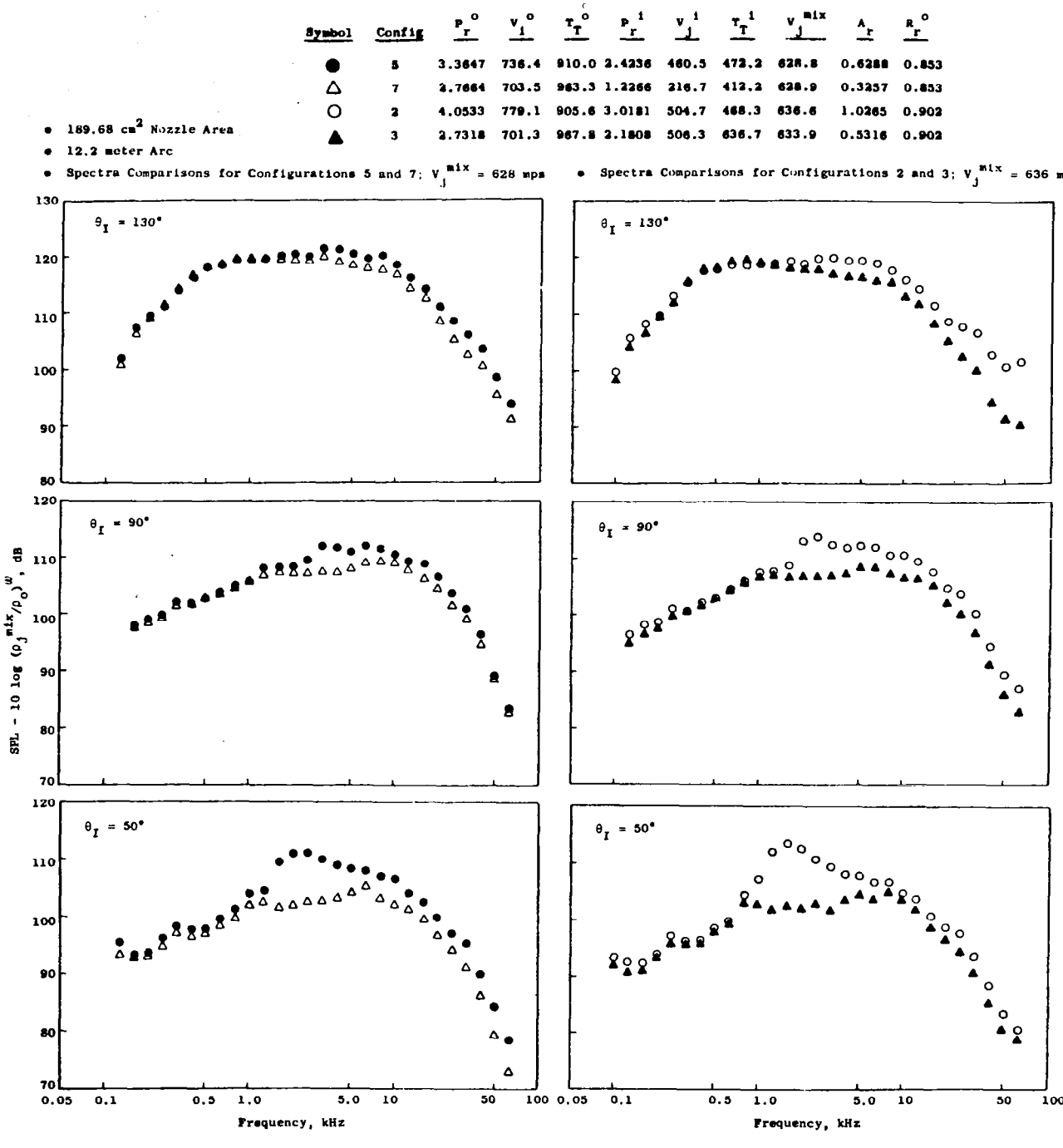

Figure 5-44. Influence of Area Ratio, at a Fixed Outer Stream Radius Ratio, on One-Third Octave Band Sound Pressure Level Spectra at θ_I = 50°, 90°, 130° - Model Scale at A_T = 189.68 cm²; 12.2 m Arc.

Symbol	Config.	R_r^o	R_r^i	A_r
●	3	0.902	0.902	0.5316
▯	5	0.853	0.800	0.6288
◿	1	0.902	0.673	1.5599
⬢	6	0.926	0.800	1.4164

● Data Scaled to A_T = 0.33 m^2; 731.5 m Sideline Distance

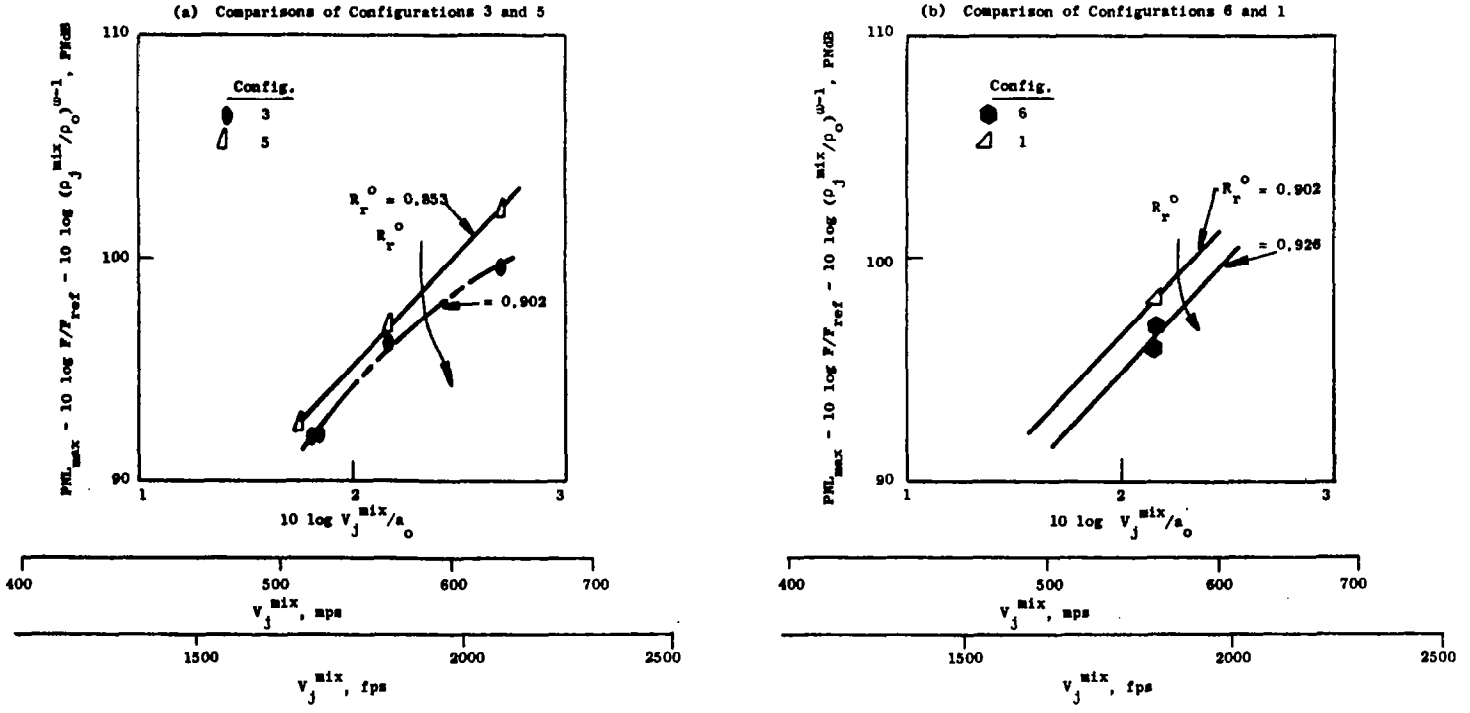

Figure 5-45. Influence of Outer Stream Radius Ratio on Normalized PNL_{max}, Holding Area Ratio Constant, Over a Range of Mixed Stream Velocities, Comparison of Configurations 3 and 5, and 6 and 1.

- Model Size, A_T = 189.68 cm^2, 12.2 meter Arc
- Scaled Data, A_T = 0.33 m^2, 731.5 m Sideline Distance

Symbol	Config.	V_j^o	P_r^o	T_T^o	V_j^i	P_r^i	T_T^i	V_j^{mix}	R_r^o	R_r^i	A_r
○	3	701.3	2.7318	967.8	506.3	2.1808	636.7	633.9	0.902	0.902	0.5316
▲	5	736.7	3.3842	907.2	503.5	2.9369	476.1	635.6	0.853	0.800	0.6288

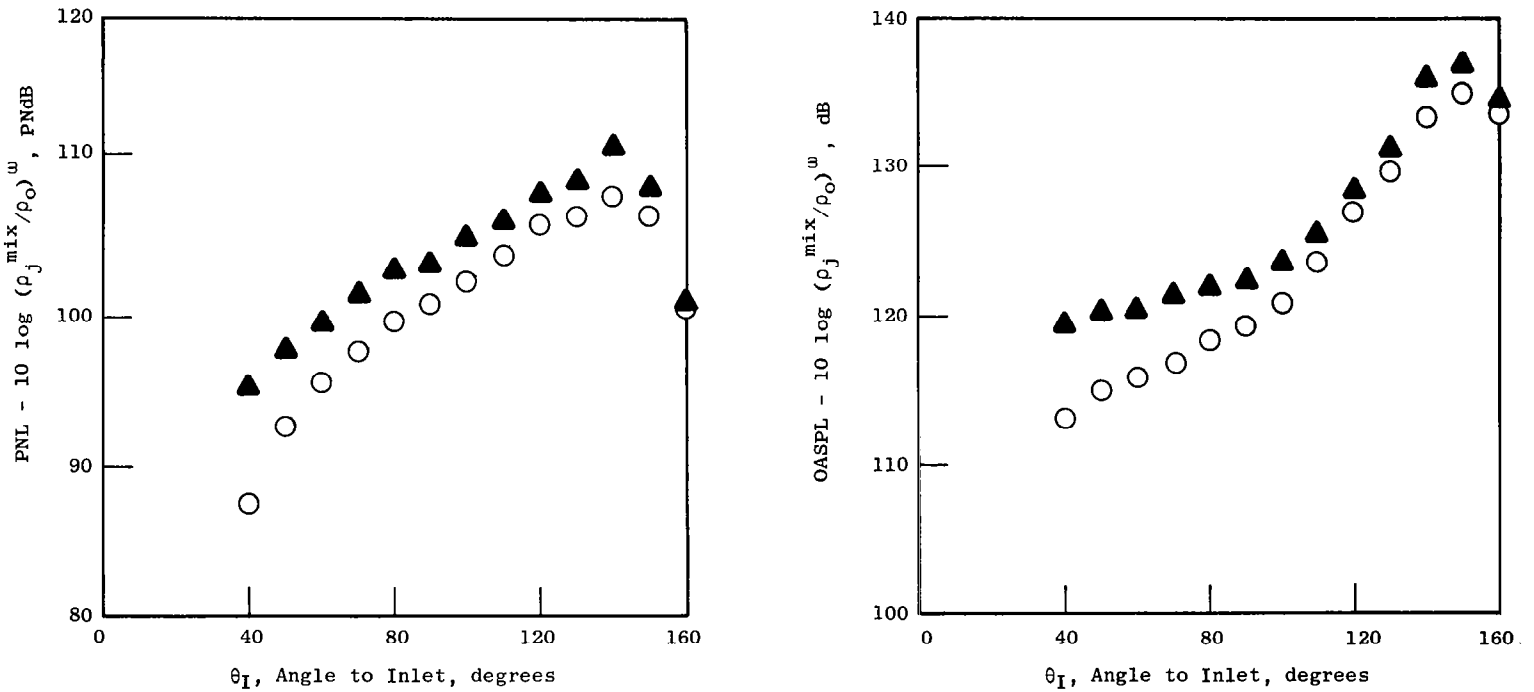

(a) Scaled PNL Directivity

(b) Model Scale OASPL Directivity

Figure 5-46. Influence of Outer Stream Radius Ratio, Holding Area Ratio Constant, for Coannular Nozzles with Plug on Scaled PNL Directivity and Model Scale OASPL Directivity.

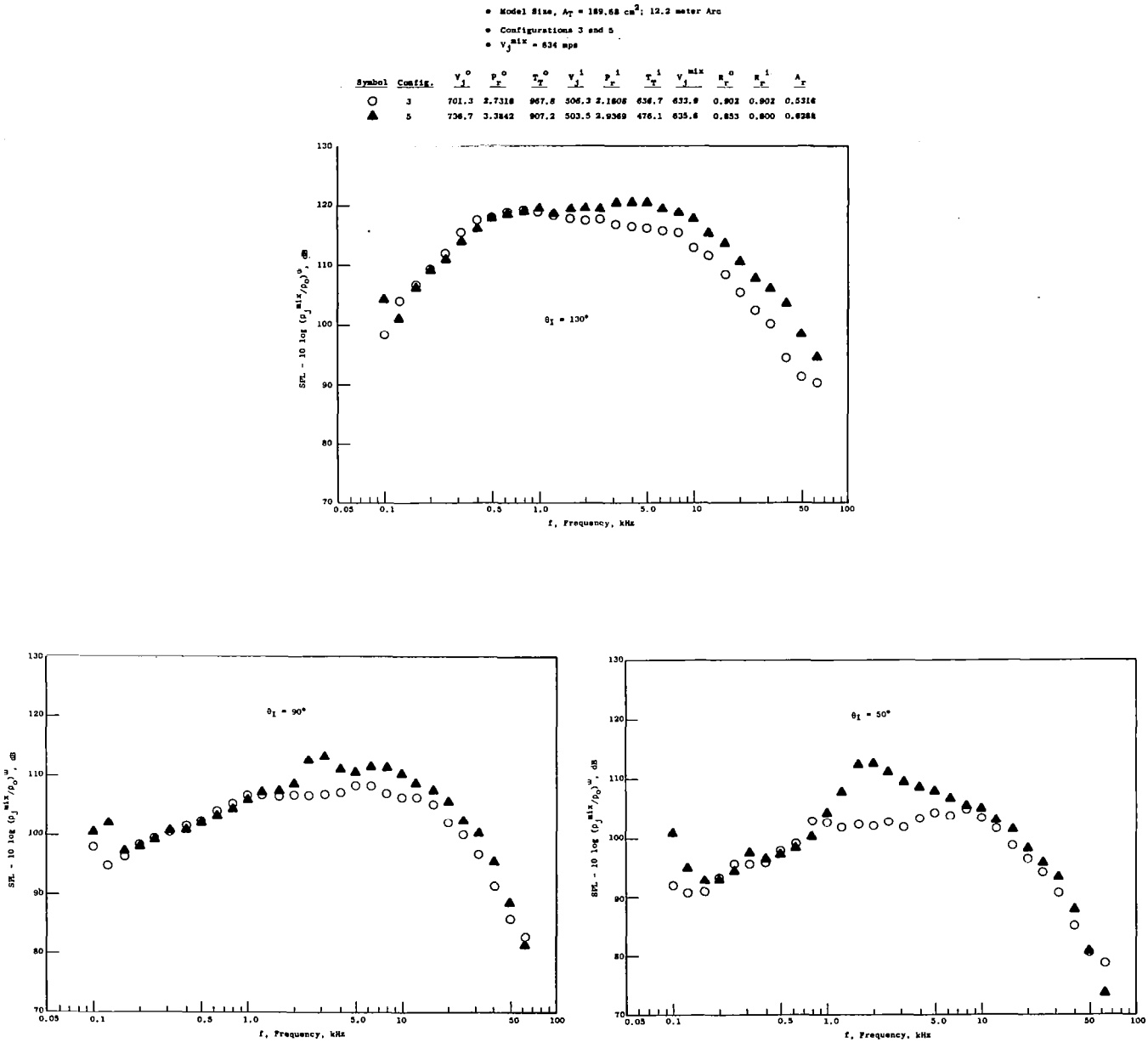

Figure 5-47. Influence of Outer Stream Radius Ratio, Holding Area Ratio Constant, for Coannular Nozzles with Plug on Model Scale One-Third Octave Band Sound Pressure Level Spectra at θ_I = 130°, 90°, 50°, Comparisons for Configurations 3 and 5.

5.3 SHOCK NOISE FOR COANNULAR NOZZLES

In the previous sections the existence of shock noise in the forward quadrant for the coannular nozzles with plug was observed. In light of recent test results (Reference 5-4) which show that shock noise can be amplified (relative to static conditions) in flight, the role of shock noise in the total evaluation of the nozzles acoustic characteristics for coannular flow systems is an important design consideration. Discussed below are some of the static shock noise characteristics observed from measurements taken on this program.

5.3.1 Some Background on Shock Noise Characteristics for Conical Nozzles

Harper-Bourne and Fisher (Reference 5-5) have set down some theoretical and experimental guidelines for estimating the characteristics of broadband shock associated noise for jets operated above critical pressure ratios. Two of the conclusions form the referenced work are:

1. The overall sound pressure levels may be predicted by:

   $$OASPL = 159 + 10 \log (D/R)^2 \beta_j^4$$

   where

   $\beta_j \equiv$ shock strength parameter $(\sqrt{M_j^2 - 1})$

2. The peak shock frequency is given by:

   $$f_p = \frac{U_c}{L\,(1 + M_c \cos \theta_I)}$$

where

U_c = Convection Velocity $(0.7\ V_j)$

L = Shock Separation Distance $(\sim 1.1\ \beta D)$

M_c = Convection Mach Number (U_c/a_o)

These two results imply that shock noise varies as β^4 and that it is omni-directional; further the shock peak frequency observes a Doppler shift. The results also imply that there is no direct density (or temperature) dependence for shock noise (other than through the definition of β). Figure 5-48 illustrates some typical measured conical nozzle shock noise characteristics.

Figure 5-48a illustrates how the OASPL's at $\theta_1 = 50°$ for a conic nozzle are influenced by shock noise for different shock strengths reflected in the shock strength parameter β. As β increases the shock noise is observed to increase substantialy above the jet turbulent mixing noise. Figure 5-48b

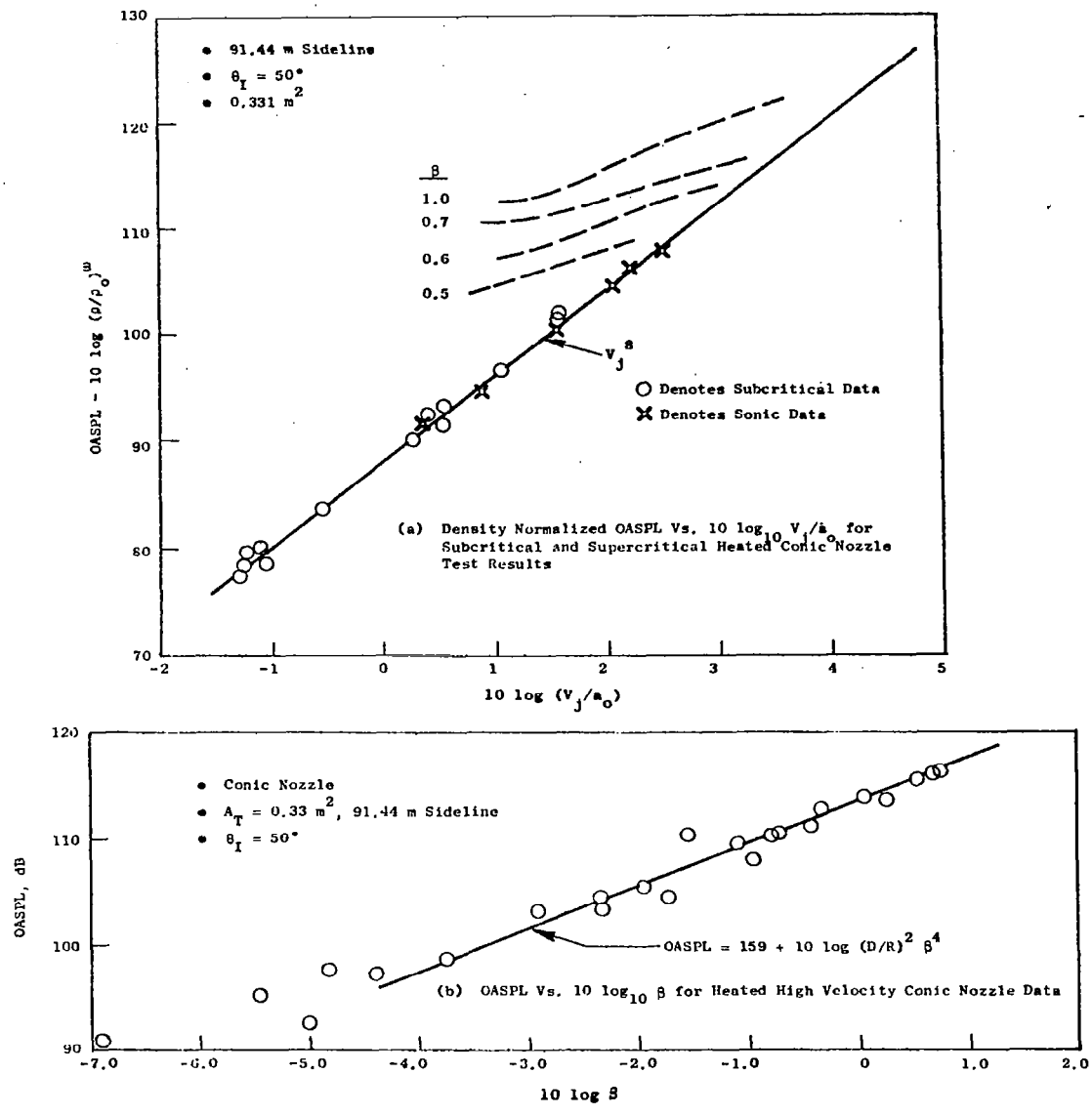

Figure 5-48. Typical Conical Nozzle Data Illustrating the Influence of Shock Noise in the Forward Quadrant.

shows OASPL levels for a conic nozzle at $\theta_I = 50°$ over a range of β compared with the prediction formula given above. The prediction formula is found to be quite good for these heated jet noise test results.

5.3.2 Typical shock Noise Results for High Radius Coannular Nozzles with Plug

When dealing with coannular flow streams the selection of the characteristic parameters which influence shock noise comes into question as did the selection of the characteristic velocity for the peak angle jet noise. When we view Schlieren photographs of coannular systems, for conditions typical of those tested in this program, a very complicated shock structure is observed. There exists a series of shocks associated with the outer stream, the inner stream, as well as larger shock systems down stream which appear associated with the total (or mixed) flow stream conditions. Following the results of jet turbulent mixing noise evaluation, the mixed stream properties (velocity and static temperature) are also selected to illustrate the shock strength parameter β. For OASPL predictions, the equivalent diameter associated with the total area of the coannular nozzle systems is used.

5.3.2.1 Typical OASPL and PNL Shock Noise Levels for High Radius Ratio Coannular Nozzles with Plug

Figure 5-49 illustrates measured model scale (A_I = 189.68 cm^2, 12.2 meter arc) test results of OASPL at an acoustic angle to the inlet, θ_I, of 50° versus the independent variable 10 log β_J^{mix}; where $\beta_J^{mix} \equiv \sqrt{(M_J^{mix})^2 - 1)}$. Test results for all the coannular nozzle configuration where $M_J^{mix} > 1,0$ are shown, as well as conic nozzle test results. There are several observations which can be made from these test results. The first is that the shock strength parameter, β_J^{mix}, seems to be a representative shock noise correlating parameter for coannular nozzles, rather than either of dual stream pressure ratios. When some of the OASPL directivity results were first examined for tests where the outer pressure ratio was fixed and the innr stream pressure ratio was varied, or vice versa, it appeared that inner pressure ratio was a strong shock noise parameter, and that there existed a substantial geometry effect. A close examination of the results shown on Figure 5-49 revealed that on a configuration by configuration basis it was β^{mix} that was the correlating parameter. The next observation is that for $M_J^{mix} > 1.18$ the coannular nozzles data is generally seen to be 7 - 9 dB lower than the conic nozzle. Table 5-7 shows results of a linear regression analysis for each of the coannular nozzles separately, the conic nozzle data and for all the coannular nozzle test results. The regression analysis shows that when all the data is used a $(\beta_J^{mix})^4$ power law is obtained; a result close to that predicted by the conic nozzle results of Reference 5.5. A general prediction equation found for high radius ratio coannular nozzles is:

OASPL High Radius Ratio Coannular Nozzles with Plug $= 152 + 10 \log (D/R)^2 \, (\beta_J^{mix})^4$

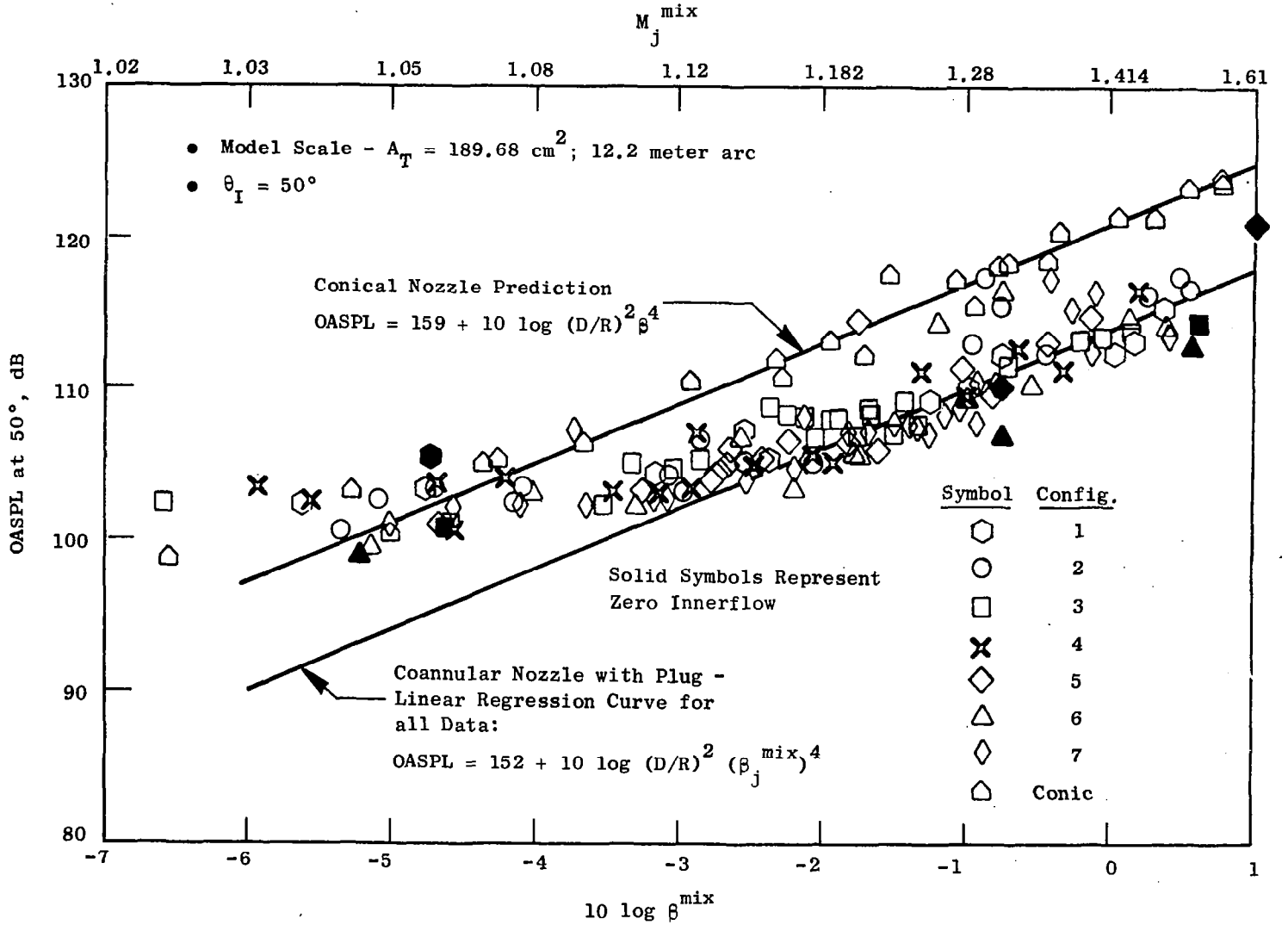

Figure 5-49. Coannular Nozzle Shock Noise Levels Compared with a Conic Nozzle.

Table 5-7. Linear Regression Analysis of Shock Noise OASPL for High Radius Ratio Coannular Nozzles with a Plug.

Prediction form*: $OASPL = a + 10 \log (D/R)^2 (\beta_j^{mix})^b$

Configuration	a	b	$\sigma_{y/x}$
1	151.53	3.187	1.595
2	153.17	4.799	0.3478
3	151.62	3.388	0.8746
4	152.82	4.524	1.74
5	153.71	5.281	1.0307
6	150.45	3.336	1.8288
7	152.63	4.777	1.2585
All Data	152.08	4.084	1.4162
Conic	158.81	3.6	1.2412

*
- $\theta_I = 50°$
- Analysis performed in Model Scale Test Data: $A_T = 189.68$ cm^2; 12.2 meter Arc
- Only results where $M_j^{mix} \geq 1.18$ were used in the Regression Analysis.
- The OASPL's used were the total levels measured at the 50° microphone location. No attempt was made to subtract or adjust for any possible jet mixing noise references.

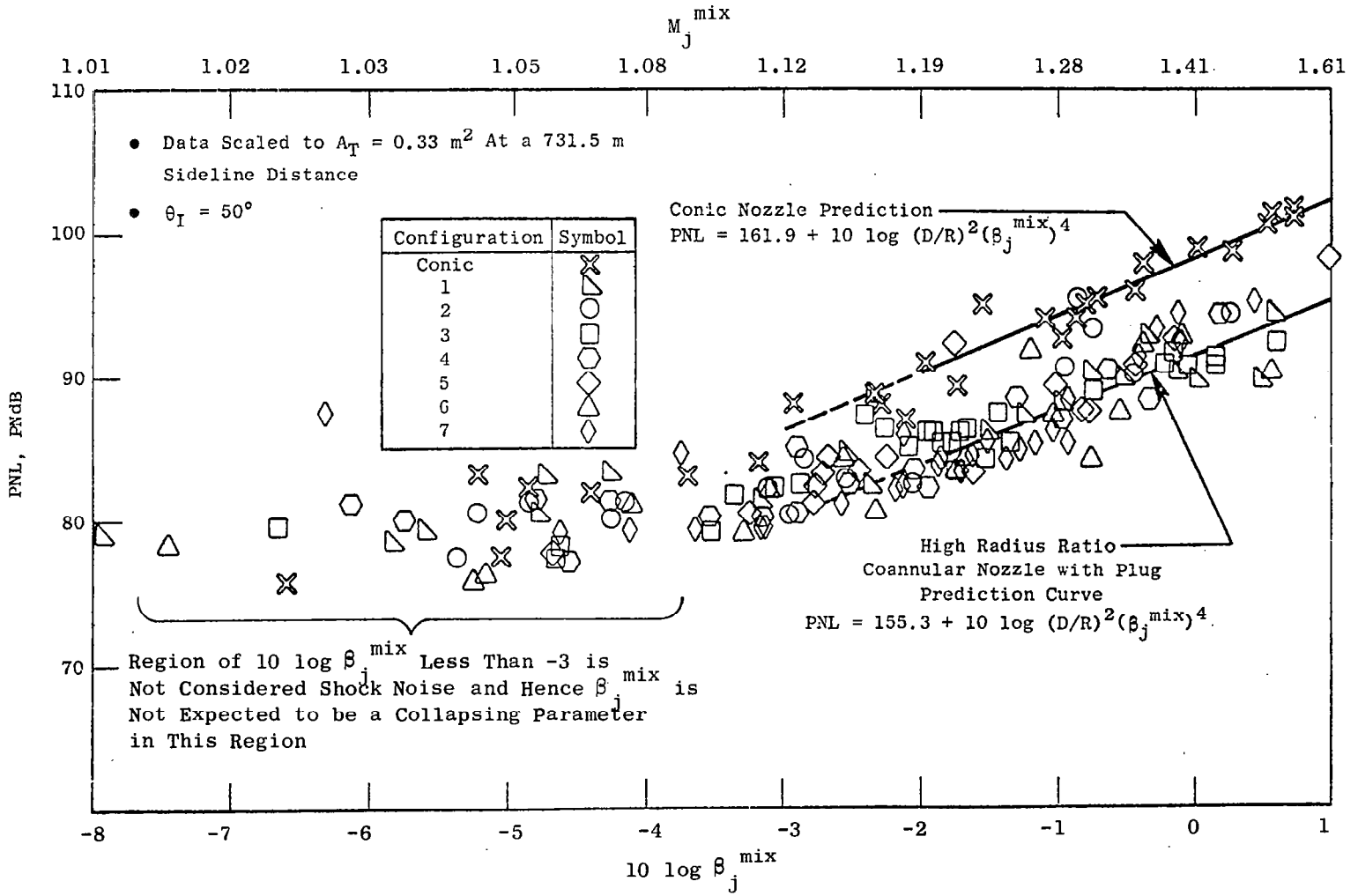

Figure 5-50. High Radius Ratio Coannular Nozzle with Plug Shock Noise Comparison with a Conic Nozzle on a PNL Basis.

Table 5-8. Linear Regression of Shock Noise PNL for High Radius Ratio Coannular Nozzles with a Plug.

Prediction Form*: $PNL = a + 10 \log (D/R)^2 (\beta_j^{mix})^b$

Configuration	a	b	$\sigma_{y/x}$
1	154.79	3.108	1.132
2	157.79	4.553	2.866
3	154.27	3.005	0.948
4	155.87	4.636	1.886
5	156.48	4.121	3.039
6	153.73	3.0	2.768
7	156.07	5.213	1.351
All Coannular Nozzles Data	155.32	3.912	2.057
Conic	161.88	4.058	1.185

*
- $\theta_I = 50°$
- Analysis performed on data scaled to $A_T = 0.33\ m^2$; at a 731.5 meter sideline distance
- Only results where $M_j^{mix} \geq 1.18$ were used in the Regression Analysis.

where the characteristic dimension, D, used here was the equivalent diameter of the total area A_t = 189.68 cm^2.

To show that the coannular nozzle noise reduction is maintained on a PNL basis, the PNL test results for all the supercritical coannular nozzle tests and conic nozzle tests at $\theta_I = 50°$ are presented in Figure 5-50. Table 5-8 summarizes the regression analysis performed on each configuration. In summary, the PNL test results at $\theta_I = 50°$ show that:

$$PNL^{Conic} \simeq 161.9 + 10 \log (D/R)^2 \beta_J^4$$

$$PNL^{All\ Coannular} \simeq 155.3 + 10 \log (D/R)^2 (\beta_J^{mix})^4$$

where D, is the equivalent dimeter based on the total area for the conic and coannular nozzles. Hence the coannular nozzles with plug are observed to have a natural 6.6 PNdB static shock noise reduction in the forward jet quadrant of observation. A study of whether the connular nozzle shock noise is omnidirectional as proposed in Reference 5-5 was not carried out at this time. Future plans for the evaluation of shock noise will however consider this directivity property more closely.

The last observation is that for certain test points the shock noise for the coannular nozzle had OASPL and PNL levels as high as the conic nozzle data for the same shock strength. This result occurred for Configurations 2, 5 and 6 when the inner stream pressure ratio, P_T^i, was at relatively high value ($P_T^i > 3.0$), and when $P_T^i > P_T^o$. These configurations are also the configurations which have the largest inner stream annular areas of the configurations tested.

5.3.2.2 Typical Shock Noise Directivity and Spectra for High Radius Ratio Coannular Nozzles with Plug

To illustrate the directivity patterns for the coannular nozzle configurations, Figure 5-51 shows the PNL directivity patterns (at A_T = 0.33 m^2; 731.5 meter sideline distance) for Configurations 2 through 7 at a shock strength parameter, $\beta_J^{mix} \sim 0.83$ as compared to a conic nozzle. The results presented are normalized with respect to ideal thrust, the mixed density, and to V_J^{mix} = 609 m/sec . The results show that generally, in the aft quadrant, the high radius ratio coannular nozzles with plug enjoy a PNL noise reduction similar to the PNL noise reduction in the forward quadrant. The specific results show that, dependent on which configuration is considered, reductions of 0 to 7 PNdB are found. Particularly, Configurations 2 and 6 show no shock noise reduction benefits for this comparison case. The results presented in Figures 5-49 and -50 also show that coannular nozzle shock noise levels could be as high as conical nozzle shock noise levels. Examination of the data on a configuration by configuration basis leads to the conclusion that the general trend for coannular nozzles is to have shock noise levels substantially lower than the conic, and the preliminary

- Scaled Data: A_T = 0.33 m^2; 731.5 meter Sideline Distance
- V_{ref} = 609.6 mps; F_{ref} = 22,818 Newtons

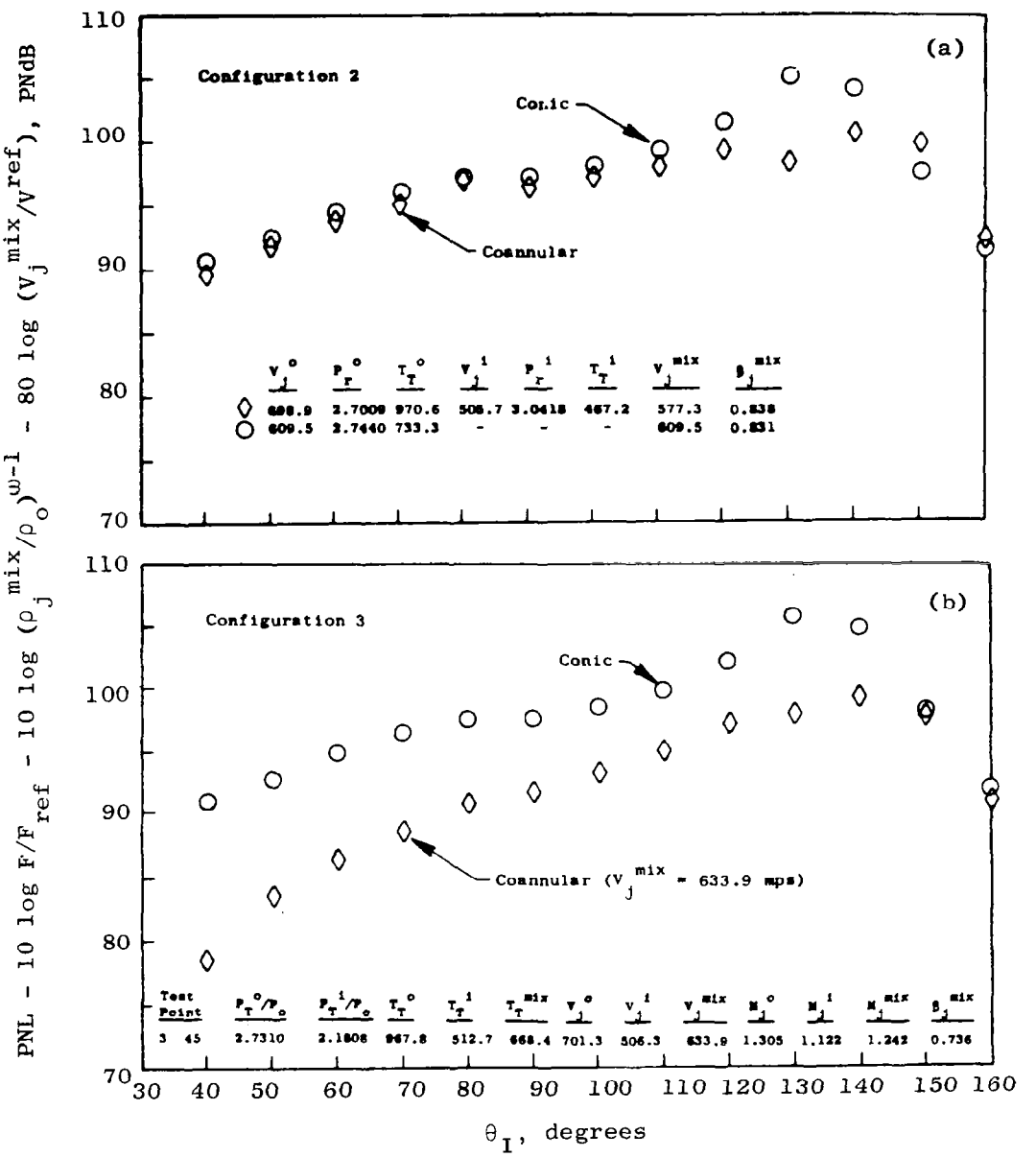

Figure 5-51. Normalized PNL Directivity of High Radius Ratio Coannular Nozzles with Plug at β_j^{mix} = 0.83 Compared with Conic Nozzle Data for Shock Noise Evaluation.

- Scaled Data: A_T = 0.33 m^2; 731.5 meter Sideline Distance
- V_{ref} = 609.6 mps; F_{ref} = 22,818 Newtons

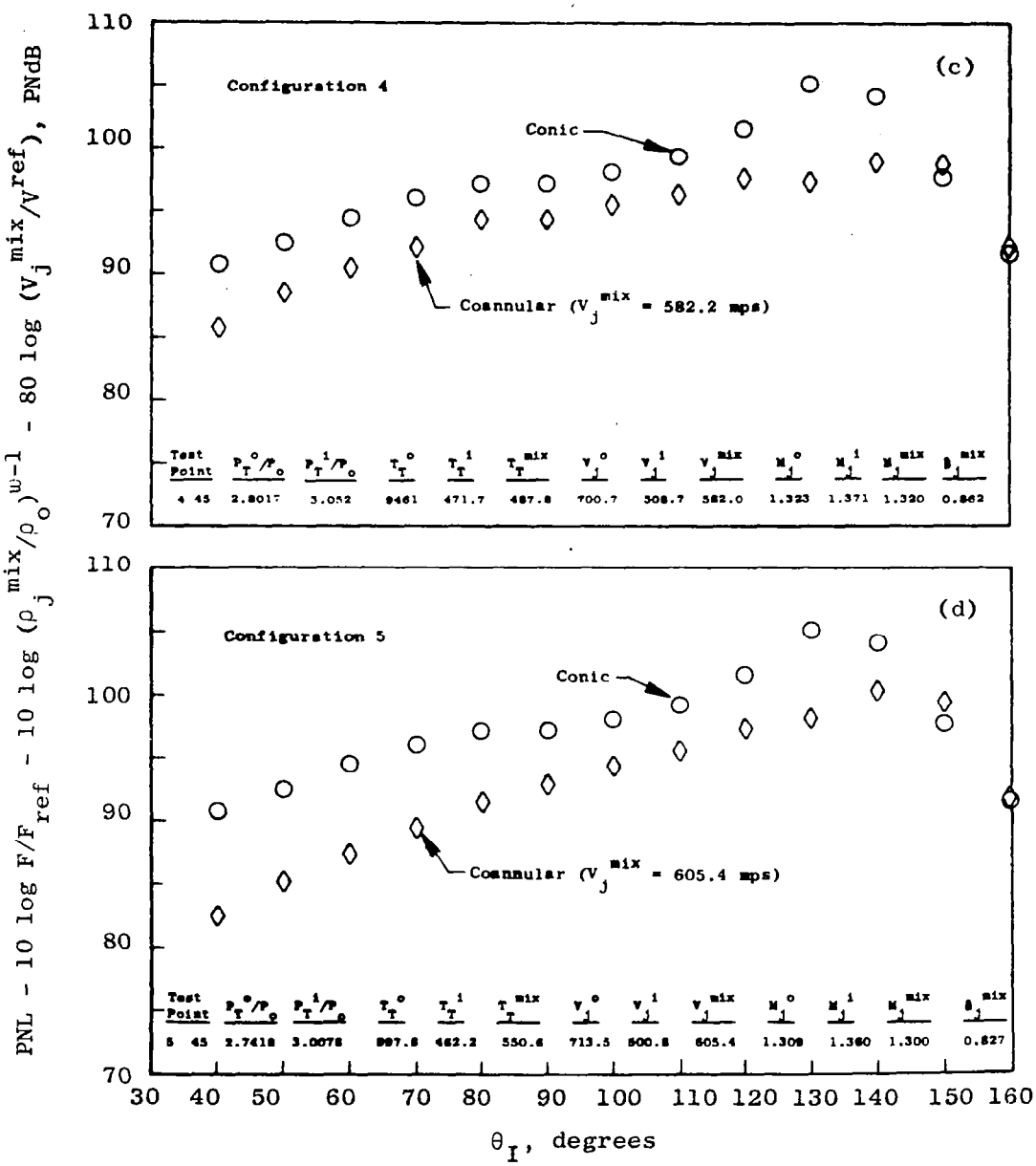

Figure 5-51. Normalized PNL Directivity of High Radius Ratio Coannular Nozzles with Plug at β_j^{mix} = 0.83 Compared with Conic Nozzle Data for Shock Noise Evaluation (Continued).

- Scaled Data: A_T = 0.33 m^2; 731.5 meter Sideline Distance
- V_{ref} = 609.6 mps; F_{ref} = 22,818 Newtons

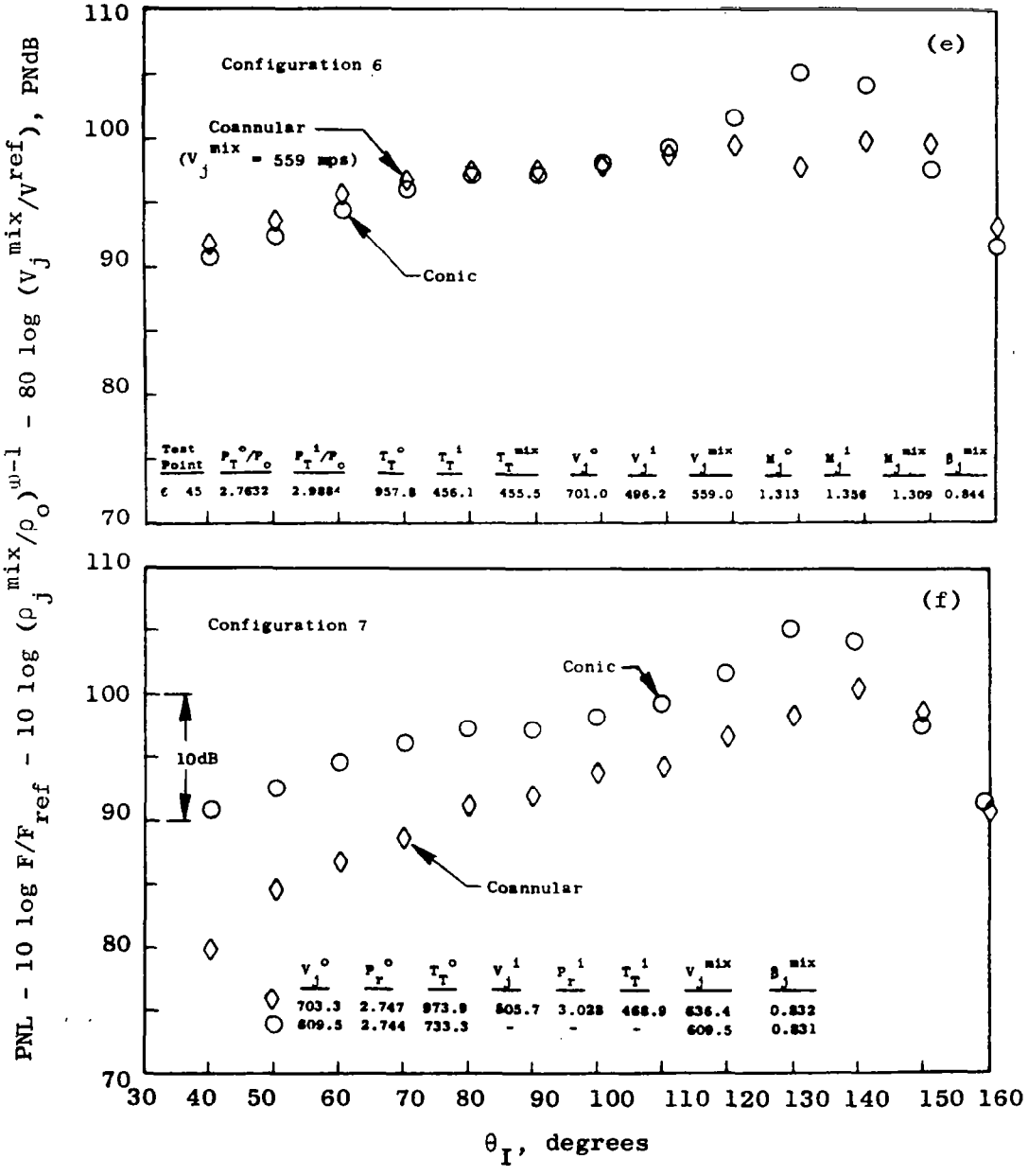

Figure 5-51. Normalized PNL Directivity of High Radius Ratio Coannular Nozzles with Plug at β_j^{mix} = 0.83 Compared with Conic Nozzle Data for Shock Noise Evaluation (Concluded).

prediction equations given on Figures 5-49 and -50 are representative of the basic shock noise level trends for coannular nozzles. Nonetheless, the occurrence of the high shock noise levels is of concern, particularly with regard to the practical design and cycle point selections for coannular nozzle applications. A preliminary rule-of-thumb to use in avoiding the unusually high coannular nozzle shock noise levels at the same shock strength level, β_{mix}, is to keep the pressure ratios of the dual streams as low as practical (below 3.0 seems to be representative) and not to operate at $P_r^i/P_r^o > 1$ at the high pressure ratios approaching 3.0.*

Figure 5-52 illustrates model scale (A_T = 189.68 cm^2, on a 12.2 meter arc) one-third octave-band spectra at $\theta_I = 50°$ for the same test points discussed above and presented in Figure 5-51. For some of the configurations (Configurations 3, 5, and 7) there appear to be two spectral peaks - a low frequency peak and a high frequency peak. This may be indicative of the notion that since both flows are at supercritical conditions, one may be associated with the outer stream and one may be associated with the inner stream. A full analysis to determine which stream may contribute to which part of the shock noise spectrum has not been performed to date. A preliminary observation is that the low frequency peak seems to be characterized by a dimension close to the equivalent diameter of the total area - suggestive of the shock pattern after the flows have initially mixed. The high frequency peak seems to be characterized by the outer stream annulus height - suggestive of the outer stream shock pattern. This observation needs additional clarification and analysis based on narrowband data, and a more thorough examination of the shock structure parameters indicative of coannular jets rather than simple conic nozzle jet flows.

Configurations 2 and 6, which are the configurations which showed no shock noise reduction benefits at the β_J^{mix} selected, indicate that the low frequency peak is considerably amplified compared to the high frequency peak. If the observation made above (the low frequency peak is governed by the mixed stream shock pattern) is correct, the criterion for shock noise control for coannular nozzle systems may lie in a more careful examination of the flow and geometry designs which drive downstream shock patterns.

5.3.3 Summary Remarks on Coannular Nozzles

In general, the results have shown that high radius ratio coannular nozzles with plugs reduce shock associated broadband noise. Up to 7 PNdB reduction has been observed relative to a conic nozzle. The characteristic parameter for establishing the level of shock noise was found to be a mixed stream shock strength parameter, β_J^{mix}, ($\beta_J^{mix} \equiv \sqrt{(M_J^{mix})^2 - 1}$). Regression analysis has shown that OASPL and PNL are proportional to 10 log $(\beta_J^{mix})^4$. The spectral

*The guideline given here is meant to be a caution. The rationale for the loss of shock noise reduction in this region ($P_r^i/P_r^o > 1$; $P_r^i > 3.0$) has not been sorted out. And in fact does not always occur. If operation in this region is necessary care must be taken so that the available shock noise relief from coannular plug nozzles is realized.

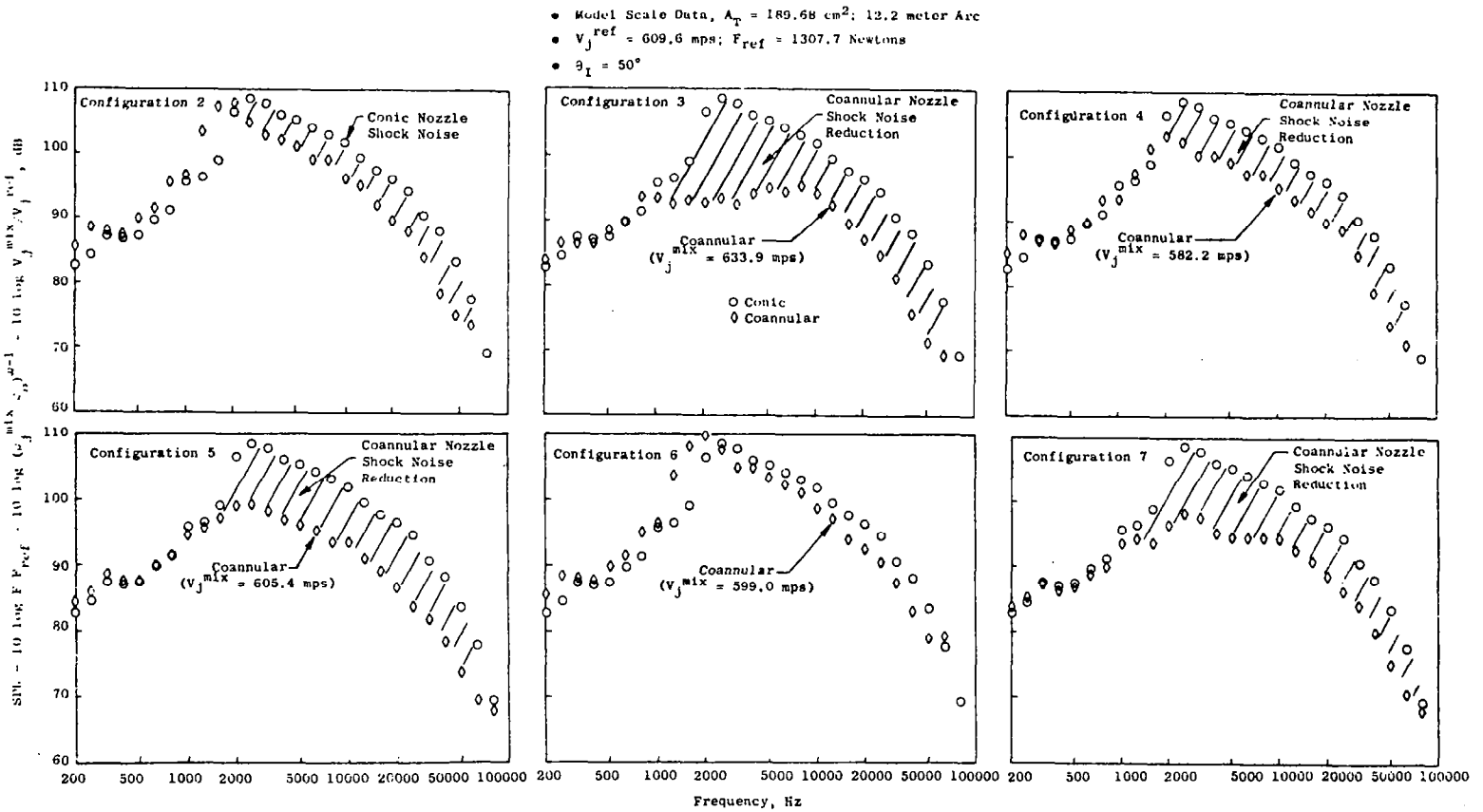

Figure 5-52. Normalized One-Third Octave Band Shock Spectra for High Radius Ratio Coannular Nozzles with Plug at β_j^{mix} = 0.83 Compared with Conic Nozzle Data. (Test Conditions are Identical to Those Given in Figure 5-51).

composition of high radius ratio coannular nozzle noise is probably constructed from the noise radiated by the complex shock patterns emitted from the outer stream, inner stream, and mixed flow streams. A preliminary observation is that there exists a low frequency shock noise peak associated with the mixed stream flow and the characteristic dimension D, based on the equivalent diameter of the total area; and a higher frequency shock noise peak associated with the outer stream flow and characteristic dimension of the outer stream annulus height. At times the coannular nozzle can radiate shock noise of the same amplitude as a conic nozzle at the same shock strength parameter. When this occurs it may be due to the mixed stream shock patterns. A rule-of-thumb seems to be to keep both of the coannular stream pressure ratios below 3.0, and at $P_T^i/P_T^o < 1$ when approaching the high pressure ratio regions.

6.0 AERODYNAMIC PERFORMANCE TEST RESULTS

The results presented in this section represent a summary of the wind tunnel aerodynamic performance test measurements taken as part of this program. A more detailed discussion of the aerodynamic test results are contained in a separate report issued under this program (Reference 3-3).

6.1 DATA QUALITY

Prior to testing the high radius ratio coannular nozzles with plug in the 8 x 6 foot tunnel, a Supersonic Tunnel Association (STA) model was run as a means of investigating the force and weight flow measurement accuracy of the facility as built up for this test. The STA model assembly is shown in Figure 6-1. The model had a 10.16 cm diameter throat and a 20.32 cm maximum outside diameter, corresponding to the 20.32 cm maximum outside diameter of the plug-nozzle models. Air could be supplied to the STA model using either the outer or inner flowpath as shown in Figure 6-2. The tests were conducted with air supplied through either the 3.1699 cm diameter meter for the outer nozzle air supply or with air supplied by the larger of the two inner flowmeters, which was 2.8951 cm in diameter. The smaller of the two inner flowmeters was not run with the STA model because sufficient air to choke the STA model could not be supplied. This did not compromise the completeness of the facility checkout with the STA nozzle because the small meter was used only to meter the flow for the low inner flow test points, where the flow rates ranged from 1% to 6% of the outer flow. Small errors in making this measurement could not affect the results.

The yardsticks against which the STA measurments were compared in order to determine the facility thrust and flow measurement accuracies were calculated values of STA thrust coefficient, flow coefficient, and dimensionless stream thrust parameter for the static tests and previous measured values for wind-on testing. The calculated static values are derived from semiempirical methods of calculating standard ASME long-radius nozzle performance, as described in Reference 3-3. These ASME equations are slightly modified to include the effect of a small difference in length of the internal flowpaths between the ASME and STA nozzles. The resulting equations, for nozzle pressure ratios equal to or greater than 1.89, are as follows:

$$C_D = 1 - 0.241\ RN^{-0.2}$$

$$C_V = 1 - 0.143\ RN^{-0.2}$$

$$f_g = G\ (1 + 1.4\ C_D)\ (0.52828)$$

where $G = 1.00012 + 9.9112 \times 10^{-6} \times P_T$; C_V is the peak thrust coefficient; and RN is the Reynolds Number. These methods are based on a large number of data and give the best possible determination of the actual static STA nozzle performance parameters. For the wind-on tests, the data are compared to previous results on the same STA model in the NASA Lewis 8 x 6 foot tunnel using different flowmetering and force measuring hardware. These previous tests are reported in Reference 6-1.

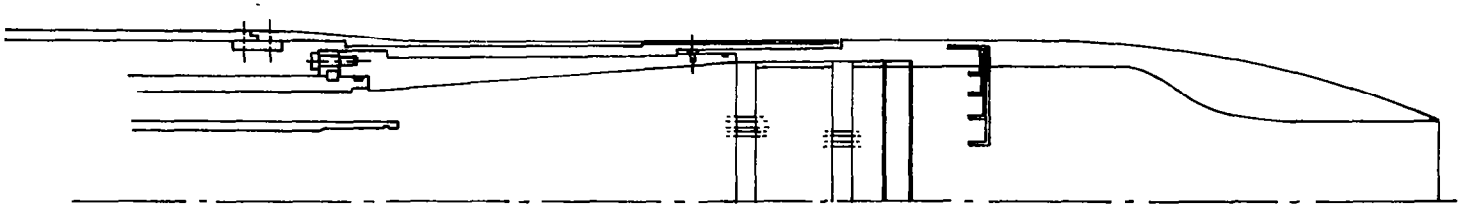

Figure 6-1. Supersonic Tunnel Association Model Assembly.

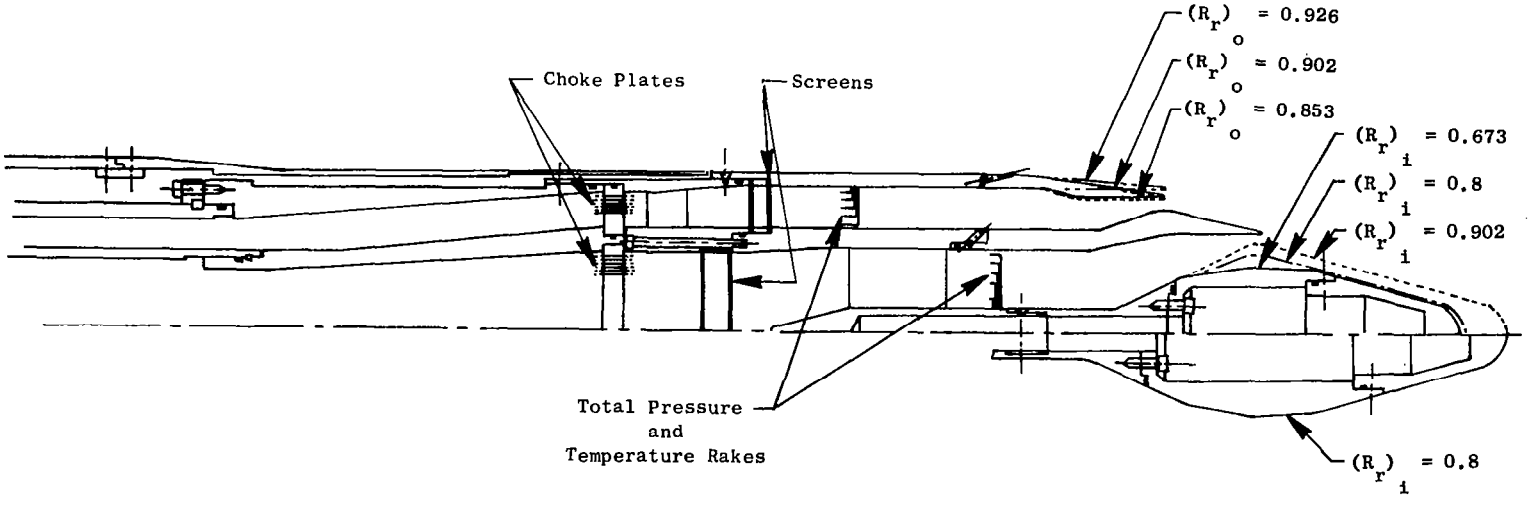

Figure 6-2. Schematic of Model Assembly.

Comparisons of the measured static thrust and flow coefficients and stream thrust parameter with the calculated values are shown in Figure 6-3 for the 3.1699 cm and 2.8951 cm diameter meters respectively. Figure 6-4 compares the measured thrust coefficient to previous test results at Mach numbers of 0.36, 0.40, and 0.45. Agreement between the measured values and the calculated or previously determined data is good, as in the repeatability of the data (5-8 static points and two wind-on points were taken at most nozzle pressure ratios). Repeatability of the wind-on data seemed to be better than the static data, possibly due to the increased tunnel vibration which would reduce hysterisis in the support bearings.

The number of repeat points taken at static conditions allowed a statistical evaluation of the data. Standard deviations and the bias of the mean-value of the data from the "known" or calculated value were calculated by the following equations:

$$\text{Standard Deviation} = \left(\sum_i (X_i - \overline{X})^2/(n-1) \right)^{1/2}$$

$$\text{Bias} = \overline{X} - m$$

where

X_i = individual measured value of the parameter (e.g. thrust coefficient or flow coefficient)

$\overline{X}$ = mean of measured values of the parameter

m = known value of parameter

n = number of samples taken of the given parameter

Standard deviation calculations were made at each pressure ratio for which repeat points were taken. Bias calculations were made at each pressure ratio above 1.89 for which repeat points were taken, as the calculation procedure for the known values does not apply below this pressure ratio. The procedure for taking repeat points was to set each data point once in the order of increasing nozzle pressure ratio and then repeat each point going down in pressure ratio, the air shut off, and the process then repeated. In some instances either wind-on data or data using the other flowmeter were run in between repeating cycles.

The results of these calculations are shown in Figure 6-5 for the thrust coefficient and flow coefficient, respectively. The thrust coefficient deviation and bias were dependent on the magnitude of the nozzle thrust being measured by the force balance and are plotted as such in Figure 6-5a. The flow coefficient parameters are shown as a function of the flowmeter total pressure over the range for which STA data were taken. The upper limit to the STA model airflow and force balance loading was the maximum supply pressure at the venturies, approximately 276-290 N/cm^2. Based on these results, the data accuracy and repeatability was felt to be generally better than ±0.5%.

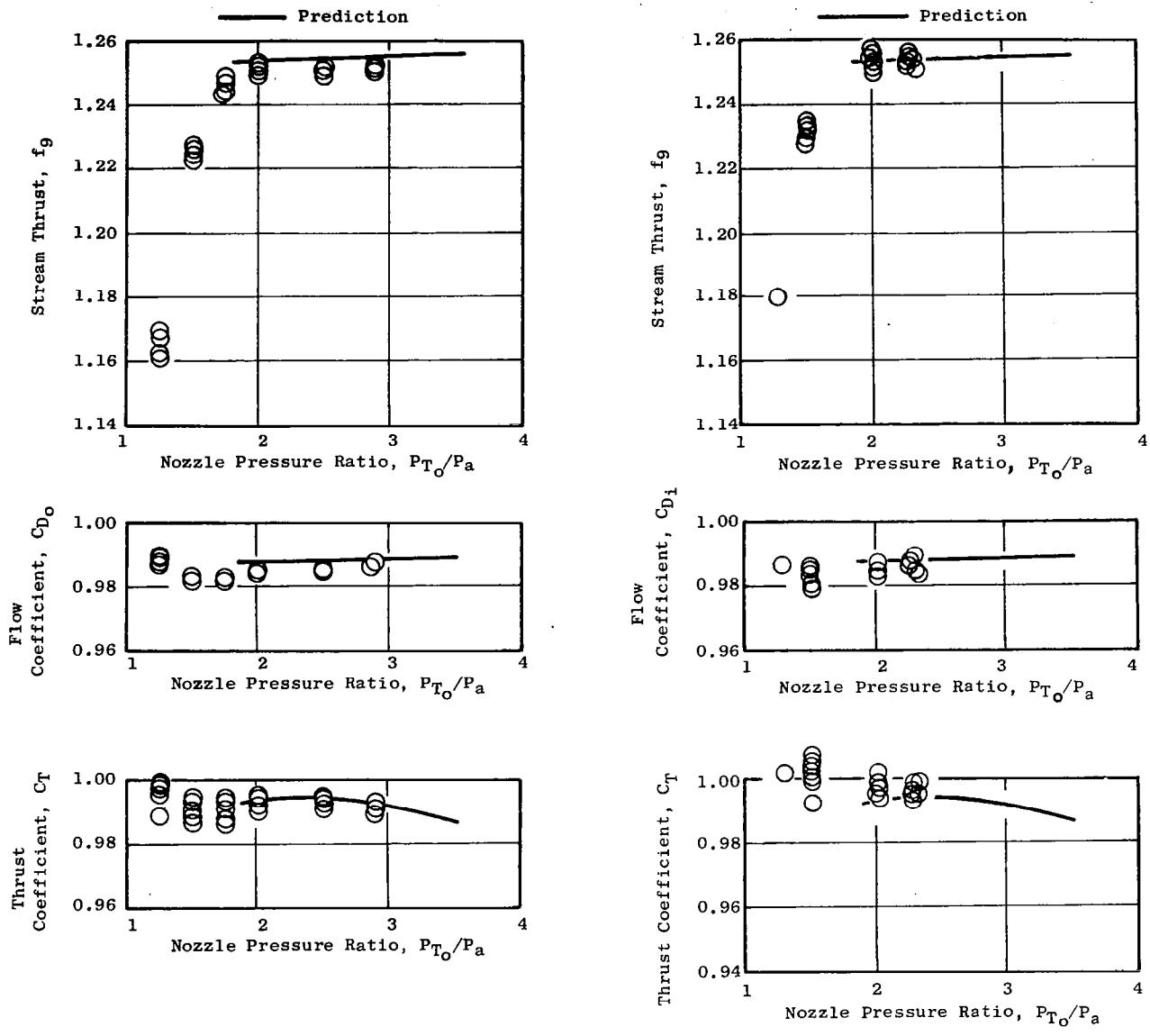

Figure 6-3. STA Static Performance.

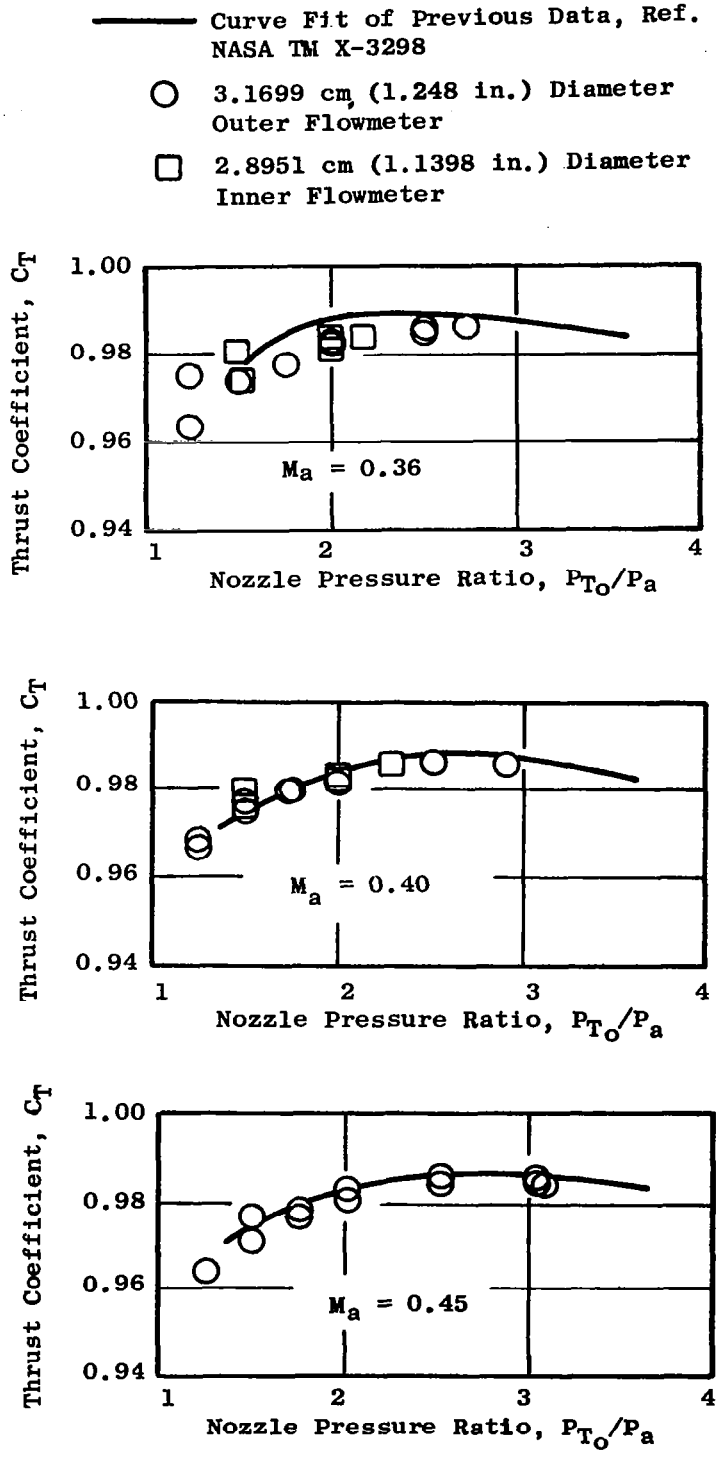

Figure 6-4. Wind-On STA Nozzle Thrust Coefficients.

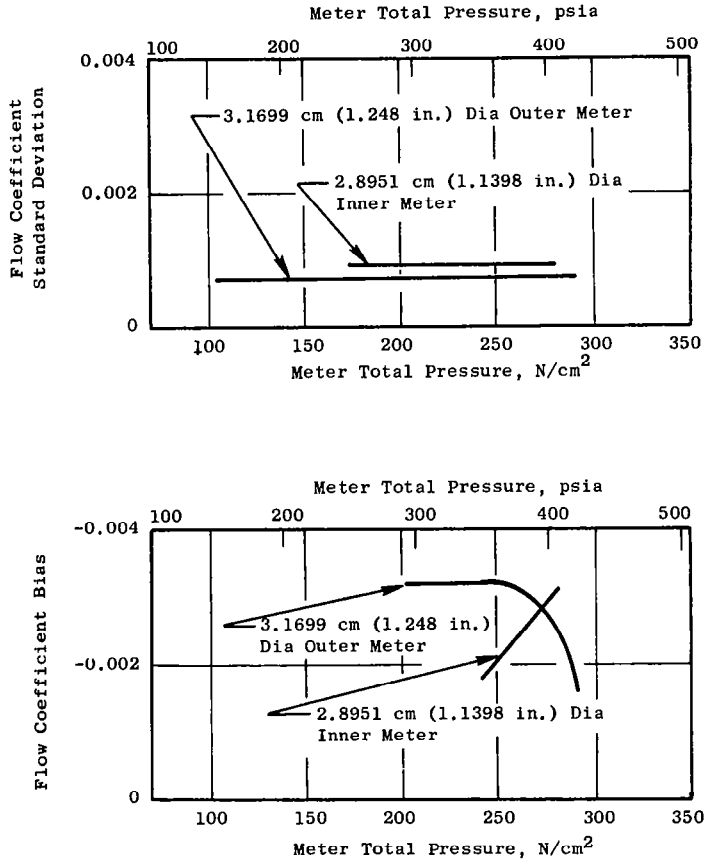

Figure 6-5 a. STA Nozzle Bias and Standard Deviation on Flow Coefficient

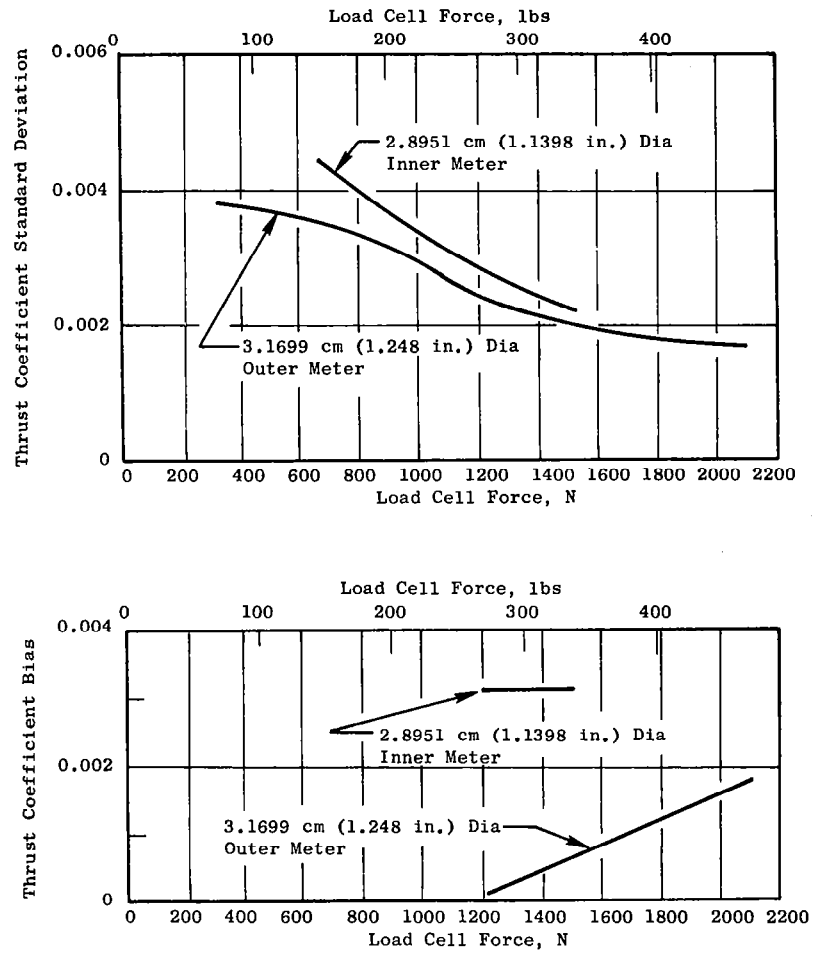

Figure 6-5 b. STA Nozzle Bias and Standard Deviation on Static Thrust Coefficient.

6.2 MODEL THRUST COEFFICIENTS

The eight coannular nozzle configurations were run at tunnel Mach numbers of 0, 0.36, and 0.45. The outer nozzle pressure ratio was varied from 1.5 to 3.5. Two separate regimes of inner nozzle flow conditions were investigated - a "low" or bleed flow regime where the inner flow was varied from zero flow up to 6% of the flow in the outer nozzle, and a "high" flow region in which the inner stream pressure ratio was varied from 1.1 to 3.5. A point-by-point listing of the aerodynamic performance test matrix was presented in Section 4.0. The matrix consists of 544 total points taken on the eight configurations. The coefficients are plotted as functions of outer nozzle pressure ratio for lines of constant inner nozzle weight flow ratio for the low inner flow conditions and lines of inner nozzle pressure ratio for high flow rates. Typically, several repeat points were taken for each model: these are shown on the plots and depicted by flagged symbols. The repeatability was generally very good and was representative of the scatter experienced with the STA model as described in Section 6.1. At low balance loads (outer nozzle pressure ratios of 1.5 with low inner flow) during static testing, the differences between repeat points occasionally was greater than 1%. For the large majority of the test matrix, the spread between repeat points was consistently better than 0.5%.

Thrust coefficients for Configuration 1 [$R_r^o = 0.902$, $R_r^i = 0.673$, bent inner plug] are shown in Figure 6-6 for high inner flow rates and for low inner flow rates. High inner flow thrust coefficients range between 0.95 and 0.972, with the peak performance occurring at an outer nozzle pressure ratio of 3.0 and an inner nozzle pressure ratio of 1.3. The low inner flow performance of Configuration 1 is quite low (between 0.86 and 0.95) at a tunnel Mach number of 0.36. This performance increases rapidly both with increasing outer nozzle pressure ratio and inner nozzle flow rate.

Configuration 1 was a smaller scale version of a model which has previously been tested statically in another facility (see Reference 6-2): these same static points were repeated on Configuration 1 in the NASA Lewis tunnel. The results of the two tests are compared in Figure 6-7, which shows excellent agreement between the two facilities.

Configuration 2 [$R_r^o = 0.902$, $R_r^i = 0.8$, conical inner plug] performance is shown in Figure 6-8 for high inner flow and for low inner flow rates. This configuration exhibits high static performance from 0.97 to 0.986 with high inner flow rates. However, wind-on performance is lowered to 0.94-0.96. Low inner flow rate performance is again low, between 0.84 and 0.943, at Mach 0.36, and, like Configuration 1, is highly dependent on the inner flow rate and the outer nozzle pressure ratio.

High inner flow rate thrust coefficients for Configuration 3 [$R_r^o = 0.902$, $R_r^i = 0.902$, conical inner plug] are presented in Figure 6-9. The thrust coefficients peak at approximately 0.974 for static testing and 0.962 for an ambient Mach number of 0.36. The low inner flow rate performance for Configuration 3, exhibits similar trends to Configurations 1 and 2 but attains better peak thrust. The measured wind-on thrust coefficient is approximately 0.96 with 6% inner bleed flow at an outer nozzle pressure ratio of 3.5.

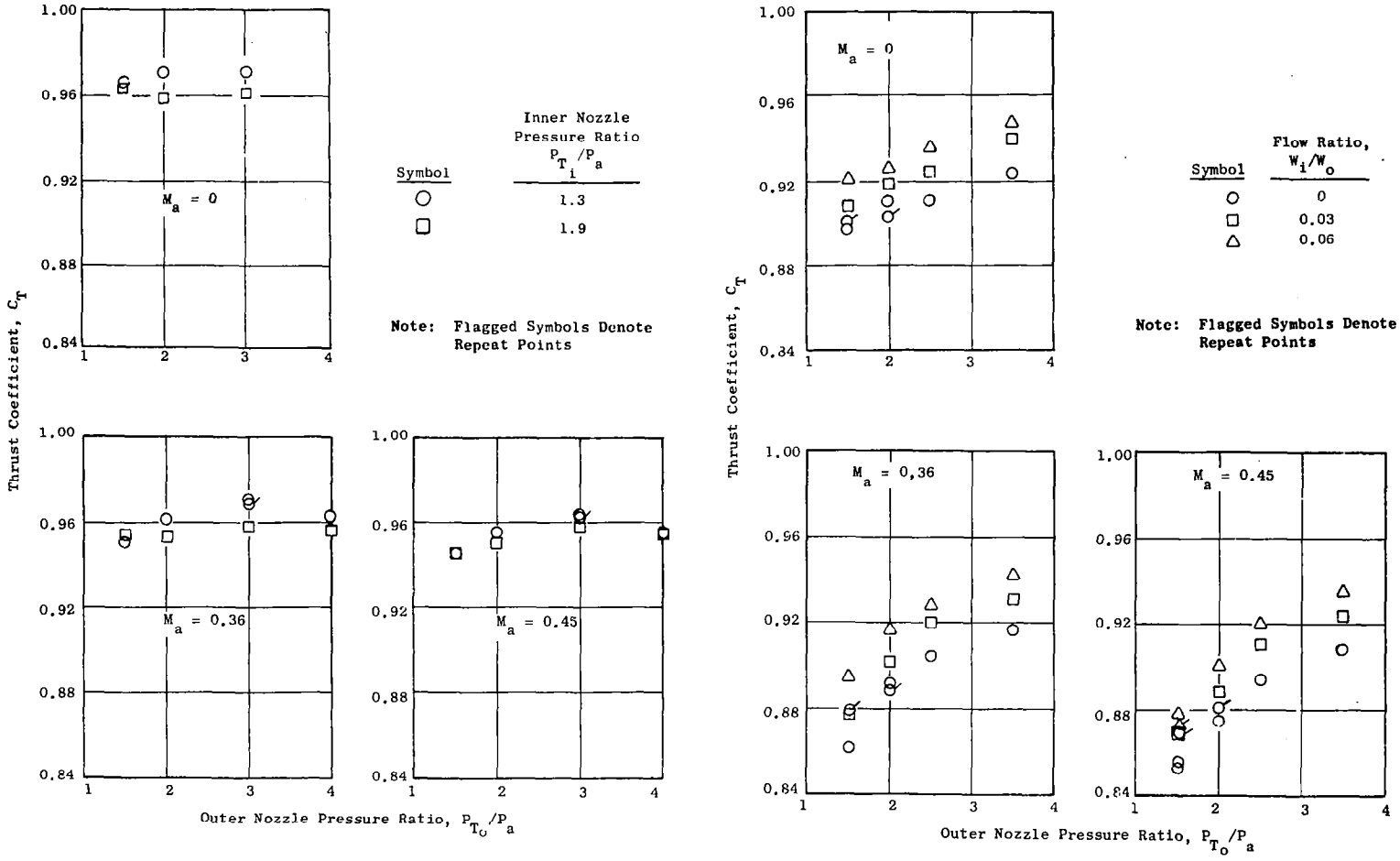

Figure 6-6. Thrust Coefficients for Configuration 1 (R_r^o = 0.902, R_r^i = 0.673, Bent Inner Plug).

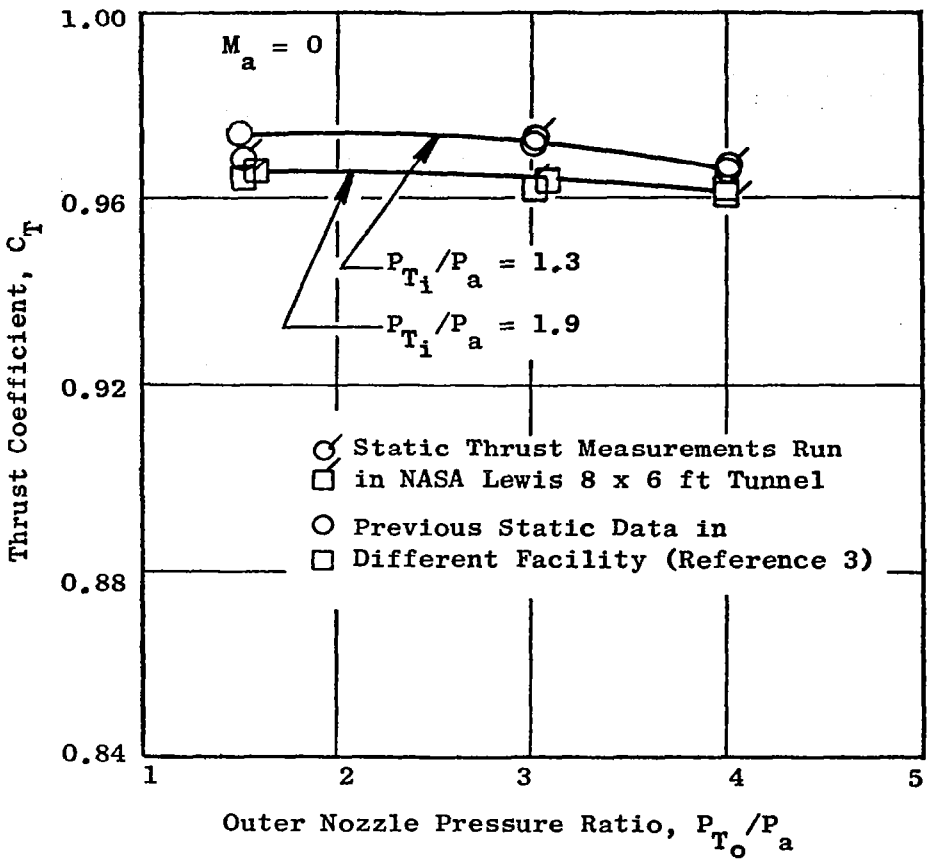

Figure 6-7. Configuration 1 Thrust Coefficients Compared to Previous Results.

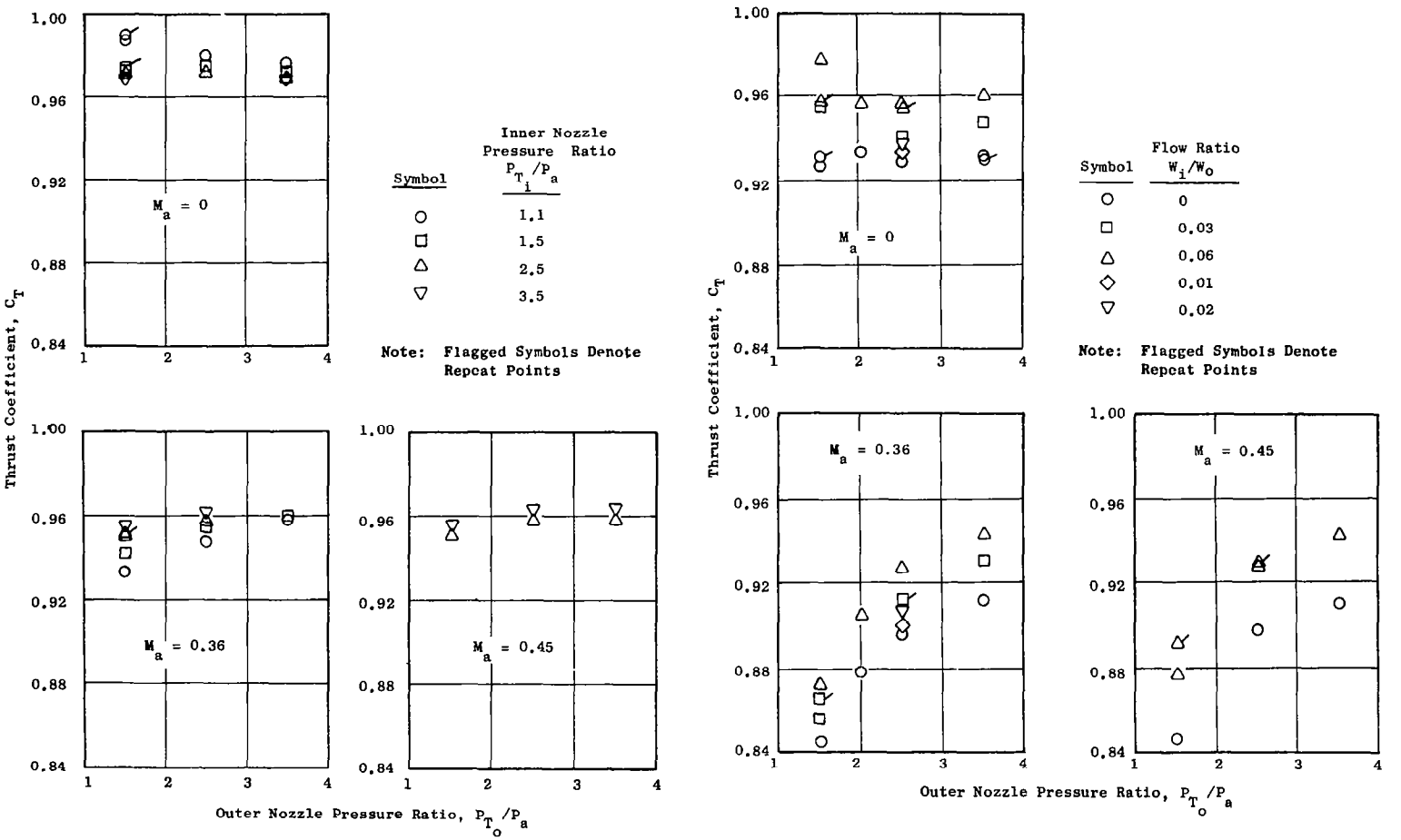

Figure 6-8. Thrust Coefficients for Configuration 2 (R_r^o = 0.902, R_r^i = 0.80, Conical Inner Plug).

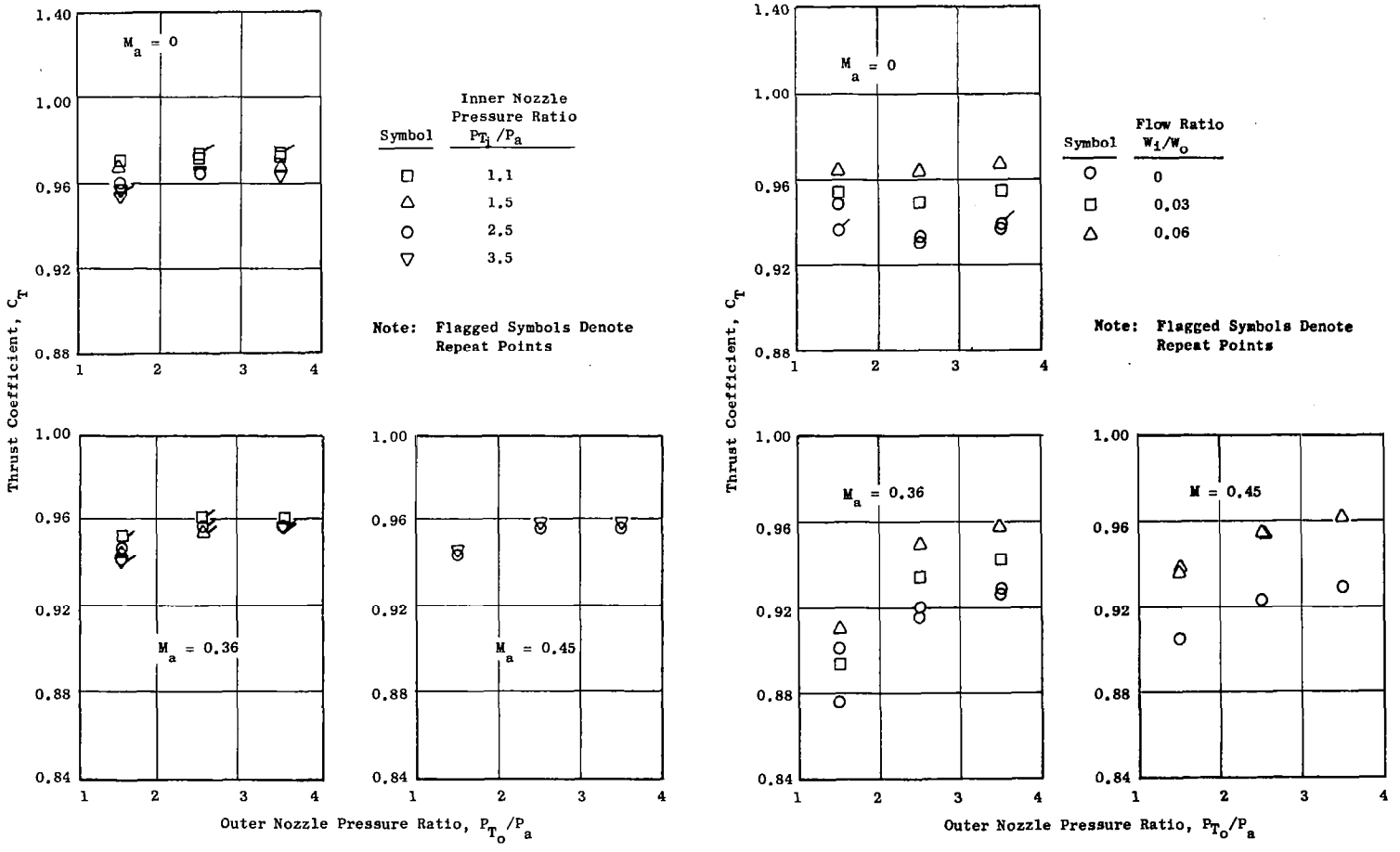

Figure 6-9. Thrust Coefficients for Configuration 3 (R_r^o = 0.902, R_r^i = 0.902, Conical Inner Plug).

Configuration 4 [R_T^o = 0.902, R_T^i = 0.8, bent inner plug] performance is shown in Figure 6-10. This configuration incurs a performance penalty at the higher inner flow rates, i.e., inner nozzle pressure ratios of 2.5 and 3.5. Thrust coefficients at these conditions with an outer nozzle pressure ratio of 2.5 range from 0.946-0.954. This performance is lower than the respective values for Configurations 2 and 3 which have conical inner plug geometries. The bent inner plug of Configuration 4 creates a rapid expansion of the supersonic inner flow in the region of the plug angular change downstream of the inner nozzle throat. This results in a low pressure region on the plug and an associated thrust loss from the pressure drag. At the lower inner nozzle pressure ratios of 1.1 and 1.5, the inner flow remains subsonic so that the expansion at the corner is not severe and performance remains high. This difference in expansion characteristics can be seen in Figure 6-11 which shows the inner plug static pressure distributions for Configuration 4 with inner nozzle pressure ratios of 1.1 and 3.5. This effect is discussed in detail in Section 6.2.3.

Configuration 5 [R_T^o = 0.853, R_T^i = 0.8, conical inner plug] demonstrated very good high inner flow rate performance, as shown in Figure 6-12. The static performance ranges from 0.965-0.982 and there is little decrease with wind-on conditions. Mach 0.36 thrust coefficients are between 0.97 and 0.975 at an outer nozzle pressure ratio of 2.5 for all the inner pressure ratios tested. The low inner flow rate performance for this configuration, is also high, reaching 0.965 statically and 0.963 at Mach 0.36 for an outer nozzle pressure ratio of 2.5 and a 6% inner flow rate.

The performance for Configuration 6 [R_T^o = 0.926, R_T^i = 0.8, conical inner plug], shown in Figure 6-13 is generally the lowest of all configurations tested. Peak high inner flow rate thrust coefficients are 0.965 statically and 0.961 with wind-on. Coefficients during low inner flow operation vary between 0.82 and 0.983.

Thrust coefficients are shown in Figure 6-14 for Configuration 7 [R_T^o = 0.853, R_T^i = 0.902, conical inner plug]. This configuration exhibited the best performance of all configurations during low inner flow testing. The peak static thrust coefficient is 0.972 at an outer nozzle pressure ratio of 2.5 and a 6% inner flow rate: there is virtually no loss in performance as the ambient velocity is increased, with the thrust coefficient measuring 0.971 at the same nozzle conditions and a Mach number of 0.36.

Configuration 8 [R_T^o = 0.853, R_T^i = 0.8, bent inner plug] exhibits high performance, shown in Figure 6-15 and, similar to Configuration 7 with one exception: the bent inner plug of Configuration 8 results in a performance loss at high inner nozzle pressure ratios. This also occurs on the bent plug configuration of Configuration 4.

The performance levels and trends exhibited by these models, as well as the effect of the major model configurational and operational variables, are discussed in the following subsections. More extensive discussion of these results is available in Reference 3-2.

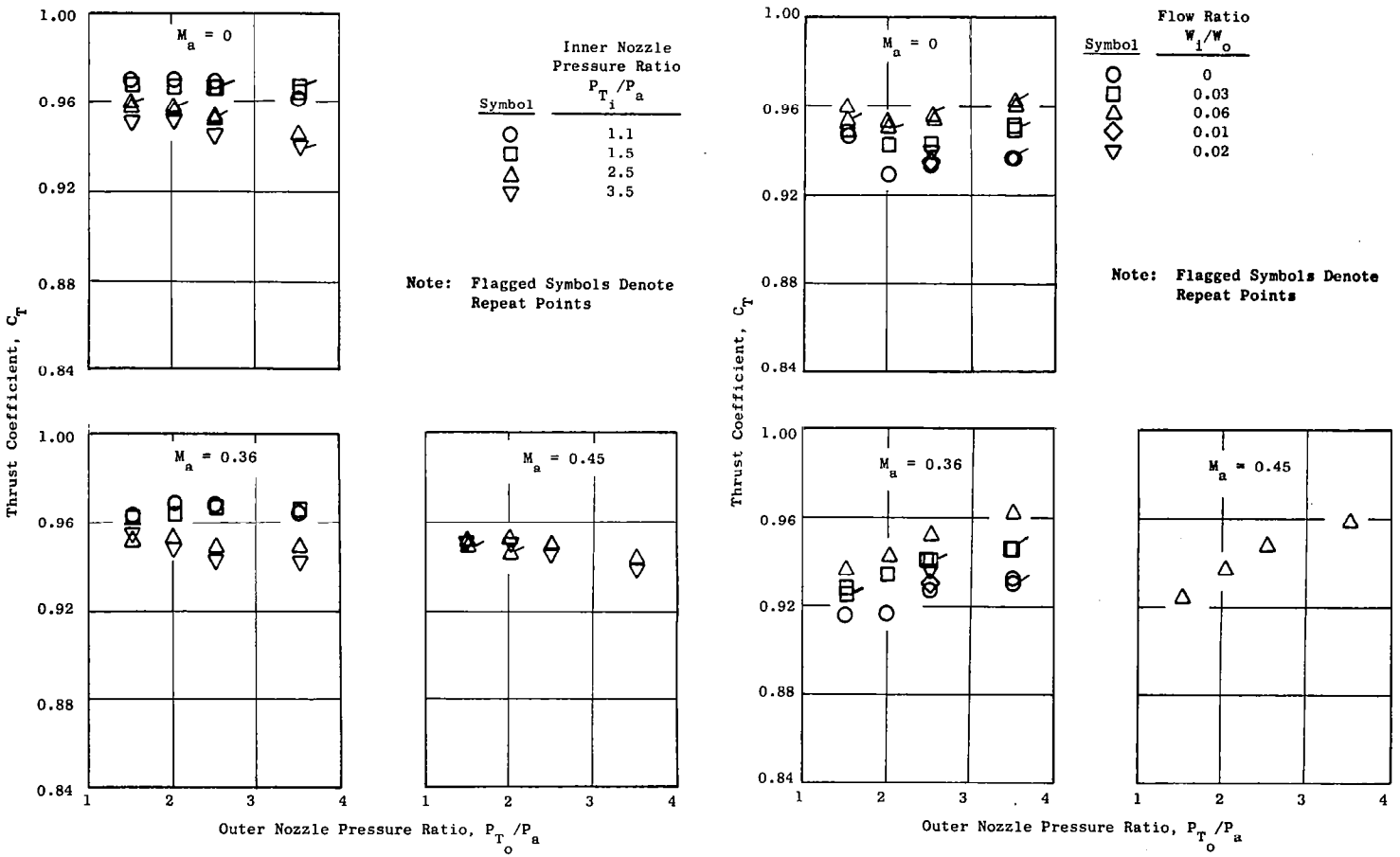

Figure 6-10. Thrust Coefficients for Configuration 4 (R_r^o = 0.902, R_r^i = 0.80, Bent Inner Plug).

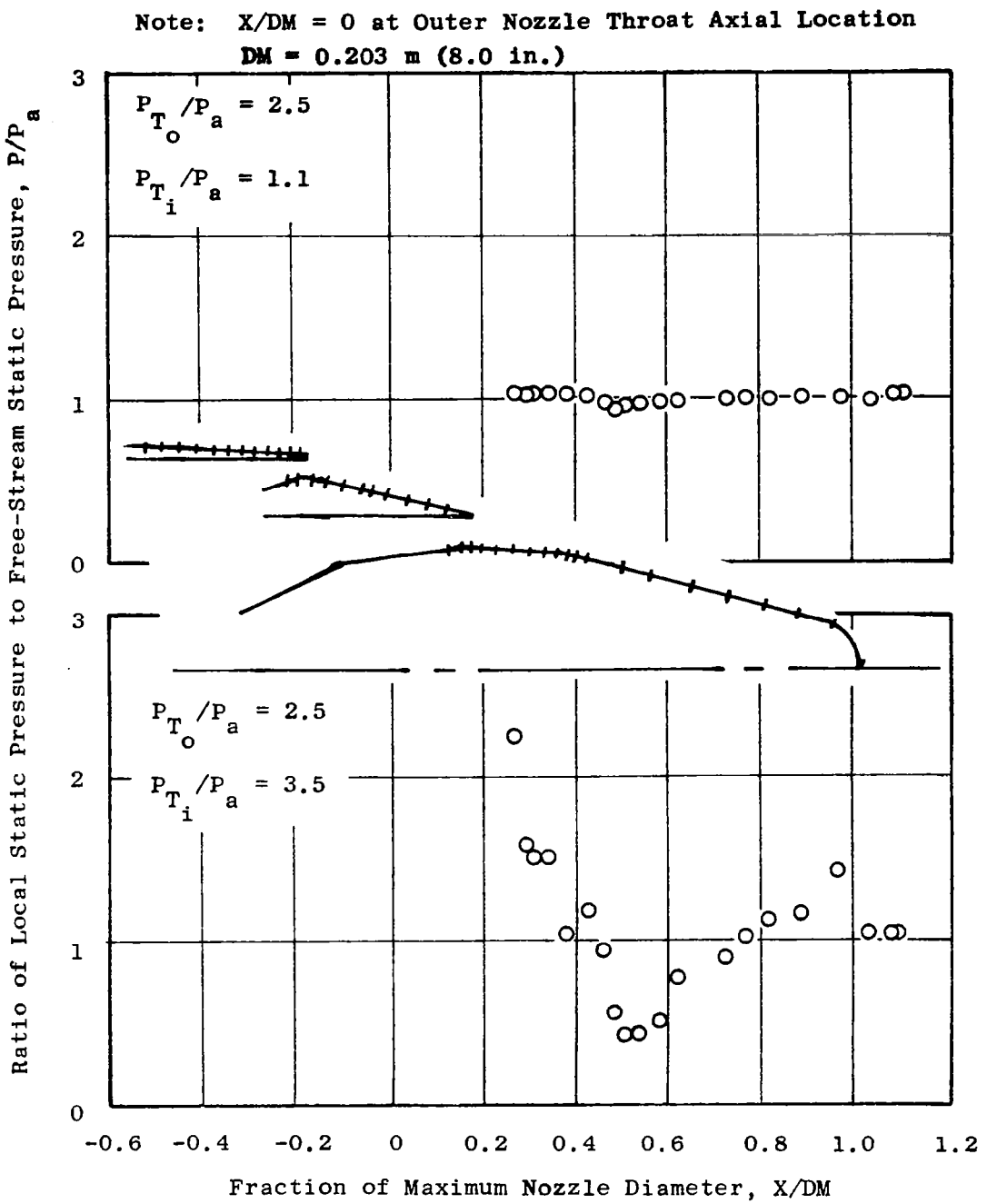

Figure 6-11. Inner Plug Distributions, Configuration 4 [R_r^o = 0.902, R_r^i = 0.80, Bent Inner Plug].

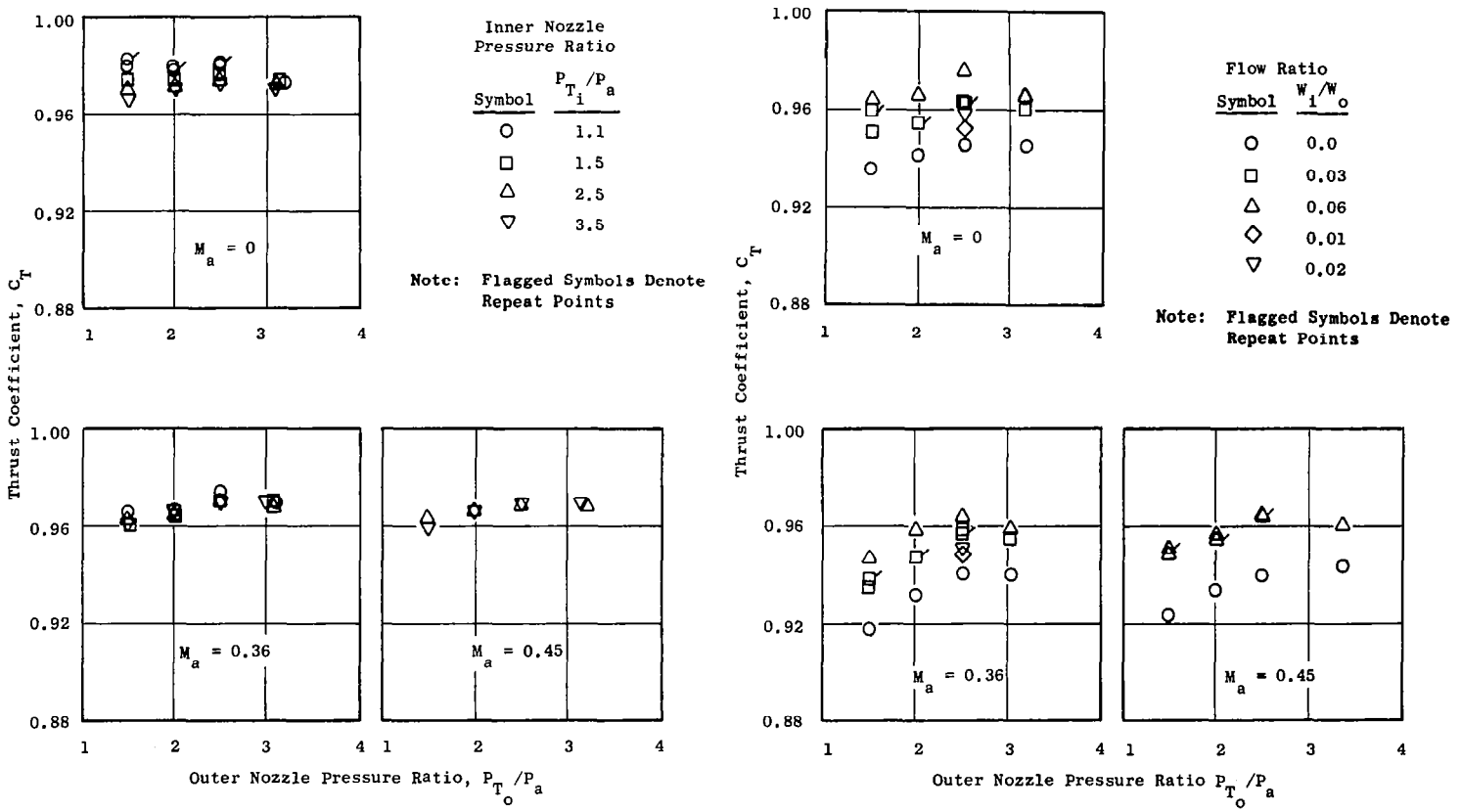

Figure 6-12. Thrust Coefficients for Configuration 5 [$R_r^o = 0.853$, $R_r^i = 0.800$, Conical Inner Plug].

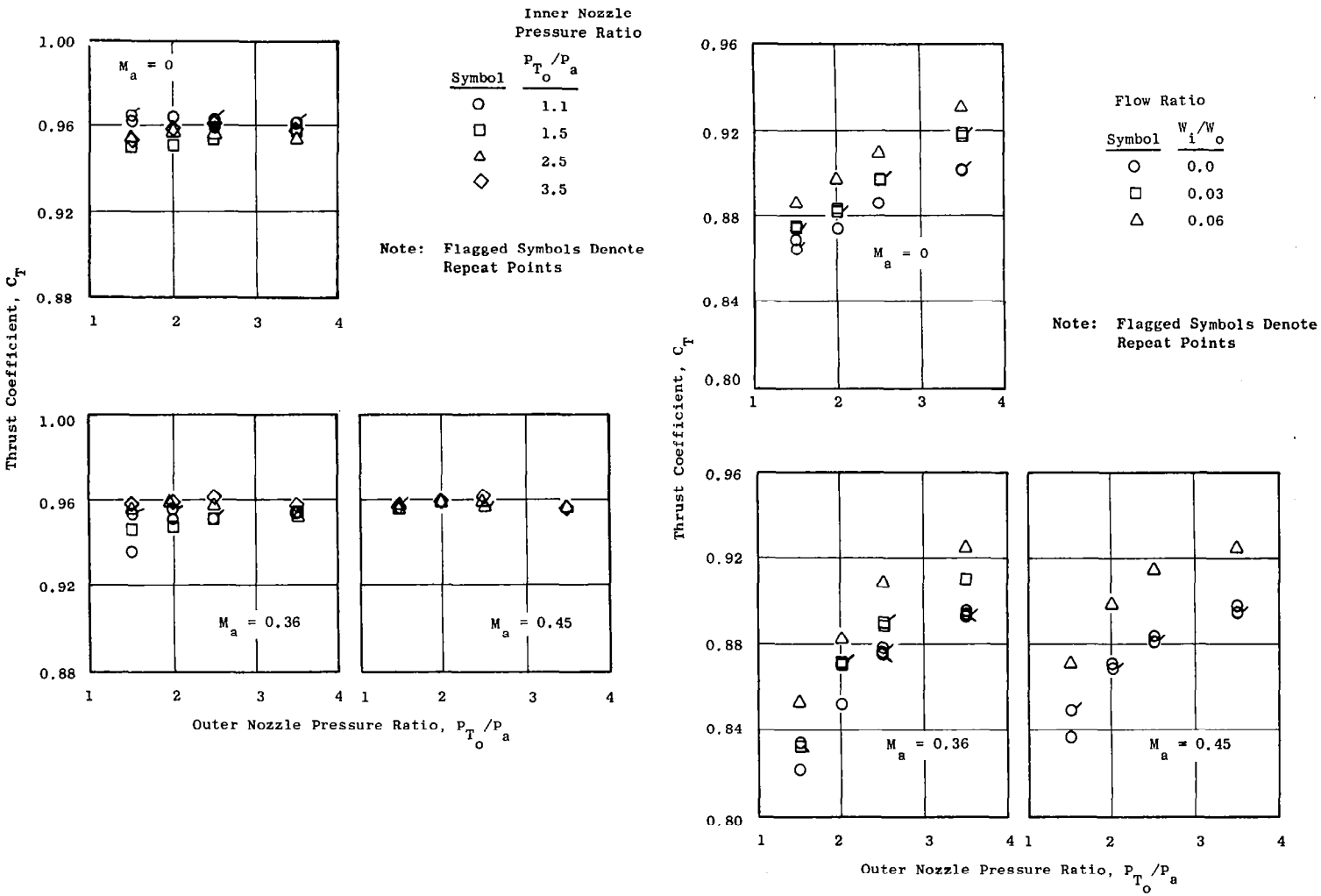

Figure 6-13. Thrust Coefficients for Configuration 6 [R_r^i = 0.926, R_r^i = 0.800, Conical Inner Plug].

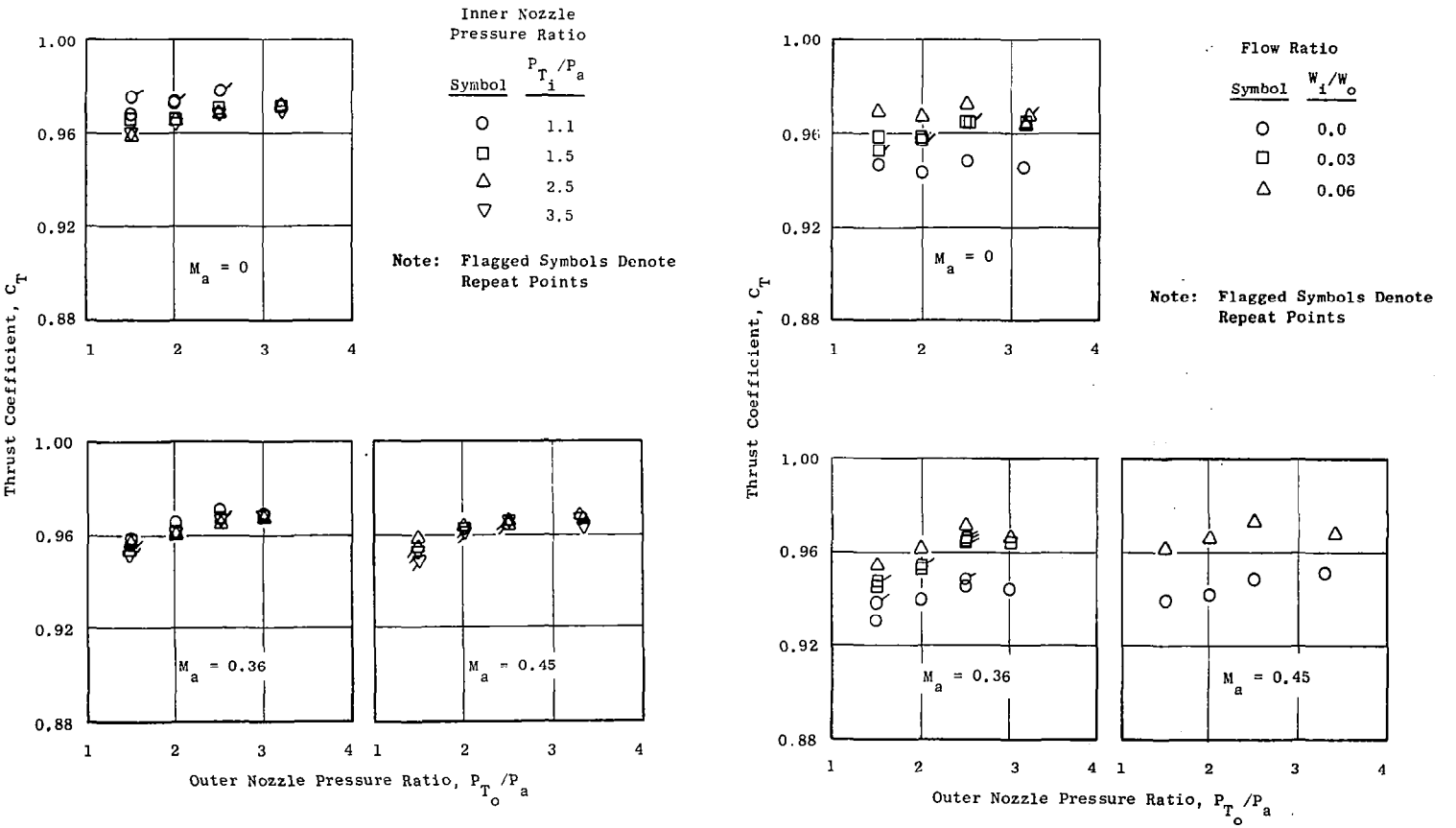

Figure 6-14. Thrust Coefficients for Configuration 7 [R_r^o = 0.853, R_r^i = 0.902, Conical Inner Plug].

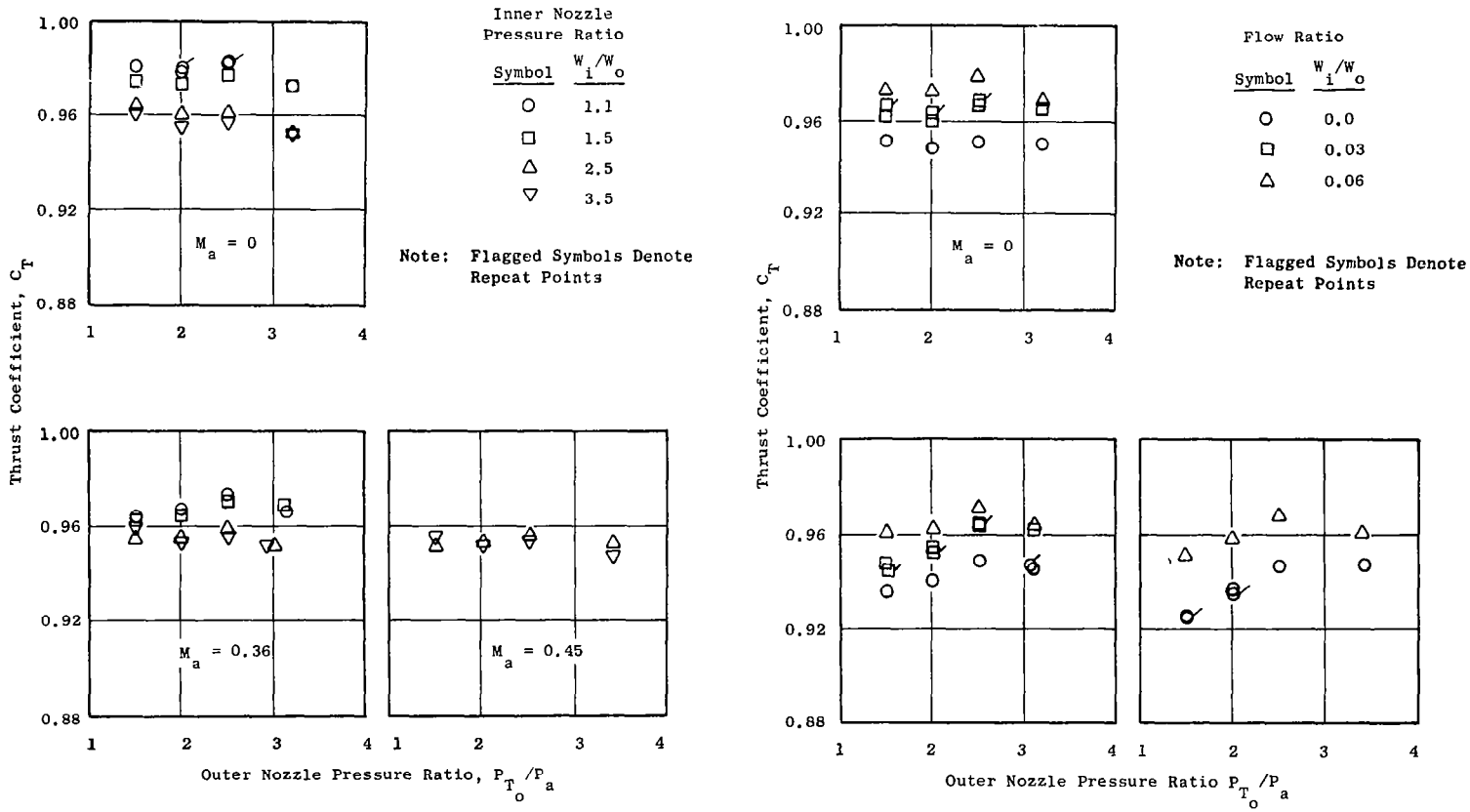

Figure 6-15. Thrust Coefficients for Configuration 8 [$R_r^o = 0.853$, $R_r^i = 0.800$, Bent Inner Plug].

6.2.1 Low Inner Flow Rate Performance Trends

Three configuration and test parameters were the principal factors determining the performance levels for low inner flow rates. These were the outer nozzle radius ratio, the inner nozzle radius ratio, and the inner nozzle flow rate.

The effect of outer nozzle radius ratio on performance can be illustrated by comparing Configurations 5, 2, and 6, which have an inner radius ratio of 0.8, a conical plug and outer radius ratios of 0.853, 0.902, and 0.926, respectively. Figure 6-16 shows thrust coefficients for these configurations plotted as a function of outer radius ratio for low inner flow rates on an outer nozzle pressure ratio of 2.5. Both statically and at Mach 0.36, the thrust coefficient decreases rapidly as the radius ratio is increased above 0.853. Configurations 4 and 8 exhibit the same trend for the bent inner plug geometry. The effect of increasing the outer nozzle radius ratio is to increase the plug size relative to the flow area, i.e., the ratio of plug expansion area and wetted surface area to the nozzle throat area increases. This results in increased skin friction drag, lowering the thrust coefficient. In addition, the inner flow duct at low flow rates creates a thrust loss, as will be discussed later in this subsection. This loss becomes a larger percent of the overall thrust as the outer radius ratio is decreased (due to decreased nozzle throat area), causing the performance to drop.

The effect of inner nozzle radius ratio can be illustrated by comparing Configurations 2 versus 3, for an outer radius ratio of 0.902 and conical inner plug geometry; Configurations 2 versus 4 for bent inner plug geometry; and Configurations 5 versus 7 for conical inner plugs at an outer radius ratio of 0.853. Figures 6-17 and 6-18 show the variation of thrust coefficient with inner radius ratio for these configurations with low inner-flow rates. Since only two configurations are used to generate each line in these figures, the plot is shown as a straight line between the two points merely to indicate the direction of the trend. The thrust coefficient, in general, increases as the inner-nozzle radius ratio is increased, this trend being more pronounced at Mach number 0.36 than during static operation. This trend is attributed to the fact that at the low inner-flow rates the total pressure of the inner airstream is actually lower than the ambient static pressure due to the outer flow stream aspirating the inner stream. This subambient pressure region is a drag force, lowering the nozzle thrust coefficient. The higher inner-nozzle radius ratio configurations have smaller inner-throat areas, resulting in a smaller low pressure region and less drag. Also, the smaller step height configurations recover higher pressure force on the inner plug with no change in the pressure forces on the outer plug and shroud. The low static pressures in the region of the inner-nozzle throat can be seen in Figure 6-19 for Configuration 2 [$R_T^o = 0.902$, $R_T^i = 0.800$, conical inner plug] with zero inner flow. The greater pressure recovery on the inner plug for smaller step heights is shown by comparing the static pressure distribution in Figure 6-19 with that of Configuration 3 [$R_T^o = 0.902$, $R_T^i = 0.902$, conical inner plug] in Figure 6-20. The plug recompression occurs much earlier, thus acting on a larger projected area, for the 0.902 inner radius ratio than for

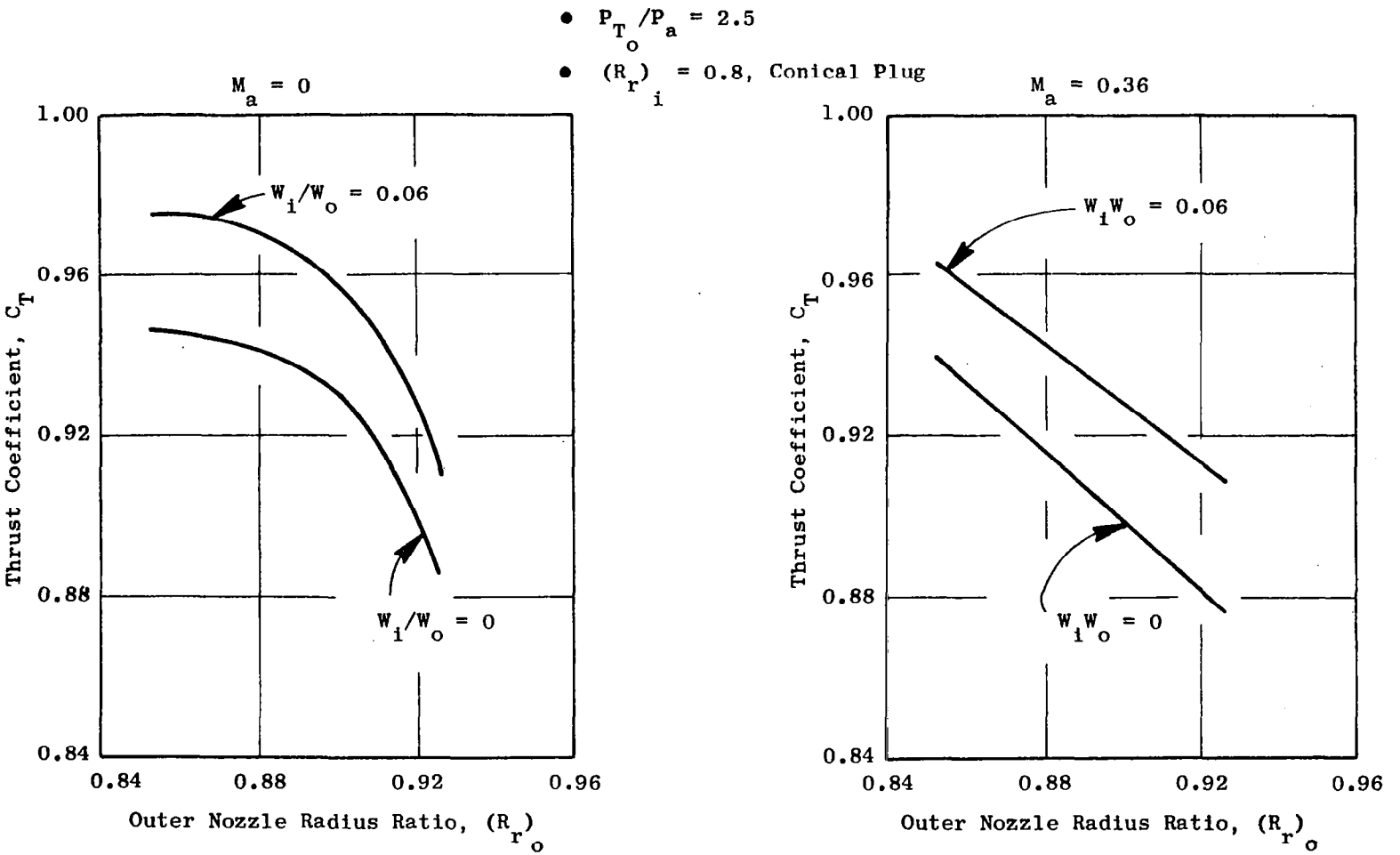

Figure 6-16. Thrust Coefficient As a Function of Outer Nozzle Radius Ratio for Low Flow Rates and Conical Inner Plug.

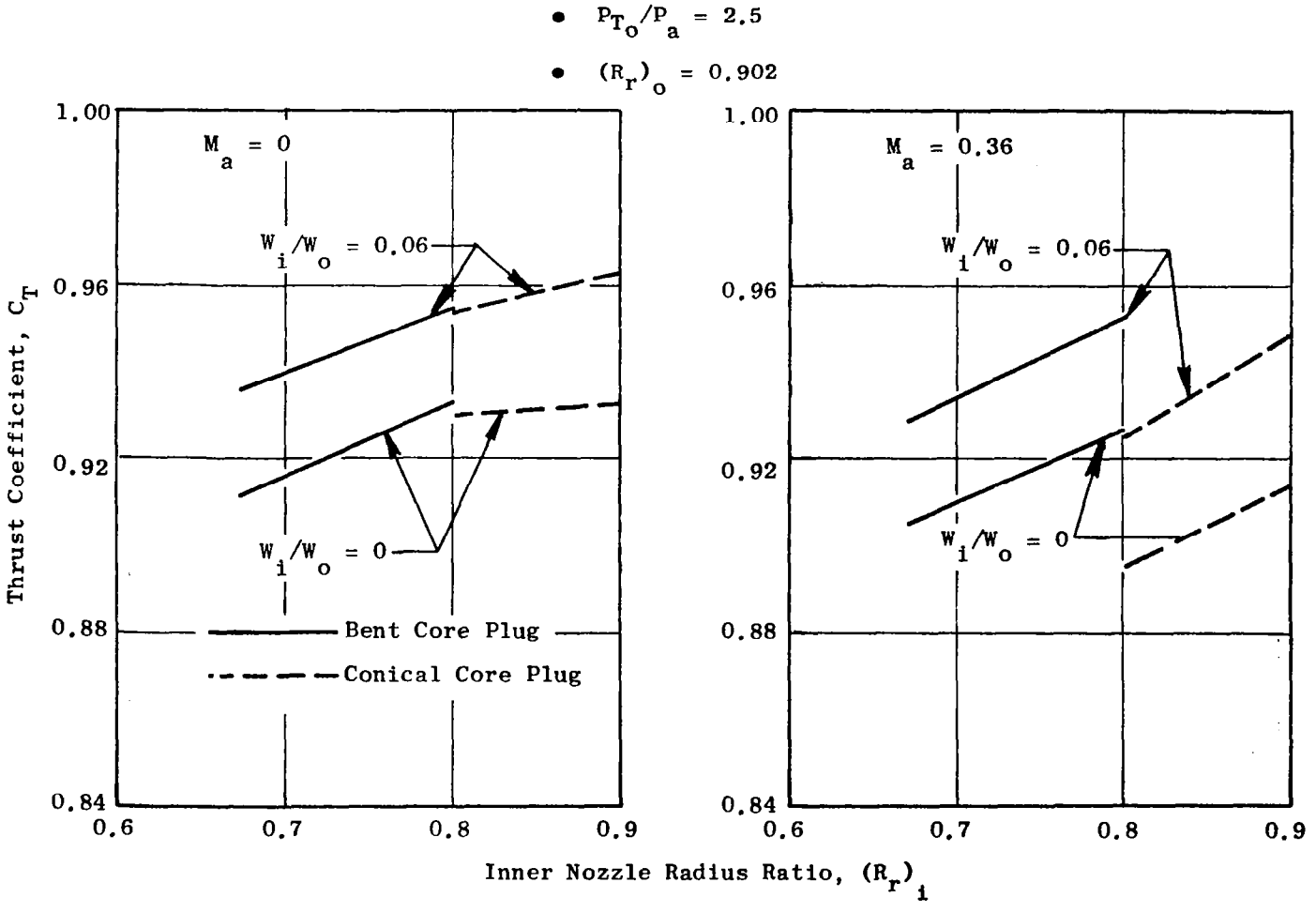

Figure 6-17. Thrust Coefficient As a Function of Inner Nozzle Radius Ratio for Low Inner Flow Rates, R_r^o = 0.902.

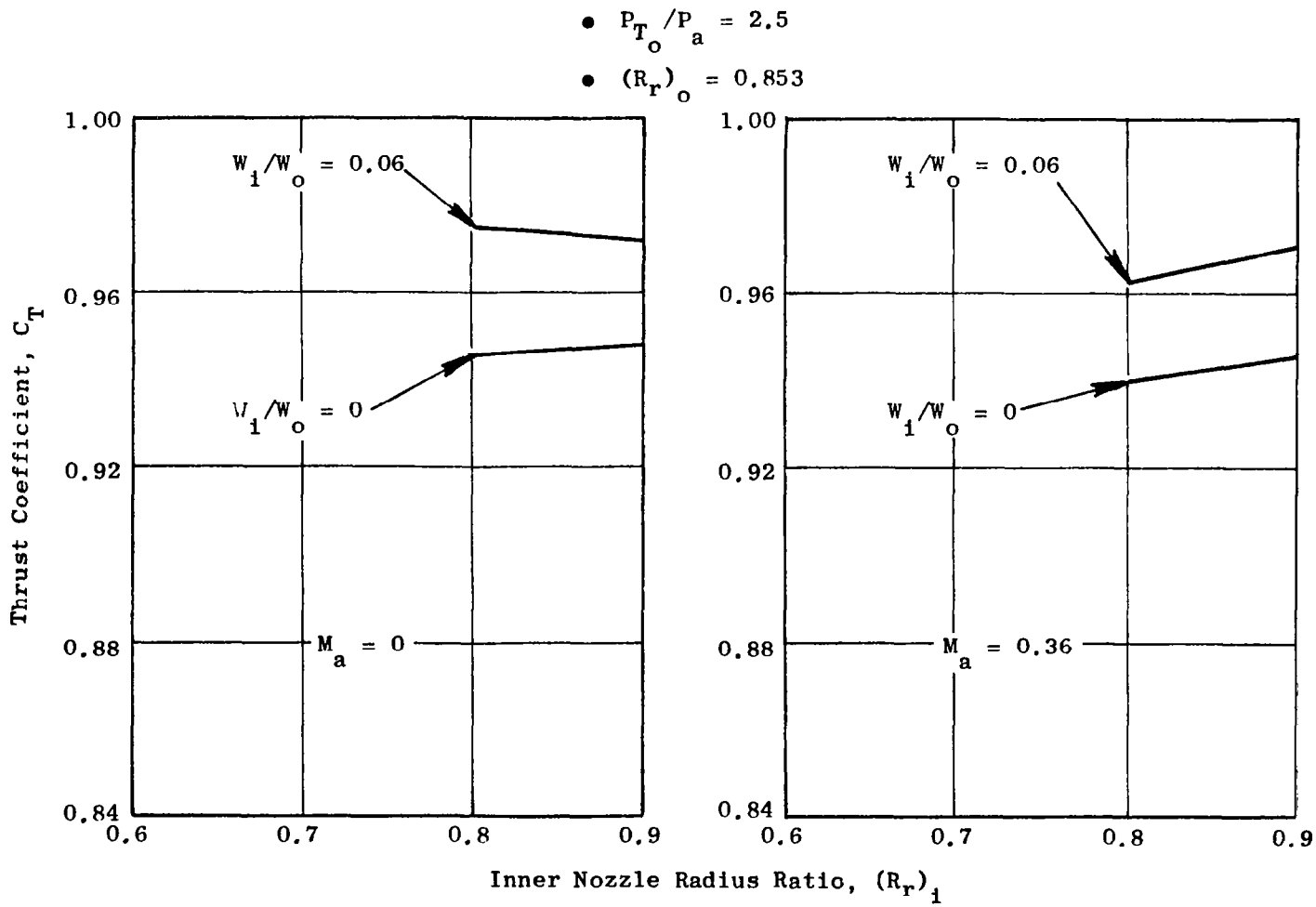

Figure 6-18. Thrust Coefficient As a Function of Inner Nozzle Radius Ratio for Low Inner Flow Rates, $R_r{}^o$ = 0.853.

- $P_{T_o}/P_a = 2.5$
- $W_i/W_o = 0$
- $M_a = 0.36$
- DM = 0.203 m (8.0 in.)

Symbol	Tap Location
○	Outer Shroud
□	Outer Plug
△	Inner Plug

Note: X/DM = 0 at Outer Nozzle Throat Axial Location

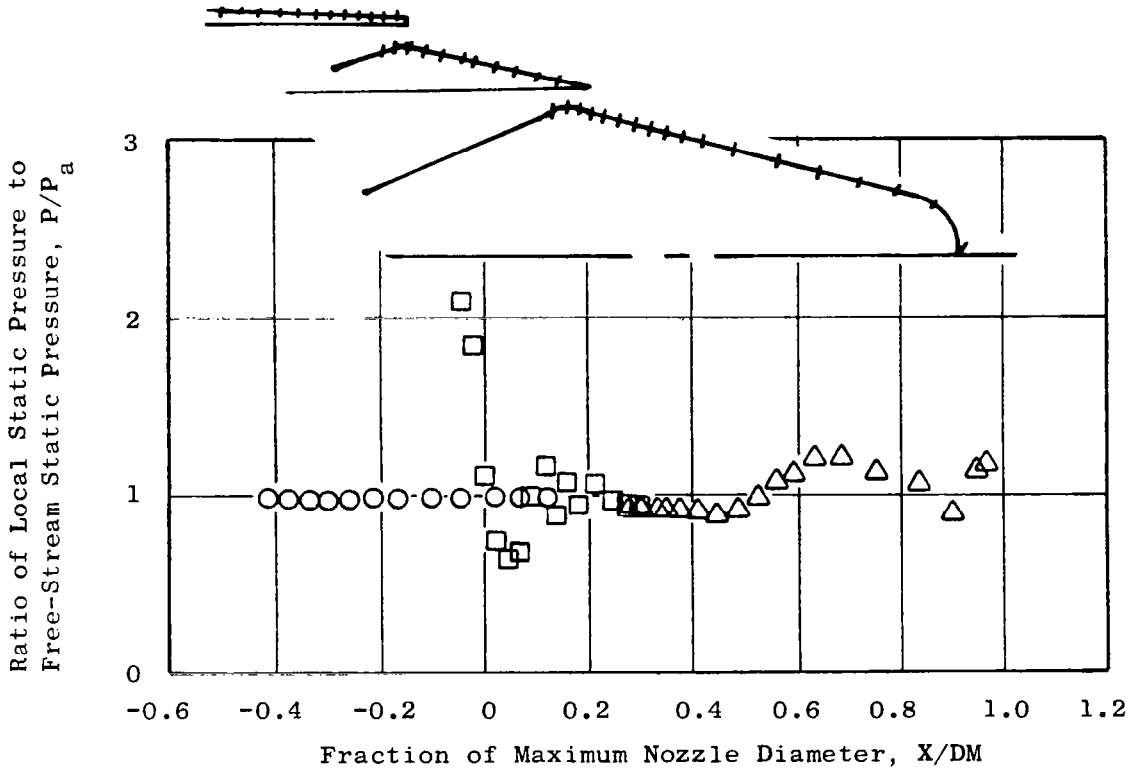

Figure 6-19. Static Pressure Distribution, Configuration 2 [R_r^o = 0.902, R_r^i = 0.800, Conical Inner Plug] with Zero Inner Flow.

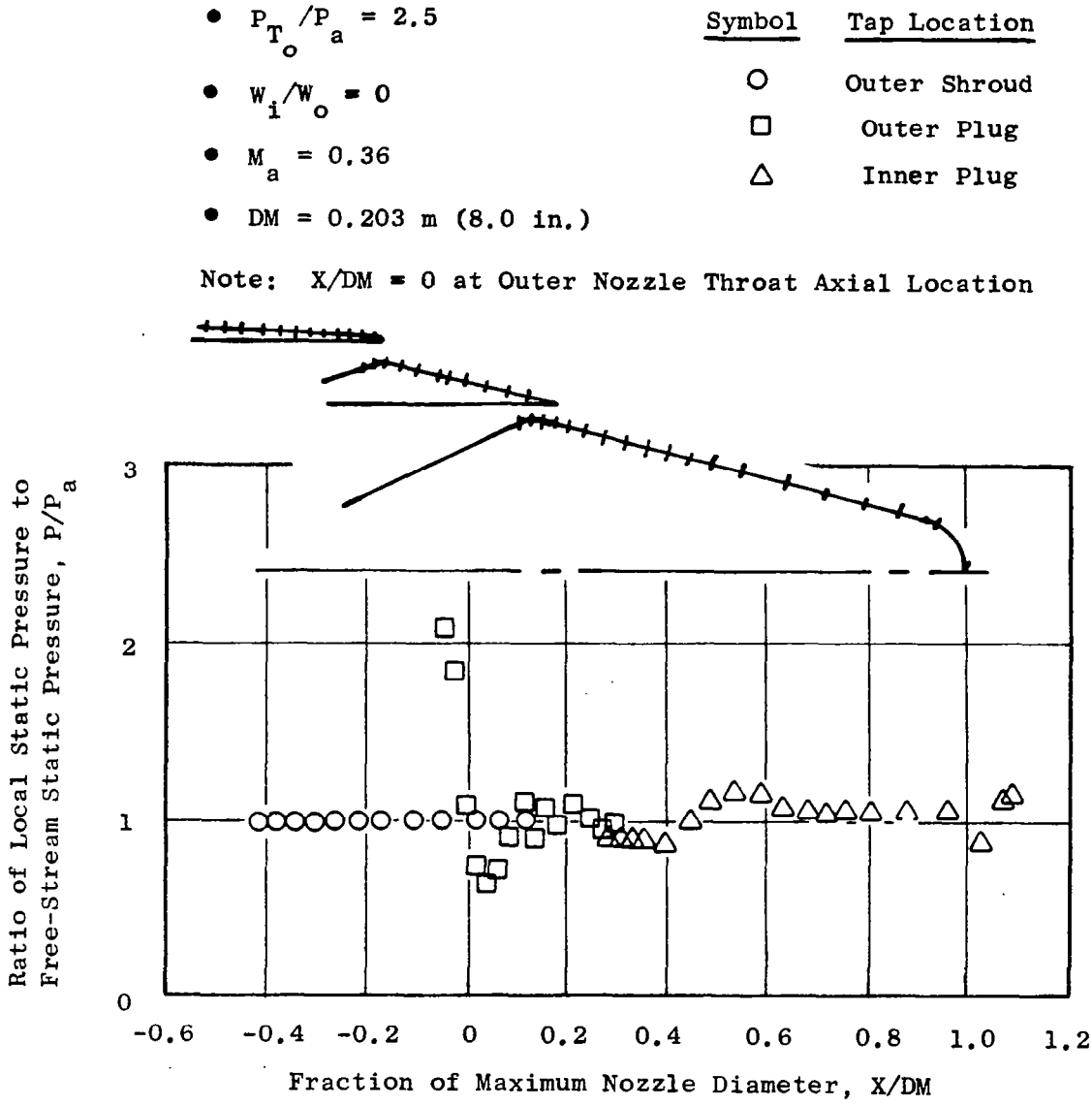

Figure 6-20. Static Pressure Distribution, Configuration 3 [R_r^o = 0.902, R_r^i = 0.902, Conical Inner Plug] with Zero Inner Flow.

the 0.80 ratio. Plots of the total inner plug pressure force from pressure integrations, normalized by the nozzle ideal thrust, are shown in Figure 6-21 for Configurations 2 and 3 demonstrating the increase in plug pressure recovery.

The effect of inner nozzle flow rate on nozzle thrust coefficient is demonstrated in Figure 6-22, which presents the thrust coefficient as a function of inner flow for an outer nozzle pressure ratio of 2.5 and a tunnel Mach number of 0.36. The rapid increase in thrust coefficient with increasing flow rate is caused by the low pressure region in the inner stream. With zero inner flow, the outer-stream pumping action lowers the static pressure in the region of the inner nozzle throat (i.e., minimum physical area) to lower than ambient levels. In this instance, the cavity pressure upstream of the inner nozzle throat, as measured by the total pressure rakes, ranges from 0.85 to 0.92 of the ambient pressure. This subambient pressure is a drag force reflected in a loss in thrust coefficient. As the inner flow rate increases from zero, the total pressure of the inner stream and the static pressure in the region of the throat steadily increase. The total-to-ambient pressure ratio at 6% flow ratio ranges from 0.96 to 1.02. This steady decrease in pressure drag is reflected by the steadily increasing thrust coefficient for all configurations, as depicted in Figure 6-22.

6.2.2 High Inner Flow Rate Performance Trends

The primary factors affecting the model performance during high inner flow rate testing were the inner plug geometry and the outer nozzle radius ratio. The effect of the bent inner plug geometry compared to the conical plug is shown in Figure 6-23 where the thrust coefficient is plotted as a function of inner nozzle pressure ratio for an outer flow pressure ratio of 2.5 and a tunnel Mach number of 0.36. The conical plug configurations show generally a small variation in thrust coefficient, whereas the bent plug configurations experience a significant decrease in performance as the inner pressure ratio increases. Comparing Configuration 2 with 4 [$R_r^o = 0.902$, $R_r^o = 0.8$] and Configuration 5 with 8 [$R_r^o = 0.853$, $R_r^o = 0.8$] in Figure 6-23, the bent plug configurations are 1.4 - 1.8% lower in thrust at an inner nozzle pressure ratio of 3.5 than the otherwise identical conical plug models. At an inner pressure ratio of 1.5, the bent plug nozzles are equal to or higher in thrust coefficient than the comparable conical plug nozzles. This loss in thrust at high inner nozzle pressure ratios by the bent plug configurations is due to expansion around the corner in the plug downstream of the throat, resulting in a low pressure area, the severity of which increases as the inner nozzle pressure ratio increases, as previously discussed in Section 6.2. This is further illustrated in Figure 6-24 where the integrated pressure force on the inner plug divided by the total nozzle ideal thrust is plotted against inner nozzle pressure ratio for Configurations 2 (conical plug) and 4 (bent plug) for an outer pressure ratio of 2.5 and tunnel Mach number of 0.36. The decrease in plug pressure force as a percentage of ideal thrust is seen to be initially much more rapid for the bent plug, being 1% lower in plug thrust than the conical plug at an inner pressure ratio of 1.1 and 3% lower at a pressure ratio of 2.5.

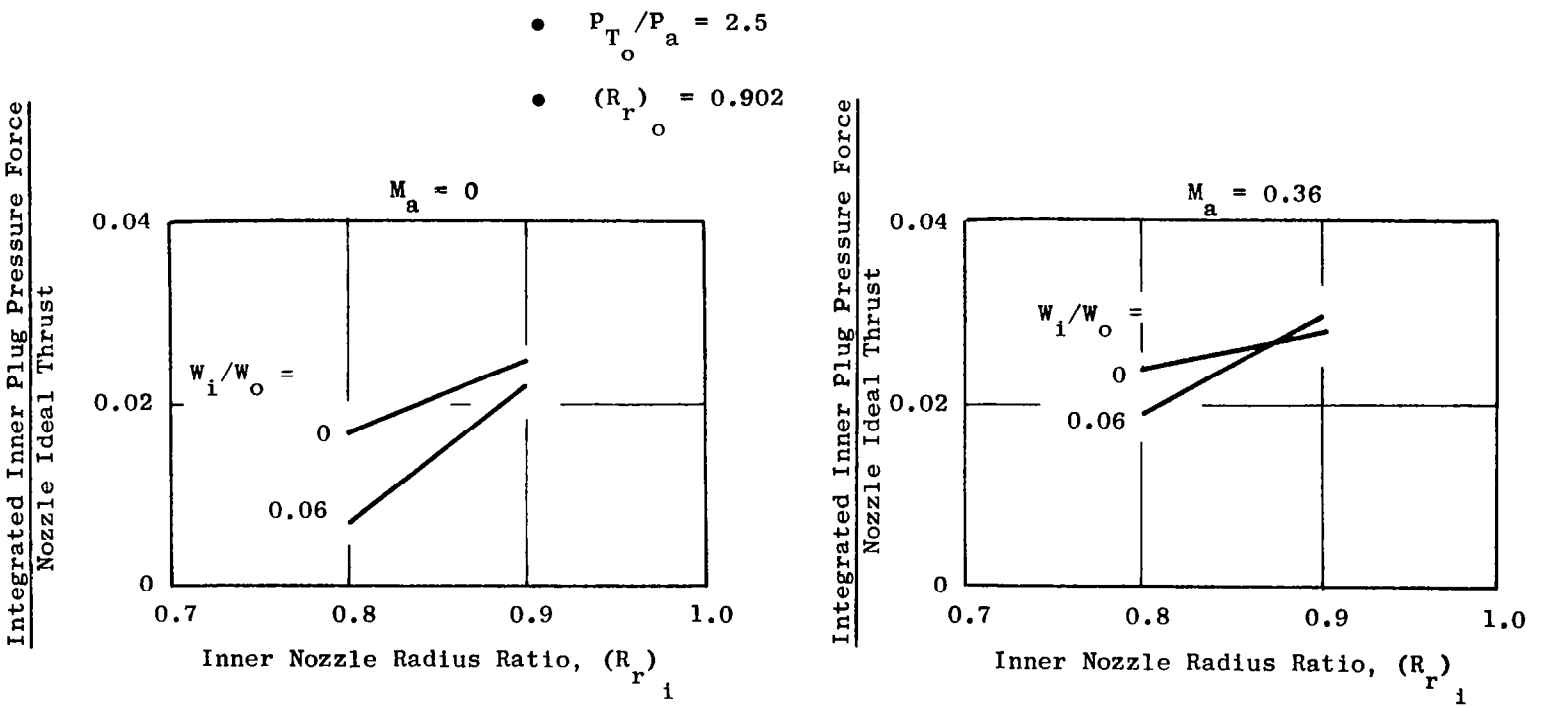

Figure 6-21. Integrated Inner Plug Pressure Force as a Function of Inner Nozzle Radius Ratio for Low Inner Flow Rates.

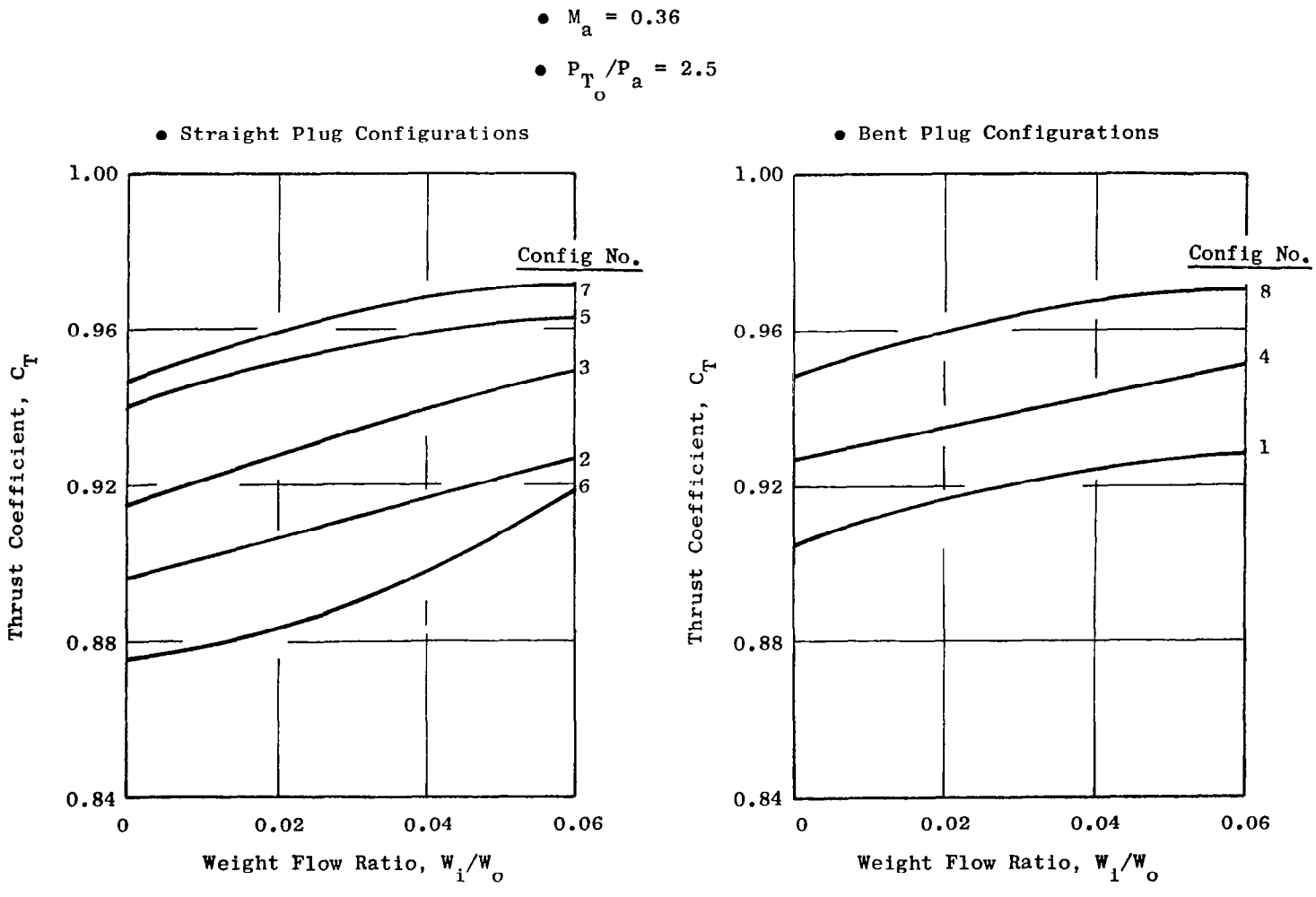

Figure 6-22. Thrust Coefficient as a Function of Inner Weight Flow for Low Inner Flow Rates, M_a = 0.36.

- $M_a = 0.36$
- $P_{T_o}/P_a = 2.5$

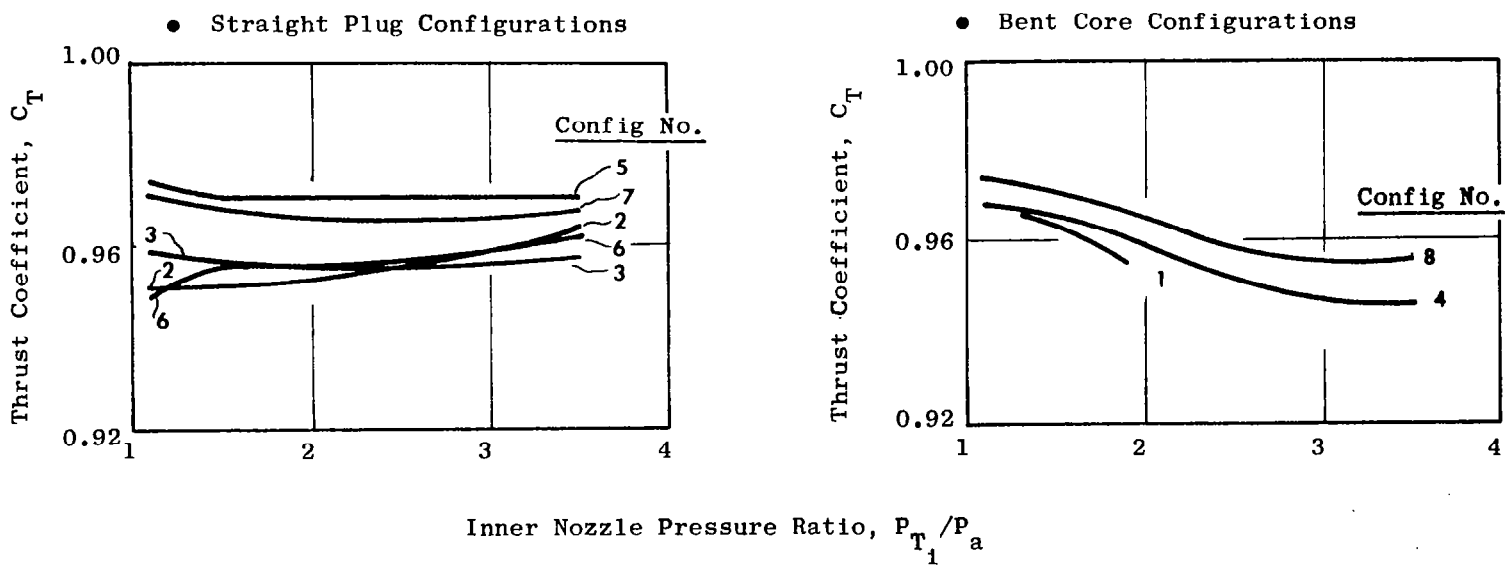

Figure 6-23. Thrust Coefficient as a Function of Inner Nozzle Pressure for High Inner Flow Rates, $M_a = 0.36$.

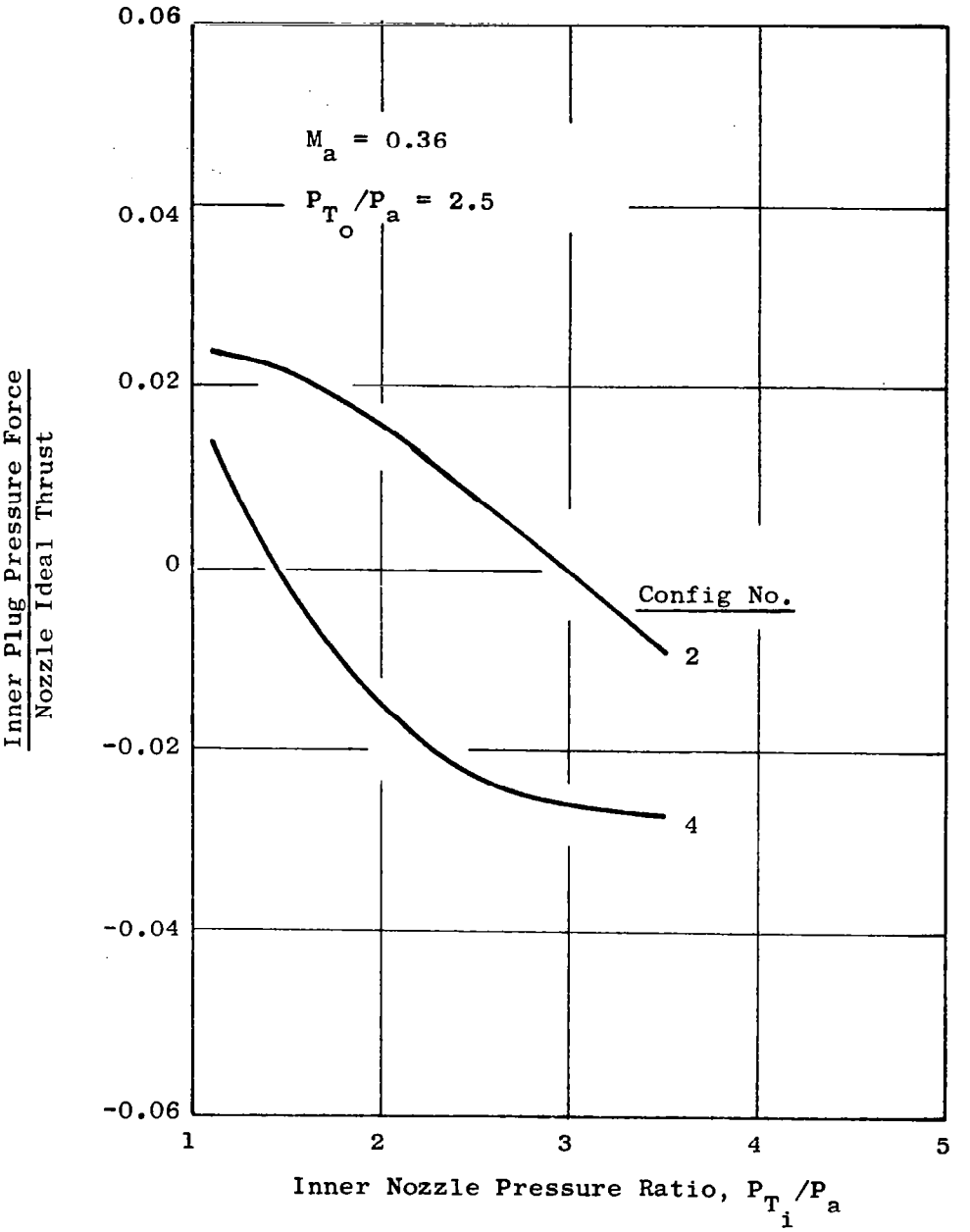

Figure 6-24. Inner Plug Integrated Pressure Force as a Function of Inner Nozzle Pressure Ratio for High Inner Flow Rates.

The effect of outer nozzle radius ratio on nozzle thrust coefficient during high inner flow testing is shown in Figure 6-25 for conical inner plugs. Although the trend is less severe than for the low inner flow conditions, the decrease in performance at the higher radius ratios is significant; the thrust coefficient is 1 - 2% lower at a 0.926 ratio than for the 0.853 configurations. This performance decrease is primarily due to the increase in wetted surface area and expansion area, relative to the nozzle throat area, at the high radius ratios, resulting in greater friction losses.

6.3 FLOW COEFFICIENTS

Flow coefficients for the outer nozzle are presented in Figure 6-26. These flow coefficients proved to be independent of both the inner nozzle flow conditions and the tunnel Mach number and are therefore shown only as a function of the outer nozzle pressure ratio for each of the three different outer nozzle geometries. Appendix V shows the inner nozzle flow coefficients as a function of inner nozzle pressure ratio during high inner flow rate testing. These coefficients did vary somewhat with different external flow conditions, as shown in the Appendix figures. For low inner flow tests, the total pressure required to supply the low amounts of air was generally less than ambient pressure due to the aspiration of the inner nozzle by the outer stream. This resulted in a calculated ideal flow rate of zero which rendered the flow coefficient meaningless.

The measured flow coefficients exhibited excellent repeatability, generally within 0.1 - 0.2%, similar to that demonstrated by the STA nozzle.

Values of outer nozzle flow coefficient ranged from 0.978 to 0.988 for pressure ratios of 2.0 and greater. At the unchoked pressure ratio of 1.5, the outer nozzle flow coefficient increased and exceeded 1.0. This was caused by the internal expansion area of the nozzles (the exit area was slightly larger than the throat area) and by the local surface curvature in the throat region. Since the exhaust stream static pressure at the exit must equal ambient at this pressure ratio, the diverging internal area and throat curvature resulted in lower than ambient pressure in the nozzle throat. The throat Mach number and flow rate were thus higher than the ideal values calculated using the overall total-to-ambient pressure ratio. This lower than ambient pressure in the throat region can be seen in the measured pressures on the outer plug, an example of which is shown in Figure 6-27.

The inner nozzle flow coefficients for choked pressure ratios varied from 0.975 to 0.988. At lower than critical pressure ratios the inner flow coefficients exhibited either of two characteristics, dependent on the plug geometry. The configurations with conical inner plugs exhibited generally higher flow coefficients when the nozzle was unchoked, for the same reasons described above for the outer nozzle. The bent core plugs invariably showed a substantial drop in flow coefficient with the nozzle unchoked. This was due to the interaction of the outer and inner streams where the two merge. The shallow angle of the bent plugs allowed the outer stream to create a

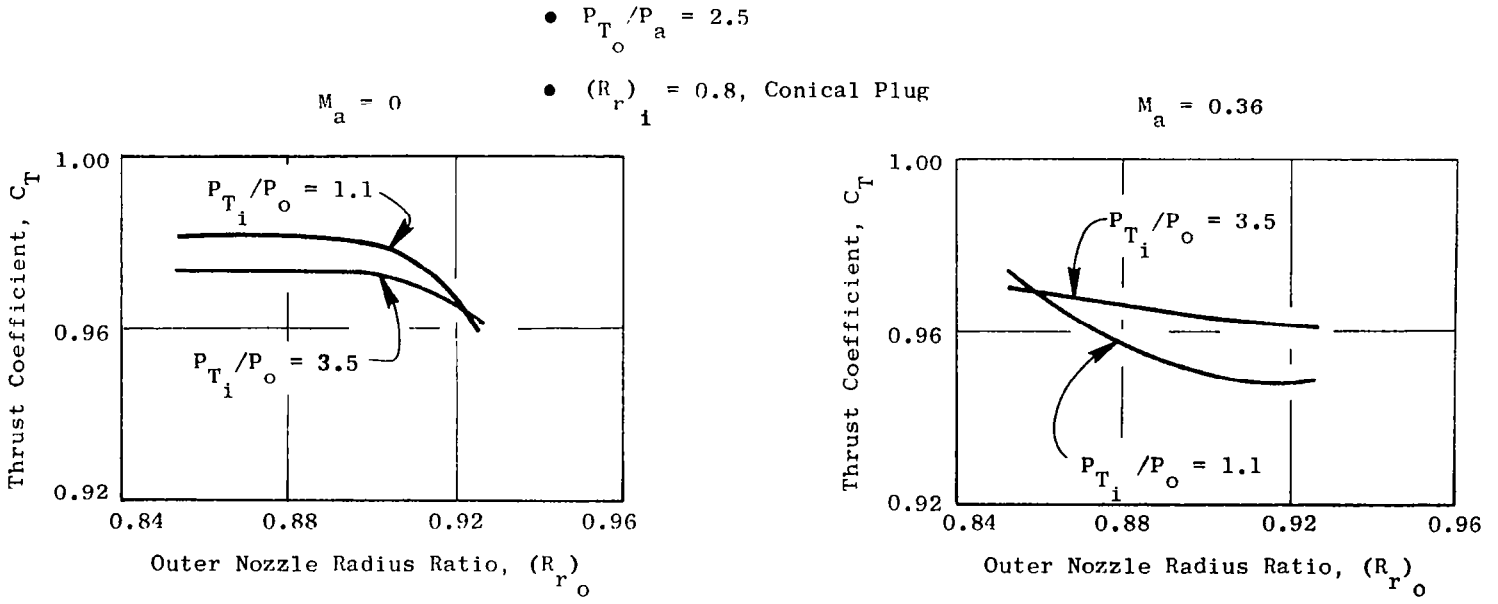

Figure 6-25. Thrust Coefficient as a Function of Outer Nozzle Radius Ratio for High Inner Flow Rates and Conical Inner Plug.

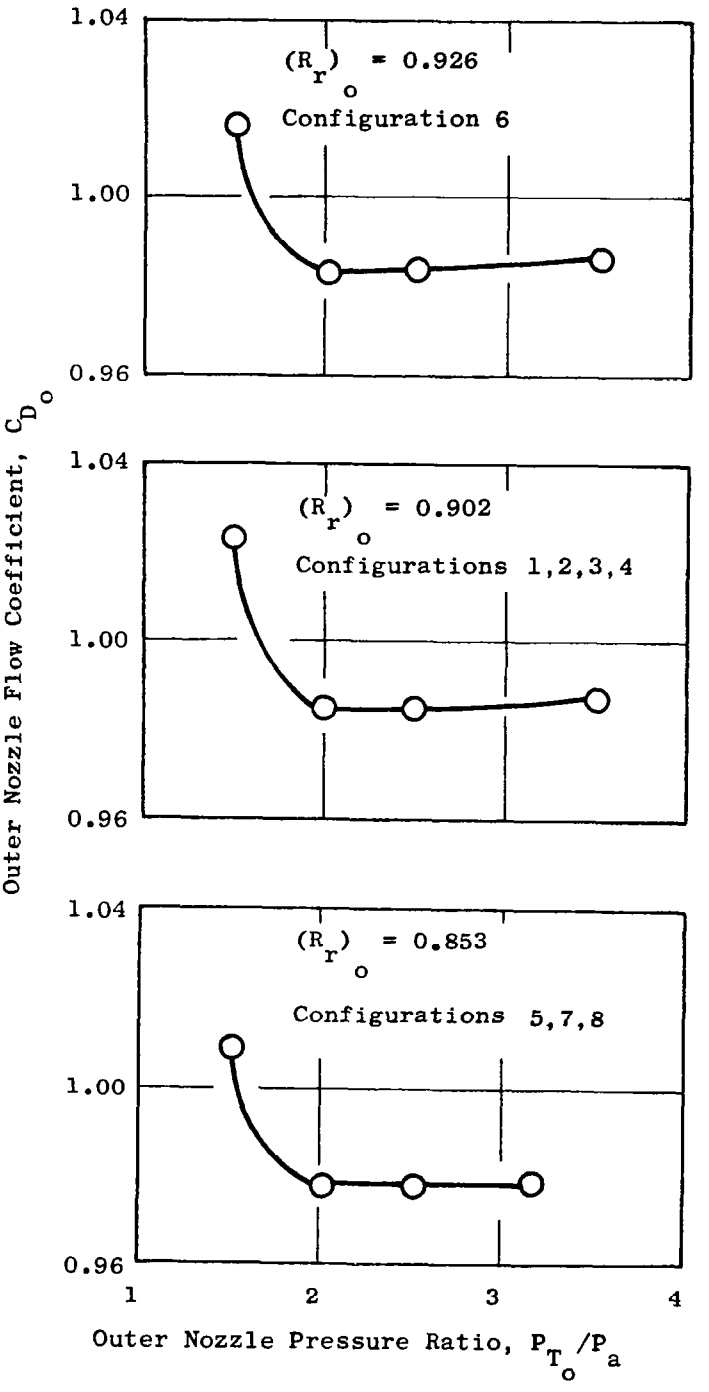

Figure 6-26. Outer Nozzle Flow Coefficients.

- $P_{T_o}/P_a = 1.5$
- $W_i/W_o = 0$
- $M_a = 0$
- DM = 0.203 m (8.0 in.)

Symbol	Tap Location
○	Outer Shroud
□	Outer Plug
△	Inner Plug

Note: X/DM = 0 at Plane of Outer Nozzle Throat

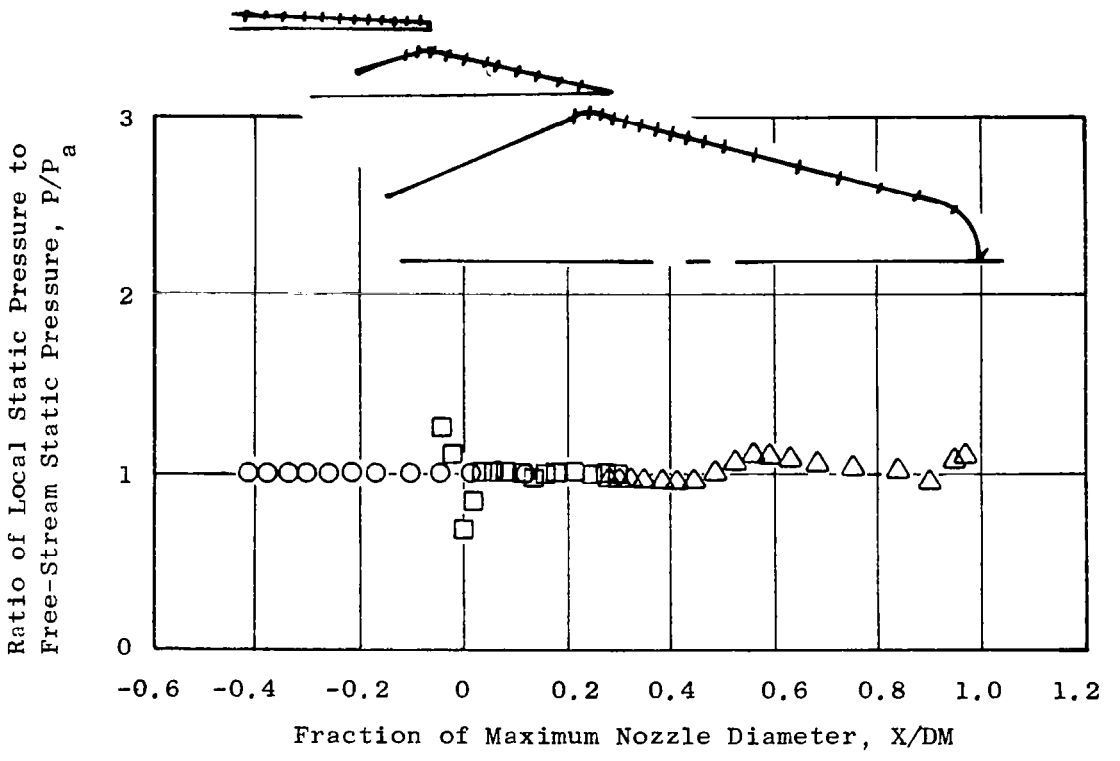

Figure 6-27. Measured Static Pressure Distribution with Unchocked Outer Nozzle, Configuration 2, Low Inner Flow.

restriction in the flow area of the inner stream, raising the static pressure in the throat region and lowering the flow coefficient. Some configurations, most notably Configuration 5, exhibited both characteristics, increasing at some combinations of inner and outer pressure ratio and decreasing at others.

7.0 SUMMARY DISCUSSION

Sections 5.0 and 6.0 discussed in detail the analysis of the static acoustic measurements performed in General Electric's Anechoic Jet Noise Facility, and the wind tunnel aerodynamic performance measurements performed in the NASA Lewis 8 x 6 foot supersonic wind tunnel of several high-radius-ratio coannular nozzles with plug. The analysis of the test measurements revealed a number of important results regarding the acoustic and aerodynamic performance of the tested coannular nozzles.

To establish the acoustic nature of the coannular nozzles tested, particular attention in the analysis was devoted toward establishing the characteristic flow and geometry parameters which govern the observed acoustic measurements. From a turbulent mixing noise point of view, it is well known that the fully expanded jet velocity and jet density are of key concern. For a simple conical nozzle, the selection of the velocity and density parameters is straightforward. However, for a dual flow system the selection of these parameters becomes somewhat more complicated. When the flows issuing through the nozzles are of the inverted type - the high velocity and high temperature gas flow are on the outside stream, and the lower velocity, lower temperature gases are on the inside stream - there is the inclination toward selecting the higher velocity outer stream velocity and density as the parameters which govern the noise production. Further consideration might also lead one to suspect that some sort of an average velocity might be more appropriate. Three acoustic power level expressions are formulated in Section 5.1 illustrating the combinations of outer stream or mixed stream parameters that can be considered. The test data were presented in various forms and compared with the conical nozzle data. Some of the key observations made were:

- For coannular nozzle flows, the characteristic velocity governing the acoustic radiation level is the mixed stream or weight flow averaged velocity, V_J^{mix}. Similarly, the characteristic density is the mixed stream static density.

- The radiated acoustic power and the acoustic efficiency parameter have distributions very similar to that of a conic nozzle when the acoustic power is illustrated in terms of a Lighthill parameter written for two flows (a synthesized conical nozzle flow) or in terms of a mixed stream acoustic Mach number ($M_o^{mix} = V_J^{mix}/a_o$) when illustrating the acoustic efficiency parameters. These similarities in distribution lead to the notion that the fundamental noise production mechanisms for coannular nozzles are similar to those of a conic nozzle. These results do show however, that the high radius ratio coannular nozzles have a fundamentally lower noise level than a conic nozzle operating at the same mixed velocity or mechanical power. The basic level of reduction can be characterized in the calculated Lighthill coefficient K. In general it was shown that high radius ratio coannular nozzles are approximately 6 dB lower in acoustic power, and that the Lighthill coefficient is a complicated function of the geometry and flow variables.

- From a practical point-of-view, the Perceived Noise Level results were presented in a normalized fashion. PNL was normalized per unit thrust and mixed stream density. This normalization is similar to viewing the acoustic efficiency except that instead of the noise per unit mechanical power, the noise per unit thrust at a variable density exponent is now considered. When the results are presented against the mixed stream velocity, any comparisons of the coannular nozzle data are assured of being performed at the proper thrust and weight flow of the system.

- Linear regression curves were generated for OAPWL and PNL_{max} for the coannular nozzles tested. These prediction curves are considered quite good over the range of the tested results. A complilation of the results show that there are geometry influences which can be used to develop acoustically better coannular plug nozzle designs. The results show that 4 to 7.8 PNdB noise level reductions relative to a conic nozzle can be obtained at $V_j^{mix} \simeq 700$ m/sec.

- A multiple regression analysis was performed on all the test data. The results of this data analysis showed that for OAPWL, the velocity power law for all the data was 8.9, the density power law was 2.5 - both of these values are somewhat higher than the classical values of 8 and 2, respectively. The Maximum Perceived Noise Level had an even higher velocity dependence, $(V_j^{mix})^{9.5}$, but more of a classical density dependence, $(\rho_j^{mix})^{1.88}$. Results also showed that PNL_{max} increases with increasing area ratio, and decreases with increasing outer stream radius ratio.

To complement the above studies, analysis of the test results of several controlled experiments were performed to further examine the temperature and velocity dependence of coannular nozzles, and to examine the general spectral content of these nozzles. The velocity and temperature dependence studies not only confirmed the previous findings discussed above, but also showed that the velocity and density exponents for OASPL varied with the observation angle. Analysis of the overall power spectra test results showed that, as is true for a conic nozzle, increasing the temperature of a coannular nozzle (but maintaining the same mixed stream velocity) tends to increase low frequency noise, decrease high frequency noise, and shift the peak of the spectrum to lower frequencies.

Examination of the sound-pressure-level spectra at various acoustic angles revealed several phenomenological notions of how coannular nozzle jet noise may be constructed. The 90° spectra are fairly regular noise spectra that have two very slight peaks at model scale frequencies of approximately 1600 Hz and 6300 Hz. The high frequency peak is believed to be associated with the outer stream jet. In the forward quadrant ($\theta_I = 50° \rightarrow 90°$), the spectra are found to be generally regular in shape and have a classical Doppler shift in peak frequency spectra. As the spectra are viewed from $\theta_I = 90°$ to 150°, a low frequency hump of noise is observed which dominates the spectra at

the peak angles of radiated noise. The low-frequency hump was observed to follow an inverse Doppler shift - a phenomenon associated with acoustic propagation influences, rather than turbulent mixing noise characteristics. These results indicate that in formulating the physical processes governing an engineering acoustic spectra prediction method, the amplitude of noise will be governed by the mixed stream velocity and static jet density, the high frequency of noise (excluding shock noise) will be associated with the outer stream of the coannular jet, and the low frequency noise will have to be characterized by acoustic propagation mechanisms.

In addition to the general acoustic characteristics observed above, a detailed analysis of the acoustic measurements were performed to illustrate the influences of the inner stream flow management and the key geometric design variables. The results of the analysis have shown that:

- When dealing with a high radius ratio coannular nozzle with absolutely no inner stream flow, or with just small amounts of inner stream flow, dramatic changes occur in spectral and directivity shaping as compared to typical conic nozzle test results. The general results are that when the outer radius ratio increases, the noise decreases; as small amounts of inner stream flow are added (holding the outer stream constant), the peak frequency noise shifts to lower frequencies, and the angle of peak noise occurs at angles closer to the jet axis than does a conical nozzle; the level of noise is governed by the V_j^{mix} velocity parameter.

- A series of tests were conducted to determine the influence of inner stream to outer stream velocity ratio, V_r, on the noise levels of all coannular nozzles. For these tests, the velocity ratio varied from $V_r = 0.1$ to 0.7. The results showed that the "best" velocity ratio occurred at $V_r \sim 0.6 \rightarrow 0.7$; for $A_r > 1$ selection of an operating V_r off this design value could amount to as much as a 4 PNdB higher noise level than at the design V_r; $A_r \leq 0.53$ the selection of the V_r was not as critical, although a $V_r \sim 0.6 \rightarrow 0.7$ is still recommended; velocity ratio rather than weight flow ratio should be used in selecting critical flow design parameters.

- The key coannular nozzle geometry parameters are the area ratio, A_r, the outer stream radius ratio, R_r^o and the inner stream plug shape. The analysis of data showed that at a constant mixed stream velocity, increasing area ratio (while holding outer stream radius ratio constant) increases the noise level of coannular nozzles. The increase in noise occurs in the higher frequencies. When the area ratio is maintained, an increase in outer stream radius ratio results in a decrease in the noise. The noise decrease was observed in the higher frequencies. The inner stream plug shape (holding V_j^{mix}, R_r^o and A_r constant) was found to have an influence on the suppression characteristics of coannular nozzles. When the inner stream plug was tested with a bent type shape (simulating a flap-and-seal arrangement), up to 2 PNdB noise level

reduction was observed compared to a similar nozzle, but with a conic plug arrangement. The spectral characteristics were such that the bent plug arrangement gave reductions uniformly over all frequencies.

In the forward quadrant of the acoustic observation angles, the high radius ratio coannular nozzles exhibited shock broad-band noise which apparently resulted from complicated outer stream, inner stream, and mixed stream shock patterns. The parameter found to govern OASPL and PNL shock noise levels was a mixed stream shock strength parameter, β_J^{mix}, defined by $\beta_J^{mix} = \sqrt{(M_J^{mix})^2-1}$. Analysis of the data showed that the shock noise for coannular nozzles varied as $(\beta_J^{mix})^4$, but were generally several dB lower than the conic nozzle shock noise levels. At certain conditions the coannular nozzle shock broad-band noise was found to reach equivalent conical nozzle shock noise levels. To avoid the conditions at which coannular nozzle shock noise approaches the conic nozzle levels it is recommended that the pressure ratios be kept below 3.0 and $P_r^i/P_r^o<1$. The frequency distribution for coannular nozzles was found to exhibit a Doppler shift; there appears to be a lower frequency shock spectra (located by using the equivalent diameter of the total area) and a higher frequency shock spectra (located by using the equivalent diameter of the total area) and a higher frequency shock spectra (located by using the annulus height of the outer stream nozzle). To obtain a better understanding of coannular nozzle shock noise spectral composition, and the key characteristic shock noise dimensions, narrow band data analysis will have to be carried out.

In formulating a physically understandable spectral prediction process for high radius ratio coannular nozzles with plug, use of some of the more interesting insights revealed during this investigation will have to be incorporated. What is obvious, however, is that, in addition to the usual turbulent mixing concepts from which prediction models can be formulated, the role of acoustic propagation influences, such as convection and fluid shielding, on the spectral features will have to be considered. Additionally, a separate effort to formulate a physically realistic view of coannular nozzle shock noise will be needed. The results of the data analysis up to this point have shown, however, that the mixed stream conditions (V_J^{mix} and ρ_J^{mix} for the nonshock related noise in the aft quadrant and β_J^{mix}, for the shock noise in the forward quadrant angles) will play an important role in correlating the overall level of noise and the spectral composition of the noise. Correlations of the overall levels (OAPWL, PNL_{max}, OASPL) of coannular nozzle noise have been adequately illustrated throughout the text.

Here a sample of the spectral collapse of coannular nozzle data will be illustrated. Figure 7-1 shows such a sample. The presentation of Figure 7-1 shows the normalized one-third octave-band sound-pressure-level spectra (normalized with respect to the overall sound pressure level) at $\theta_I = 130°$ versus 10 log fD/V_J^{mix} for Configurations 6 and 7 (configurations which represent the largest variations of outer stream radius ratio [R_r^o)Config 6 = 0.926 ; R_r^o) Confiug 7 = 0.853] and area ratio [A_r)Config 6 = 1.42 ; A_r)Config 7 = 0.33] tested during this program. Measurements are presented over a wide range of mixed velocities corresponding to subcritical, critical , and supercritical nozzle conditions. The general data collapse shown for each configuration, as well as comparison between the two configurations is striking. The

Symbol	Angle	Conf	Point	V_j^i	V_j^o	V_j^{mix}	V_j^i/V_j^o	P_r^i	P_r^o	T_T^i	T_T^o
○	130°	6	640	409.35	493.2	435.6	0.83	1.9701	1.7241	473.3	833.9
◇	130°	6	643	416.4	583.4	473.0	0.71	2.0091	2.0439	477.2	907.8
□	130°	6	645	496.2	701.1	559.0	0.71	2.9884	2.7632	465.1	957.8
○	130°	7	760	321.6	326.4	324.8	0.99	1.4929	1.3114	475.6	709.4
◇	130°	7	777	440.1	654.7	590.0	0.67	2.2093	2.4002	475.6	952.2
□	130°	7	781	477.6	719.6	664.5	0.66	2.5148	3.6493	490.0	826.1

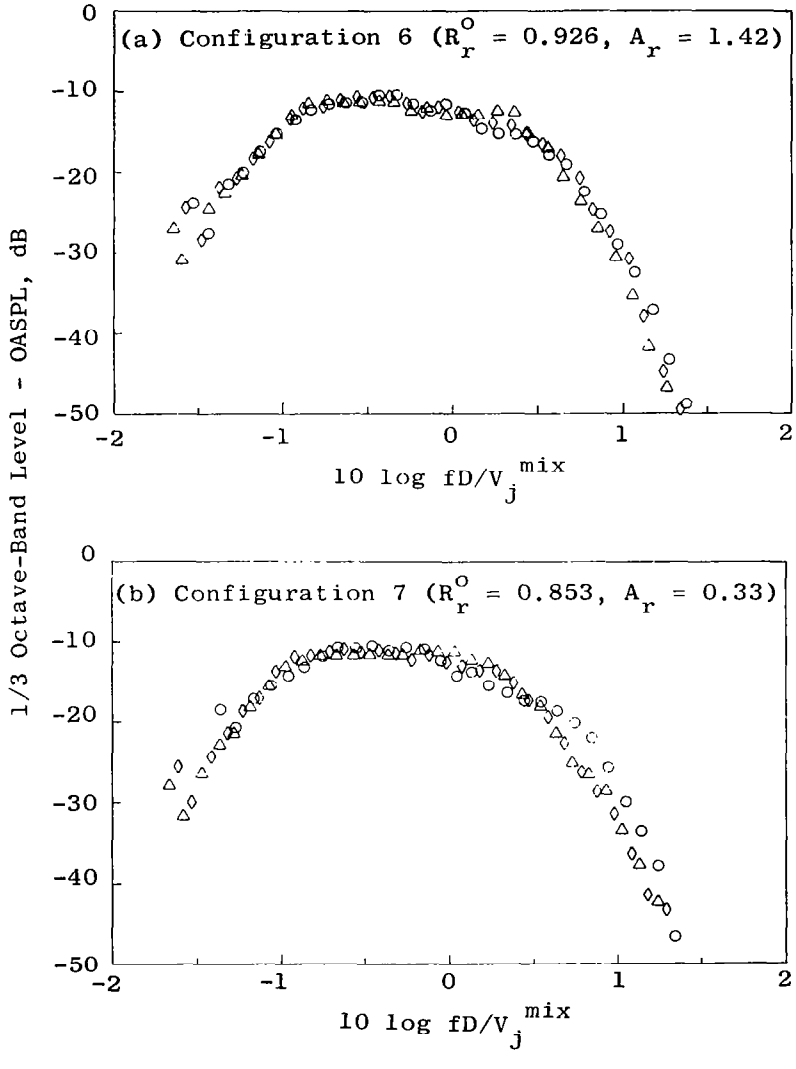

Figure 7-1. Normalized 1/3 Octave Band Sound Pressure-Level Spectra for Configurations 6 and 7 Over Subcritical, Sonic and Supercritical Flow Conditions.

power of the mixed stream velocity in correlating the coannular nozzle noise characteristics, but now used in the specification of the frequency parameter, is again illustrated. Data presentations at other observation angles have been reviewed. The results are similar to what is found in Figure 7-1, but there is a slightly greater variation in the high frequency part of the spectra. It is speculated that such variations could be taken care of with some engineering correction for the Strouhal number to account for differences in perhaps velocity ratio, area ratio, and outer stream radius ratio.

The wind tunnel aerodynamic performance measurements obtained for the high radius ratio coannular nozzles in the NASA Lewis 8 x 6 foot supersonic wind tunnel were also very encouraging. Analysis of the measurements showed that the facility yielded high quality data (generally better than $\pm 0.5\%$ accuracy and repeatability). Generally, the coannular nozzles exhibited high levels of static and flight performance values of static gross thrust coefficients, C_T, up to 0.98, and simulated flight gross thrust coefficients up to 0.974 at an ambient stream Mach numbers of 0.36. As was found for the acoustic measurements, the performance trends for the tested coannular configurations were observed to be sensitive to nozzle geometry and flow variations.

The coannular plug nozzle configurations operating with low, or bleed inner flow rates experienced a pump-down in pressure of the inner nozzle flow area. This low pressure region results in a substantial thrust loss, particularly at zero inner flow conditions, and at the lower inner stream flow bleed test cases on configuratins for which the inner stream flow area was large. The bent inner plug geometry also incurred a performance loss at high inner-nozzle pressure ratios. Relative to a conical plug geometry, 1% to 2% thrust coefficient losses were measured.

To illustrate the performance levels measured at conditions typical of variable cycle engine operating conditions, Figure 7-2 is given. Shown on Figure 7-2 is the thrust coefficients for Configurations 1 through 6 at an ambient Mach number of 0.36 where the inner and outer stream pressure ratios are approximately 3.0, and the mixed stream velocity is 692 m/sec. Configurations 5 and 7, which have the lowest outer stream radius ratio ($R_T^o = 0.853$), have the best flight performance ($C_T \sim 0.97$).

To summarize the static acoustic, and wind tunnel performance characteristics for the tested configurations two additional illustrations are given. Figure 7-3 presents the measured perceived noise level reductions relative to a conical nozzle operating at the same thrust and weight flow conditions. Maximum PNL reductions are observed to range from 4.7 to 6.8 Δ PNdB. Figure 7-4 combines the results from Figures 7-2 and 7-3 to illustrate typical variable cycle engine takeoff static PNL reduction (relative to a conic nozzle) per unit percent thrust loss (relative to a single plug nozzle) at an ambient Mach number of 0.36. The static PNL noise level reductions per unit percent flight thrust coefficient loss, $\Delta PNL_{max}^{static}/\Delta C_T)^{M_a=0.36}$, are found to range from 1.3 for Configuration 1 and up to 3.2 for Configuration 7.

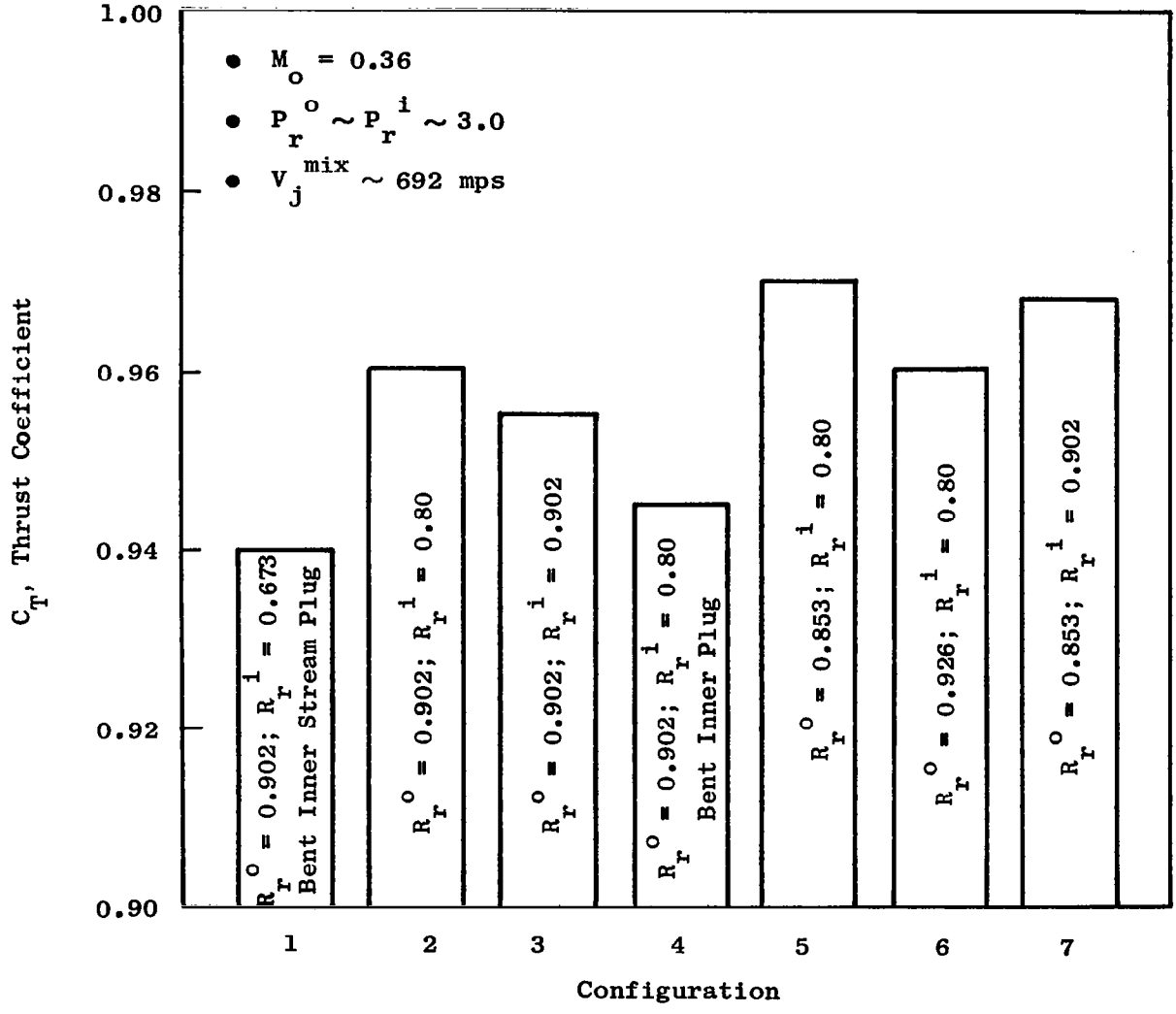

Figure 7-2. Wind Tunnel Thrust Coefficients for High Radius Ratio Coannular Nozzles at Typical Variable Cycle Engine Takeoff Conditions at an Ambient Mach Number of 0.36.

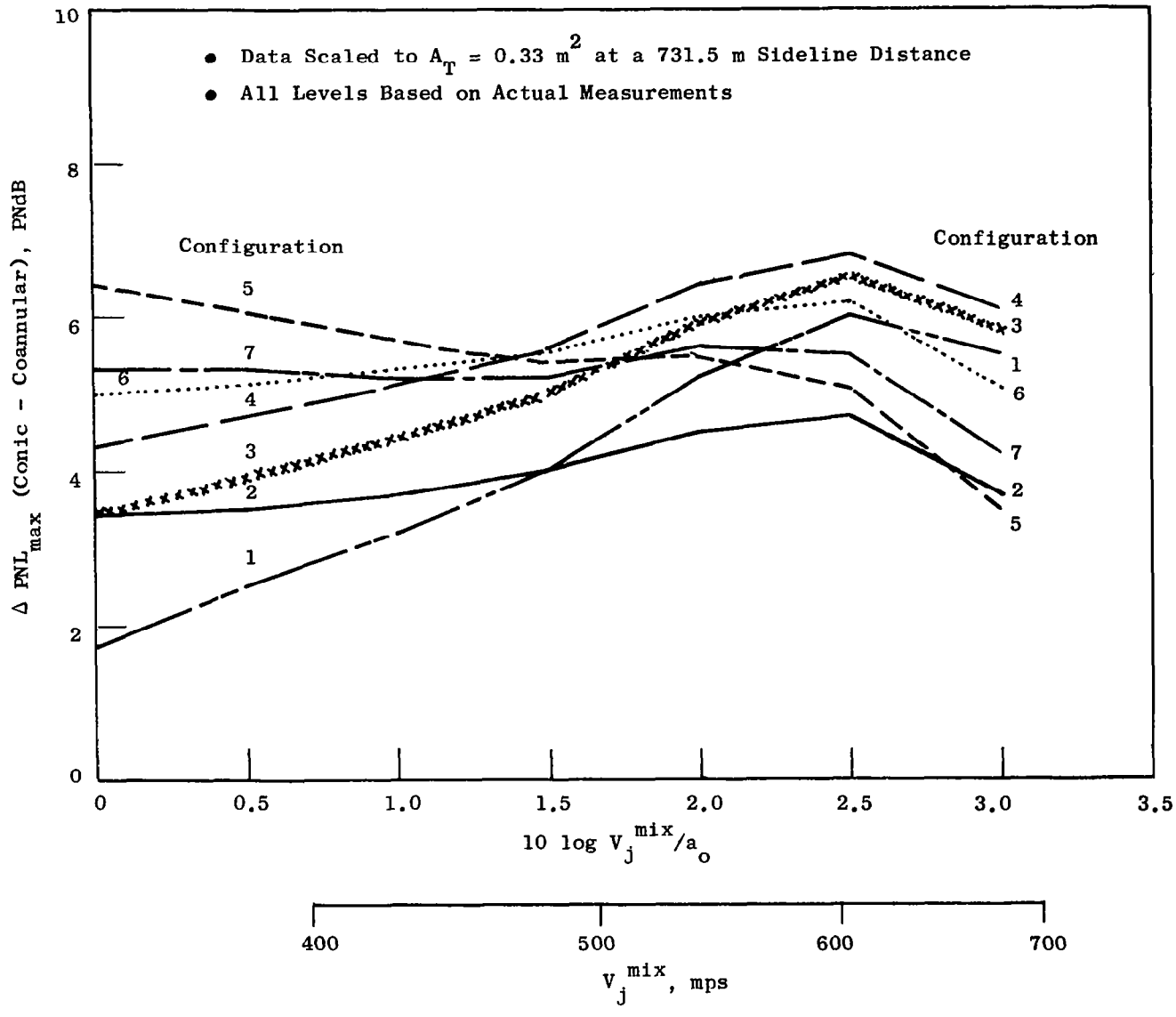

Figure 7-3. Measured Perceived Noise Level Reductions for High Radius Ratio Coannular Nozzle Relative to a Conic Nozzle at the Same Thrust and Weight Flow Conditions.

- Acoustic Data Based on Static Data Scaled to A_T = 0.33 m^2 at a 731.5 meter Sideline Distance
- $V_j^{mix} \sim$ 692 mps - Conditions at Typical VCE Takeoff
- Wind Tunnel Performance Measurements at Ambient Mach Number of 0.36
- $C_T)_{ref}$ = 0.981 (for Unsuppressed Single Flow Plug Nozzle at M_o = 0.36)

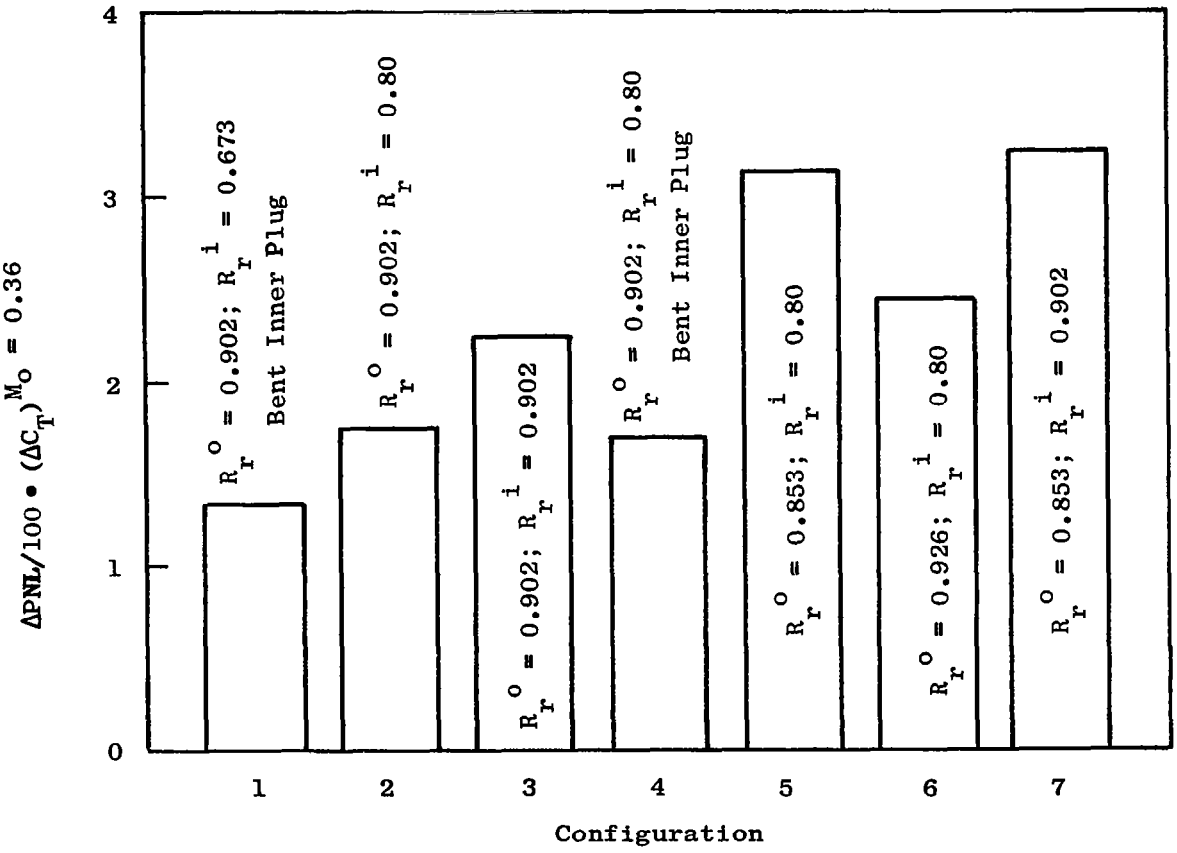

Figure 7-4. Typical Static Acoustic Perceived Noise Level Reductions per Unit Percent Flight Thrust Coefficient Loss at Typical Variable Cycle Engine Takeoff Conditions.

8.0 CONCLUSIONS AND RECOMMENDATIONS

8.1 CONCLUSIONS

In all, seven acoustic models and eight aerodynamic performance models were successfully tested for the evaluation of high-radius-ratio coannular plug nozzles as candidate exhaust nozzle configurations for advanced supersonic transport (AST) engine applications. The acoustic tests were static whereas the aerodynamic performance tests were performed in a wind tunnel for static and simulated flight evaluation. The nozzle geometric variables included outer stream radius ratio (ranging from 0.853 to 0.926), inner stream to outer stream area ratio (ranging from 0.33 to 1.56) and inner stream plug shape. Outer stream total temperatures ranged from 400 to 970 K. Inner stream velocities ranged from 0 to 550 m/sec and inner stream total temperatures ranged from ambient to 925 K. All tests were of the inverted flow type - high velocity and temperature flows on the outer stream, and lower velocity and temperature on the inside stream.

The following are the most significant results:

- The overall acoustic results* (OAPWL, PNL_{max}, OASPL) were best correlated using mixed stream velocity or specific thrust, V_J^{mix} (defined as the ratio of the ideal total thrust to the ideal total mass flow) and the mixed stream density. When compared to a conic nozzle at the same specific thrust, the static acoustic results showed up to 7 PNdB peak aft angle noise reductions for product size engines.

- The shock noise from high-radius-ratio coannular plug nozzles was correlated well using a mixed stream shock parameter defined as $\sqrt{(M_J^{mix})^2-1}$. Additionally these nozzles enjoyed considerable shock noise reduction relative to the conic nozzle (up to 7 PNdB at θ_I = 50°, at product size).

*Since the completion of the work for this contract a considerable amount of work has been spent on formulating a spectral prediction process for high-radius-ratio coannular plug nozzles under contract NAS3-20619. In essence we have found that

1. V_J^{mix} is still an excellent correlating parameter for the overall acoustic properties such as PNL_{max}, OAPWL, and OASPL.
2. Based on (a) a low frequency 90° spectrum (characterized by V_J^{mix}, T_J^{mix} D_{eq}), (b) a high frequency 90° spectrum (characterized V_j^o, T_j^o, $D_{hydrolic}$), (c) a universal (single curve) fluid shielding function devised from modern theoretical jet acoustic concepts, (and calibrated from our coannular plug nozzle test results), and
3. By applying the theoretical expressions for convective amplification and Doppler shift, an excellent spectral prediction process has evolved.

- Outer stream velocity ratio, inner stream to outer stream area ratio, and inner stream to outer stream velocity ratio were all found to influence the noise reduction characteristics of the coannular plug nozzle. A rank ordering of these parameters could be listed as follows:
  - V_j^{mix} - the strongest parameter (the lower the better)
  - Outer stream radius ratio R_r^o - higher radius ratio means greater noise reduction (for single stream and dual stream plug nozzles)
  - Inner stream to outer velocity ratio, V_r - V_r ~0.6 seems to be about the best, however, the level of mitigation of coannular plug nozzle noise reduction due to "off-optimum" V_r^i does depend on the area ratio.
  - Inner stream to outer stream area ratio, A_r as a sole acoustic parameter seemed to have the least rank order in priority, however, it should be kept in mind that velocity ratio and area ratio are samples and at product aircraft/engine approach conditions the selection of these area ratio will influence the specific thrust - the trade between opeating at an off optimum A_r could be well off-set by a much lower V_j^{mix}.

- Note should be taken that when tests were run with no inner flow, high radius ratio was again a key geometry parameter, and substantial noise reduction was obtained.

- Wind tunnel aerodynamic tests showed that static and simulated flight thrust coefficients at typical takeoff conditions are quite good - up to 0.98 at static conditions and 0.974 at a takeoff Mach number of 0.36. At low inner stream flow conditions significant thrust loss was observed. Using an inner stream conic plug resulted in 1% to 2% thrust coefficient losses as measured.

8.2 RECOMMENDATIONS

Based on the studies conducted during the contract efforts, the following items warrant future investigation:

- A systematic investigation of the acoustic flight effects on unsuppressed high-radius-ratio coannular-plug nozzles should be carried out. This investigation should include additional static acoustic measurements, and detailed aerodynamic-plume surveys aimed at illustrating the mean velocity and turbulent velocity profiles for the tested nozzles. Minimization of coannular-plug-nozzle shock noise should be one of the major test efforts. Additionally, systematic investigations of high radius ratio single stream plug nozzles should be pursued (particularly for flight evaluation).

- The development of an engineering acoustic prediction process should be undertaken. The formulation of the prediction process should rely on the many key experimental findings of this program as well as the latest turbulent-mixing, acoustic-propagation and shock-noise theories.

9.0 NOMENCLATURE

A	Cross-sectional area
A*	Critical flow area
a	Speed of sound
cm	Centimeter
C_D	Flow coefficient
C_T	Thrust coefficient
c, $\hat{c}$	Constant of proportionality
CDR	Comprehensive data report
D	Drag
dB	Decibel
D	Diameter
F	Thrust
f	Frequency
f_9	Dimensionless stream thrust parameter
FM	Frequency modulated
FSDR	Full scale data reduction computer program
h	Annular step height dimension
Hz	Hertz, cycles per second
I	Acoustic intensity
ips	Inches per second
JENOTS	General Electric Jet Engine Noise Outdoor Test Site
K	Lighthill coefficient
k	Critical flow factor
kHz	Kilohertz
L	Lighthill parameter (Section 5.1), shock separation distance (Section 5.3)
m	Known value of parameter

M	Mach number
M_c	Convection Mach number
M_a	Ambient Mach number
M_o	Acoustic Mach number
M.P.	Mechanical power
mm	Millimeter
mps	Meter per second
m	Mass
n	Number of samples taken of a given parameter
N	Newtons
OAPWL	Overall sound-power-level
OASPL	Ovewrall sound-pressure-level
1/3 OBPWL	1/3 octave band sound-power-level
1/3 OBSPL	1/3 octave band sound-pressure-level
P_T	Total pressure
P	Static pressure
PNL	Perceived noise level
RH	Relative humidity
RN	Reynold's number
R_r	Radius ratio
R	Radial Dimension of Models, Acoustic Range
SPL	Sound-pressure-level
STA	Supersonic tunnel association
T_T	Total temperature
T	Static temperature
U_c	Convection velocity
V	Ideally expanded velocity
VCE	Variable cycle engine

$\dot{W}$	Weight flow rate
$\bar{X}$	Mean of measured values of a parameter
X_i	Individual measured value of the parameter
β	Shock strength parameter
η	Acoustic efficiency
θ	Angle
θ_I	Angle measured relative to the inlet centerline
π	Radiated acoustic power
ρ	Jet static density
$\sigma y/x$	Standard error of estimate, dB
ω	Density exponent

Subscripts

eq	Equivalent
max	Maximum
o	Ambient conditions
j	Based on ideal jet conditions
ref	Reference
r	Ratio
s	Static
V	Measured at the choked venturi meter

Superscripts

i	Inner stream
o	Outer stream
mix	Fully mixed conditions
P	Peak

10.0 REFERENCES

2-1. Dosanjh, D.S., Abdelhamid, A.N., Yu, J.C., "Noise Reduction from Interacting Supersonic Jet Flows," NASA SP-207, Basic Aerodynamic Noise Research, 1969.

2-2. Dosanjh, D.S., Bhutiani, P.K., Ahuja, K.K., and Bassiouni, M.R., "Supersonic Jet Noise Suppression by Coaxial Cold/Heated Jet Flows," AIAA Paper No. 76-507, July 1976.

2-3. Dosanjh, D.S., Bhutiani, P.K., Ahuja, K.K., "Supersonic Jet Noise Reduction by Coaxial Cold/Heated Jet Flows," Final Report to DOT under grant DOT-OS-20094, March 1977.

2-4. Kozlowski, Hilary and Packman, Allan B, "Aerodynamic and Acoustic Tests of Duct-Burning Turbofan Exhaust Nozzles," NASA CR-2628, 1976.

2-5. Knott, P.R., Stringas, E.J., Brausch, J.F., Staid, P.S., Heck, P.H., and Latham, D., "Acoustic Tests of Duct-Burning Turbofan Jet Noise Simulation," NASA CR-2966, 1978.

2-6. Knott, P.R., Whittaker, R.W., Bhutiana, P.K., "Acoustic and Aerodynamic Nozzle Performance Design Considerations for the AST/VCE Early Acoustic Nozzle Program," General Electric Report R78AEG241-3, August 1978.

2-7. Pao, S.P., "A Correlation of Mixing Noise from Coannular Jets with Inverted Flow Profiles," NASA Technical Paper 1301, April 1979.

3-1. Savell, C.T., Stringas, E.J., "High Velocity Jet Noise Reduction Task I - Activation of Facilities," FAA - RD - 76 - 79 I and Ia, 1977.

3-2. Knott, P.R., Stringas, E.J., Brausch, J.F., Staid, P.S., Heck, P.H., and Latham, D., "Acoustic Tests of Duct-Burning Turbofan Jet Noise Simulation," NASA CR-2966, 1978.

3-3. Staid, P.S., "Wind Tunnel Performance Tests of Coannular Plug Nozzles," NASA CR2990, 1977.

5-1. Crow, E.L., Davis, F.A., Maxfield, N.W., "Statistics Manual," Dover Publications, Inc., 1960.

5-2. Hoch, R.G., Duponchel, J.P., Crocking, B.J., Bryce, W.D., "Studies of the Influence of Density on Jet Noise," First International Symposium on Air Breathing Engines, Marseille, 19-23, June 1972.

5-3. Furguson, D.R., Smith, M.A., Knott, P.R., "Supersonic Jet Noise Investigation," Volume III - Computer User's Manual for Aero Acoustic Prediction, p. 610, July 1976.

5-4. Drevet, P., Duponchel, J.P., Jaques, J.R., "Effect of Flight on Noise from Convergent Nozzles as Observed in the Bertain Aerotrain," AIAA 76-557.

5-5. Harper-Bourne, Fisher, M., "The Noise from Shock Waves in Supersonic Jets," AGARD Conference Proceedings, No. 131, 1973.

6-1. Harrington, D.E., Schloemer, J.J., and Skebe, S.A., "Thrust Performance of Isolated 36-Chute Suppressor Plug Nozzles with and without Ejectors at Mach Numbers from 0 to 0.45," NASA TMX-3298, October, 1975.

6-2. Blozy, J.T., Knott, P.R., Staid, P.S., "Acoustic and Performance Investigation of Annular Plug Nozzles with Base Bleed," Concept Screening Report, NASA Contract, NAS3-19777, 1976.

TABLE I-1A AERODYNAMIC TEST DATA - CONFIGURATION 1

A^i = 71.335 cm^2(11.057 in^2)
A^o = 111.277cm^2(17.248 in^2)
A_r = 1.56

DATA PT	V^i_j m/sec	T^i_t °K	T^i_j °K	P^i_r	V^o_j m/sec	T^o_t °K	T^o_j °K	P^o_r	V^{mix}_j m/sec	T^{mix}_t °K	T^{mix}_j °K	P^{mix}_r	V^i_j / V^o_j	W^i/W^o
1	304.8	292.8	246.6	1.8247	257.3	383.3	350.4	1.3693	291.7	317.7	275.4	1.6494	1.1848	2.6267
2	298.7	292.2	247.8	1.7801	294.7	395.0	351.8	1.5002	297.5	323.9	279.9	1.6676	1.0134	2.2440
3	299.9	298.9	254.1	1.7643	448.7	538.9	438.8	2.0536	352.6	383.9	322.1	1.8497	0.6685	1.8216
4	302.7	303.3	257.8	1.7680	621.5	770.0	587.9	2.7092	422.6	478.9	390.1	2.0511	0.4870	1.6573
5	369.1	549.4	482.8	1.5846	240.5	405.6	376.8	1.2938	324.3	499.3	447.2	1.4730	1.5349	1.8684
6	370.6	550.0	482.8	1.5902	300.2	405.6	360.7	1.5070	341.8	490.8	432.7	1.5544	1.2345	1.4387
7	374.6	549.4	480.8	1.6081	371.2	469.4	400.9	1.7379	373.1	514.8	445.8	1.6581	1.0090	1.3124
8	374.6	558.3	489.9	1.5950	555.3	657.2	507.8	2.5271	462.1	606.2	502.6	1.9598	0.6745	1.0646
9	372.5	557.8	490.1	1.5868	739.1	919.4	668.1	3.3491	560.3	743.0	595.4	2.2709	0.5039	0.9525
10	451.1	724.4	629.7	1.6891	832.1	970.0	649.7	4.5207	677.3	870.3	658.6	2.8630	0.5421	0.6841
12	14.6	855.0	854.9	1.0004	780.3	957.2	677.9	3.7048	765.4	955.2	687.2	3.5026	0.0188	0.0198
13	29.3	848.3	848.0	1.0018	780.9	960.0	680.5	3.6964	751.9	955.7	697.8	3.3224	0.0375	0.0401
14	41.5	800.0	799.2	1.0037	783.9	966.1	684.7	3.7036	741.7	956.7	706.3	3.1928	0.0529	0.0603
16	10.7	857.8	857.7	1.0002	699.5	961.1	740.5	2.7378	686.3	959.1	747.2	2.6285	0.0153	0.0195
17	22.3	875.6	875.3	1.0010	702.9	968.3	746.0	2.7437	676.7	964.8	759.4	2.5331	0.0317	0.0400
18	31.7	837.8	837.3	1.0021	702.3	967.8	745.8	2.7401	664.6	960.5	762.6	2.4513	0.0451	0.0596
20	7.6	760.6	760.5	1.0001	577.9	894.4	744.0	2.0378	566.5	891.8	747.4	1.9812	0.0132	0.0203
21	15.5	788.9	788.8	1.0005	577.9	888.3	737.7	2.0491	556.5	884.5	745.1	1.9413	0.0269	0.0396
22	22.6	762.2	762.0	1.0012	575.8	887.2	737.7	2.0392	544.6	880.2	746.7	1.8893	0.0392	0.0598
23	2.7	365.0	365.0	1.0000	395.0	753.3	681.8	1.4608	387.2	745.6	676.8	1.4440	0.0069	0.0202
24	10.7	482.2	482.2	1.0004	398.7	760.6	687.8	1.4660	376.9	744.9	679.8	1.4154	0.0268	0.0595
25	5.2	621.7	621.7	1.0001	460.6	795.0	698.3	1.6411	451.7	791.6	698.6	1.6121	0.0113	0.0197
26	16.8	661.1	661.0	1.0007	463.3	807.8	710.2	1.6374	437.8	799.4	712.3	1.5558	0.0362	0.0606
27	8.8	811.1	811.1	1.0002	641.6	948.9	764.5	2.3163	629.1	946.2	769.1	2.2402	0.0138	0.0201
28	25.9	801.1	800.8	1.0015	643.1	952.8	767.7	2.3176	608.4	944.2	779.1	2.1175	0.0403	0.0597
29	68.0	711.7	709.6	1.0114	702.3	965.0	742.8	2.7495	619.5	932.0	759.8	2.2097	0.0968	0.1500
30	71.9	701.7	699.3	1.0129	781.2	962.2	682.6	3.6870	705.2	934.3	708.1	2.8904	0.0921	0.1199
150	0.0	288.3	288.3	1.0000	780.6	961.1	681.9	3.6849	780.6	961.1	681.9	3.6849	0.0000	0.0000
151	0.0	288.3	288.3	1.0000	700.7	968.3	747.4	2.7245	700.7	968.3	747.4	2.7245	0.0000	0.0000
152	0.0	288.3	288.3	1.0000	569.4	898.3	752.7	1.9850	569.4	898.3	752.7	1.9850	0.0000	0.0000
153	0.0	288.3	288.3	1.0000	461.5	823.9	727.6	1.6139	461.5	823.9	727.6	1.6139	0.0000	0.0000
154	0.0	288.3	288.3	1.0000	404.2	768.9	694.3	1.4757	404.2	768.9	694.3	1.4757	0.0000	0.0000

NOMENCLATURE

P_r - Pressure Ratio

V_j - Fully Expanded Jet Velocity, m/sec

T_t - Total Temperature, °K

T_j - Static Temperature, °K

SUPERSCRIPTS

o - Outer stream

i - Inner stream

mix - Fully mixed inner & outer stream

SUBSCRIPT

t - Total

TABLE I - 1B ACOUSTIC TEST DATA - CONFIGURATION 1

				OASPL , dB MODEL SCALE ; 12.19 m (40 ft) ARC ; STD DAY							
				θ^i, degrees to inlet							
DATA POINT	T_{dry} °K	T_{wet} °K	BAROM n/m^2	50°	70°	90°	110°	130°	140°	150°	OAPWL, dB
1	287	285	99360.	89.4	91.4	93.4	95.9	99.0	101.4	103.5	139.7
2	287	286	99560.	90.4	92.2	94.3	96.8	100.0	102.4	104.0	140.5
3	287	286	99560.	96.5	98.2	100.5	103.4	107.0	108.1	109.0	146.9
4	286	284	99560.	105.4	106.4	107.6	111.0	115.2	116.1	116.7	155.2
5	302	293	99560.	90.6	92.5	95.3	99.1	104.3	107.6	109.4	10.0
6	302	293	99560.	91.7	93.6	96.5	100.3	105.5	108.6	110.4	145.5
7	302	293	99560.	93.7	95.5	98.5	102.1	107.0	109.9	111.7	147.1
8	302	293	99560.	101.5	102.8	105.1	109.0	113.3	114.7	116.3	153.0
9	302	293	99560.	110.0	111.1	111.9	115.7	121.4	123.0	123.7	160.9
10	303	294	99560.	112.5	113.8	115.9	120.0	126.9	130.4	130.9	166.9
12	290	288	99215.	111.0	112.7	114.1	118.3	128.1	130.4	129.2	165.9
13	290	288	99215.	108.6	111.0	113.2	118.0	127.3	129.3	128.9	165.2
14	290	288	99215.	108.1	110.7	113.1	118.0	126.4	129.5	129.0	165.1
16	291	288	99215.	105.7	107.5	109.6	113.6	122.5	125.5	124.6	160.8
17	291	288	99215.	104.8	106.9	109.3	113.6	121.5	125.3	125.4	160.7
18	291	288	99215.	104.0	106.4	109.2	113.5	121.4	124.0	124.4	160.0
20	290	288	99215.	104.8	101.5	104.2	107.9	113.0	117.0	117.9	153.3
21	290	288	99215.	99.0	100.8	103.4	107.2	112.7	116.2	117.5	152.6
22	290	288	99215.	96.1	100.6	103.7	107.5	112.6	115.5	117.4	152.5
23	289	287	99215.	97.8	94.6	95.9	99.9	102.2	103.9	105.2	142.5
24	289	287	99215.	91.8	93.6	96.8	99.3	101.4	103.0	104.2	141.7
25	289	287	99215.	90.1	98.9	103.0	105.5	107.1	109.0	110.0	147.4
26	290	288	99215.	97.6	98.1	102.5	104.7	106.5	108.3	110.6	147.3
27	290	288	99215.	98.7	103.8	106.7	110.7	117.5	121.4	121.0	156.8
28	290	288	99215.	100.9	103.0	106.2	110.7	117.0	120.3	120.7	156.3
29	291	288	99215.	100.1	105.6	108.6	113.1	119.6	122.7	123.4	159.0
30	290	288	99215.	102.8	110.6	112.7	117.5	124.1	127.9	128.4	163.9
150	286	282	99560.	109.1	112.7	114.2	118.8	130.0	128.0	127.1	166.3
151	287	283	99560.	112.1	107.6	109.5	114.3	123.6	124.6	124.0	162.2
152	288	283	99560.	107.6	101.3	104.0	107.7	113.6	117.0	117.4	154.4
153	288	283	99560.	101.1	98.0	101.4	103.1	106.8	108.7	110.5	147.8
154	289	284	99560.	100.9	94.6	97.2	98.7	102.7	104.1	104.7	143.6

TABLE I - 2A AERODYNAMIC DATA - CONFIGURATION 2

A^i = 73.226 cm^2(11.350 in^2)
A^o = 71.335 cm^2(11.057 in^2)
A_r = 1.026

DATA PT	V^i_j m/sec	T^i_t °K	T^i_j °K	P^i_r	V^o_j m/sec	T^o_t °K	T^o_j °K	P^o_r	V^{mix}_j m/sec	T^{mix}_t °K	T^{mix}_j °K	P^{mix}_r	V^i_j / V^o_j	W^i/W^o
240	413.0	477.2	392.4	1.9844	497.1	834.4	722.5	1.7398	446.0	617.1	521.2	1.8402	0.8308	1.5530
241	472.1	477.2	366.3	2.5236	556.9	890.0	750.6	1.9346	501.8	621.6	499.3	2.1934	0.8478	1.8581
242	498.7	415.6	291.8	3.4449	596.5	890.6	729.7	2.1540	527.0	553.2	415.8	2.7343	0.8360	2.4508
243	416.7	480.6	394.2	2.0006	573.6	893.3	745.2	2.0164	481.8	651.8	540.6	1.9737	0.7264	1.4109
244	469.1	475.6	366.1	2.4986	653.8	950.0	758.2	2.3993	541.9	662.5	520.9	2.3828	0.7175	1.5380
245	505.7	467.2	340.0	3.0418	698.9	970.6	751.0	2.7009	577.3	653.8	491.3	2.7744	0.7235	1.6978
246	415.7	471.7	385.7	2.0229	662.3	959.4	762.9	2.4374	526.0	689.7	558.0	2.1708	0.6277	1.2374
247	465.4	471.7	363.9	2.4793	753.2	920.0	658.3	3.5374	607.7	693.4	514.9	2.9223	0.6180	1.0222
248	504.7	468.3	341.6	3.0181	779.1	905.6	622.5	4.0533	636.6	678.4	480.1	3.4222	0.6479	1.0810
2107	136.6	373.9	364.6	1.0919	699.8	961.1	740.3	2.7405	542.8	797.5	661.6	2.0247	0.1951	0.3864
2108	206.3	371.7	350.5	1.2288	698.3	958.3	738.4	2.7361	512.4	736.6	613.8	1.9718	0.2955	0.6075
2110	274.9	472.8	435.2	1.3366	703.5	964.4	741.4	2.7626	535.0	771.2	638.3	2.0327	0.3908	0.6478
2112	422.5	475.0	386.2	2.0633	699.8	961.7	740.9	2.7386	553.3	704.5	558.8	2.3341	0.6037	1.1205
2113	491.9	474.4	354.0	2.7860	699.2	959.4	739.0	2.7407	574.5	667.6	507.7	2.6754	0.7036	1.5110
2114	171.0	366.1	351.6	1.1525	701.0	960.6	738.9	2.7536	524.5	762.6	634.8	1.9898	0.2439	0.4993
2115	353.6	476.7	414.5	1.6313	702.9	963.3	740.7	2.7608	539.9	736.3	599.3	2.1442	0.5030	0.8747
2116	391.1	475.0	398.9	1.8422	700.7	963.3	742.1	2.7413	545.0	717.7	577.2	2.2298	0.5581	1.0123
2117	449.0	471.7	371.4	2.3087	698.3	955.6	735.4	2.7456	559.7	686.6	536.3	2.4516	0.6430	1.2510
284	503.2	470.0	344.0	2.9809	798.6	895.6	595.6	4.5270	654.8	688.4	478.4	3.6469	0.6302	0.9486

NOMENCLATURE

P_r - Pressure Ratio

V_j - Fully Expanded Jet Velocity, m/sec

T_t - Total Temperature, °K

T_j - Static Temperature, °K

SUPERSCRIPTS

o - Outer stream

i - Inner stream

mix - Fully mixed inner & outer stream

SUBSCRIPT

t - Total

TABLE I - 2B ACOUSTIC DATA - CONFIGURATION 2

				OASPL , dB MODEL SCALE ; 12.19 m (40 ft) ARC ; STD DAY							
				θ^i, degrees to inlet							
DATA POINT	T_{dry} °K	T_{wet} °K	BAROM n/m^2	50°	70°	90°	110°	130°	140°	150°	OAPWL, dB
240	[illegible]	289	99560.	97.6	99.8	102.4	106.1	110.8	113.4	115.3	150.8
241	291	288	99560.	105.6	106.4	107.5	110.5	115.4	119.3	122.6	156.9
242	289	287	99560.	116.5	116.7	116.8	117.3	118.8	123.4	127.1	162.5
243	291	288	99560.	99.5	102.0	104.9	109.1	113.3	115.9	117.9	153.5
244	291	288	99560.	105.4	107.3	109.5	113.2	118.0	121.9	115.4	156.9
245	291	288	99560.	114.5	115.0	115.4	117.4	121.2	126.3	128.5	163.0
246	291	288	99905.	102.2	105.1	107.9	112.2	115.0	119.5	122.1	10.0
247	291	288	99905.	111.3	112.9	114.3	117.8	122.9	126.7	128.9	163.9
248	291	288	99560.	115.2	116.3	117.3	119.9	125.4	129.9	131.3	166.5
2107	291	288	99560.	116.4	117.5	118.4	120.9	127.0	132.0	132.3	168.1
2108	290	288	99905.	101.4	105.3	108.7	113.2	118.0	120.4	121.3	157.5
2110	291	288	99905.	101.5	105.1	108.4	113.0	117.4	119.2	118.8	156.5
2112	291	288	99905.	102.4	105.7	108.3	112.7	118.5	119.9	120.0	157.3
2113	291	288	99905.	104.2	106.9	109.3	113.6	119.3	121.3	123.4	158.9
2114	291	288	99905.	111.8	112.8	113.5	116.1	120.3	125.5	127.9	162.4
2115	290	288	99905.	102.3	105.5	108.8	113.4	118.1	118.9	119.4	156.7
2116	290	288	99560.	103.2	106.4	109.0	113.2	118.6	119.9	121.0	157.8
2117	291	288	99905.	104.0	107.1	109.1	113.4	118.7	120.9	122.4	158.4
284	290	288	99905.	105.9	108.0	110.1	114.2	119.3	122.5	125.1	160.0

TABLE I - 3A AERODYNAMIC DATA - CONFIGURATION 3

A^i = 37.923 cm^2(5.878 in^2); A^o = 71.335 cm^2(11.057 in^2); A_r = .532

DATA PT	V^i_j m/sec	T^i_t °K	T^i_j °K	P^i_r	V^o_j m/sec	T^o_t °K	T^o_j °K	P^o_r	V^{mix}_j m/sec	T^{mix}_t °K	T^{mix}_j °K	P^{mix}_r	V^i_j / V^o_j	W^i/W^o
312	108.8	718.3	713.0	1.0292	782.4	959.4	678.7	3.7229	744.3	945.8	692.7	3.2773	0.1391	0.0600
313	170.1	756.7	743.6	1.0695	783.6	963.3	681.9	3.7166	732.9	946.2	701.5	3.1383	0.2170	0.0902
314	208.2	702.8	682.9	1.1151	781.5	958.9	678.8	3.7126	720.0	931.4	694.7	3.0597	0.2664	0.1201
316	77.4	695.6	692.8	1.0151	696.2	957.2	738.6	2.7206	661.1	942.4	745.7	2.4742	0.1112	0.0600
317	118.3	712.2	705.9	1.0349	696.5	957.2	738.4	2.7233	648.8	937.0	747.6	2.3961	0.1698	0.0899
318	150.0	681.7	671.3	1.0596	695.9	955.0	736.5	2.7253	637.5	925.8	742.7	2.3440	0.2155	0.1196
320	50.9	580.0	578.8	1.0078	578.5	895.6	744.9	2.0392	548.2	877.5	742.0	1.9115	0.0880	0.0608
321	78.0	593.3	590.5	1.0181	577.0	892.2	742.2	2.0368	535.2	867.2	738.0	1.8643	0.1352	0.0914
322	103.0	588.9	583.9	1.0320	576.1	887.2	737.5	2.0409	524.9	854.9	730.4	1.8339	0.1788	0.1214
323	41.5	611.7	610.9	1.0049	369.1	658.3	594.2	1.4611	351.1	655.8	597.8	1.4088	0.1123	0.0581
324	74.4	551.7	549.0	1.0177	367.9	655.0	591.3	1.4602	337.4	644.3	590.6	1.3790	0.2022	0.1157
325	50.6	713.3	712.2	1.0063	460.2	804.4	708.1	1.6297	437.8	799.4	712.4	1.5557	0.1099	0.0581
326	89.9	635.0	631.2	1.0225	456.3	798.9	704.1	1.6211	418.0	781.7	702.2	1.5074	0.1971	0.1168
327	68.9	727.2	725.1	1.0114	645.6	951.1	764.5	2.3383	613.4	938.6	770.4	2.1579	0.1067	0.0592
328	127.4	680.0	672.5	1.0427	653.2	953.3	762.1	2.3864	598.6	925.0	764.5	2.0980	0.1951	0.1157
329	192.0	620.0	602.7	1.1108	695.2	954.4	736.3	2.7217	621.8	905.7	730.9	2.2843	0.2762	0.1708
330	223.4	645.0	621.7	1.1471	781.2	955.6	675.4	3.7294	712.4	917.3	684.9	3.0377	0.2860	0.1407
3150	0.0	288.3	288.3	1.0000	782.7	959.4	678.4	3.7276	782.7	959.4	678.4	3.7276	0.0000	0.0000
3151	0.0	288.3	288.3	1.0000	698.3	961.1	741.4	2.7267	698.3	961.1	741.4	2.7267	0.0000	0.0000
3152	0.0	288.3	288.3	1.0000	567.5	889.4	744.4	1.9905	567.5	889.4	744.4	1.9905	0.0000	0.0000
340	421.8	502.8	414.2	1.9698	500.5	831.7	718.1	1.7575	466.4	688.9	586.3	1.8135	0.8429	0.7668
341	479.1	502.2	388.0	2.4673	560.2	890.0	748.8	1.9515	521.6	705.5	576.7	2.0993	0.8553	0.9080
342	517.2	487.8	354.7	3.0507	608.7	918.3	751.8	2.1709	562.0	698.6	547.7	2.4279	0.8498	1.0418
343	436.8	517.8	422.9	2.0315	577.0	895.6	745.7	2.0308	518.8	738.8	612.9	2.0048	0.7570	0.7093
344	491.3	513.9	393.8	2.5390	652.6	956.7	766.0	2.3738	581.5	761.5	602.8	2.3801	0.7529	0.7883
345	506.3	636.7	512.7	2.1808	701.3	967.8	746.4	2.7318	633.9	853.2	668.4	2.5197	0.7219	0.5289
346	427.6	737.2	652.7	1.5821	664.5	966.7	769.2	2.4344	597.4	901.7	740.8	2.1363	0.6436	0.3953
347	505.4	924.4	811.5	1.6705	750.4	958.9	702.4	3.2874	697.3	951.4	731.7	2.7503	0.6734	0.2771
348	556.0	696.1	548.5	2.3846	781.8	947.2	665.8	3.7937	718.1	876.4	636.9	3.3095	0.7111	0.3929
3107	144.8	520.6	510.4	1.0734	706.5	967.2	742.3	2.7812	633.3	909.0	727.6	2.3563	0.2049	0.1498
3108	234.1	521.7	495.0	1.2065	702.6	963.3	740.9	2.7580	608.5	874.6	706.1	2.2677	0.3332	0.2514
3110	294.4	408.3	365.2	1.4781	699.2	961.7	741.3	2.7331	577.1	794.7	640.2	2.2511	0.4211	0.4321
3112	436.5	723.3	634.8	1.6310	704.1	962.8	739.2	2.7740	632.8	899.0	717.3	2.3784	0.6199	0.3633
3113	496.5	694.4	577.8	1.9675	701.3	967.8	746.4	2.7318	637.2	882.2	696.9	2.4587	0.7080	0.4559
3114	178.9	505.6	489.9	1.1185	704.4	963.3	739.6	2.7749	619.4	889.3	715.1	2.3074	0.2540	0.1929
3115	365.2	388.3	322.0	1.9264	701.0	971.1	750.2	2.7180	573.8	750.3	595.4	2.3532	0.5209	0.6100

NOMENCLATURE

P_r - Pressure Ratio

V_j - Fully Expanded Jet Velocity, m/sec

T_t - Total Temperature, °K

T_j - Static Temperature, °K

SUPERSCRIPTS

o - Outer stream

i - Inner stream

mix - Fully mixed inner & outer stream

SUBSCRIPT

t - Total

TABLE I - 3B ACOUSTIC DATA - CONFIGURATION 3

				OASPL , dB MODEL SCALE ; 12.19 m (40 ft) ARC ; STD DAY							
				θ^i, degrees to inlet							
DATA POINT	T_{dry} °K	T_{wet} °K	BAROM n/m^2	50°	70°	90°	110°	130°	140°	150°	OAPWL, dB
312	291	289	99215.	109.2	110.6	112.6	118.1	126.8	129.4	127.9	164.6
313	291	289	99215.	109.0	110.4	112.5	117.8	127.0	129.4	128.3	164.8
314	290	289	99215.	108.9	110.3	112.3	117.6	125.7	129.0	128.6	164.5
316	291	289	99215.	104.6	105.9	108.1	113.3	121.4	124.5	124.4	160.1
317	291	289	99215.	103.9	105.4	108.1	113.3	119.9	124.7	125.0	160.0
318	291	289	99215.	103.7	105.1	107.7	113.0	120.2	123.8	123.8	159.4
320	291	289	99215.	98.1	99.5	102.5	107.1	112.8	116.8	117.8	153.1
321	291	289	99215.	97.7	99.4	102.3	107.1	112.3	116.3	116.2	152.1
322	290	289	99215.	98.7	98.9	102.0	106.7	112.5	114.9	116.1	151.8
323	289	288	99215.	86.9	89.6	91.8	95.2	98.4	100.6	101.4	138.3
324	289	288	99215.	87.0	89.5	91.8	95.3	98.3	99.8	100.9	138.1
325	290	289	99215.	91.5	96.5	96.4	100.4	105.3	106.9	108.5	144.6
326	289	288	99215.	90.9	93.5	96.2	100.4	104.9	105.7	107.4	143.8
327	290	289	99215.	100.9	102.7	105.3	110.7	117.8	121.3	120.8	156.8
328	290	289	99215.	100.6	102.8	115.6	110.7	117.4	120.3	121.3	156.6
329	291	289	99215.	103.6	105.1	107.6	112.9	119.1	122.1	122.7	158.4
330	290	289	99215.	108.8	110.0	112.2	117.6	124.6	128.7	129.0	164.2
3150	292	291	99215.	109.9	111.2	112.9	118.3	127.3	130.2	128.1	165.3
3151	289	289	99215.	105.2	106.8	108.4	113.3	121.9	125.0	124.2	160.3
3152	292	291	99215.	96.5	99.2	102.0	106.6	112.5	116.8	117.5	152.6
340	293	291	99560.	98.0	99.2	102.5	105.4	110.4	112.4	113.6	149.7
341	292	290	99560.	99.7	101.4	104.3	108.3	113.5	116.7	119.3	154.0
342	292	290	99560.	106.3	106.9	108.4	111.3	116.5	121.5	123.4	157.9
343	293	291	99560.	98.7	100.7	103.9	108.0	113.2	115.4	117.2	152.8
344	292	290	99560.	103.5	104.9	107.5	111.6	117.1	121.2	122.6	157.7
345	292	290	99560.	105.3	107.0	109.4	113.8	120.1	123.8	125.4	160.3
346	291	289	99560.	102.2	104.7	107.4	111.8	117.4	120.8	123.0	157.8
347	291	289	99560.	109.2	109.8	111.8	115.9	124.5	127.1	127.1	163.0
348	292	290	99560.	110.9	112.2	114.5	118.4	126.7	131.0	129.3	165.8
3107	290	288	99560.	104.8	105.6	108.3	112.9	120.1	122.3	123.4	158.9
3108	290	288	99560.	105.4	106.4	108.4	111.7	119.0	121.1	122.3	158.2
3110	291	289	99560.	106.2	106.6	108.3	112.1	118.0	119.7	120.3	157.2
3112	291	289	99560.	104.8	106.6	109.2	113.8	120.0	123.0	124.4	159.7
3113	291	289	99560.	104.5	106.9	109.3	113.4	120.5	124.2	125.1	160.4
3114	290	288	99560.	104.3	105.4	108.1	112.6	119.1	122.3	122.8	158.4
3115	291	289	99560.	105.5	106.5	108.3	112.3	118.5	119.9	120.6	157.4

TABLE I - 4A AERODYNAMIC DATA - CONFIGURATION 4

A^i = 73.226 cm^2(11.350 in^2)
A^o = 71.335 cm^2(11.057 in^2)
A_r = 1.026

DATA PT	V^i_j m/sec	T^i_t °K	T^i_j °K	P^i_r	V^o_j m/sec	T^o_t °K	T^o_j °K	P^o_r	V^{mix}_j m/sec	T^{mix}_t °K	T^{mix}_j °K	P^{mix}_r	V^i_j / V^o_j	W^i/W^o
440	412.1	465.0	380.5	2.0174	497.7	834.4	722.2	1.7424	445.1	607.2	511.4	1.8557	0.8279	1.5979
441	463.6	467.2	360.3	2.4834	570.0	904.4	758.7	1.9779	501.3	622.1	500.0	2.1881	0.8134	1.8239
442	506.3	467.8	340.3	3.0467	605.6	906.1	740.8	2.1777	539.0	612.3	469.5	2.5623	0.8359	2.0329
443	421.5	469.4	381.0	2.0757	581.3	902.8	750.9	2.0412	486.1	644.7	531.2	2.0181	0.7252	1.4721
444	464.5	466.7	359.3	2.4967	657.8	963.9	770.4	2.3927	539.8	660.3	519.7	2.3726	0.7062	1.5683
445	508.7	471.7	342.9	3.0520	700.7	946.1	723.8	2.8017	582.2	653.3	487.8	2.8346	0.7260	1.6123
446	410.3	469.4	385.7	1.9891	668.1	980.6	781.5	2.4255	525.4	697.6	566.6	2.1451	0.6141	1.2399
447	474.9	481.7	369.5	2.5298	755.0	907.2	643.0	3.6443	615.4	695.1	511.9	3.0076	0.6290	0.9940
448	495.3	451.1	329.1	3.0168	783.9	920.0	634.4	4.0261	631.5	672.4	477.0	3.3884	0.6318	1.1187
4107	146.3	405.6	394.9	1.0976	697.1	972.8	754.6	2.6777	541.5	812.6	678.0	1.9877	0.2099	0.3937
4108	217.3	363.9	340.4	1.2632	697.1	973.3	755.2	2.6760	503.1	726.9	608.3	1.9384	0.3118	0.6791
4110	276.8	472.2	434.1	1.3425	703.2	968.3	745.8	2.7465	533.8	771.3	639.1	2.0253	0.3936	0.6589
4112	418.8	471.1	383.8	2.0482	710.5	983.3	756.8	2.7623	556.3	712.7	565.6	2.3327	0.5894	1.1206
4113	488.0	466.7	348.2	2.7872	704.7	971.7	748.3	2.7491	573.6	666.2	506.8	2.6726	0.6925	1.5303
4114	173.1	381.7	366.8	1.1497	697.4	975.0	756.7	2.6733	521.9	776.4	650.4	1.9477	0.2483	0.5030
4115	348.1	465.0	404.7	1.6257	710.2	961.7	733.9	2.8356	543.0	732.3	593.6	2.1756	0.4901	0.8578
4116	385.3	455.6	381.7	1.8571	697.4	948.3	728.4	2.7622	539.3	698.8	560.4	2.2429	0.5524	1.0259
4118	107.6	436.1	430.4	1.0476	698.9	974.4	755.1	2.6883	575.1	861.7	711.4	2.0843	0.1539	0.2649

NOMENCLATURE

P_r - Pressure Ratio

V_j - Fully Expanded Jet Velocity, m/sec

T_t - Total Temperature, °K

T_j - Static Temperature, °K

SUPERSCRIPTS

o - Outer stream

i - Inner stream

mix - Fully mixed inner & outer stream

SUBSCRIPT

t - Total

TABLE I - 4B ACOUSTIC DATA - CONFIGURATION 4

				OASPL , dB MODEL SCALE ; 12.19 m (40 ft) ARC ; STD DAY							
				θ^i, degrees to inlet							
DATA POINT	T_{dry} °K	T_{wet} °K	BAROM n/m^2	50°	70°	90°	110°	130°	140°	150°	OAPWL,dB
440	298	294	99560.	97.3	100.1	102.7	106.7	110.8	113.4	115.4	151.1
441	298	294	99560.	102.2	104.3	106.6	110.2	115.0	118.3	121.5	156.3
442	298	294	99560.	109.9	110.7	111.2	113.5	118.0	122.4	125.9	160.2
443	298	294	99560.	99.5	102.3	105.1	109.2	113.2	116.0	118.1	153.8
444	303	297	99560.	104.0	106.1	108.6	112.5	117.1	119.7	123.1	158.1
445	298	294	99560.	111.5	112.6	113.3	116.0	120.6	124.9	127.9	162.5
446	302	296	99560.	101.9	104.6	107.4	111.4	115.9	117.9	119.9	156.0
447	301	296	99560.	110.0	111.9	113.3	116.9	122.6	126.0	128.7	163.5
448	301	296	98871.	115.3	116.2	117.0	119.4	124.0	128.3	130.6	165.6
4107	296	287	99560.	102.6	105.2	108.3	112.6	118.1	120.4	120.1	157.3
4108	284	284	99560.	102.2	105.0	108.3	112.7	117.7	118.7	119.1	158.5
4110	298	294	99560.	102.7	105.5	108.1	112.5	117.6	119.3	120.0	157.4
4112	304	297	******	104.4	107.2	109.3	113.5	117.9	120.7	123.0	158.5
4113	301	296	99560.	108.2	109.9	111.3	115.0	119.5	123.5	126.5	161.1
4114	285	284	99560.	101.4	104.7	108.1	112.5	117.6	119.0	119.5	156.7
4115	298	294	99560.	105.7	107.9	109.3	113.1	118.2	119.6	120.9	158.0
4116	298	294	99560.	103.6	106.6	108.8	112.5	117.4	119.2	121.2	157.3
4118	285	284	99560.	101.9	104.8	108.1	112.4	118.7	121.5	122.6	158.5

TABLE I - 5A AERODYNAMIC DATA - CONFIGURATION 5

A^i = 73.226 cm^2(11.350 in^2)
A^o = 116.445 cm^2(18.049 in^2)
A_r = .629

DATA PT	V^i_j m/sec	T^i_t °K	T^i_j °K	P^i_r	V^o_j m/sec	T^o_t °K	T^o_j °K	P^o_r	V^{mix}_j m/sec	T^{mix}_t °K	T^{mix}_j °K	P^{mix}_r	V^i_j / V^o_j	W^i/W^o
540	416.1	456.7	370.5	2.0780	504.7	846.7	731.5	1.7563	460.0	650.0	549.0	1.8518	0.8243	1.0168
541	464.5	461.1	353.8	2.5284	562.1	891.1	749.0	1.9591	509.9	661.3	536.6	2.1355	0.8265	1.1475
542	499.0	460.6	336.7	2.9935	610.8	933.3	766.3	2.1533	548.3	669.1	524.3	2.4150	0.8169	1.2673
543	417.9	472.2	385.3	2.0373	580.0	896.7	745.2	2.0456	504.3	698.3	578.0	2.0055	0.7204	0.8773
544	471.2	467.2	356.7	2.5708	651.7	953.9	763.6	2.3742	561.9	711.7	561.5	2.3811	0.7231	0.9909
545	500.8	462.2	337.4	3.0078	713.5	997.8	770.1	2.7418	605.4	725.5	550.6	2.7362	0.7018	1.0338
546	410.0	468.3	384.7	1.9904	658.7	958.9	764.6	2.4120	551.6	747.6	605.0	2.1951	0.6224	0.7563
547	460.6	472.2	366.7	2.4236	736.4	910.0	659.9	3.3647	628.8	739.2	550.5	2.9312	0.6254	0.6395
548	503.5	476.1	350.0	2.9369	736.7	907.2	656.7	3.3842	635.6	720.2	525.8	3.1218	0.6835	0.7659
5107	128.9	395.0	386.7	1.0769	701.3	967.2	745.8	2.7337	601.2	867.2	702.5	2.2368	0.1838	0.2119
5108	207.6	473.3	452.0	1.1761	700.4	965.6	744.7	2.7310	589.1	854.3	696.0	2.1863	0.2963	0.2919
5110	286.5	466.1	425.3	1.3784	698.6	957.8	737.6	2.7408	575.7	811.1	658.2	2.1999	0.4101	0.4250
5112	429.2	464.4	372.8	2.1580	701.6	967.2	745.6	2.7364	586.7	755.2	593.1	2.4437	0.6116	0.7293
5113	481.6	456.1	340.7	2.7755	702.6	970.0	748.0	2.7354	595.0	719.8	550.8	2.6540	0.6855	0.9487
5114	176.5	400.6	385.1	1.1481	703.2	966.7	744.0	2.7522	585.0	839.6	682.9	2.1937	0.2510	0.2893
5115	357.5	458.9	395.3	1.6857	697.7	955.0	735.3	2.7419	574.3	775.0	621.1	2.2842	0.5125	0.5694
5150	0.0	288.3	288.3	1.0000	724.2	765.6	511.8	4.2599	724.2	765.6	511.8	4.2599	0.0000	0.0000
5151	0.0	288.3	288.3	1.0000	699.2	961.1	740.7	2.7350	699.2	961.1	740.7	2.7350	0.0000	0.0000

NOMENCLATURE

P_r - Pressure Ratio

V_j - Fully Expanded Jet Velocity, m/sec

T_t - Total Temperature, °K

T_j - Static Temperature, °K

SUPERSCRIPTS

o - Outer stream

i - Inner stream

mix - Fully mixed inner & outer stream

SUBSCRIPT

t - Total

TABLE I - 5B ACOUSTIC DATA - CONFIGURATION 5

				OASPL , dB MODEL SCALE ; 12.19 m (40 ft) ARC ; STD DAY							
				θ^i, degrees.to inlet							
DATA POINT	T_{dry} °K	T_{wet} °K	BAROM n/m^2	50°	70°	90°	110°	130°	140°	150°	OAPWL,dB
540	305	297	99215.	99.2	101.2	103.8	107.7	112.3	114.5	116.7	10.0
541	304	296	99215.	103.8	105.3	107.4	111.3	116.0	119.3	122.9	157.2
542	302	294	99215.	114.9	115.2	115.0	116.2	119.3	123.9	127.3	162.1
543	304	296	99215.	101.2	103.5	106.5	110.6	115.4	117.7	119.9	155.3
544	302	294	99215.	107.0	108.6	110.7	114.7	120.1	123.8	127.0	161.3
545	301	294	98871.	110.5	112.0	113.8	117.5	123.3	128.0	130.0	164.5
546	301	294	98871.	104.4	106.8	109.5	114.0	119.3	121.8	124.1	159.2
547	297	293	98871.	113.5	114.7	115.8	119.7	125.6	129.3	130.7	166.1
548	297	293	99215.	115.1	116.2	117.1	120.3	126.3	130.8	131.6	167.0
5107	300	293	99215.	105.9	108.6	111.0	116.0	122.0	124.4	125.4	161.3
5108	305	293	99215.	105.0	107.8	110.5	115.4	121.8	122.8	123.9	160.2
5110	305	297	98871.	106.4	108.2	110.6	115.0	121.1	122.3	123.8	159.9
5112	305	297	99215.	106.3	108.6	111.3	116.0	121.9	124.6	126.5	161.8
5113	297	297	98871.	111.9	112.9	113.9	117.4	122.6	126.7	129.1	163.8
5114	305	293	99215.	105.6	108.5	110.8	115.9	121.5	122.9	123.4	10.0
5115	284	297	98871.	107.0	108.8	111.1	115.5	121.1	123.9	124.7	160.8
5150	285	283	99215.	121.4	122.3	123.1	125.6	134.6	137.6	137.7	173.5
5151	255	283	99215.	110.7	112.7	114.9	119.5	129.9	131.3	131.0	167.1

TABLE I - 6A AERODYNAMIC DATA - CONFIGURATION 6

A^i = 73.226 cm^2(11.350 in^2)
A^o = 51.697 cm^2(8.013 in^2)
A_r = 1.416

DATA PT	V^i_j m/sec	T^i_t °K	T^i_j °K	P^i_r	V^o_j m/sec	T^o_t °K	T^o_j °K	P^o_r	V^{mix}_j m/sec	T^{mix}_t °K	T^{mix}_j °K	P^{mix}_r	V^i_j / V^o_j	W^i/W^o
640	409.3	473.3	390.0	1.9701	493.2	833.9	723.8	1.7241	435.9	587.5	495.0	1.8455	0.8300	2.1576
641	466.0	467.8	359.7	2.5077	557.2	871.1	730.8	1.9673	492.1	582.9	463.7	2.2462	0.8364	2.5035
642	504.1	472.2	345.8	2.9768	595.6	874.4	713.4	2.1831	529.1	581.8	442.8	2.6045	0.8465	2.6702
643	416.4	477.2	391.0	2.0091	583.4	907.8	755.0	2.0439	472.9	623.1	515.0	1.9869	0.7137	1.9523
644	467.3	471.7	363.0	2.4996	652.6	946.7	755.5	2.3989	526.5	623.5	488.2	2.3934	0.7160	2.1287
645	496.2	456.1	333.6	2.9884	701.0	957.8	736.0	2.7632	559.0	609.9	455.5	2.7975	0.7078	2.2625
646	422.5	486.7	397.9	2.0239	659.0	964.4	770.2	2.4001	509.7	662.9	538.4	2.1295	0.6411	1.7113
647	468.2	474.4	365.4	2.4945	759.6	922.2	655.8	3.6167	590.3	662.2	492.4	2.8832	0.6164	1.3855
648	509.3	476.1	347.0	3.0242	781.8	918.9	634.9	3.9973	617.7	652.2	464.3	3.3253	0.6515	1.5141
684	510.5	478.9	349.2	3.0202	804.7	903.3	599.1	4.5811	638.2	663.1	462.4	3.5750	0.6345	1.3036
6107	139.0	375.6	365.9	1.0950	700.7	967.8	746.8	2.7263	502.5	758.8	641.7	1.8764	0.1983	0.5455
6108	210.3	472.2	450.3	1.1818	700.7	967.8	746.8	2.7263	503.8	768.8	651.5	1.8662	0.3001	0.6747
6110	281.6	464.4	425.0	1.3645	699.8	966.1	745.7	2.7237	495.9	721.5	606.2	1.9092	0.4024	0.9518
6112	426.4	482.2	391.8	2.0692	698.0	961.7	742.2	2.7221	533.0	670.4	534.0	2.2820	0.6109	1.5477
6113	488.9	470.6	351.6	2.7722	700.1	965.0	744.3	2.7302	557.1	630.2	478.1	2.6682	0.6983	2.0980
6114	169.8	361.7	347.3	1.1521	705.0	973.9	750.4	2.7443	484.7	721.9	611.9	1.8492	0.2408	0.6997
6115	355.4	475.0	412.2	1.6432	699.5	965.0	744.7	2.7247	509.2	694.0	571.1	2.0464	0.5081	1.2373
6116	393.0	484.4	407.3	1.8353	698.9	963.3	743.3	2.7248	521.7	685.1	555.4	2.1528	0.5635	1.3861
6117	453.2	477.8	375.6	2.3220	698.9	961.7	741.5	2.7304	542.9	654.4	511.8	2.4222	0.6485	1.7400
6150	0.0	288.3	288.3	1.0000	776.9	952.8	675.7	3.6826	776.9	952.8	675.7	3.6826	0.0000	0.0000
6151	0.0	288.3	288.3	1.0000	701.0	966.7	745.4	2.7328	701.0	966.7	745.4	2.7328	0.0000	0.0000
6152	0.0	288.3	288.3	1.0000	565.1	901.1	757.8	1.9583	565.1	901.1	757.8	1.9583	0.0000	0.0000

NOMENCLATURE

P_r - Pressure Ratio

V_j - Fully Expanded Jet Velocity, m/sec

T_t - Total Temperature, °K

T_j - Static Temperature, °K

SUPERSCRIPTS

o - Outer stream

i - Inner stream

mix - Fully mixed inner & outer stream

SUBSCRIPT

t - Total

TABLE I - 6B ACOUSTIC DATA - CONFIGURATION 6

				OASPL , dB MODEL SCALE ; 12.19 m (40 ft) ARC ; STD DAY							
				ϕ^i, degrees to inlet							
DATA POINT	T_{dry} °K	T_{wet} °K	BAROM n/m^2	50°	70°	90°	110°	130°	140°	150°	OAPWL,dB
640	287	286	99215.	96.2	98.9	101.5	105.2	109.6	112.5	114.5	10.0
641	287	286	99215.	105.0	105.9	107.0	109.5	104.1	118.1	121.3	10.0
642	289	288	99215.	112.4	112.9	113.0	113.9	117.5	122.4	125.1	10.0
643	287	286	99215.	97.9	100.5	100.4	107.4	111.9	114.2	116.1	10.0
644	289	288	99215.	105.2	106.5	108.1	111.5	115.9	119.3	123.1	10.0
645	291	289	99215.	114.9	115.3	115.5	116.5	119.2	123.9	126.7	10.0
646	288	287	99215.	100.4	103.0	105.9	110.3	114.8	116.7	119.1	10.0
647	289	288	99215.	108.5	110.1	113.1	115.4	120.6	124.5	127.1	10.0
648	290	288	99215.	113.0	114.0	115.0	118.1	123.0	127.8	130.1	10.0
684	291	289	99215.	112.8	114.1	115.5	119.1	124.6	129.3	131.1	166.3
6107	287	286	99560.	98.2	102.9	107.0	111.6	114.1	115.0	116.0	154.2
6108	287	286	99560.	98.6	102.7	105.7	110.3	114.4	115.1	114.6	153.6
6110	286	285	99560.	99.3	102.9	105.7	110.3	114.4	115.8	116.2	154.0
6112	287	286	99560.	101.7	104.7	107.5	111.6	116.2	118.4	120.9	10.0
6113	287	286	99215.	107.8	109.3	110.7	114.0	118.5	123.4	125.9	10.0
6114	286	285	99560.	98.7	103.3	106.9	111.6	114.6	115.6	116.0	154.4
6115	286	285	99560.	101.4	104.4	106.7	110.9	115.3	116.4	117.1	10.0
6116	287	286	99560.	102.3	104.8	107.2	111.3	115.9	116.8	118.9	10.0
6117	287	286	99215.	103.9	106.1	108.3	112.3	117.3	119.8	122.6	10.0
6150	292	289	99560.	106.8	109.8	110.7	114.8	125.3	127.0	125.3	163.0
6151	292	289	99560.	100.8	104.2	106.3	109.9	117.6	121.4	121.8	158.1
6152	292	289	99560.	92.9	97.2	99.2	102.1	106.1	109.2	106.4	146.1

TABLE I - 7A AERODYNAMIC DATA - CONFIGURATION 7

A^i = 37.923 cm^2(5.878 in^2); A^o = 116.445 cm^2(18.049 in^2); A_r = .326

DATA PT	V_j^i m/sec	T_t^i °K	$T_{j\,°K}^i$	P_r^i	V_j^o m/sec	T_t^o °K	$T_{j\,°K}^o$	P_r^o	$V_{j\,m/sec}^{mix}$	T_t^{mix} °K	$T_{j\,°K}^{mix}$	P_r^{mix}	V_j^i / V_j^o	W^i/W^o
762	438.0	465.6	370.1	2.2323	439.2	796.7	708.9	1.5632	438.7	669.5	578.4	1.7129	0.9972	0.6236
763	467.0	468.9	360.4	2.5118	471.8	817.2	716.2	1.6592	469.9	679.1	574.5	1.8494	0.9897	0.6574
764	507.8	468.9	340.6	3.0613	512.7	846.1	727.2	1.7913	510.6	684.6	560.6	2.0784	0.9905	0.7487
767	429.2	475.0	383.4	2.1173	525.8	862.8	738.1	1.8269	493.2	732.0	618.4	1.8754	0.8162	0.5090
768	472.7	473.9	362.7	2.5495	559.9	876.7	735.1	1.9722	527.9	728.5	597.6	2.0837	0.8443	0.5817
769	504.4	466.7	340.1	3.0274	608.7	929.4	763.5	2.1483	567.3	745.6	594.1	2.3166	0.8287	0.6592
773	465.7	468.9	361.0	2.4980	655.3	952.8	760.2	2.4032	592.9	793.3	629.8	2.3725	0.7107	0.4914
774	505.7	468.9	341.7	3.0277	705.3	973.9	750.2	2.7471	636.4	799.6	609.9	2.7368	0.7169	0.5271
779	507.5	468.3	340.2	3.0612	743.1	945.0	692.8	3.2664	670.9	799.0	586.7	3.1281	0.6829	0.4414
790	498.3	479.4	355.9	2.8380	430.7	736.7	650.9	1.5939	459.3	628.0	526.5	1.8924	1.1571	0.7310
791	495.6	485.6	363.4	2.7587	488.0	768.9	659.0	1.7895	490.9	659.3	544.0	2.0132	1.0156	0.6307
792	495.9	485.6	363.2	2.7627	538.3	787.2	653.3	2.0188	522.8	677.1	546.5	2.1836	0.9213	0.5745
793	504.4	495.6	369.0	2.8082	611.4	829.4	656.9	2.4108	575.9	718.5	560.8	2.4781	0.8250	0.4973
794	489.8	462.8	343.4	2.8409	674.2	876.7	667.5	2.8055	616.0	746.0	565.8	2.7562	0.7265	0.4614
795	498.0	482.2	358.8	2.8141	716.0	896.7	660.3	3.1759	653.7	778.3	576.0	3.0262	0.6956	0.3998
796	502.6	529.4	403.8	2.5820	740.4	836.1	576.7	3.9223	689.4	770.4	542.9	3.5725	0.6789	0.2726
797	420.9	491.7	403.5	1.9968	613.6	617.8	430.5	3.5407	580.5	596.1	428.5	3.1767	0.6860	0.2071
798	408.4	323.9	240.9	2.8184	612.0	666.7	483.5	3.1391	551.1	564.0	413.0	2.9782	0.6673	0.4273
799	405.7	322.2	240.3	2.7904	609.6	721.7	543.9	2.7996	542.0	589.3	443.4	2.7113	0.6655	0.4959
7100	408.7	312.2	229.1	2.9548	611.1	772.8	597.2	2.5978	535.5	600.7	459.2	2.5803	0.6688	0.5964
7101	410.3	312.2	228.5	2.9830	604.1	812.2	643.1	2.4045	526.5	612.0	476.1	2.4396	0.6791	0.6677
7102	413.3	317.8	232.8	2.9722	610.8	935.0	768.1	2.1499	523.4	661.8	530.1	2.2338	0.6766	0.7939
7103	411.5	316.1	231.9	2.9585	613.0	892.2	722.0	2.2561	527.5	647.8	513.3	2.3125	0.6713	0.7368
7104	415.7	463.9	377.9	2.0495	609.9	968.3	803.4	2.0820	547.6	806.6	668.6	2.0343	0.6817	0.4720
7107	140.5	460.0	450.2	1.0785	705.6	960.0	735.2	2.7980	654.2	914.5	720.5	2.4993	0.1991	0.1000
7108	216.7	412.2	388.9	1.2266	703.5	963.3	740.2	2.7664	628.9	878.9	698.5	2.4039	0.3081	0.1809
7110	292.3	391.7	349.2	1.4950	697.7	960.6	741.2	2.7231	610.1	837.6	666.3	2.3766	0.4190	0.2757
7112	429.8	577.8	487.6	1.8316	699.5	962.8	742.3	2.7321	638.9	876.3	689.7	2.4899	0.6144	0.2896
7113	504.1	500.0	373.5	2.7744	695.6	953.9	735.5	2.7263	634.8	809.7	621.8	2.6804	0.7248	0.4654
7114	189.0	428.3	410.6	1.1598	703.8	963.3	740.0	2.7692	636.9	893.8	709.4	2.4233	0.2685	0.1493
7115	357.8	376.7	313.0	1.9127	702.6	975.6	753.9	2.7169	608.0	811.3	639.7	2.4386	0.5093	0.3781
760	321.6	475.6	424.1	1.4929	326.4	709.4	660.3	1.3114	324.8	631.5	581.7	1.3540	0.9851	0.4995
761	415.4	476.7	390.8	2.0041	416.7	779.4	700.3	1.5053	416.2	668.8	587.1	1.6178	0.9971	0.5758
765	326.1	475.0	422.1	1.5120	388.9	751.7	682.4	1.4443	369.7	666.9	602.8	1.4553	0.8386	0.4415
766	413.3	469.4	384.5	2.0118	496.5	836.7	725.1	1.7345	468.6	713.2	618.5	1.7839	0.8324	0.5063
770	319.1	473.9	423.2	1.4855	455.4	805.6	711.3	1.6108	417.6	713.6	632.5	1.5710	0.7008	0.3836
771	415.4	480.0	394.1	1.9935	575.5	902.2	753.5	2.0107	525.8	771.2	643.1	1.9792	0.7219	0.4499
772	438.9	472.8	376.9	2.2099	611.1	930.6	763.2	2.1607	555.6	783.0	639.8	2.1345	0.7182	0.4755
775	330.1	475.6	421.3	1.5275	487.4	829.4	721.8	1.7060	444.2	732.4	640.9	1.6508	0.6773	0.3779
776	415.4	475.6	389.7	2.0077	619.4	925.0	752.7	2.2236	559.3	792.7	647.9	2.1359	0.6708	0.4172
777	440.1	475.6	379.2	2.2093	654.7	952.2	760.0	2.4002	590.0	808.5	647.3	2.3075	0.6723	0.4318
778	469.7	476.1	366.3	2.5024	700.1	957.2	736.0	2.7567	631.2	813.3	627.8	2.6333	0.6709	0.4268
780	326.7	478.3	425.2	1.5098	572.7	901.7	754.4	1.9970	511.2	795.7	675.8	1.8585	0.5705	0.3338
781	477.6	490.0	376.5	2.5148	719.6	826.1	581.4	3.6493	664.5	749.5	537.8	3.3382	0.6637	0.2953

NOMENCLATURE

P_r - Pressure Ratio

V_j - Fully Expanded Jet Velocity, m/sec

T_t - Total Temperature, °K

T_j - Static Temperature, °K

SUPERSCRIPTS

o - Outer stream

i - Inner stream

mix - Fully mixed inner & outer stream

SUBSCRIPT

t - Total

TABLE I - 7B ACOUSTIC DATA - CONFIGURATION 7

				OASPL , dB MODEL SCALE ; 12.19 m (40 ft) ARC ; STD DAY							
				θ^i, degrees to inlet							
DATA POINT	T_{dry} °K	T_{wet} °K	BAROM n/m^2	50°	70°	90°	110°	130°	140°	150°	OAPWL,dB
762	293	291	99560.	99.0	99.4	101.8	104.5	110.2	113.7	115.0	150.4
763	294	290	99560.	101.3	101.3	103.8	106.3	112.3	115.8	118.2	153.0
764	293	289	99560.	106.6	107.7	107.9	110.2	115.3	120.1	122.1	156.8
767	295	291	99560.	100.3	101.6	104.7	107.8	114.2	116.8	118.6	153.8
768	294	290	99560.	101.7	103.3	106.2	109.3	115.8	119.0	121.6	156.3
769	294	290	99560.	107.4	108.2	109.8	112.4	118.9	123.9	125.9	160.3
773	292	289	99560.	105.6	107.2	110.2	113.6	120.8	124.5	126.4	161.1
774	294	290	99560.	109.8	111.0	113.1	116.4	123.6	128.1	129.6	164.2
779	293	289	99560.	115.6	116.2	117.3	119.2	126.9	131.0	131.1	167.0
790	293	289	99560.	103.7	104.2	105.7	107.2	113.6	117.8	118.9	154.0
791	293	289	99560.	101.3	102.5	104.9	107.6	114.1	118.9	120.7	155.1
792	293	289	99560.	103.0	104.3	107.0	109.8	116.9	121.3	123.7	157.9
793	293	289	99560.	107.2	108.2	110.3	113.2	120.2	125.7	127.4	161.7
794	292	289	99560.	109.1	110.3	112.5	115.4	123.0	127.9	129.1	163.7
795	293	291	99560.	114.5	115.0	116.1	118.4	126.4	130.7	130.6	166.4
796	293	290	99560.	116.6	117.5	118.5	120.1	128.4	133.6	132.7	168.8
797	300	293	99560.	113.9	115.1	115.5	116.8	121.9	125.9	128.3	163.6
798	298	292	99560.	113.0	113.9	114.2	116.1	121.1	124.5	126.9	162.4
799	297	292	99560.	107.1	108.8	110.7	114.0	119.6	122.8	124.9	160.2
7100	297	292	99560.	106.3	108.2	110.3	113.9	119.2	121.9	124.1	159.5
7101	296	291	99560.	105.2	107.1	109.5	113.3	118.6	121.1	123.5	158.7
7102	296	291	99560.	103.2	105.5	108.3	112.6	117.2	119.8	122.0	157.3
7103	296	291	99560.	104.0	106.2	108.9	113.1	118.0	120.3	123.3	158.2
7104	293	290	99560.	101.9	104.0	107.3	110.6	117.6	119.7	121.3	156.7
7107	293	291	99560.	106.4	108.5	111.2	114.8	123.4	127.1	127.7	162.9
7108	292	290	99560.	106.4	108.6	111.3	114.7	122.5	125.5	126.3	161.8
7110	292	289	99560.	106.3	108.3	111.0	114.4	122.3	125.2	126.6	161.8
7112	292	289	99560.	106.7	108.6	111.4	115.1	123.5	127.1	128.3	163.4
7113	292	290	99560.	109.7	110.6	112.9	116.0	123.7	128.2	128.5	163.8
7114	293	291	99560.	106.7	108.6	111.3	114.8	123.0	126.4	126.8	162.4
7115	292	290	99560.	106.1	108.1	111.0	114.9	122.4	124.7	125.8	161.6
760	292	291	99215.	88.6	91.0	93.7	96.5	100.2	102.8	103.7	140.0
761	293	292	99215.	94.2	96.5	109.4	102.7	107.6	110.9	112.9	148.8
765	292	291	99215.	90.4	92.9	95.7	98.9	102.9	105.2	105.5	142.3
766	293	292	99215.	97.3	99.8	102.9	106.9	111.8	114.2	116.2	151.4
770	292	291	99215.	94.4	97.1	100.2	103.7	108.3	109.9	110.8	147.3
771	299	294	99905.	100.2	102.8	105.9	110.4	116.0	118.4	120.2	155.5
772	296	293	99215.	102.1	104.7	107.6	111.8	117.6	120.8	122.8	157.8
775	292	291	99215.	96.1	98.8	101.7	105.6	110.3	112.1	113.5	149.5
776	297	293	99215.	102.0	104.7	107.8	112.3	118.2	120.9	123.2	158.0
777	294	293	99215.	104.4	106.9	109.7	114.4	120.3	123.7	125.6	160.5
778	292	289	99215.	107.6	109.3	112.0	115.6	123.5	127.5	128.7	163.6
780	293	292	99215.	99.4	102.0	105.3	109.6	115.0	116.9	118.2	154.2
781	294	292	99215.	112.0	113.8	115.4	119.1	126.4	130.8	131.6	166.6

TABLE I - 8A AERODYNAMIC DATA - REFERENCE CONICAL NOZZLE

$A = 109.14\ cm^2 (16.917\ in^2)$

DATA PT	V_j^i m/sec	T_t^i °K	T_j^i °K	P_r^i	V_j^o m/sec	T_t^o °K	T_j^o °K	P_r^o	V_j^{mix} m/sec	T_t^{mix} °K	T_j^{mix} °K	P_r^{mix}	V_j^i / V_j^o	W^i/W^o
101	0.0	288.3	288.3	1.0000	786.1	967.2	684.3	3.7287	786.1	967.2	684.3	3.7287	0.0000	0.0000
102	0.0	288.3	288.3	1.0000	699.8	976.1	756.3	2.6910	699.8	976.1	756.3	2.6910	0.0000	0.0000
103	0.0	288.3	288.3	1.0000	638.9	949.4	766.8	2.2965	638.9	949.4	766.8	2.2965	0.0000	0.0000
104	0.0	288.3	288.3	1.0000	601.4	922.2	760.1	2.1192	601.4	922.2	760.1	2.1192	0.0000	0.0000
105	0.0	288.3	288.3	1.0000	564.8	898.9	755.7	1.9604	564.8	898.9	755.7	1.9604	0.0000	0.0000
106	0.0	288.3	288.3	1.0000	489.5	470.6	351.3	2.7804	489.5	470.6	351.3	2.7804	0.0000	0.0000
107	0.0	288.3	288.3	1.0000	473.7	468.9	357.3	2.5898	473.7	468.9	357.3	2.5898	0.0000	0.0000

NOMENCLATURE

P_r - Pressure Ratio

V_j - Fully Expanded Jet Velocity, m/sec

T_t - Total Temperature, °K

T_j - Static Temperature, °K

SUPERSCRIPTS

o - Outer stream

i - Inner stream

mix - Fully mixed inner & outer stream

SUBSCRIPT

t - Total

TABLE I - 8B ACOUSTIC DATA - REFERENCE CONIC NOZZLE

				OASPL , dB MODEL SCALE ; 12.19 m (40 ft) ARC ; STD DAY							
				θ^i, degrees to inlet							
DATA POINT	T_{dry} °K	T_{wet} °K	BAROM n/m^2	50°	70°	90°	110°	130°	140°	150°	OAPWL, dB
101	289	288	99974.	121.0	121.2	122.4	124.8	132.4	131.5	129.1	169.8
102	289	288	99974.	114.0	114.3	116.3	120.0	129.5	128.4	126.4	165.8
103	290	289	99974.	107.6	108.6	111.7	116.8	125.9	127.0	123.8	162.7
104	290	289	99974.	104.3	106.1	109.6	114.5	121.4	126.0	123.6	161.2
105	290	289	99974.	103.3	104.7	108.5	113.1	121.2	123.5	122.7	159.2
106	289	288	99974.	119.0	116.5	116.9	115.0	118.8	123.1	123.8	161.6
107	289	288	99974.	116.2	113.8	114.6	113.1	117.2	121.7	122.3	159.5

APPENDIX II -

Aerodynamic Test Matrix

Table II-1. Aerodynamic Test Matrix.

Configuration 1

M_a	P_{T_o}/P_a	P_{T_i}/P_a	ω_i/ω_o	M_a	P_{T_o}/P_a	P_{T_i}/P_a	ω_i/ω_o
0	1.5	1.3	--	0.36	2.5	--	0.0
	2.0		--		3.5	--	
	3.0		--		1.5	--	0.03
	4.0		--		2.0	--	
	1.5	1.9	--		2.5	--	
	2.0		--		3.5	--	
	3.0		--		1.5	--	0.06
	4.0		--		2.0	--	
	1.5	--	0.0		2.5	--	
	2.0	--			3.5	--	
	2.5	--		0.45	1.5	1.3	--
	3.5	--			2.0		--
	1.5	--	0.03		3.0		--
	2.0	--			4.0		--
	2.5	--			1.5	1.9	--
	3.5	--			2.0		--
	1.5	--	0.06		3.0		--
	2.0	--			4.0		--
	2.5	--			1.5	--	0.0
	3.5	--			2.0	--	
0.36	1.5	1.3	--		2.5	--	
	2.0		--		3.5	--	
	3.0		--		1.5	--	0.03
	4.0		--		2.0	--	
	1.5	1.9	--		2.5	--	
	2.0		--		3.5	--	
	3.0		--		1.5	--	0.06
	4.0		--		2.0	--	
	1.5	--	0.0		2.5	--	
	2.0	--			3.5	--	

Table II-1. Aerodynamic Test Matrix (Continued).

Configuration 2

M_a	P_{T_o}/P_a	P_{T_i}/P_a	ω_i/ω_o	M_a	P_{T_o}/P_a	P_{T_i}/P_a	ω_i/ω_o
0	1.5	1.1	--	0.36	1.5	2.5	--
	2.5	↓	--	↓	2.5	↓	--
	3.5	↓	--		3.5	↓	--
	1.5	1.5	--		1.5	3.5	--
	2.5	↓	--		2.5	↓	--
	3.5	↓	--		3.5	↓	--
	1.5	2.5	--		1.5	--	0.0
	2.5	↓	--		2.0	--	↓
	3.5	↓	--		2.5	--	
	1.5	3.5	--		3.5	--	
	2.5	↓	--		2.5	--	0.01
	3.5	↓	--		2.5	--	0.02
	1.5	--	0.0		1.5	--	0.03
	2.0	--	↓		2.5	--	↓
	2.5	--			3.5	--	
	3.5	--			1.5	--	0.06
	2.5	--	0.01		2.0	--	↓
	2.5	--	0.02		2.5	--	
	1.5	--	0.03		3.5	--	
	2.5	--	↓	0.45	1.5	2.5	--
	3.5	--		↓	2.5	↓	--
	1.5	--	0.06		3.5	↓	--
	2.0	--	↓		1.5	3.5	--
	2.5	--			2.5	↓	--
↓	3.5	--			3.5	↓	--
0.36	1.5	1.1	--		1.5	--	0.0
↓	2.5	↓	--		2.5	--	↓
	3.5	↓	--		3.5	--	
	1.5	1.5	--		1.5	--	0.06
↓	2.5	↓	--	↓	2.5	--	↓
	3.5	↓	--		3.5	--	

Table II-1. Aerodynamic Test Matrix (Continued).

Configuration 3

M_a	P_{T_o}/P_a	P_{T_i}/P_a	ω_i/ω_o	M_a	P_{T_o}/P_a	P_{T_i}/P_a	ω_i/ω_o
0.0	1.5	1.1	--	0.36	1.5	2.5	--
	2.5	↓	--	↓	2.5	↓	--
	3.5	↓	--	↓	3.5	↓	--
	1.5	1.5	--	↓	1.5	3.5	--
	2.5	↓	--	↓	2.5	↓	--
	3.5	↓	--	↓	3.5	↓	--
	1.5	2.5	--	↓	1.5	--	0.0
	2.5	↓	--	↓	2.5	--	↓
	3.5	↓	--	↓	3.5	--	↓
	1.5	3.5	--	↓	1.5	--	0.03
	2.5	↓	--	↓	2.5	--	↓
	3.5	↓	--	↓	3.5	--	↓
	1.5	--	0.0	↓	1.5	--	0.06
	2.5	--	↓	↓	2.5	--	↓
	3.5	--	↓	↓	3.5	--	↓
	1.5	--	0.03	0.45	1.5	2.5	--
	2.5	--	↓	↓	2.5	↓	--
	3.5	--	↓	↓	3.5	↓	--
	1.5	--	0.06	↓	1.5	3.5	--
	2.5	--	↓	↓	2.5	↓	--
	3.5	--	↓	↓	3.5	↓	--
0.36	1.5	1.1	--	↓	1.5	--	0.0
	2.5	↓	--	↓	2.5	--	↓
	3.5	↓	--	↓	3.5	--	↓
	1.5	1.5	--	↓	1.5	--	0.06
	2.5	↓	--	↓	2.5	--	↓
↓	3.5	↓	--	↓	3.5	--	↓

Table II-1. Aerodynamic Test Matrix (Continued).

Configuration 4

M_a	P_{T_o}/P_a	P_{T_i}/P_a	ω_i/ω_o	M_a	P_{T_o}/P_a	P_{T_i}/P_a	ω_i/ω_o
0	1.5	1.1	--	0.36	1.5	1.1	--
	2.0		--		2.0		--
	2.5		--		2.5		--
	3.5		--		3.5		--
	1.5	1.5	--		1.5	1.5	--
	2.0		--		2.0		--
	2.5		--		2.5		--
	3.5		--		3.5		--
	1.5	2.5	--		1.5	2.5	--
	2.0		--		2.0		--
	2.5		--		2.5		--
	3.5		--		3.5		--
	1.5	3.5	--		1.5	3.5	--
	2.0		--		2.0		--
	2.5		--		2.5		--
	3.5		--		3.5		--
	1.5	--	0.0		1.5	--	0.0
	2.0	--			2.0	--	
	2.5	--			2.5	--	
	3.5	--			3.5	--	0.01
	2.5	--	0.01		2.5	--	0.02
	2.5	--	0.02		1.5	--	0.03
	1.5	--	0.03		2.0	--	
	2.0	--			2.5	--	
	2.5	--			3.5	--	
	3.5	--			1.5	--	0.06
	1.5	--	0.06		2.0	--	
	2.0	--			2.5	--	
	2.5	--			3.5	--	
	3.5	--					

Table II-1. Aerodynamic Test Matrix (Continued).

Configuration 4 (Concluded)

M_a	P_{T_o}/P_a	P_{T_i}/P_a	ω_i/ω_o	M_a	P_{T_o}/P_a	P_{T_i}/P_a	ω_i/ω_o
0.36	3.5	--	0.06	↓	↓	↓	↓
0.45	1.5	2.5	--				
↓	2.0	↓	--				
	2.5		--				
	3.5		--				
	1.5	3.5	--				
	2.0	↓	--				
	2.5		--				
	3.5		--				
	1.5	--	0.0				
	2.0	--	↓				
	2.5	--					
	3.5	--					
	1.5	--	0.06				
	2.0	--	↓				
	2.5	--					
↓	3.5	--	↓	↓	↓	↓	↓

Table II-1. Aerodynamic Test Matrix (Continued).

Configuration 5

M_a	P_{T_o}/P_a	P_{T_i}/P_a	ω_i/ω_o	M_a	P_{T_o}/P_a	P_{T_i}/P_a	ω_i/ω_o
0	1.5	1.1	--	0.36	1.5	1.1	--
↓	2.0	↓	--	↓	2.0	↓	--
	2.5		--		2.5		--
	3.2		--		3.1		--
	1.5	1.5	--		1.5	1.5	--
	2.0	↓	--		2.0	↓	--
	2.5		--		2.5		--
	3.2		--		3.0		--
	1.5	2.5	--		1.5	2.5	--
	2.0	↓	--		2.0	↓	--
	2.5		--		2.5		--
	3.1		--		3.0		--
	1.5	3.5	--		1.5	3.5	--
	2.0	↓	--		2.0	↓	--
	2.5		--		2.5		--
	3.1		--		3.0		--
	1.5	--	0.0		1.5	--	0.0
	2.0	--	↓		2.0	--	↓
	2.5	--			2.5	--	
	3.2	--			3.1	--	
	2.5	--	0.01		2.5	--	0.01
	2.5	--	0.02		2.5	--	0.02
	1.5	--	0.03		1.5	--	0.03
	2.0	--	↓		2.0	--	↓
	2.5	--			2.5	--	
	3.2	--			3.1	--	
	1.5	--	0.06		1.5	--	0.06
	2.0	--	↓		2.0	--	↓
	2.5	--			2.5	--	
↓	3.2	--	↓	↓	3.1	--	↓

Table II-1. Aerodynamic Test Matrix (Continued).

Configuration 5 (Concluded)

M_a	P_{T_o}/P_a	P_{T_i}/P_a	ω_i/ω_o	M_a	P_{T_o}/P_a	P_{T_i}/P_a	ω_i/ω_o
0.45	1.5	2.5	--	↓	↓	↓	↓
↓	2.0	↓	--				
	2.5		--				
	3.3		--				
	1.5	3.5	--				
	2.0	↓	--				
	2.5		--				
	3.3		--				
	1.5	--	0.0				
	2.0	--	↓				
	2.5	--					
	3.3	--					
	1.5	--	0.06				
	2.0	--	↓				
	2.5	--					
↓	3.3	--					

Table II-1. Aerodynamic Test Matrix (Continued).

Configuration 6

M_a	P_{T_o}/P_a	P_{T_i}/P_a	ω_i/ω_o	M_a	P_{T_o}/P_a	P_{T_i}/P_a	ω_i/ω_o
0	1.5	1.1	--	0.36	2.5	1.1	--
↓	2.0	↓	--	↓	3.5	↓	--
↓	2.5	↓	--	↓	1.5	1.5	--
↓	3.5	↓	--	↓	2.0	↓	--
↓	1.5	1.5	--	↓	2.5	↓	--
↓	2.0	↓	--	↓	3.5	↓	--
↓	2.5	↓	--	↓	1.5	2.5	--
↓	3.5	↓	--	↓	2.0	↓	--
↓	1.5	2.5	--	↓	2.5	↓	--
↓	2.0	↓	--	↓	3.5	↓	--
↓	2.5	↓	--	↓	1.5	3.5	--
↓	3.5	↓	--	↓	2.0	↓	--
↓	1.5	3.5	--	↓	2.5	↓	--
↓	2.0	↓	--	↓	3.5	↓	--
↓	2.5	↓	--	↓	1.5	--	0.0
↓	3.5	↓	--	↓	2.0	--	↓
↓	1.5	--	0.0	↓	2.5	--	↓
↓	2.0	--	↓	↓	3.5	--	↓
↓	2.5	--	↓	↓	1.5	--	0.03
↓	3.5	--	↓	↓	2.0	--	↓
↓	1.5	--	0.03	↓	2.5	--	↓
↓	2.0	--	↓	↓	3.5	--	↓
↓	2.5	--	↓	↓	1.5	--	0.06
↓	3.5	--	↓	↓	2.0	--	↓
↓	1.5	--	0.06	↓	2.5	--	↓
↓	2.0	--	↓	↓	3.5	--	↓
↓	2.5	--	↓	0.45	1.5	2.5	--
↓	3.5	--	↓	↓	2.0	↓	--
0.36	1.5	1.1	--	↓	2.5	↓	--
↓	2.0	↓	--	↓	3.5	↓	--

Table II-1. Aerodynamic Test Matrix (Continued).

Configuration 6 (Concluded)

M_a	P_{T_o}/P_a	P_{T_i}/P_a	ω_i/ω_o	M_a	P_{T_o}/P_a	P_{T_i}/P_a	ω_i/ω_o
0.45	1.5	3.5	--	↓	↓	↓	↓
↓	2.0	↓	--				
	2.5		--				
	3.5		--				
	1.5	--	0.0				
	2.0	--	↓				
	2.5	--					
	3.5	--					
	1.5	--	0.06				
	2.0	--	↓				
	2.5	--					
↓	3.5	--					

Table II-1. Aerodynamic Test Matrix (Continued).

Configuration 7

M_a	P_{T_o}/P_a	P_{T_i}/P_a	ω_i/ω_o	M_a	P_{T_o}/P_a	P_{T_i}/P_a	ω_i/ω_o
0	1.5	1.1	--	0.36	2.5	1.1	--
	2.0		--		3.0		--
	2.5		--		1.5	1.5	--
	3.2		--		2.0		--
	1.5	1.5	--		2.5		--
	2.0		--		3.0		--
	2.5		--		1.5	2.5	--
	3.2		--		2.0		--
	1.5	2.5	--		2.5		--
	2.0		--		3.0		--
	2.5		--		1.5	3.5	--
	3.2		--		2.0		--
	1.5	3.5	--		2.5		--
	2.0		--		3.0		--
	2.5		--		1.5	--	0.0
	3.2		--		2.0	--	
	1.5	--	0.0		2.5	--	
	2.0	--			3.0	--	
	2.5	--			1.5	--	0.03
	3.2	--			2.0	--	
	1.5	--	0.03		2.5	--	
	2.0	--			3.0	--	
	2.5	--			1.5	--	0.06
	3.2	--			2.0	--	
	1.5	--	0.06		2.5	--	
	2.0	--			3.0	--	
	2.5	--		0.45	1.5	2.5	--
	3.2	--			2.0		--
0.36	1.5	1.1	--		2.5		--
	2.0		--		3.3		--

Table II-L. Aerodynamic Test Matrix (Continued).

Configuration 7 (Concluded)

M_a	P_{T_o}/P_a	P_{T_i}/P_a	ω_i/ω_o	M_a	P_{T_o}/P_a	P_{T_i}/P_a	ω_i/ω_o
0.45	1.5	3.5	--	↓	↓	↓	↓
↓	2.0	↓	--				
	2.5		--				
	3.3		--				
	1.5	--	0.0				
	2.0	--	↓				
	2.5	--					
	3.3	--					
	1.5	--	0.06				
	2.0	--	↓				
	2.5	--					
↓	3.3	--	↓				

Table II-1. Aerodynamic Test Matrix (Continued).

Configuration 8

M_a	P_{T_o}/P_a	P_{T_i}/P_a	ω_i/ω_o	M_a	P_{T_o}/P_a	P_{T_i}/P_a	ω_i/ω_o
0	1.5	1.1	--	0.36	1.5	1.1	--
↓	2.0	↓	--	↓	2.0	↓	--
	2.5		--		2.5		--
	3.5		--		3.5		--
	1.5	1.5	--		1.5	1.5	--
	2.0	↓	--		2.0	↓	--
	2.5		--		2.5		--
	3.5		--		3.5		--
	1.5	2.5	--		1.5	2.5	--
	2.0	↓	--		2.0	↓	--
	2.5		--		2.5		--
	3.5		--		3.5		--
	1.5	3.5	--		1.5	3.5	--
	2.0	↓	--		2.0	↓	--
	2.5		--		2.5		--
	3.5		--		3.5		--
	1.5	--	0.0		1.5	--	0.0
	2.0	--	↓		2.0	--	↓
	2.5	--			2.5	--	
	3.5	--			3.5	--	
	1.5	--	0.03		1.5	--	0.03
	2.0	--	↓		2.0	--	↓
	2.5	--			2.5	--	
	3.5	--			3.5	--	
	1.5	--	0.06		1.5	--	0.06
	2.0	--	↓		2.0	--	↓
	2.5	--		↓	2.5	--	
↓	3.5	--	↓		3.5	--	↓

Table II-1. Aerodynamic Test Matrix (Concluded).

Configuration 8 (Concluded)

M_a	P_{T_o}/P_a	P_{T_i}/P_a	ω_i/ω_o	M_a	P_{T_o}/P_a	P_{T_i}/P_a	ω_i/ω_o
0.45	1.5	2.5	--	↓	↓	↓	↓
↓	2.0	↓	--				
	2.5		--				
	3.5		--				
	1.5	3.5	--				
	2.0	↓	--				
	2.5		--				
	3.5		--				
	1.5	--	0.0				
	2.0	--	↓				
	2.5	--					
	3.5	--					
	1.5	--	0.06				
	2.0	--	↓				
	2.5	--					
↓	3.5	--	↓				

APPENDIX III -

Power Spectral Density Data and One-Third Octave Band Sound Pressure Directivity Results for Configurations 2 Through 7

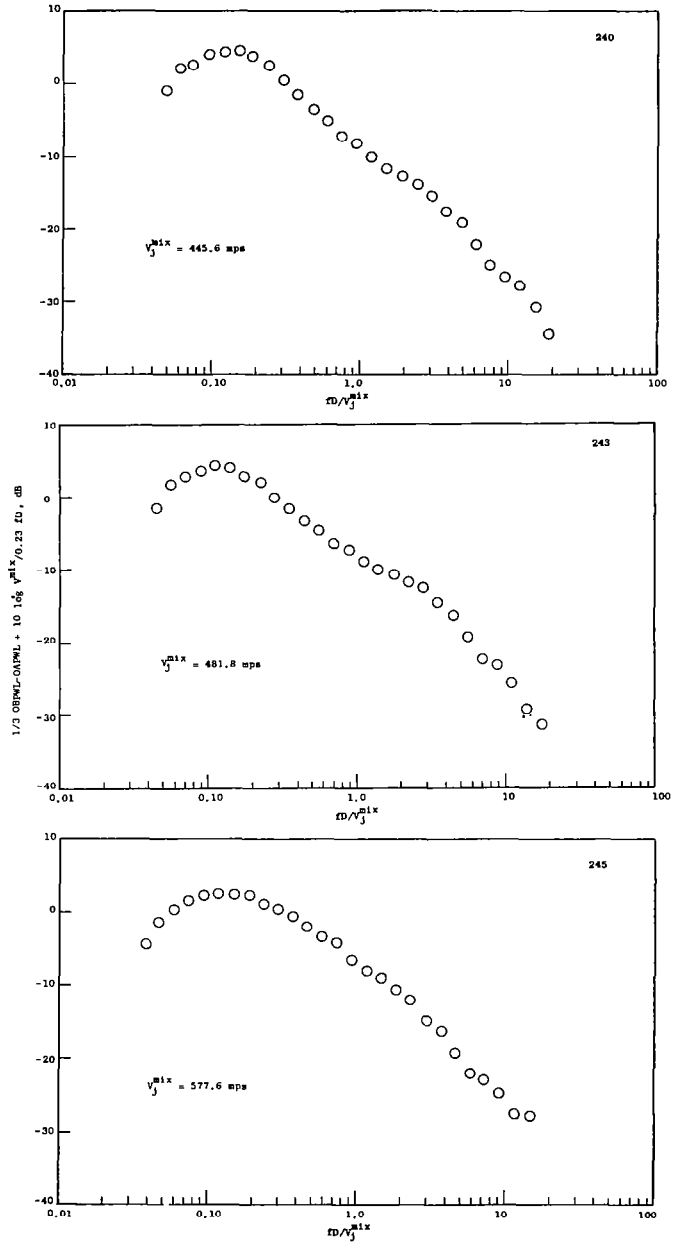

Figure III-1. Power Spectral Density Data for Configuration 2.

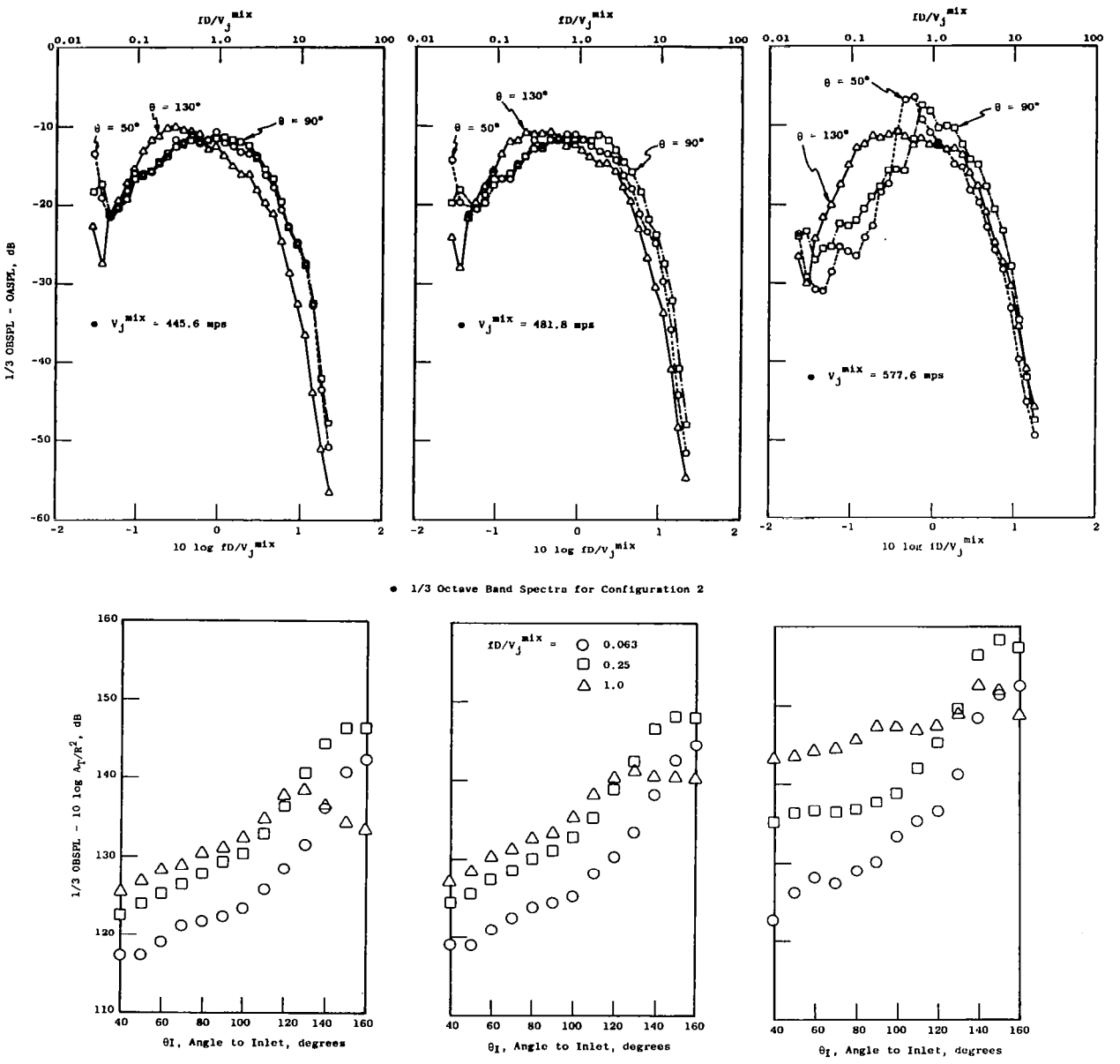

Figure III-2. One-Third Octave Band Sound Pressure Directivity Results for Configuration 2.

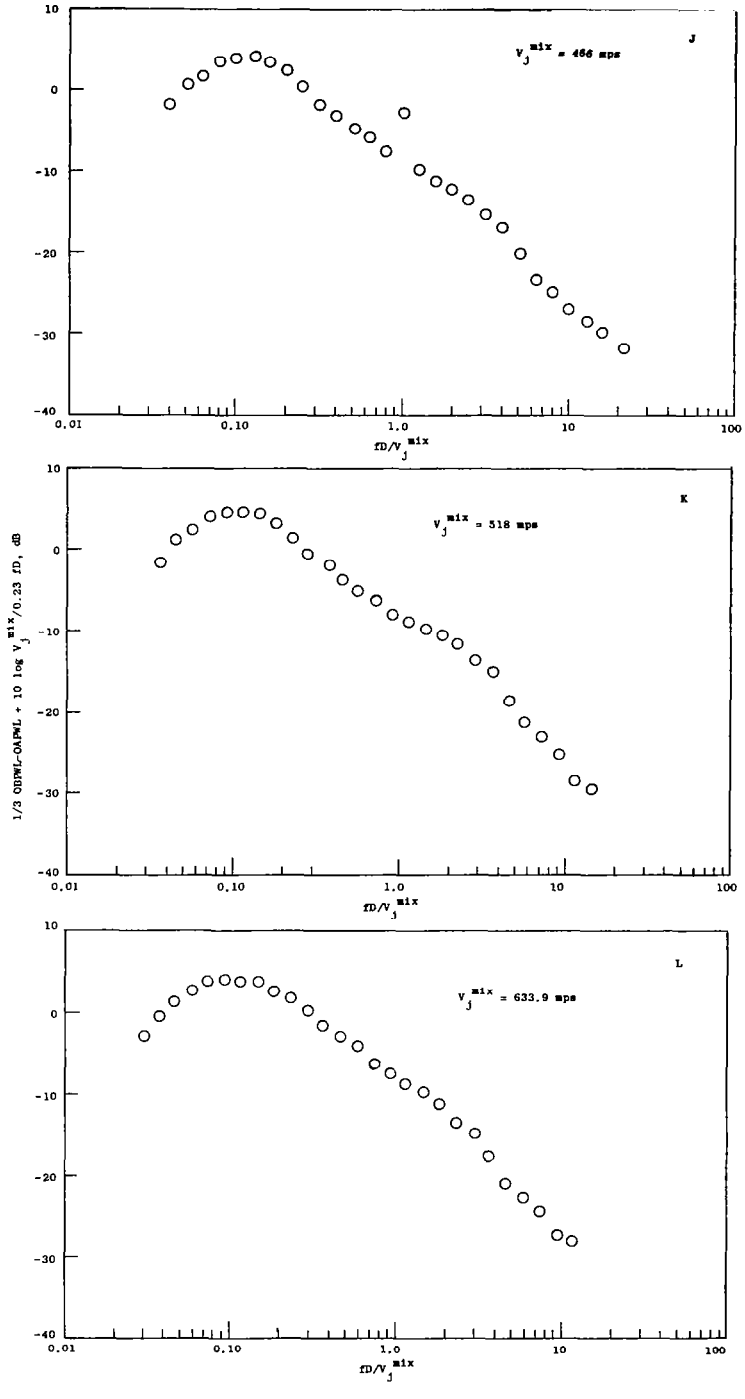

Figure III-3. Power Spectral Density Data for Configuration 3.

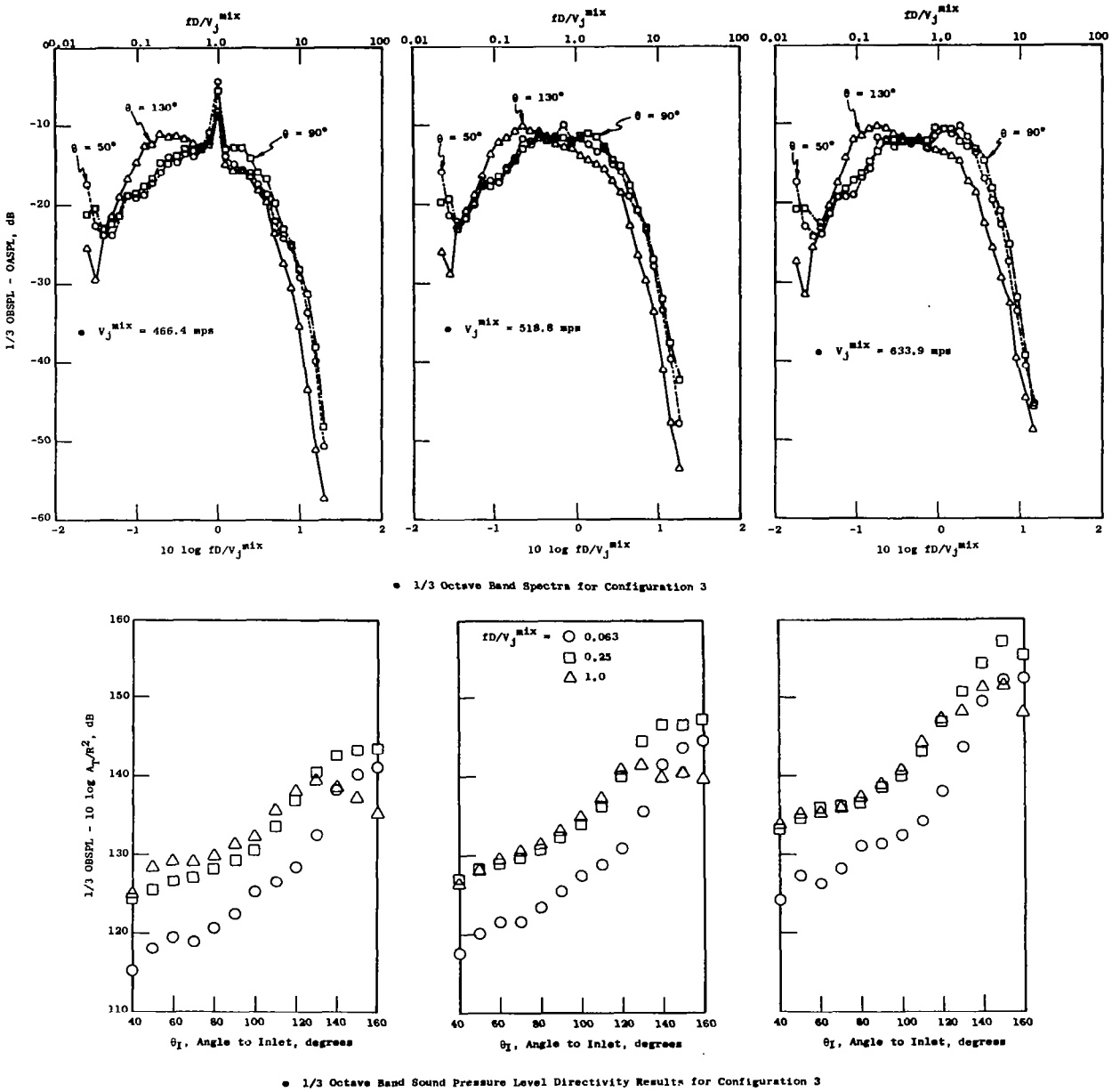

• 1/3 Octave Band Spectra for Configuration 3

• 1/3 Octave Band Sound Pressure Level Directivity Results for Configuration 3

Figure III-4. One-Third Octave Band Sound Pressure Directivity Results for Configuration 3.

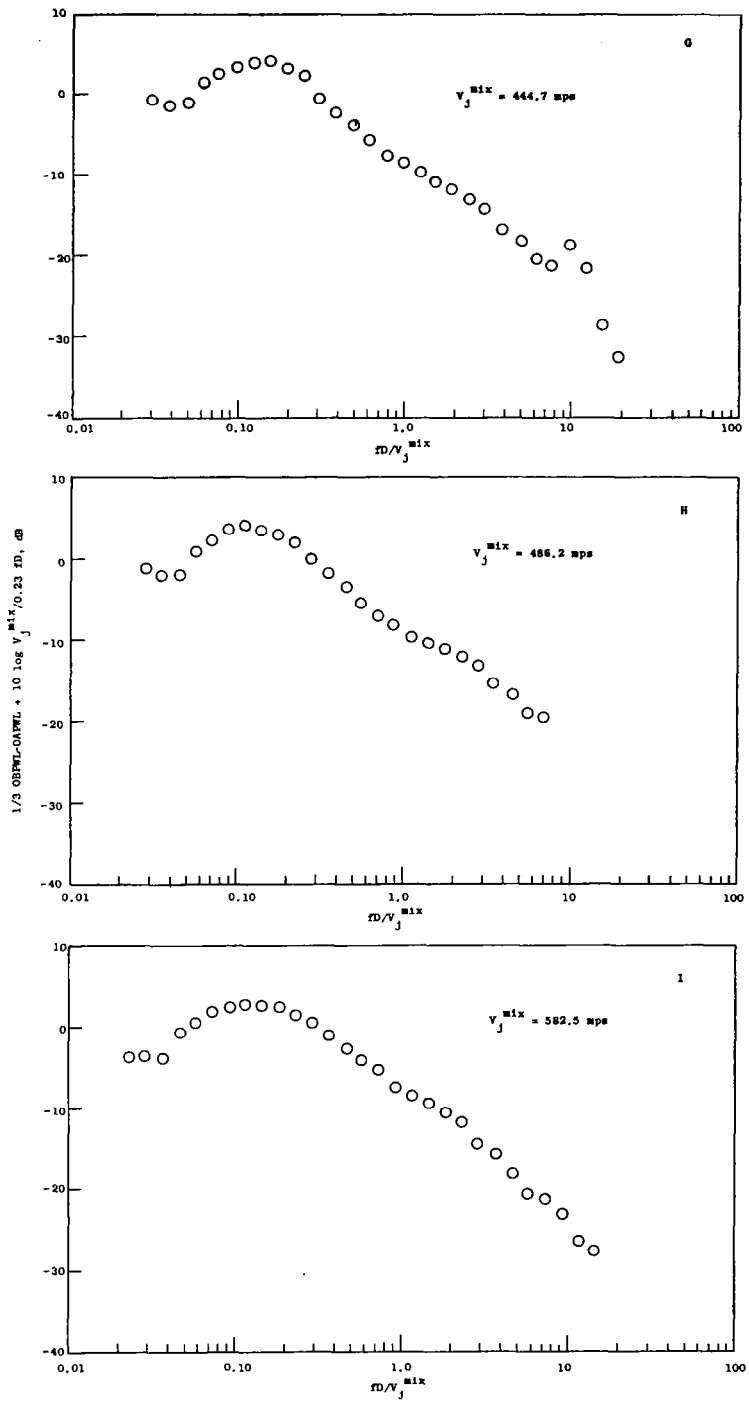

Figure III-5. Power Spectral Density Data for Configuration 4.

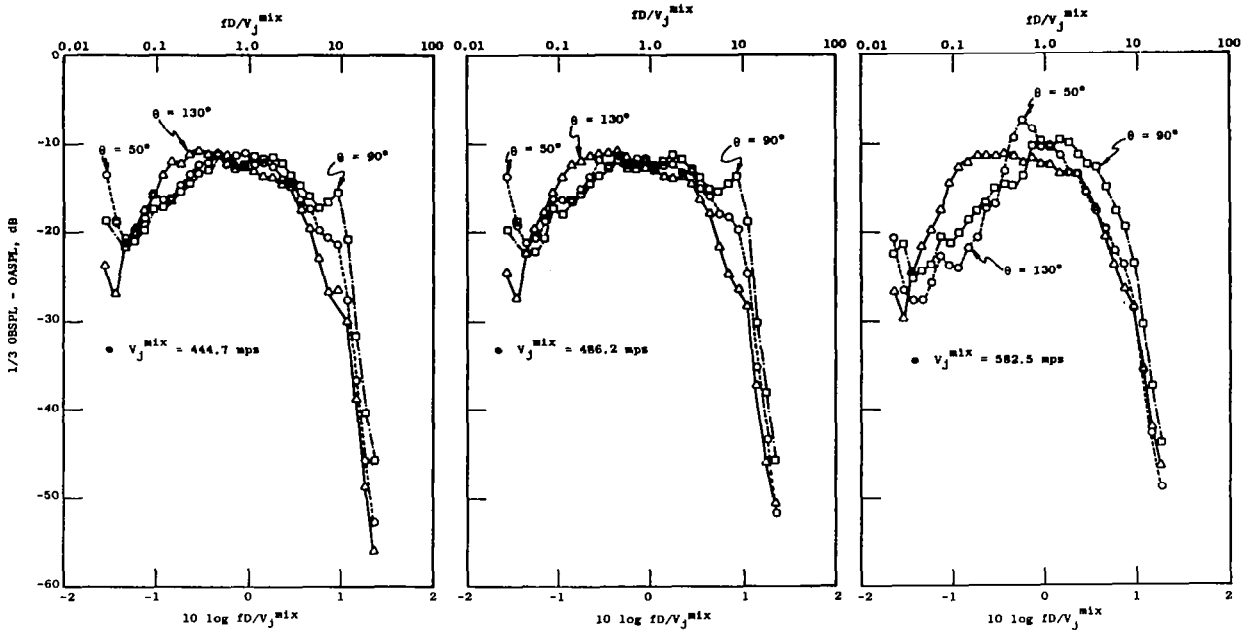

• 1/3 Octave Band Spectra for Configuration 4

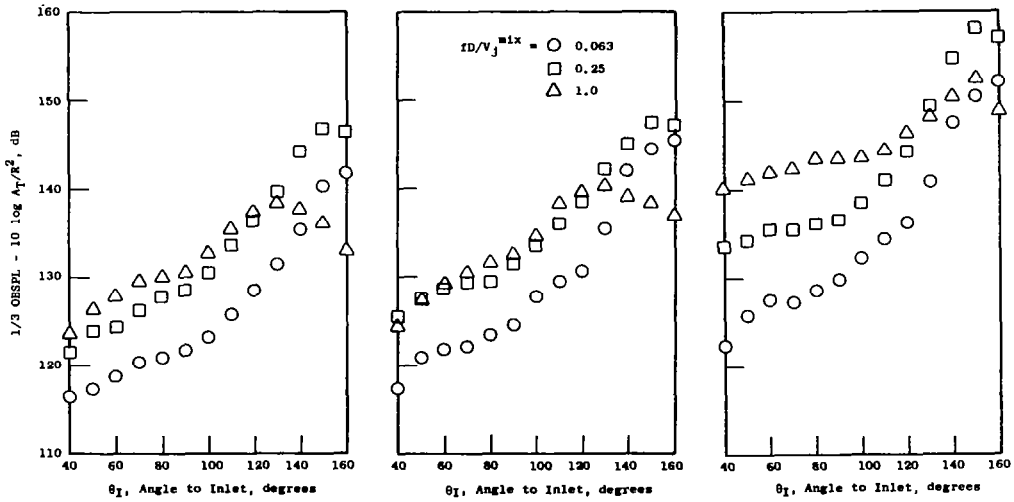

• 1/3 Octave Band Sound Pressure Level Directivity Results for Configuration 4

Figure III-6. One-Third Octave Band Sound Pressure Directivity Results for Configuration 4.

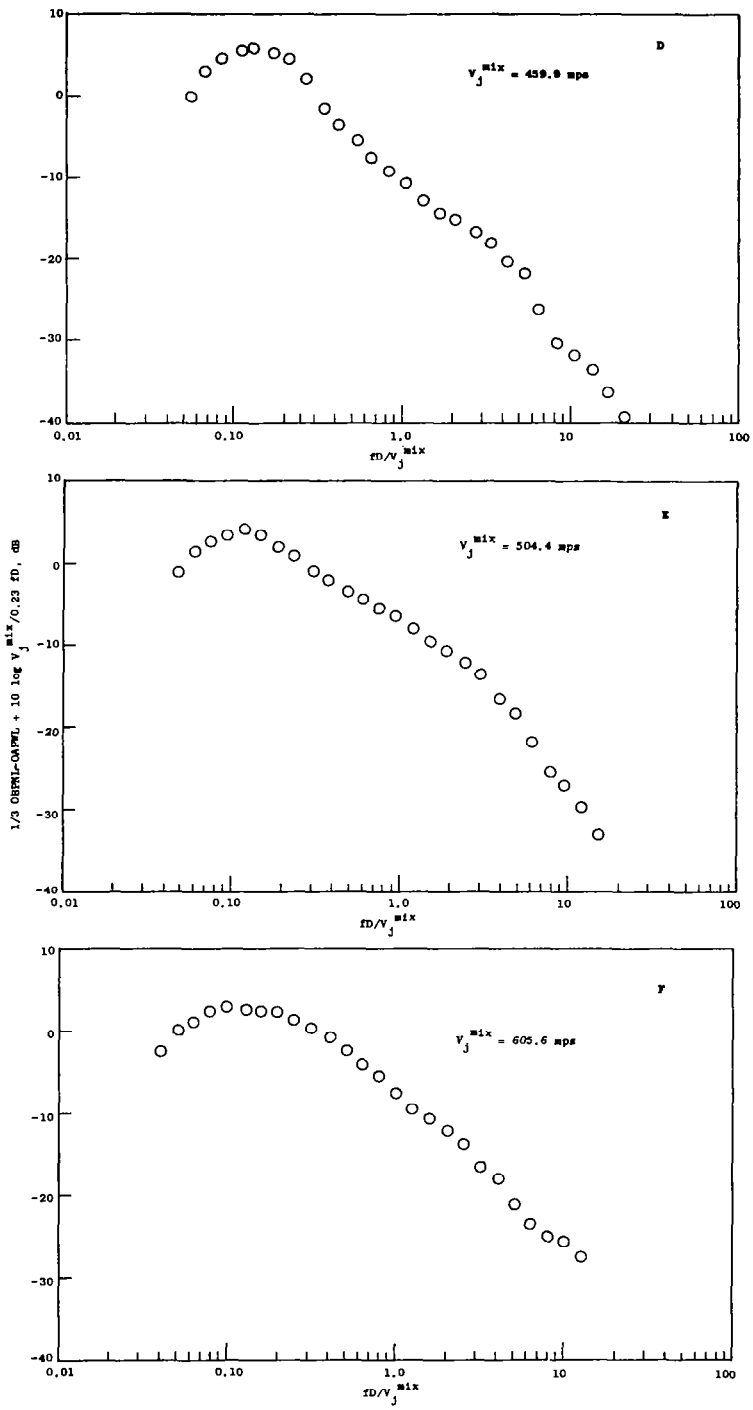

Figure III-7. Power Spectral Density Data for Configuration 5.

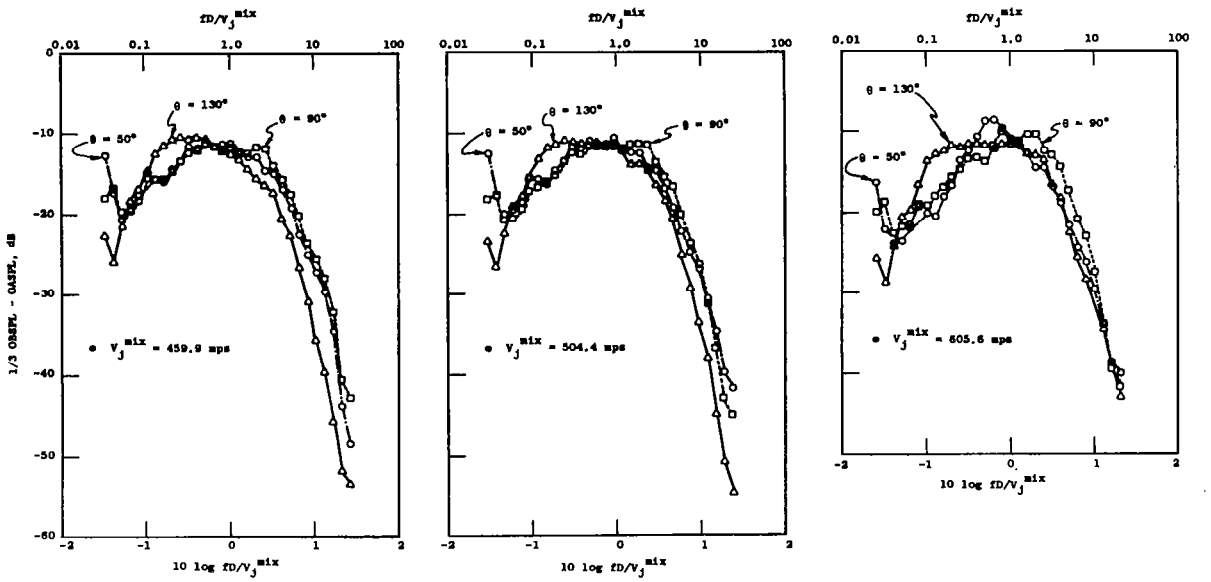

• 1/3 Octave Band Spectra for Configuration 5

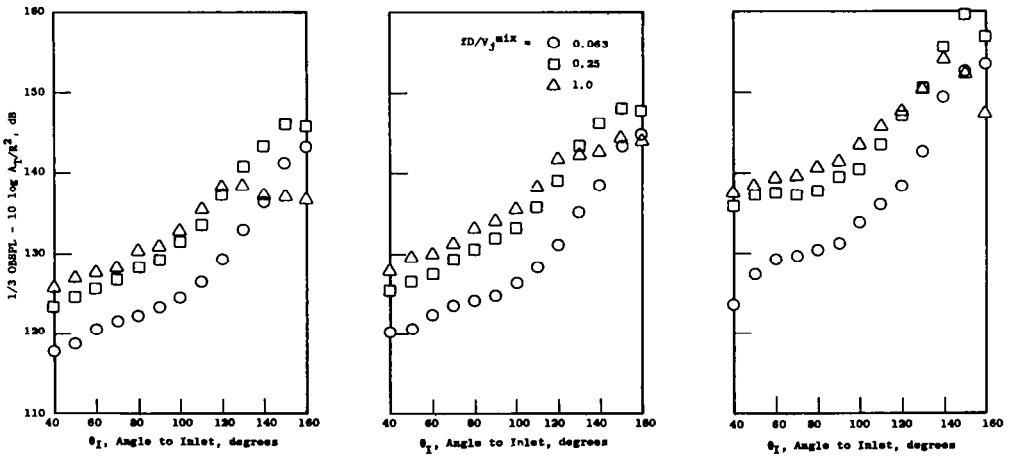

• 1/3 Octave Band Sound Pressure Level Directivity Results for Configuration 5

Figure III-8. One-Third Octave Band Sound Pressure Directivity Results for Configuration 5.

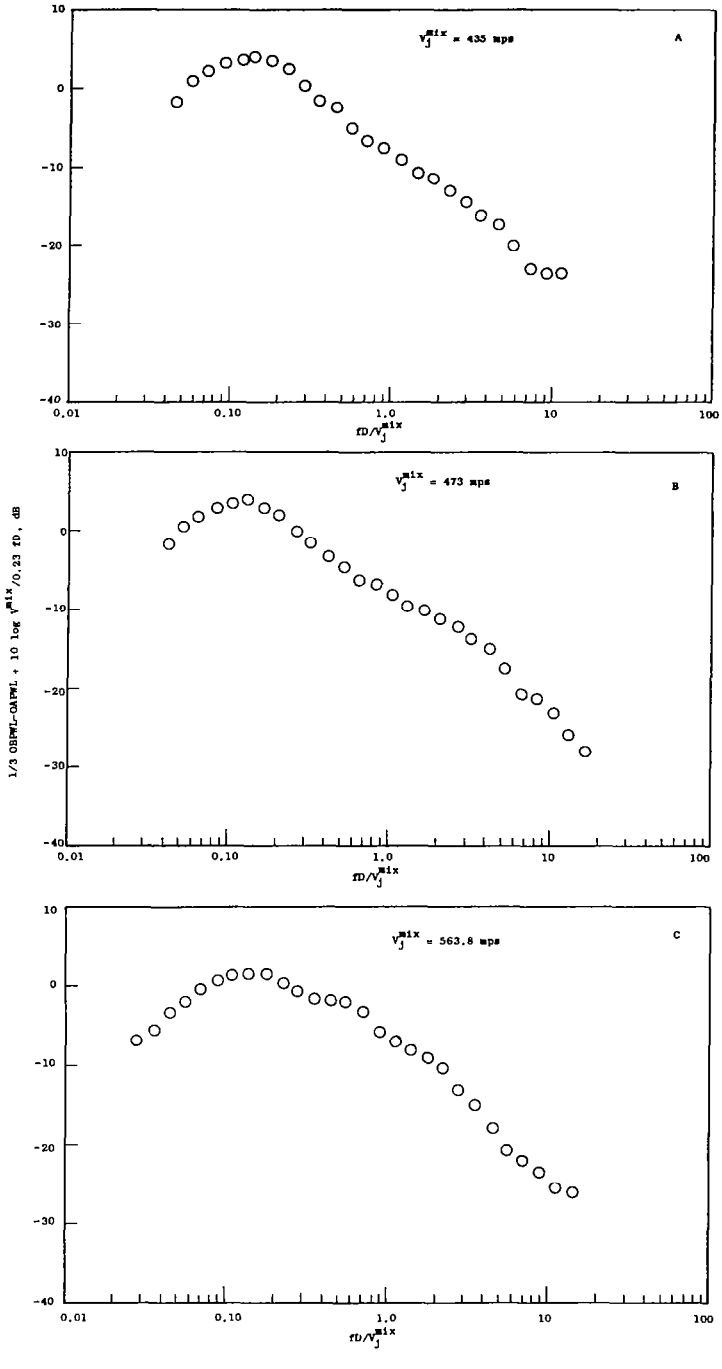

Figure III-9. Power Spectral Density Data for Configuration 6.

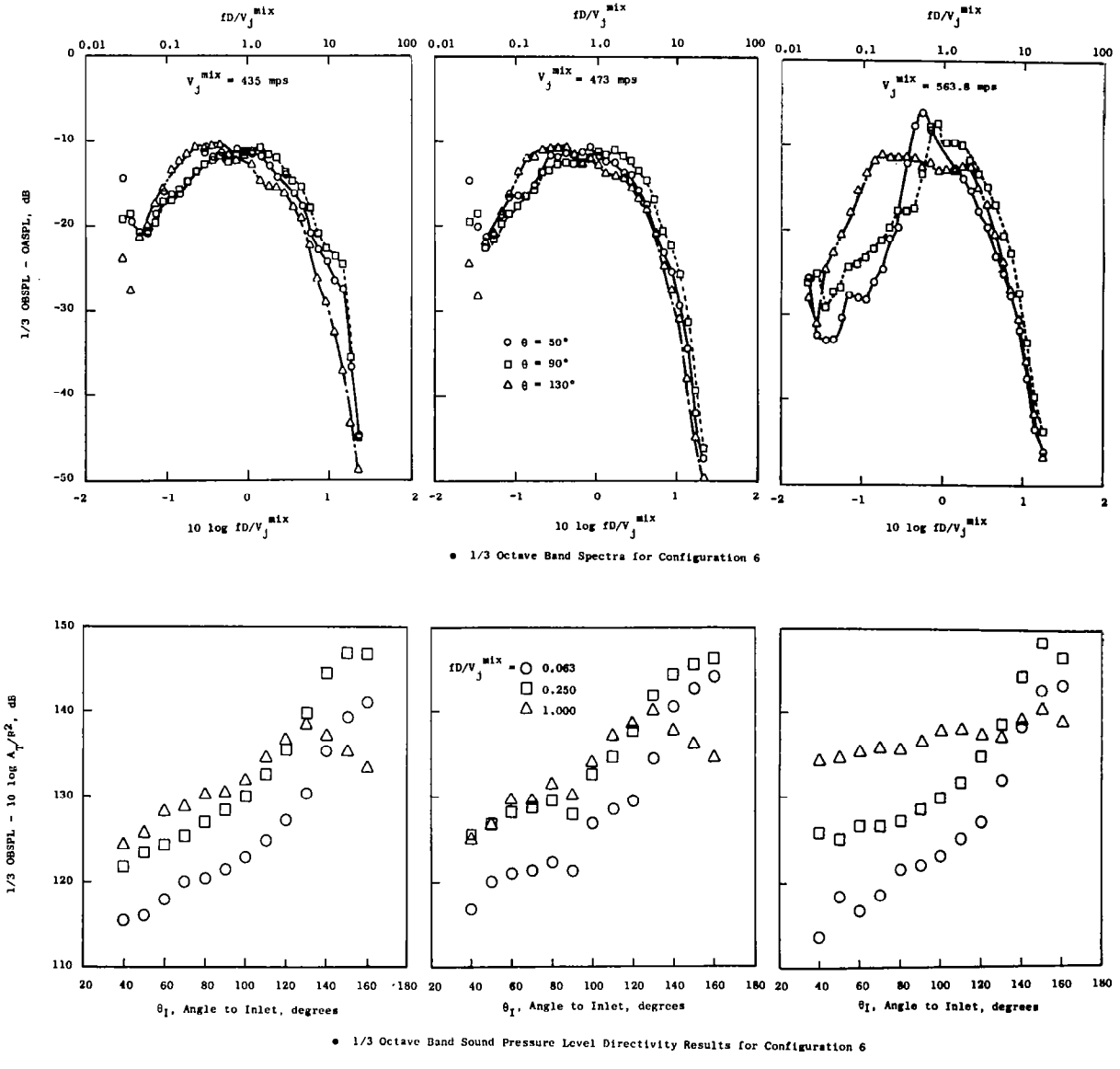

Figure III-10. One-Third Octave Band Sound Pressure Directivity Results for Configuration 6.

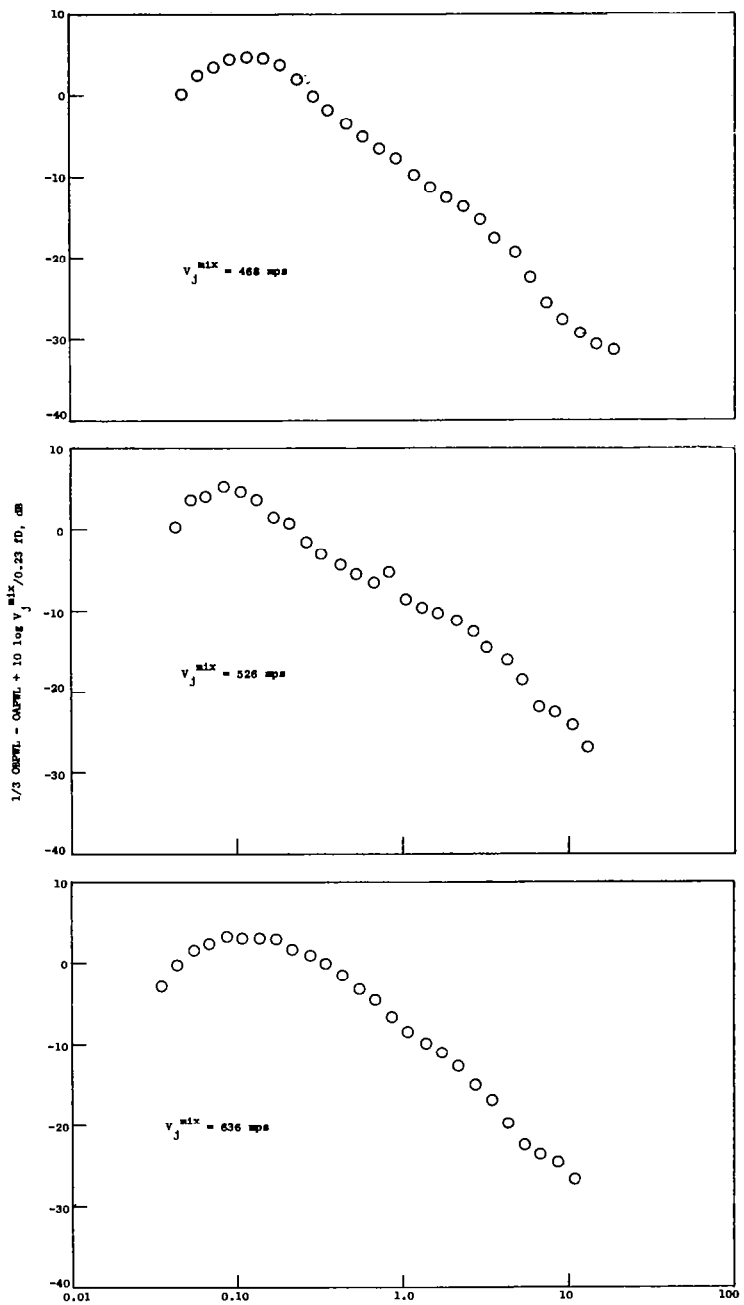

Figure III-11. Power Spectral Density Data for Configuration 7.

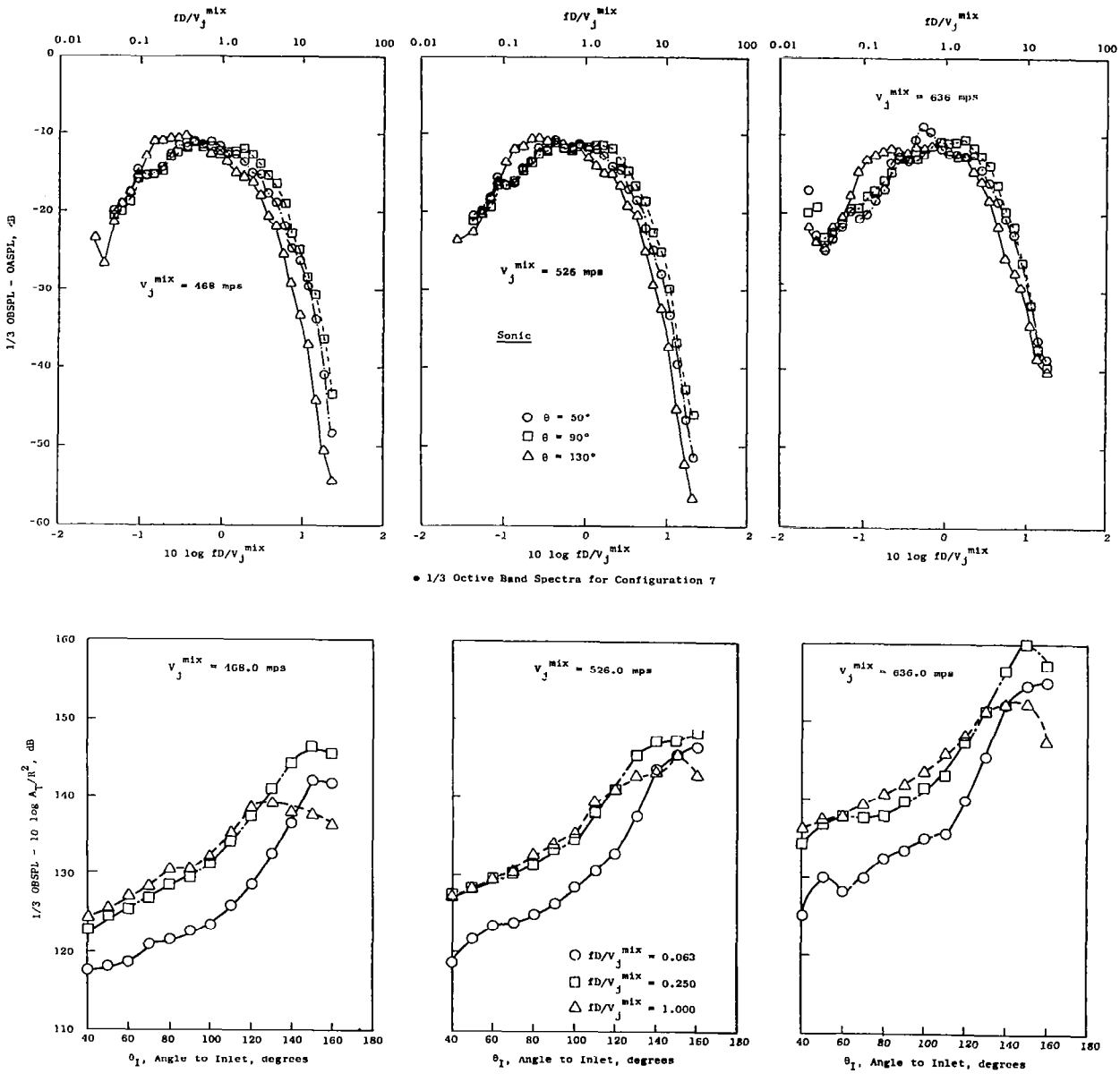

Figure III-12. One-Third Octave Band Sound Pressure Directivity Results for Configuration 7.

APPENDIX IV -

Spectra for High Radius Ratio Coannular Nozzles with Plug --

Configurations 2 through 7, Covering the Following Combinations:

- Subsonic/Sonic in Outer/Inner Streams
- Sonic/Sonic in Outer/Inner Streams
- Supersonic/Supersonic in Both Streams

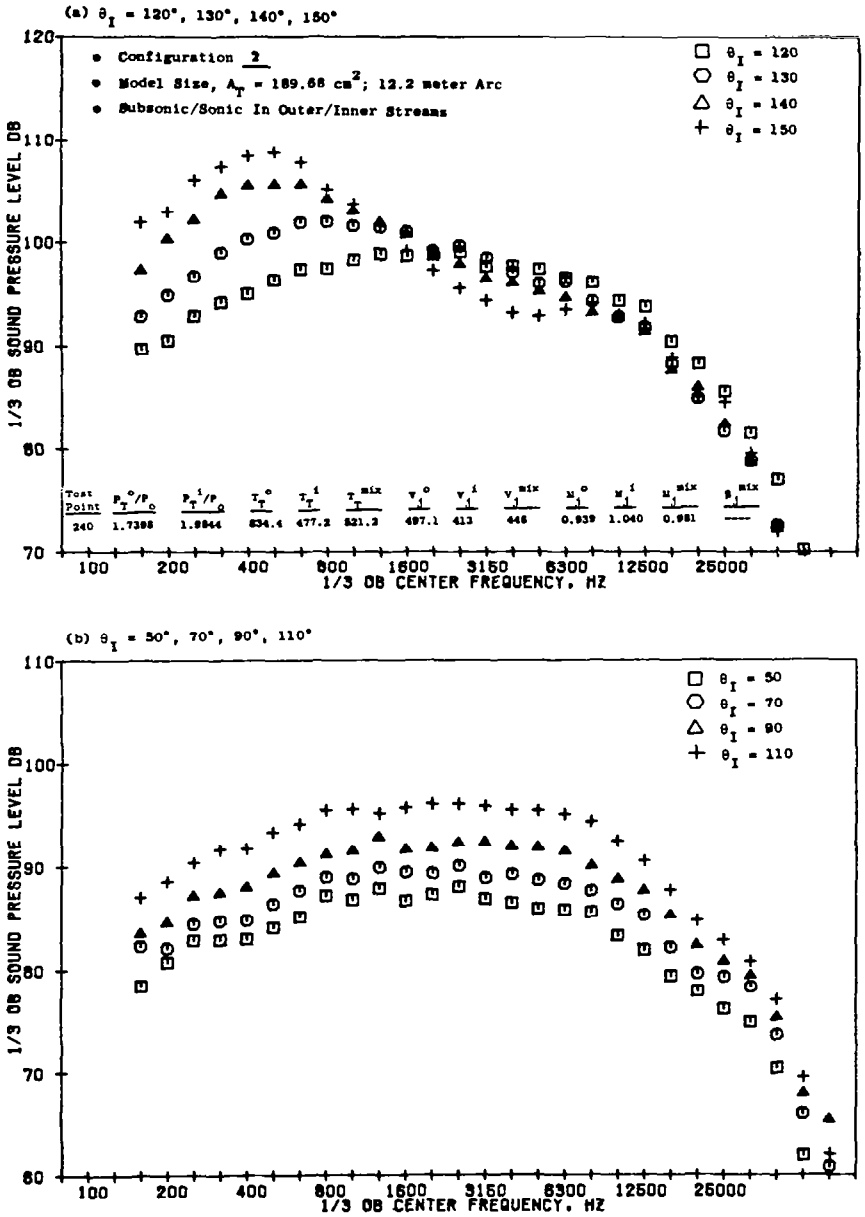

Figure IV-1. One-Third Octave Band Spectra at Various Angles for High Subsonic/Sonic Test Conditions for a High Radius Ratio Coannular Nozzle with Plug Configuration 2.

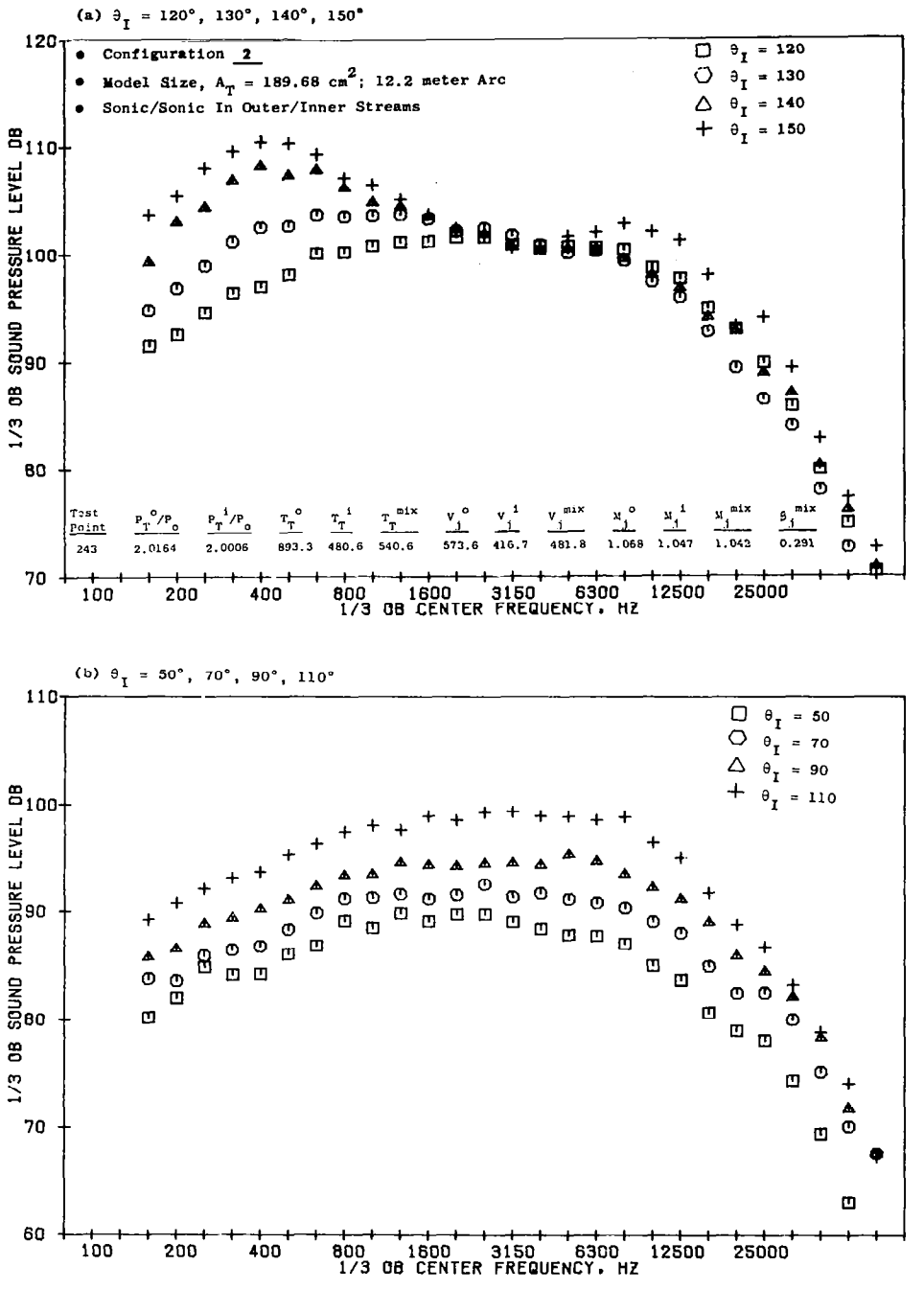

Figure IV-2. One-Third Octave Band Spectra at Various Angles and with Sonic/Sonic Test Conditions for a High Radius Ratio Coannular Nozzle with a Plug Configuration 2.

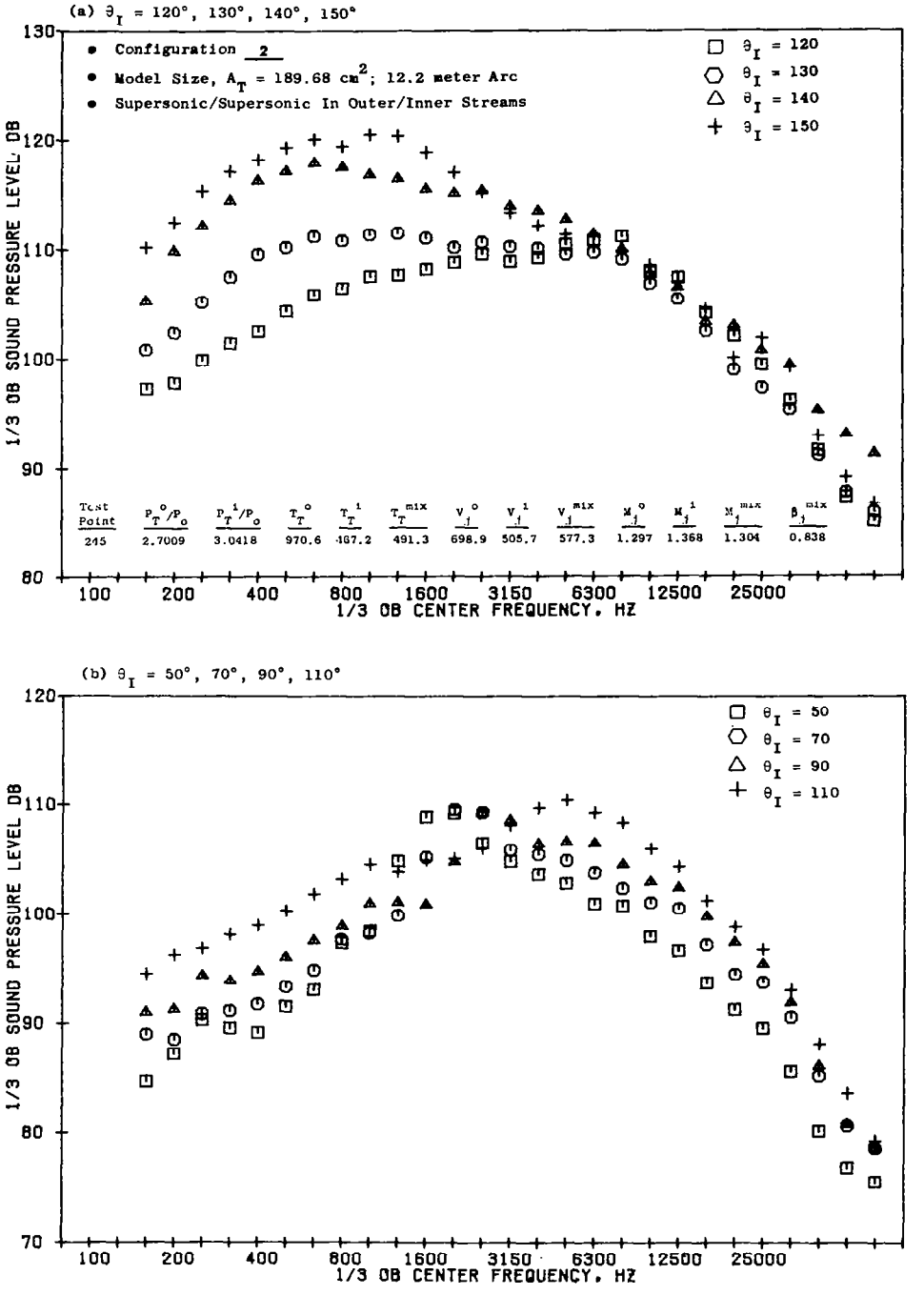

Figure IV-3. One-Third Octave Band Spectra at Various Angles and with Supersonic/Supersonic Test Conditions for a High Radius Ratio Coannular Nozzle with a Plug Configuration 2.

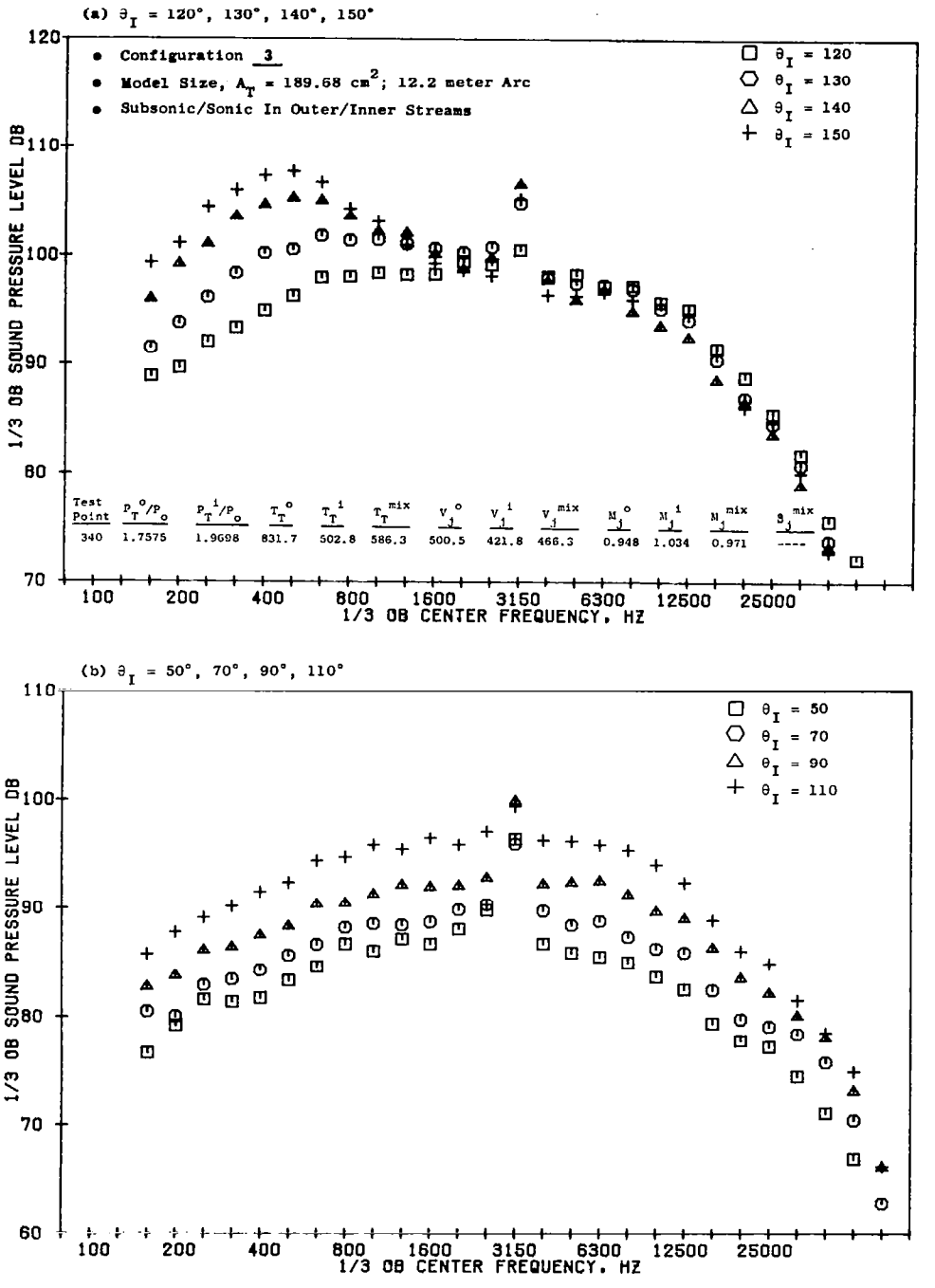

Figure IV-4. One-Third Octave Band Spectra at Various Angles and with High Subsonic/Sonic Test Conditions for a High Radius Ratio Coannular Nozzle with Plug Configuration 3.

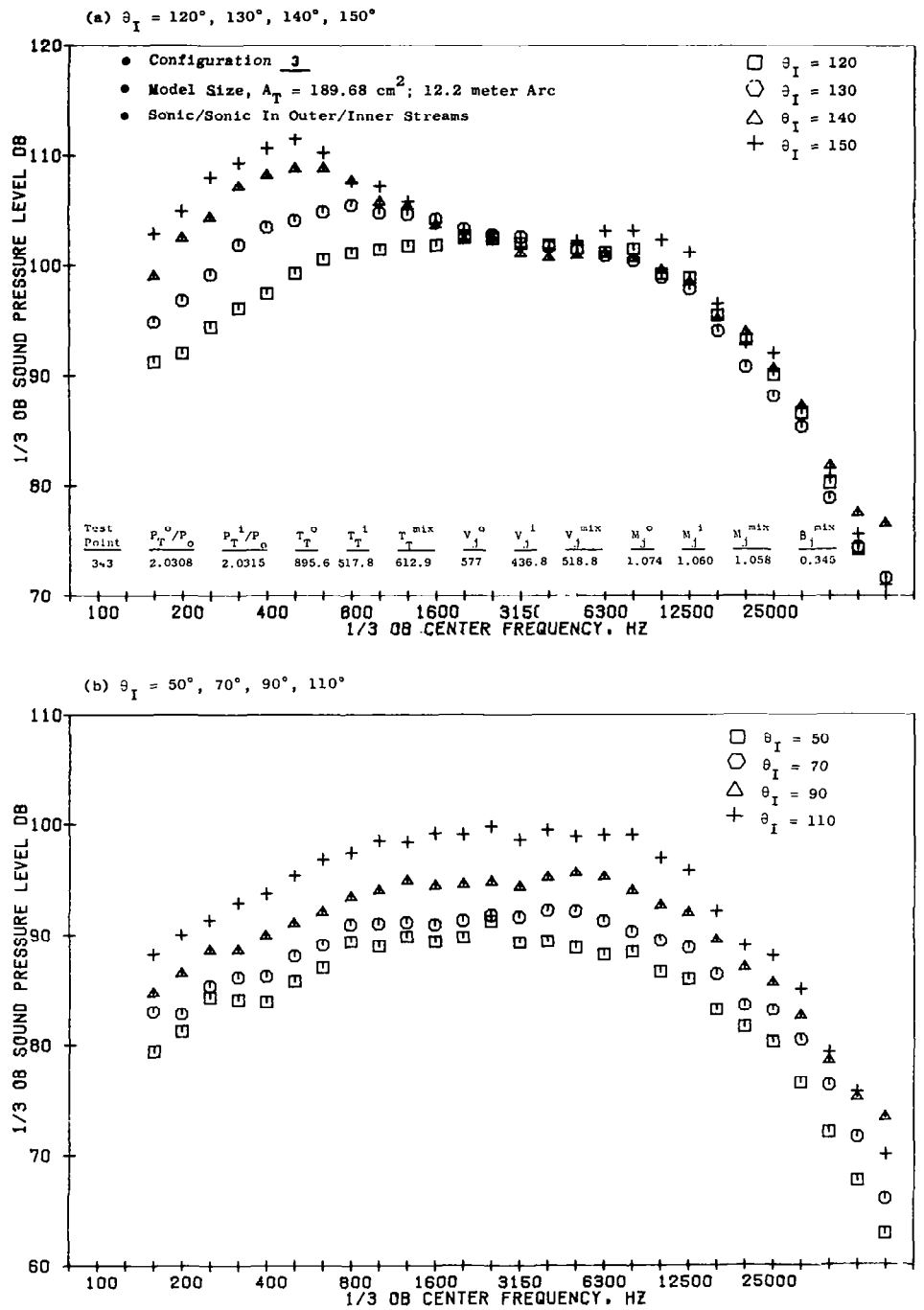

Figure IV-5. One-Third Octave Band Spectra at Various Angles and with Sonic/Sonic Test Conditions for a High Radius Ratio Coannular Nozzle with a Plug Configuration 3.

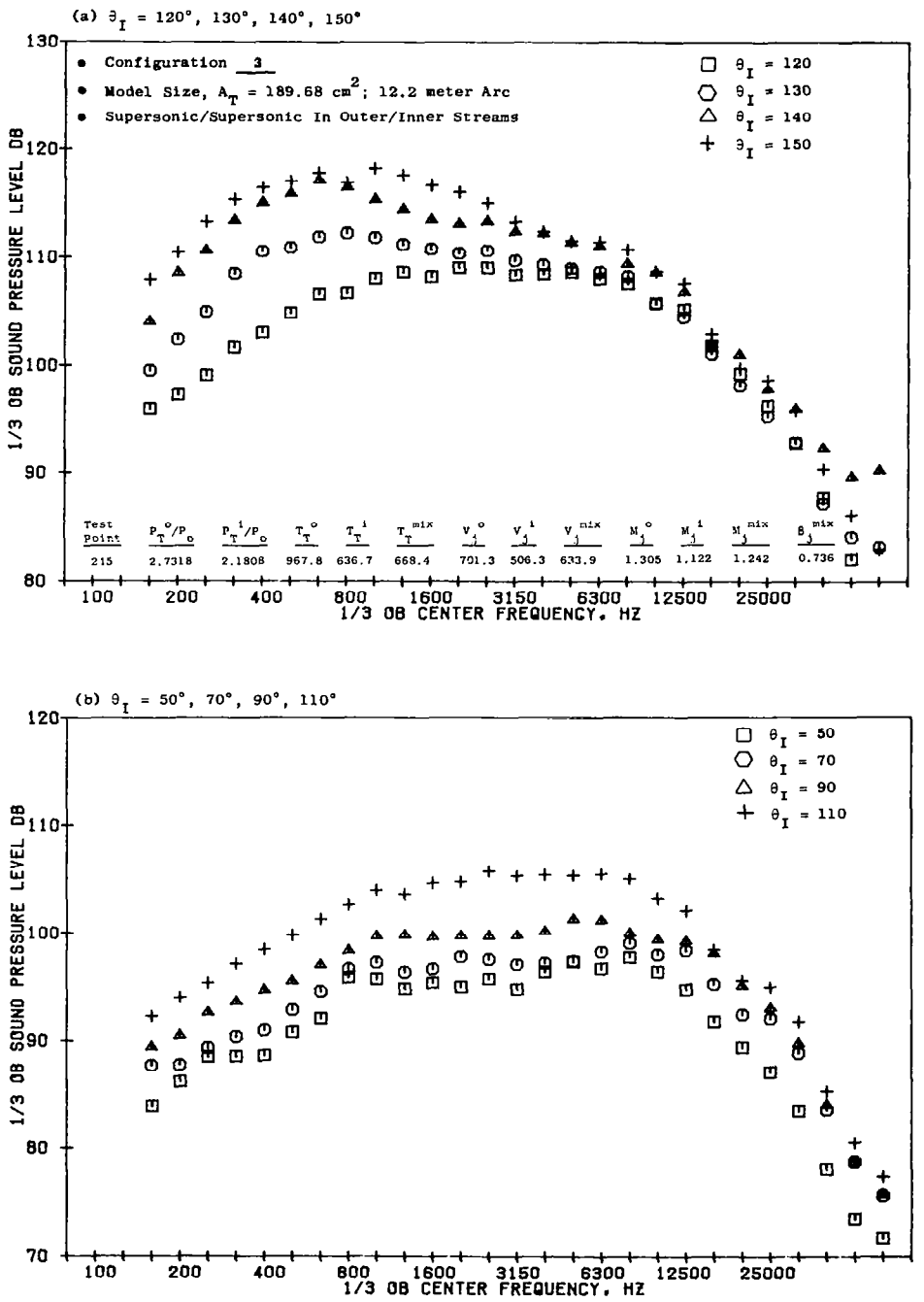

Figure IV-6. One-Third Octave Band Spectra at Various Angles and with Supersonic/Supersonic Test Conditions for a High Radius Ratio Coannular Nozzle with a Plug Configuration 3.

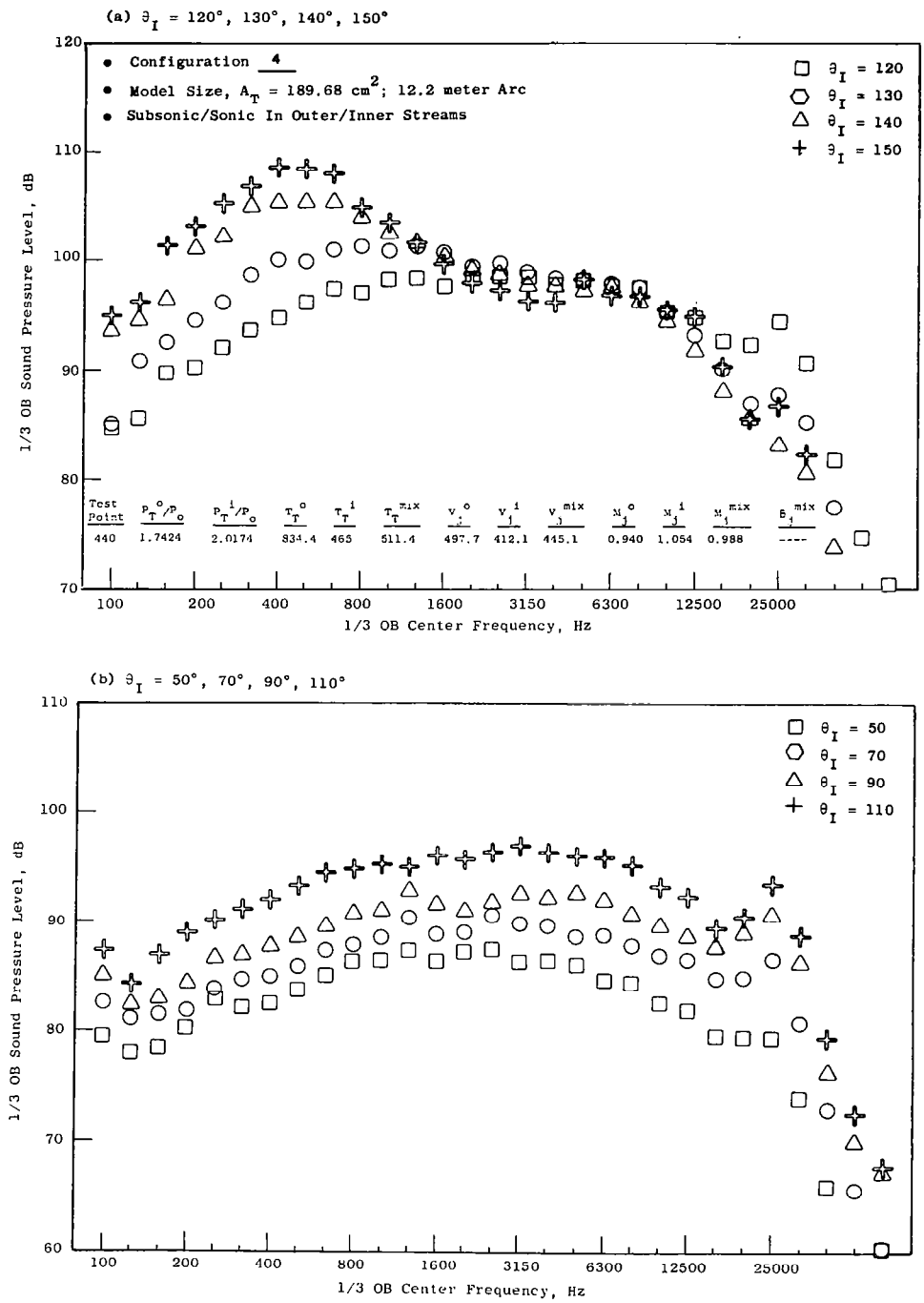

Figure IV-7. One-Third Octave Band Spectra at Various Angles and with Subsonic/Sonic Test Conditions for a High Radius Ratio Coannular Nozzle with a Plug Configuration 4.

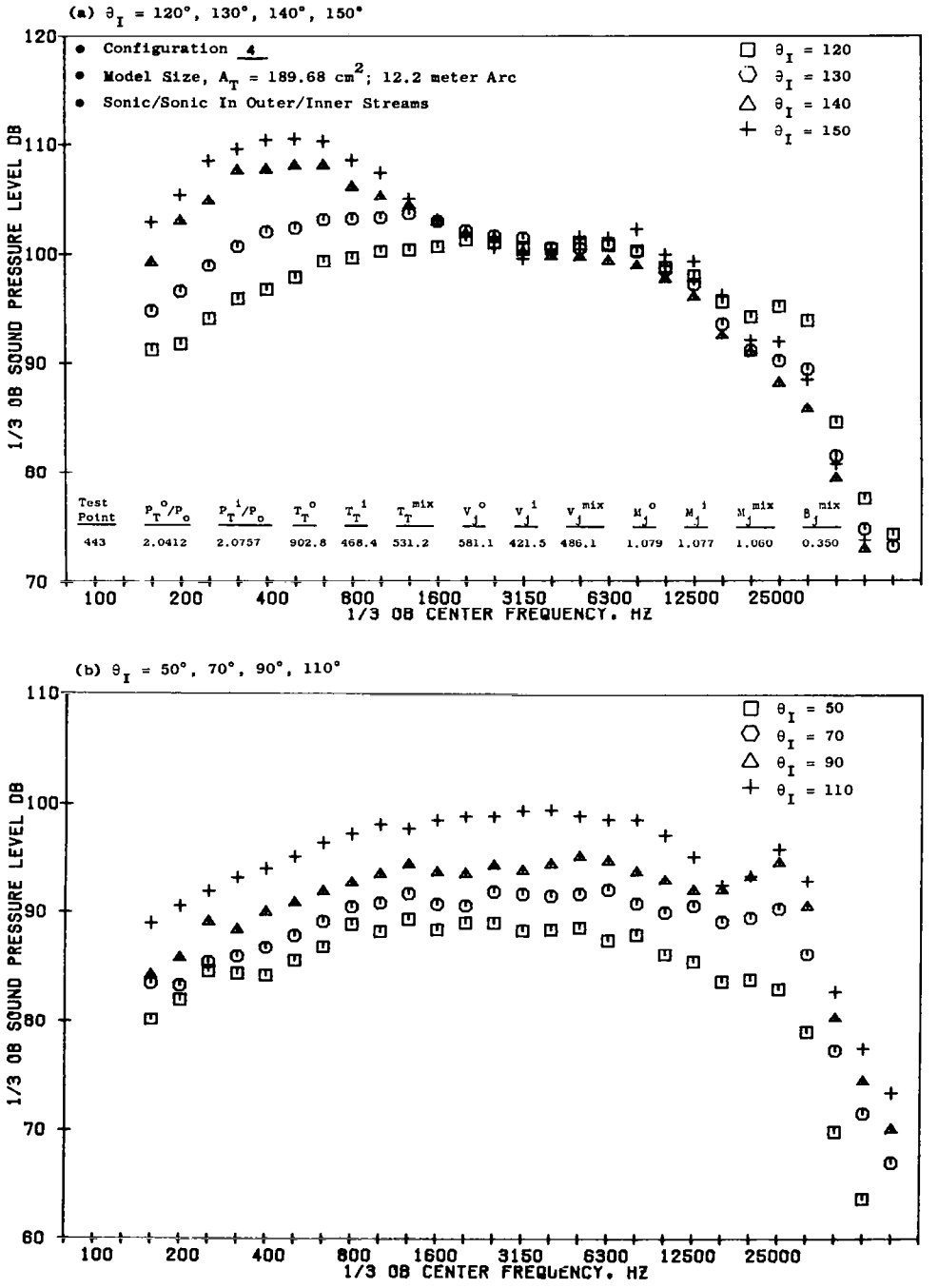

Figure IV-8. One-Third Octave Band Spectra at Various Angles and with Sonic/Sonic Test Conditions for a High Radius Ratio Coannular Nozzle with a Plug Configuration 4.

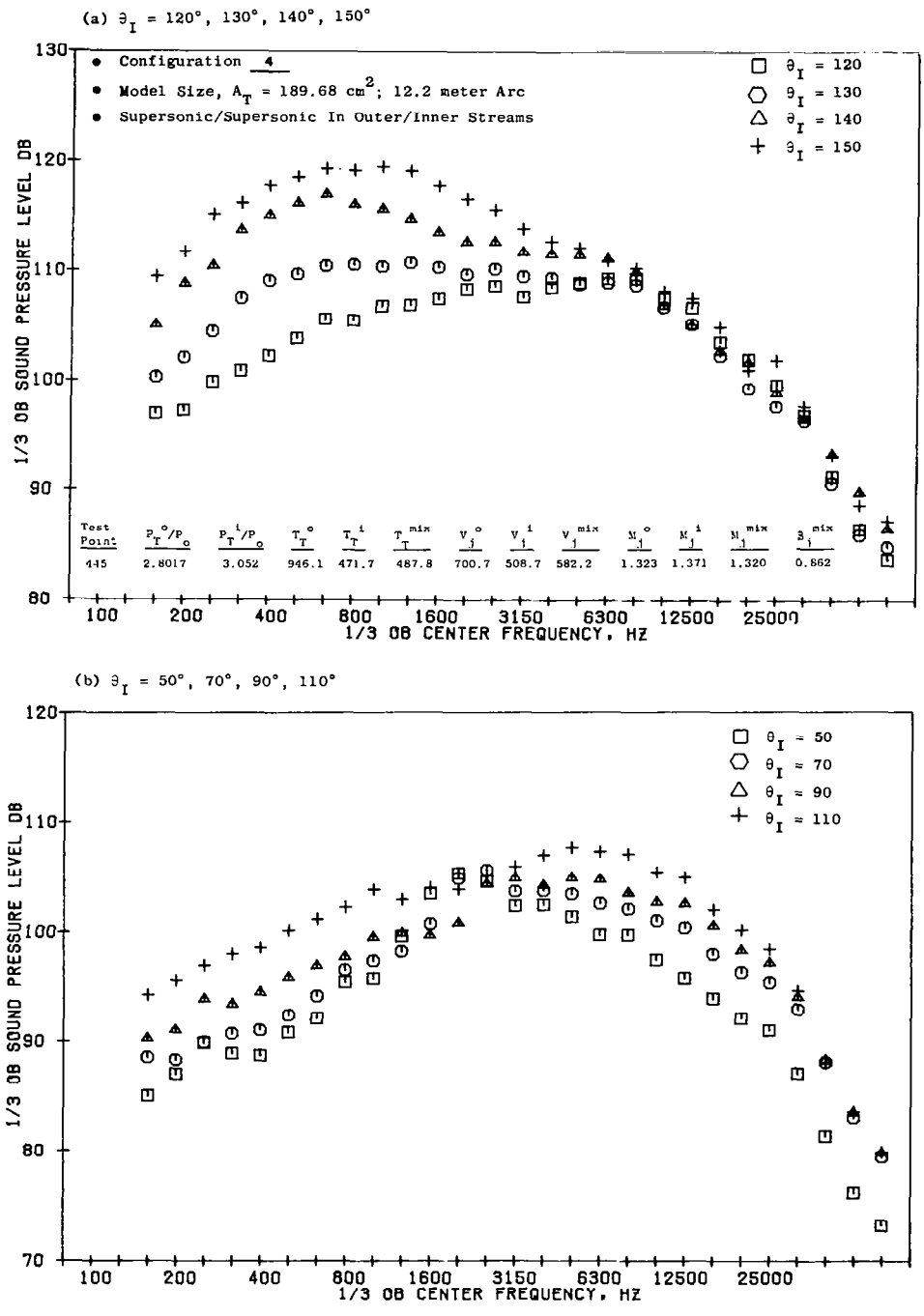

Figure IV-9. One-Third Octave Band Spectra at Various Angles and with Supersonic/Supersonic Test Conditions for a High Radius Ratio Coannular Nozzle with a Plug Configuration 4.

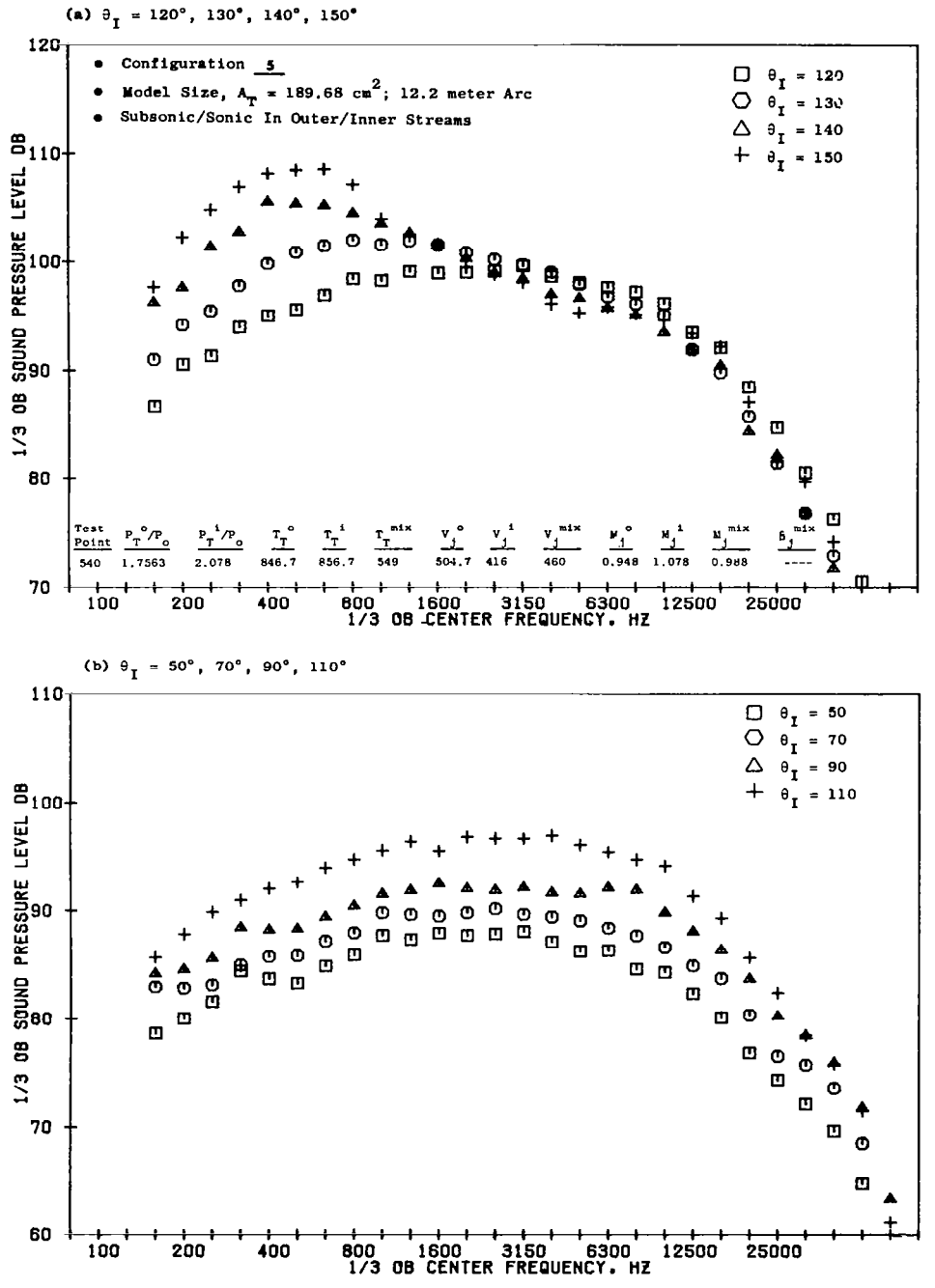

Figure IV-10. One-Third Octave Band Spectra at Various Angles and with Subsonic/Sonic Test Conditions for a High Radius Ratio Coannular Nozzle with a Plug Configuration 5.

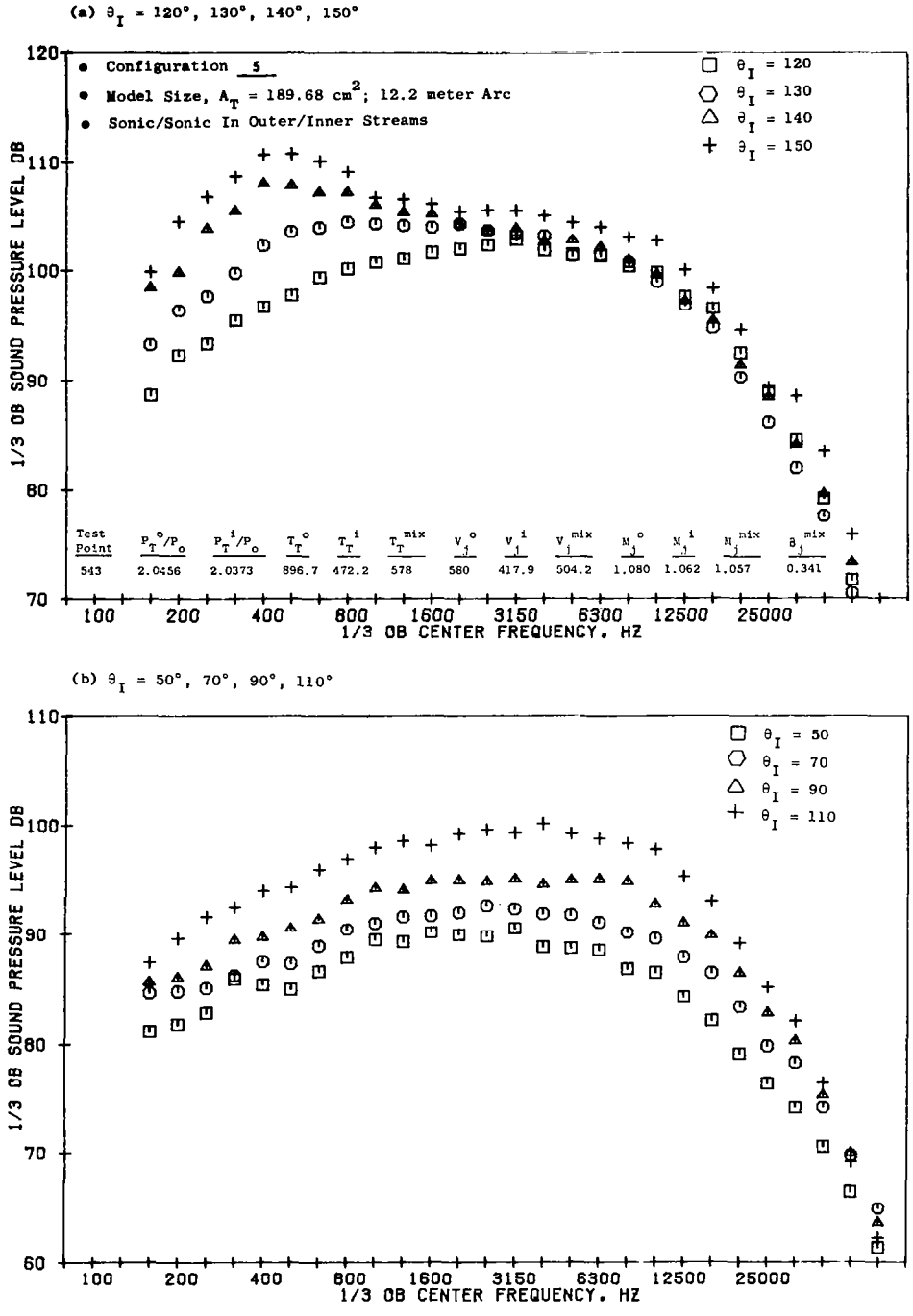

Figure IV-11. One-Third Octave Band Spectra at Various Angles and with Sonic/Sonic Test Conditions for a High Radius Ratio Coannular Nozzle with a Plug Configuration 5.

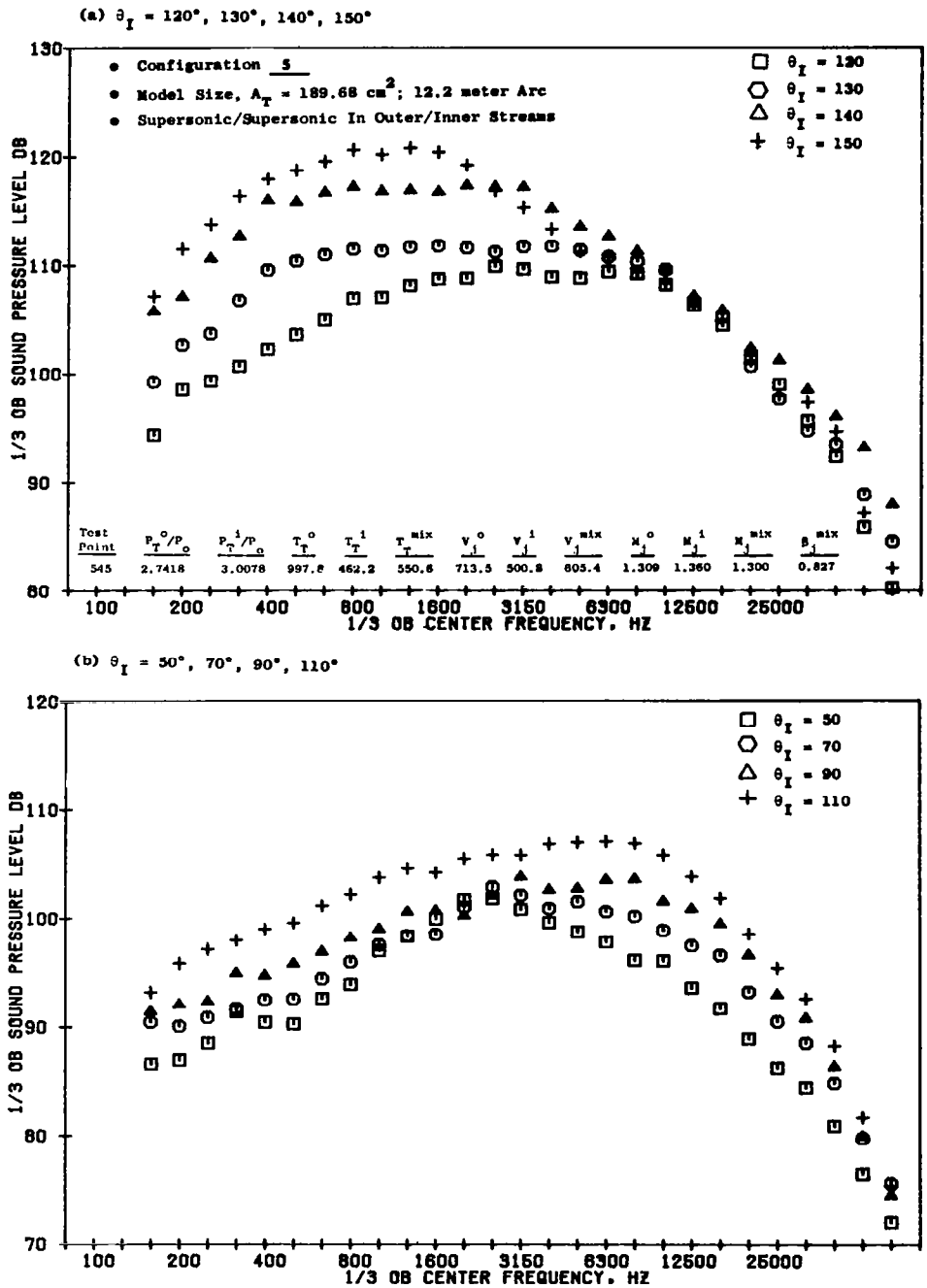

Figure IV-12. One-Third Octave Band Spectra at Various Angles and with Supersonic/Supersonic Test Conditions for a High Radius Ratio Coannular Nozzle with a Plug Configuration 5.

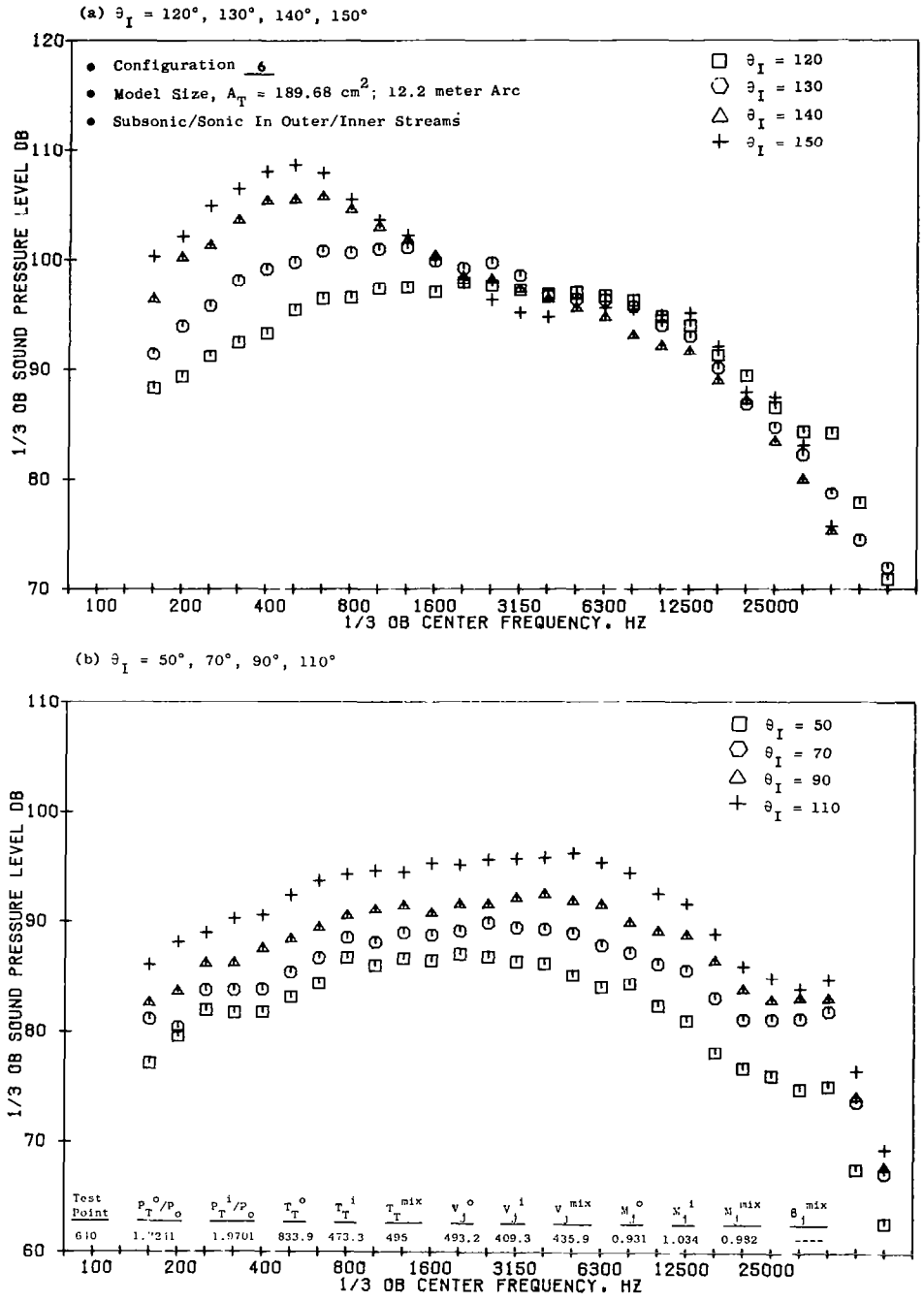

Figure IV-13. One-Third Octave Band Spectra at Various Angles and with Subsonic/Sonic Test Conditions for a High Radius Ratio Coannular Nozzle with a Plug Configuration 6.

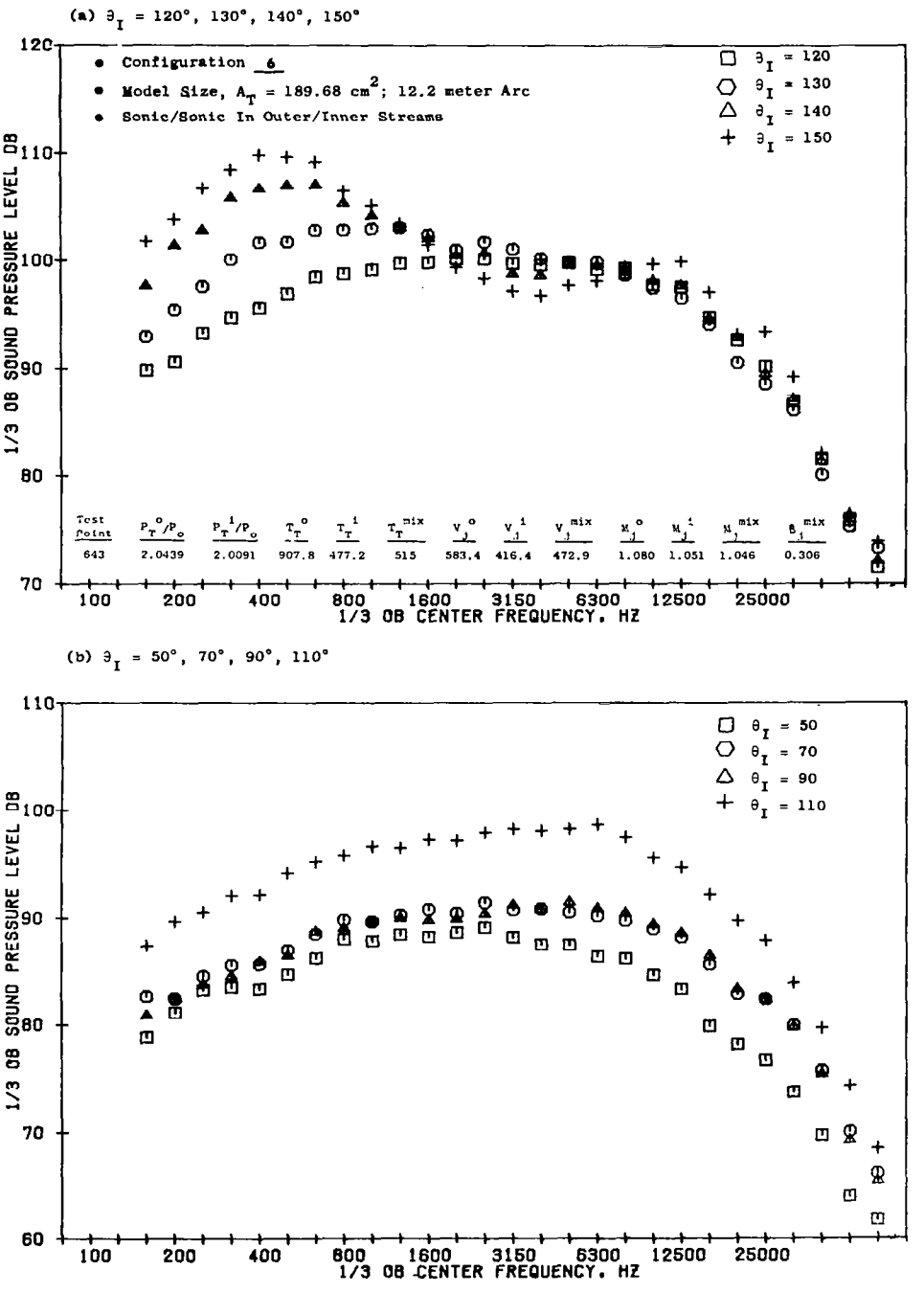

Figure IV-14. One-Third Octave Band Spectra at Various Angles and with Sonic/Sonic Test Conditions for a High Radius Ratio Coannular Nozzle with a Plug Configuration 6.

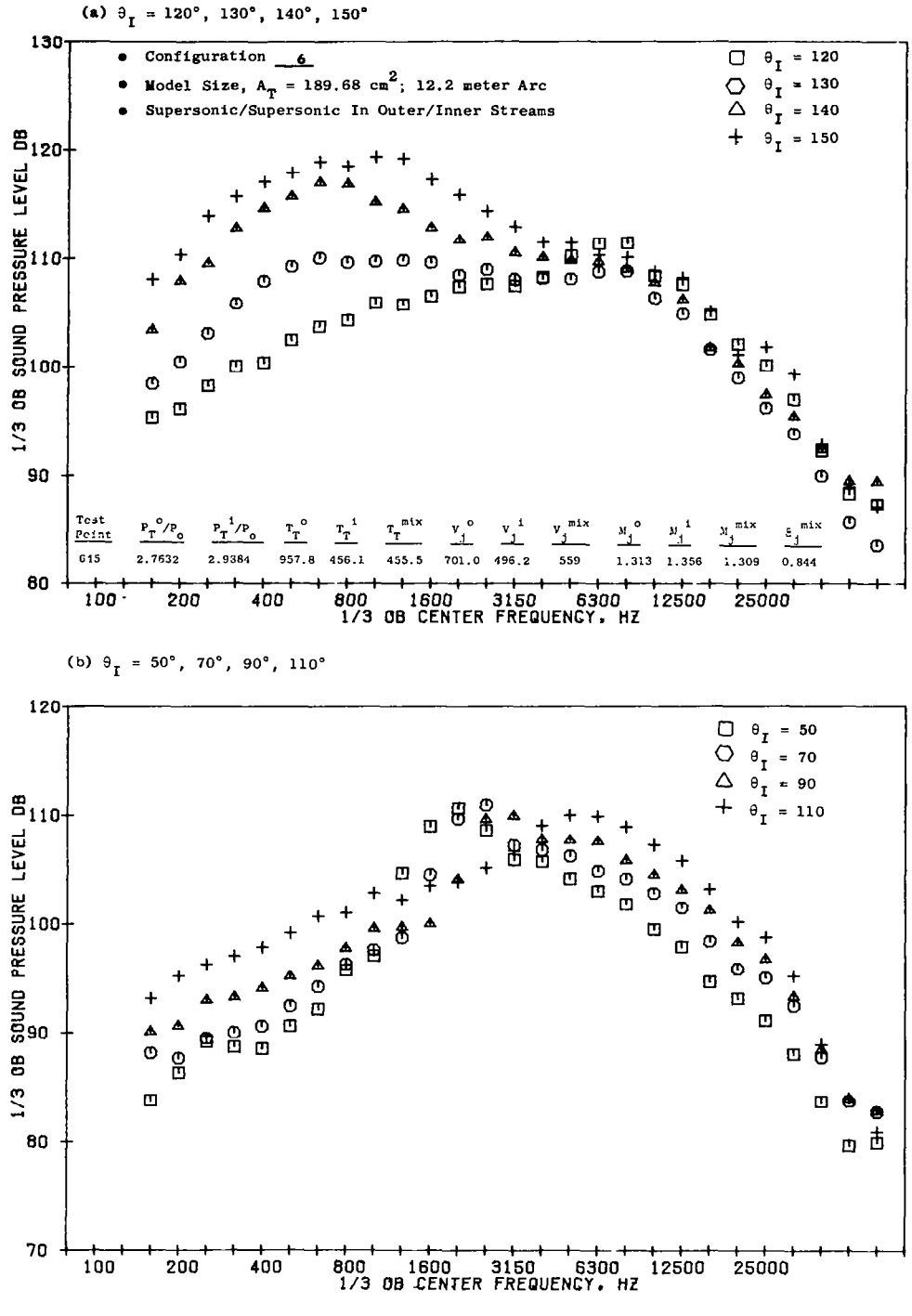

Figure IV-15. One-Third Octave Band Spectra at Various Angles and with Supersonic/Supersonic Test Conditions for a High Radius Ratio Coannular Nozzle with a Plug Configuration 6.

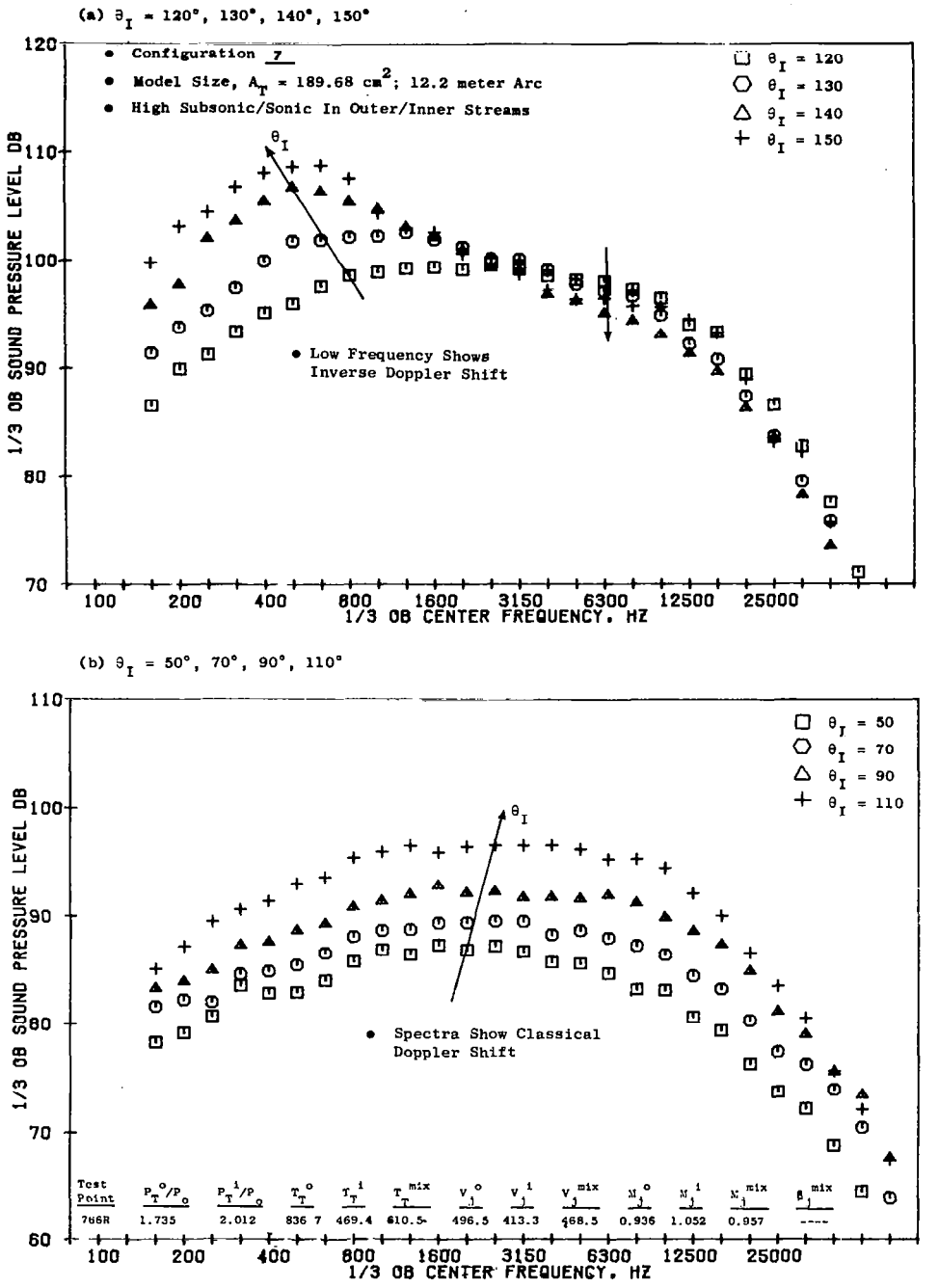

Figure IV-16. One-Third Octave Band Spectra at Various Angles and with High Subsonic/Sonic Test Conditions for a High Radius Ratio Coannular Nozzle with a Plug Configuration 7.

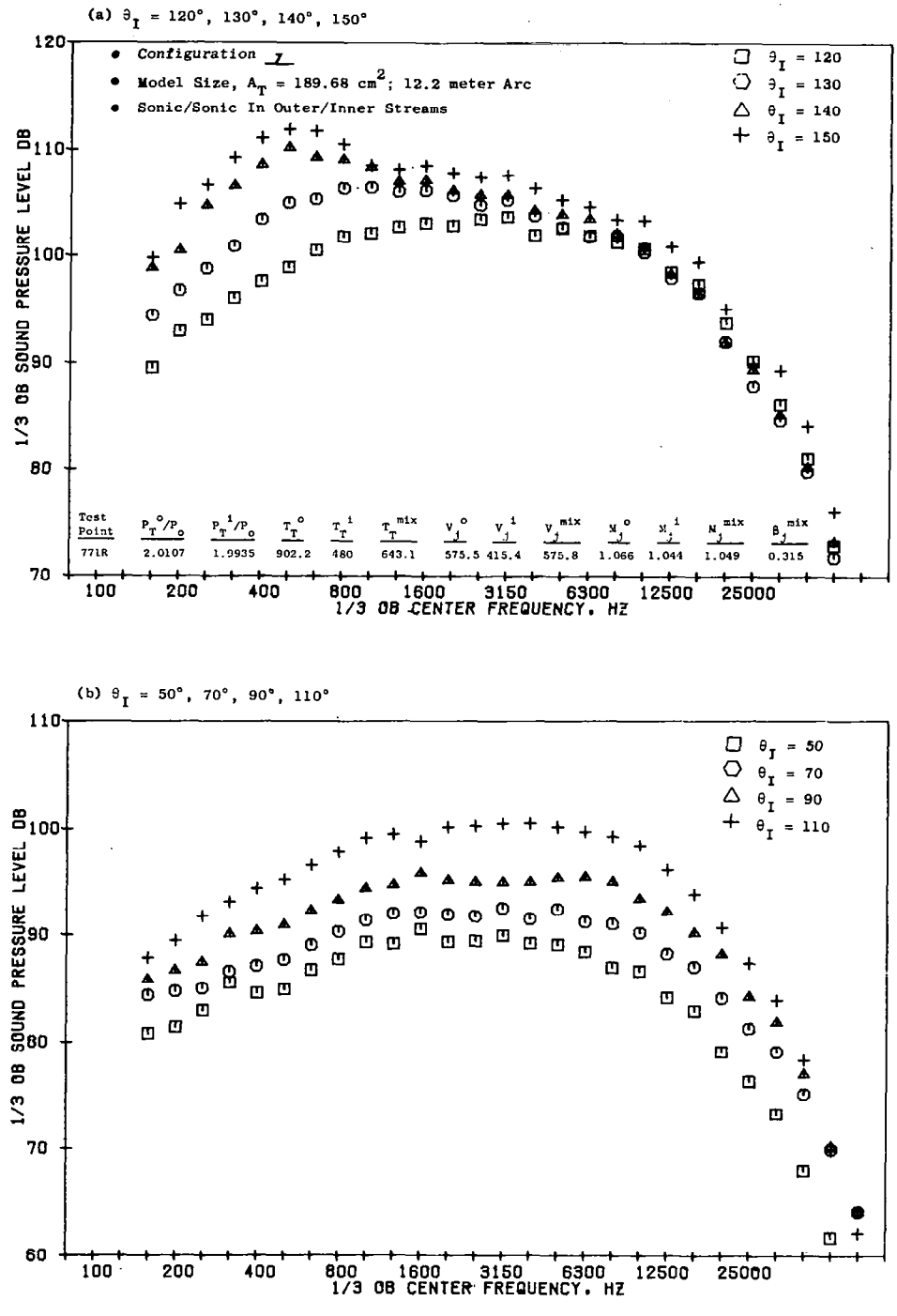

Figure IV-17. One-Third Octave Band Spectra at Various Angles and with Sonic/Sonic Test Conditions for a High Radius Ratio Coannular Nozzle with a Plug Configuration 7.

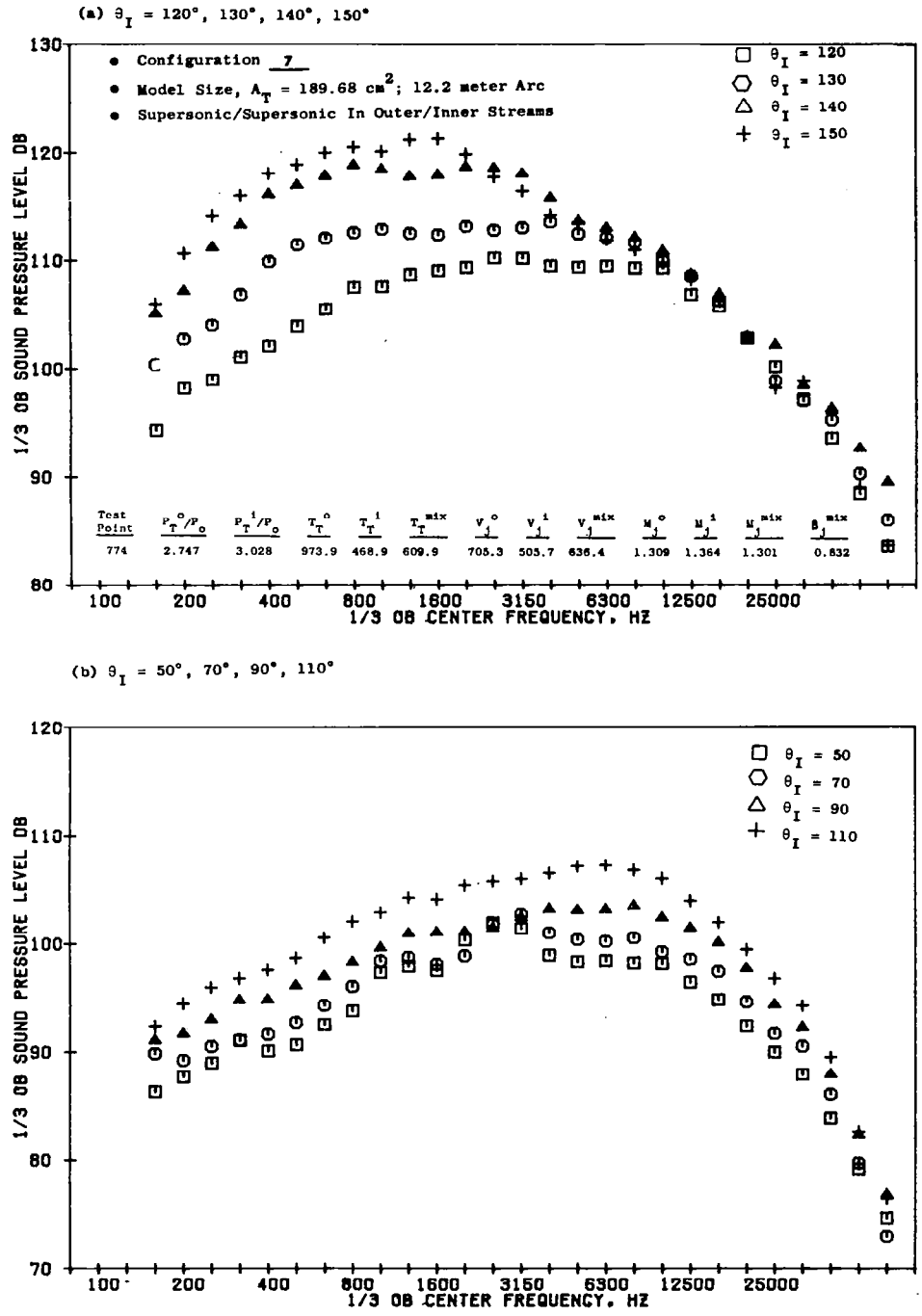

Figure IV-18. One-Third Octave Band Spectra at Various Angles and with Supersonic/Supersonic Test Conditions for a High Radius Ratio Coannular Nozzle with a Plug Configuration 7.

APPENDIX V -

Inner Nozzle Flow Coefficients for Configurations 1 Through 8

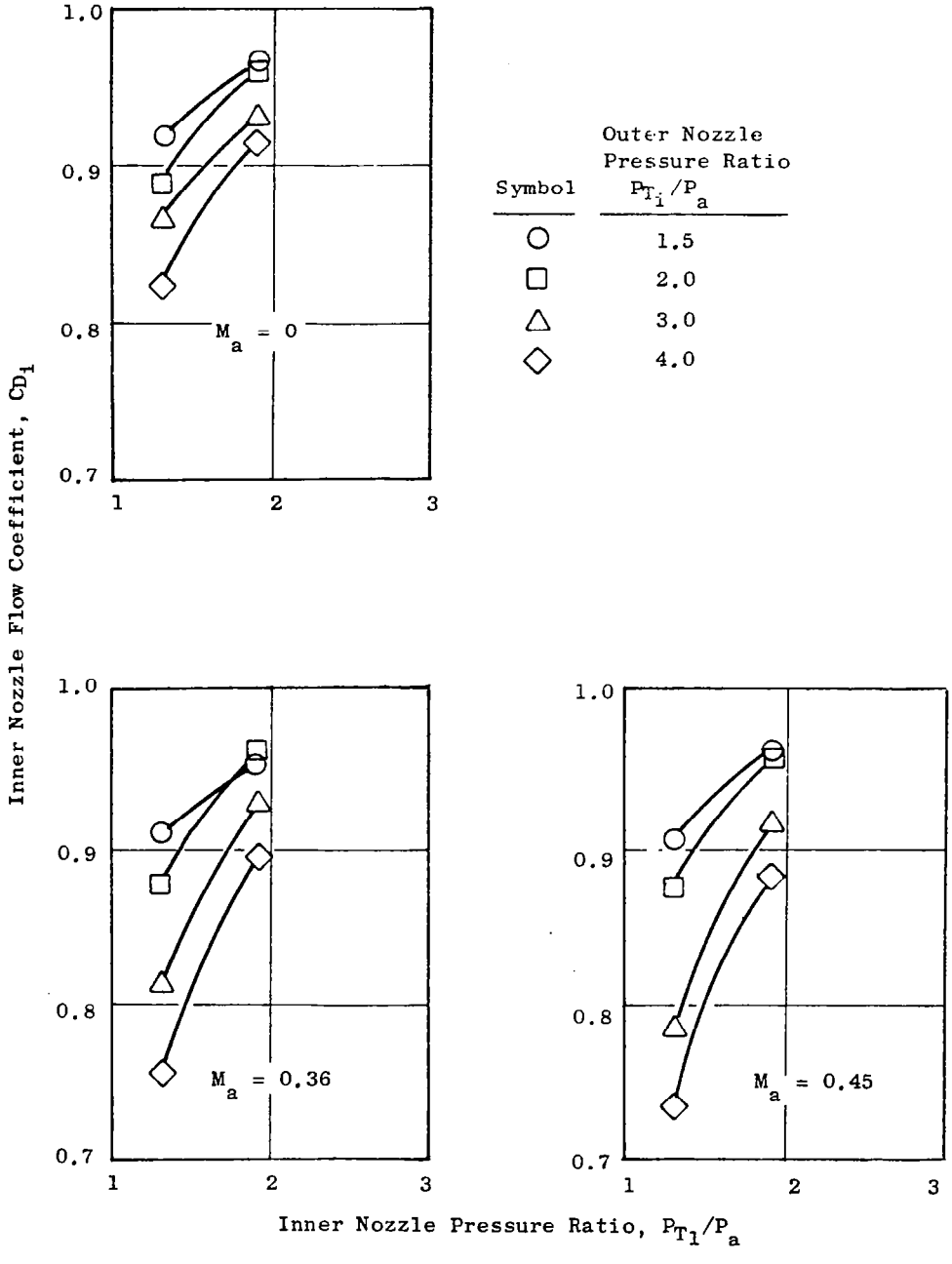

Figure V-1. Inner Nozzle Flow Coefficients for Configuration 1 [R_r^o = 0.902, R_r^i = 0.673, Bent Inner Plug].

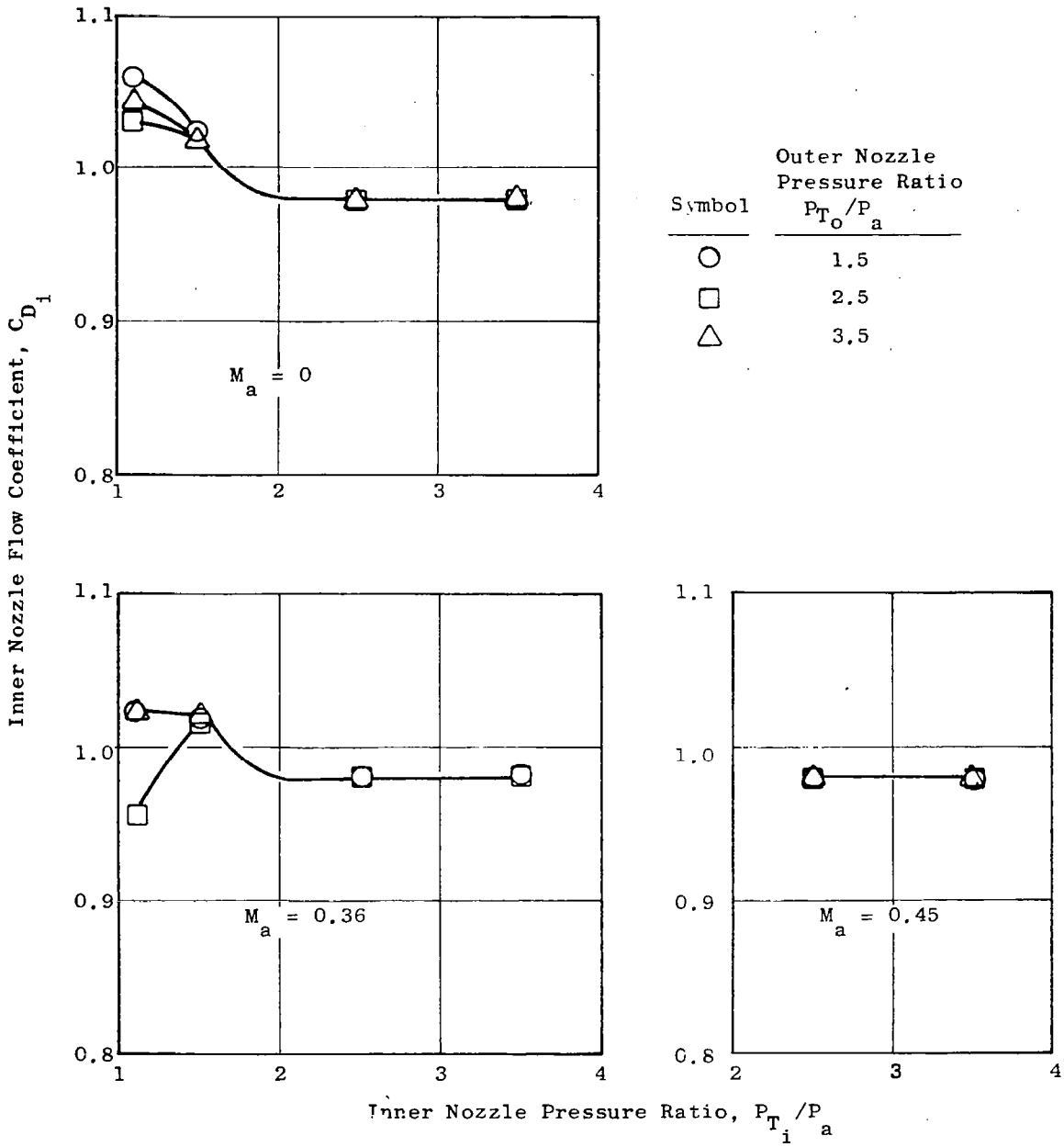

Figure V-2. Inner Nozzle Flow Coefficients for Configuration 2 [R_r^o = 0.902, R_r^i = 0.8, Conical Inner Plug].

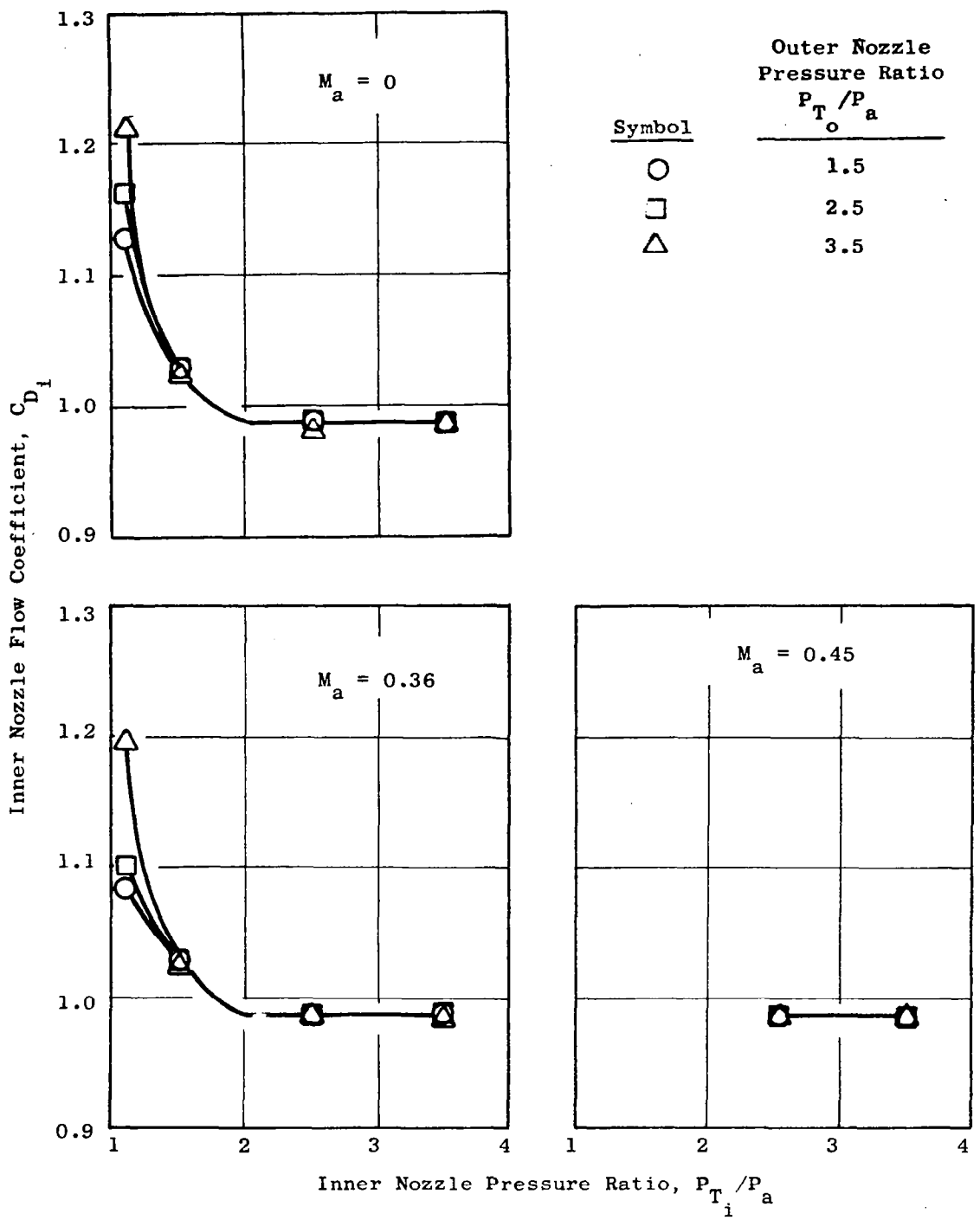

Figure V-3. Inner Nozzle Flow Coefficients for Configuration 3 [R_r^o = 0.902, R_r^i = 0.902, Conical Inner Plug].

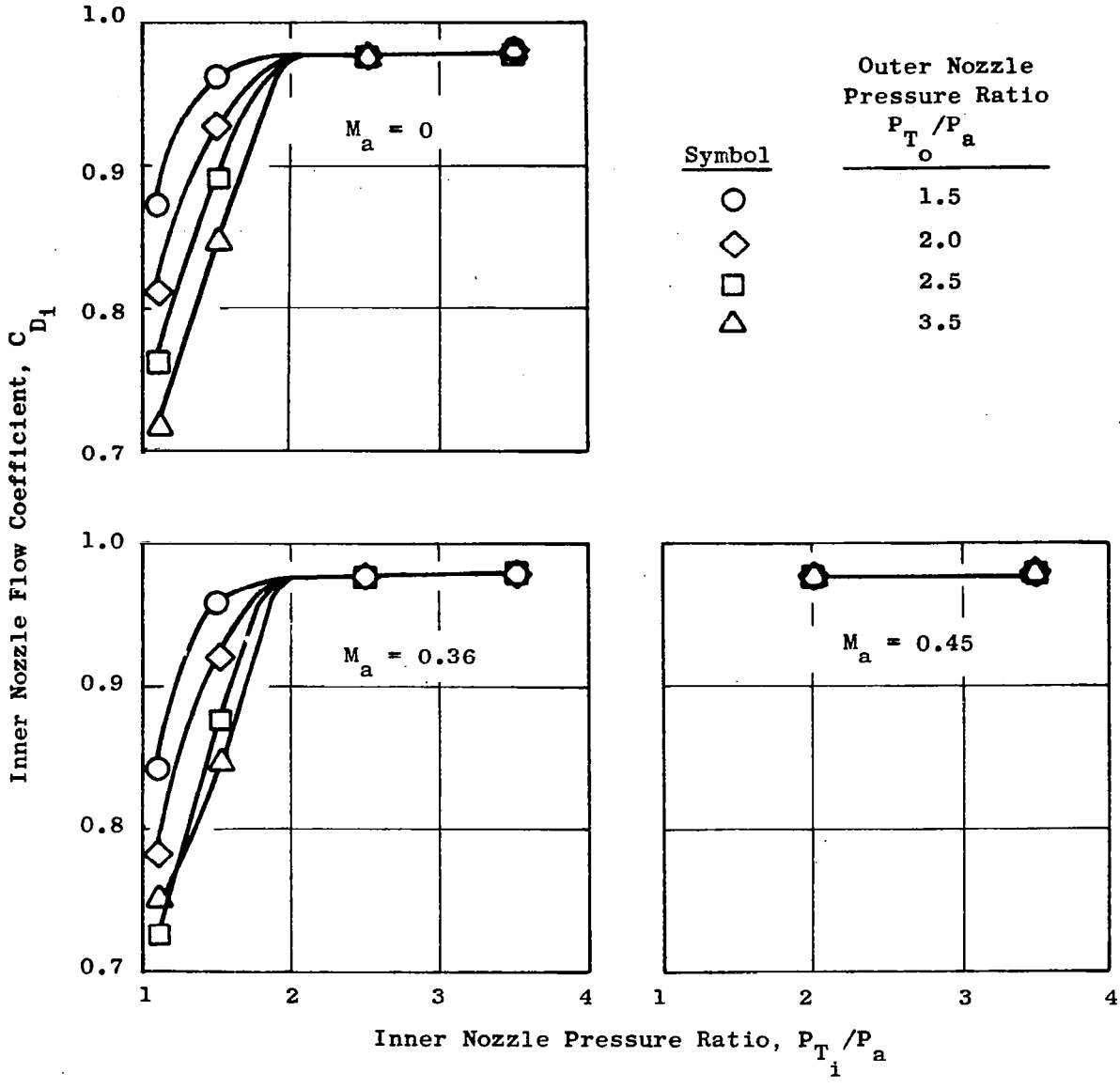

Figure V-4. Inner Nozzle Flow Coefficients for Configuration 4 [R_r^o = 0.902, R_r^i = 0.8, Bent Inner Plug].

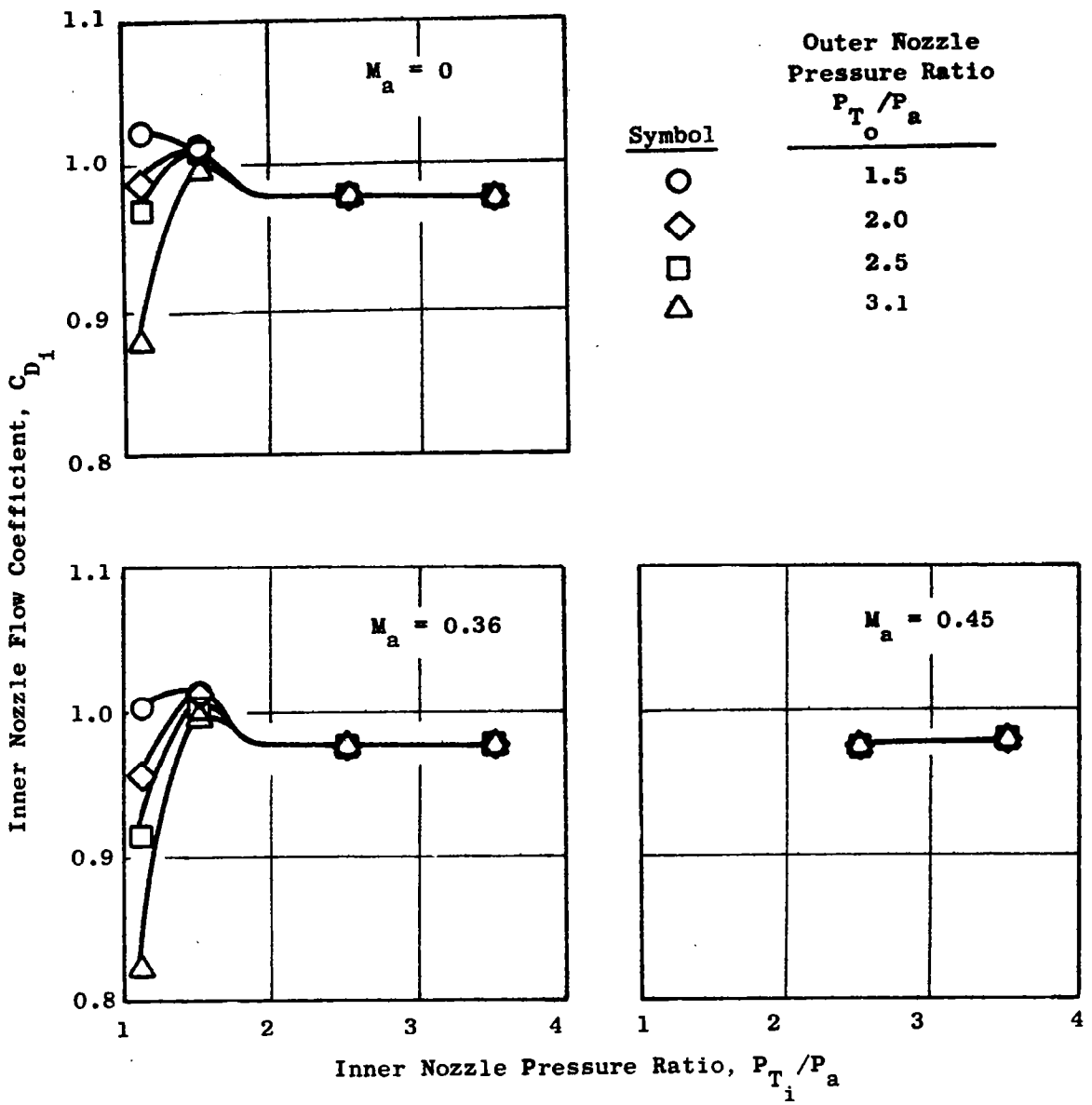

Figure V-5. Inner Nozzle Flow Coefficients for Configuration 5 [R_r^o = 0.853, R_r^i = 0.8, Conical Inner Plug].

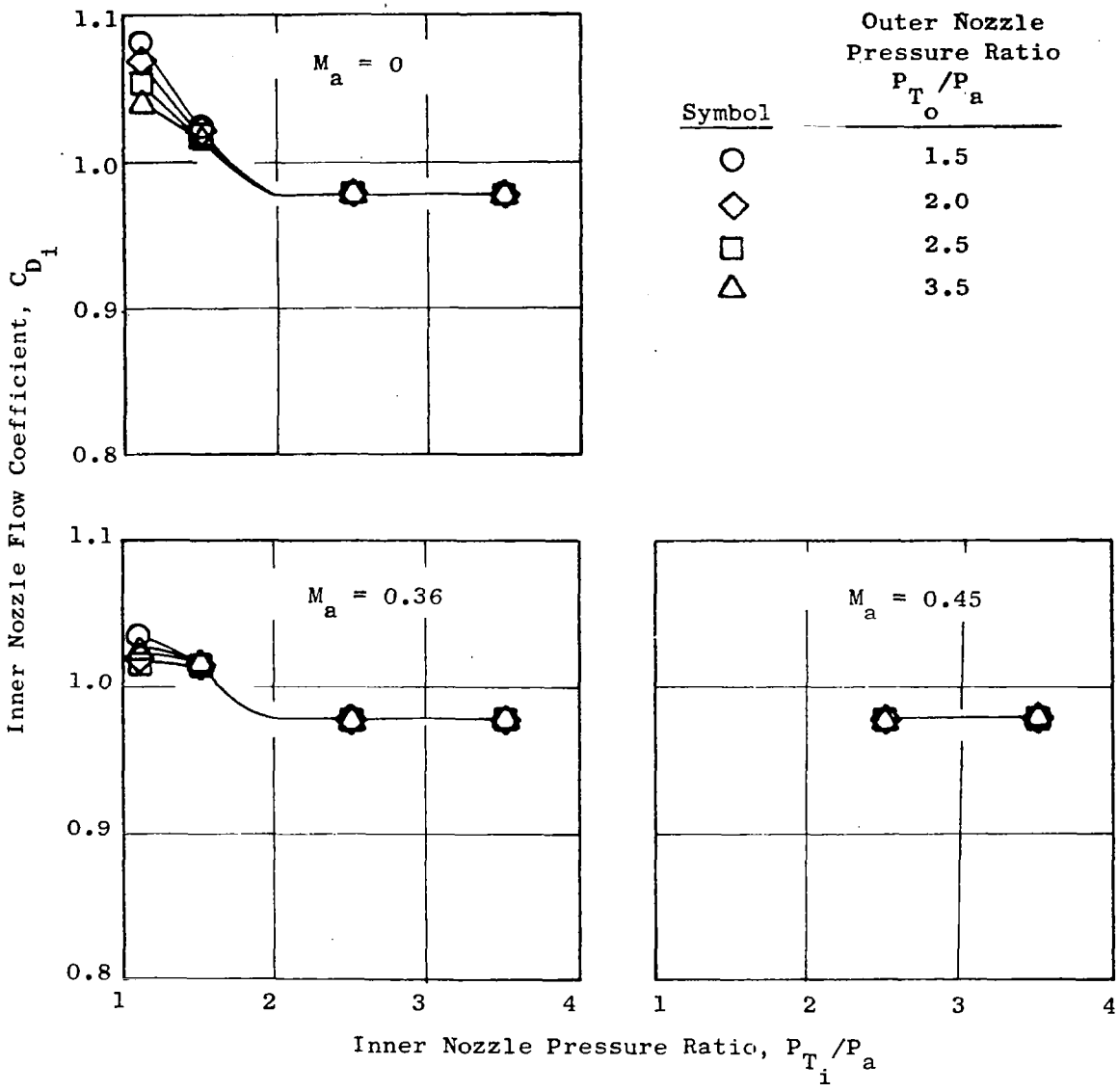

Figure V-6. Inner Nozzle Flow Coefficients for Configuration 6 [R_r^o = 0.926, R_r^i = 0.8, Conical Inner Plug].

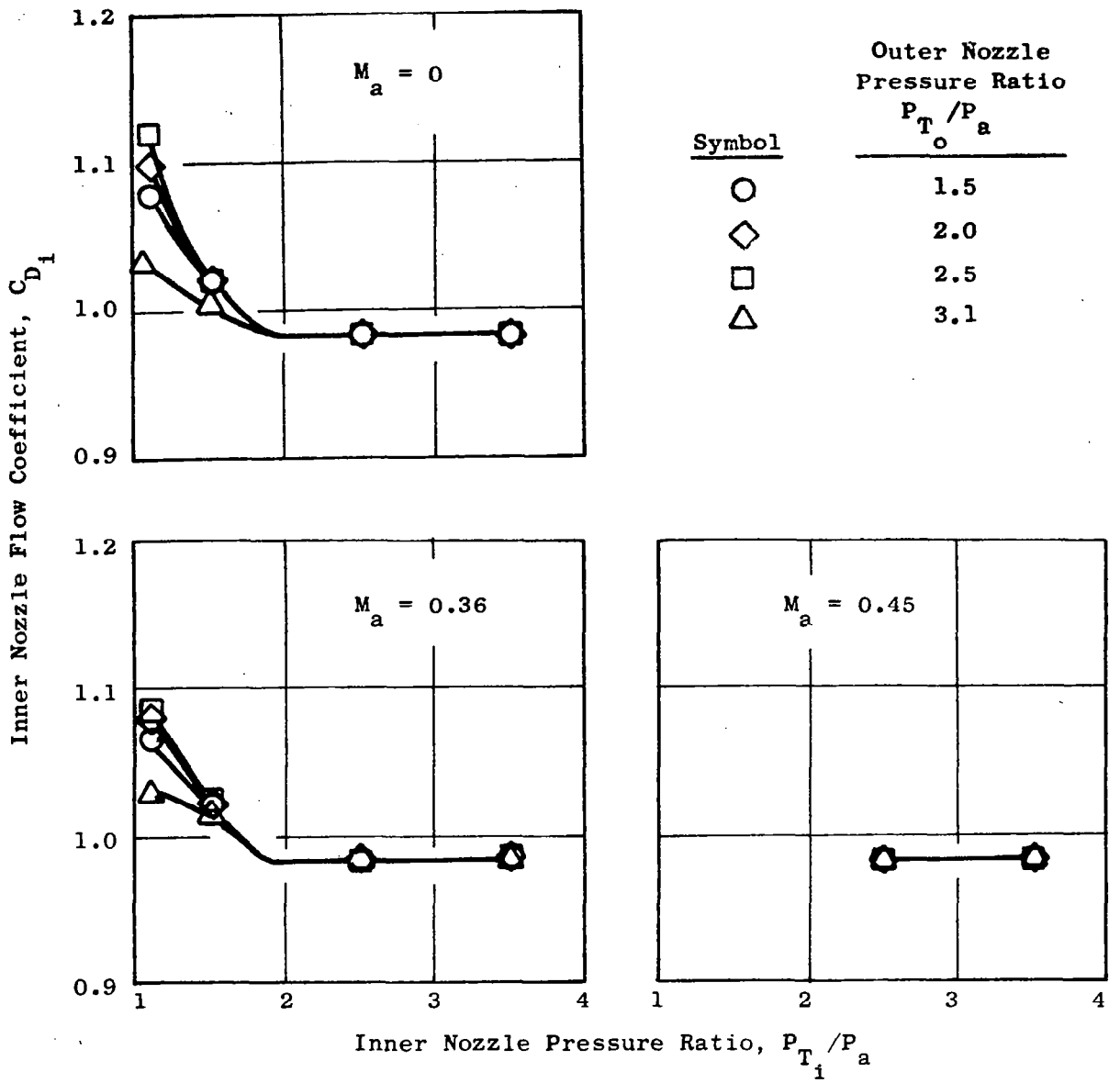

Figure V-7. Inner Nozzle Flow Coefficients for Configuration 7 [R_r^o = 0.853, R_r^i = 0.902, Conical Inner Plug].

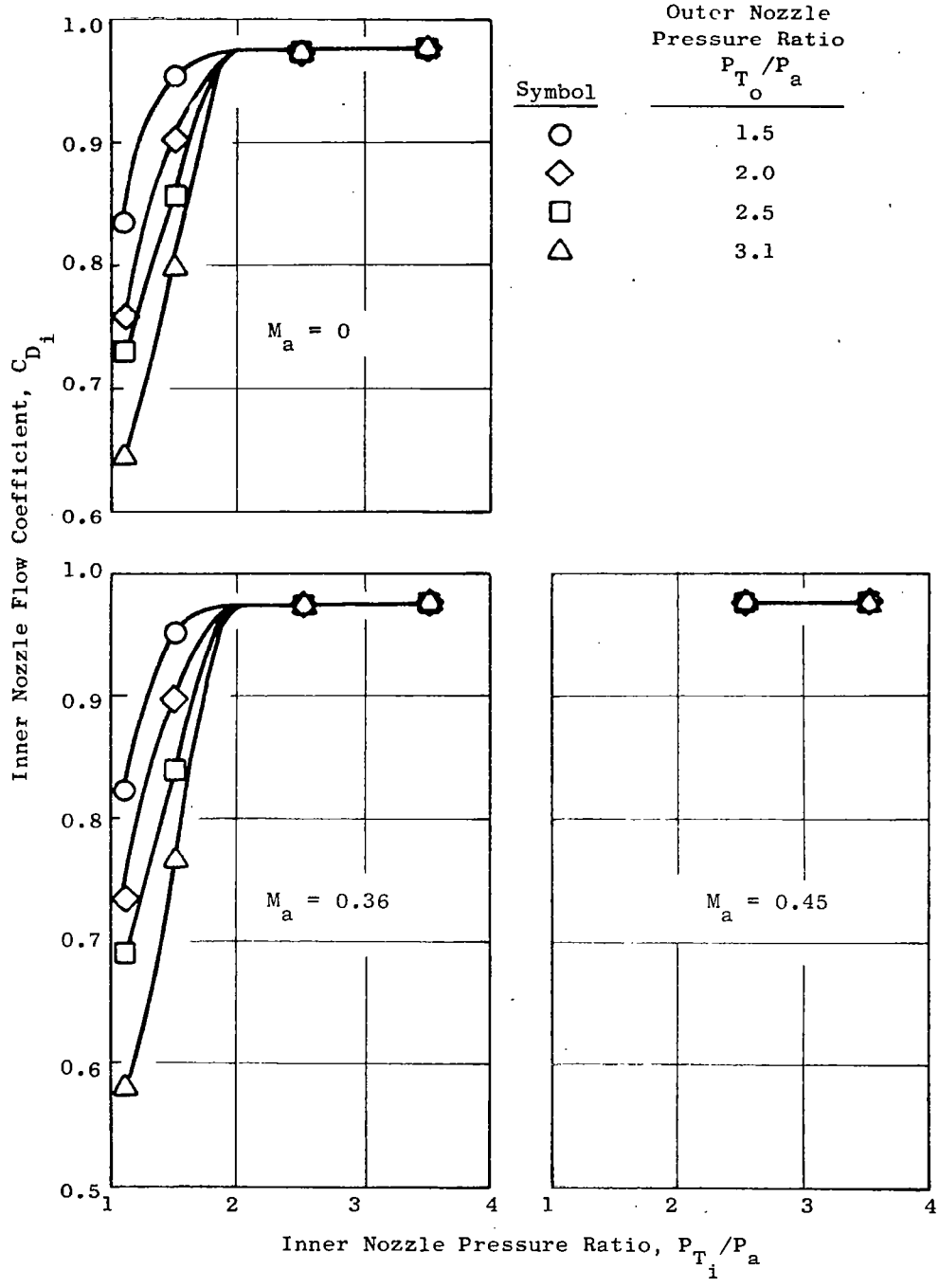

Figure V-8. Inner Nozzle Flow Coefficients for Configuration 8 [R_r^o = 0.853, R_r^i = 0.8, Bent Inner Plug].

1. Report No. NASA CR-3149	2. Government Accession No.	3. Recipient's Catalog No.
4. Title and Subtitle ACOUSTIC AND AERODYNAMIC PERFORMANCE INVESTIGATION OF INVERTED VELOCITY PROFILE COANNULAR PLUG NOZZLES		5. Report Date February 1981 6. Performing Organization Code
7. Author(s) P. R. Knott, J. T. Blozy, and P. S. Staid		8. Performing Organization Report No. R79AEG388 10. Work Unit No.
9. Performing Organization Name and Address General Electric Company Aircraft Engine Group Cincinnati, Ohio 45215		11. Contract or Grant No. NAS3-19777 13. Type of Report and Period Covered Contractor Report
12. Sponsoring Agency Name and Address National Aeronautics and Space Administration Washington, D.C. 20546		14. Sponsoring Agency Code

15. Supplementary Notes

Final report. Project Manager, Orlando A. Gutierrez, Fluid Mechanics and Acoustics Division, NASA Lewis Research Center, Cleveland, Ohio 44135.

16. Abstract

This report summarizes the results of model scale parametric static and wind tunnel aerodynamic performance tests on unsuppressed coannular plug nozzle configurations with inverted velocity profile. The nozzle configurations are high-radius-ratio coannular plug nozzles applicable to dual-stream exhaust systems typical of a variable cycle engine for Advanced Supersonic Transport application. In all, seven acoustic models and eight aerodynamic performance models were tested. The nozzle geometric variables included outer stream radius ratio (ranging from 0.85 to 0.926), inner stream to outer stream ratio (ranging from 0.33 to 1.56), and inner stream plug shape. Outer stream velocities ranged from 300 to 780 m/sec and outer stream total temperatures ranged from 400 to 970 K. Inner stream velocities ranged from 0 to 550 m/sec and inner stream total temperatures ranged from ambient to 925 K. All tests were of the inverted flow type - high velocity and temperature flows on the outside stream, and lower velocity and temperature on the inside stream. When compared to a conical nozzle at the same specific thrust, the results of the static acoustic tests with the coannular nozzles showed noise reductions of up to 7PNdB. Extensive data analysis showed that the overall acoustic results (OAPWL, PNL_{max}, OASPL) can be well correlated using the mixed stream velocity, $V_j mix$ (defined as the ratio of the ideal total thrust to the ideal weight flow), and the mixed stream density. Using only the outer stream velocity instead of the mixed stream velocity was found to be insufficient and to result in a poor data collapse. Results also showed that suppression levels are geometry and flow regulation dependent with the outer stream radius ratio, inner stream-to-outer stream velocity ratio and inner stream plug shape, as the primary suppression parameters. In addition, high-radius ratio coannular plug nozzles were found to yield shock associated noise level reductions relative to a conical nozzle, and a good engineering shock noise correlation parameter was determined to be the mixed stream shock strength defined as $\sqrt{(M_j^{mix})^2 - 1}$. The wind tunnel aerodynamic tests showed that static and simulated flight thrust coefficients at typical takeoff conditions are quite good - up to 0.98 at static conditions and 0.974 at a takeoff Mach number of 0.36. At low inner stream flow conditions significant thrust loss was observed. Using an inner stream conical plug resulted in 1% to 2% higher performance levels than nozzle geometries using a bent inner plug. All the detailed acoustic and aerodynamic test data obtained during this investigation are reported in detail in the Comprehensive Data Report, NASA CR-159575 and the NASA Contract Report 2990.

17. Key Words (Suggested by Author(s))	18. Distribution Statement		
Coannular plug nozzle jet noise; Supersonic jet noise reduction; Variable-cycle engine; Acoustic tests; Aerodynamic wind tunnel performance tests	Unclassified - unlimited STAR Category 71		
19. Security Classif. (of this report) Unclassified	20. Security Classif. (of this page) Unclassified	21. No. of Pages 258	22. Price* A12

* For sale by the National Technical Information Service, Springfield, Virginia 22161